

**TSUNAMI LOADS ON STRAIGHT AND
SKEWED BRIDGES – PART 1:
EXPERIMENTAL INVESTIGATION AND
DESIGN RECOMMENDATIONS**

Final Report

PROJECT TPF 5-307



Oregon Department of Transportation

**TSUNAMI LOADS ON STRAIGHT AND SKEWED BRIDGES –
PART 1: EXPERIMENTAL INVESTIGATION AND DESIGN
RECOMMENDATIONS**

Final Report

PROJECT TPF 5-307

by

Denis Istrati, Assistant Research Professor, Ph.D.
Ian G Buckle, Foundation Professor, Ph.D.

Department of Civil and Environmental Engineering
University of Nevada, Reno

for

Oregon Department of Transportation
Research Section
555 13th Street NE, Suite 1
Salem OR 97301

and

Federal Highway Administration
1200 New Jersey Avenue SE
Washington, DC 20590

February 2021

1. Report No. FHWA-OR-RD-21-12	2. Government Accession No.	3. Recipient's Catalog No.	
4. Title and Subtitle Tsunami Loads on Straight and Skewed Bridges – Part 1: Experimental Investigation and Design Recommendations		5. Report Date February 2021	
		6. Performing Organization Code	
7. Author(s) Denis Istrati, https://orcid.org/0000-0002-1210-0338 Ian G Buckle, https://orcid.org/0000-0002-7858-7054		8. Performing Organization Report No.	
9. Performing Organization Name and Address Department of Civil and Environmental Engineering University of Nevada, Reno, MS 0258 Reno, Nevada 89557		10. Work Unit No. (TRAIS)	
		11. Contract or Grant No.	
12. Sponsoring Agency Name and Address Oregon Dept. of Transportation Research Section 555 13 th Street NE, Suite 1 Salem, OR 97301		13. Type of Report and Period Covered Federal Highway Admin. 1200 New Jersey Avenue SE Washington, DC 20590 Final Report	
		14. Sponsoring Agency Code	
15. Supplementary Notes			
16. Abstract: This report presents the results of a large-scale experimental investigation of tsunami impact on straight and skewed bridges. The 1:5 scale specimens had realistic structural components and dynamic properties, and were subjected to a range of simplified unbroken solitary waves and more realistic bores. The unique experimental data revealed: (a) the complexity of the tsunami inundation mechanism of bridges and the overloading of the offshore bearings and columns, due to the large overturning moment (OTM) generated by the wave slamming the offshore girder and overhang, (b) the significant difference between the effects introduced by simplified unbroken solitary waves and more realistic bores, (c) the major role of structural dynamics and fluid-structure interaction for the estimation of design forces, and the possibility of dynamic amplification when the bridge is impacted by a bore, (d) the increase of both the total uplift forces and the OTM in bridges with diaphragms due to the air-entrapment, (e) the dependence of the tsunami loads on the bridge type, with box-girder bridges witnessing on average uplift forces 134% higher than those in I-girder bridges, (f) the modification of the hydrodynamic flow caused by solid rails, which increases both the horizontal and downward tsunami loads, and (g) the promising use of air-vents in the deck as a mitigation strategy against tsunamis, in which both the number and the location of the venting holes are optimized in order to maximize the air release. Based on the above findings, the authors developed two simplified methods that can be used for the tsunami design of bearings and other structural components necessary for the survival of straight bridges. While the above findings are applicable to straight bridges, skewed ones witness more complex loads, including significant roll and yaw moments, which should be considered in their design. These moments lead to non-uniform distribution of the tsunami loads to the two supports of the deck and the individual bearings with (i) one abutment having to sustain up to 96% of the total horizontal force, and the other one up to 146% of the total uplift, and (ii) the bearings of the offshore obtuse corner attracting 95% of the total deck uplift.			
17. Key Words Tsunami, Loads, Flume experiments, Bores, Solitary Waves, Bridges, Skew, Design recommendations		18. Distribution Statement Copies available from NTIS, and online at www.oregon.gov/ODOT/TD/TP_RES/	
19. Security Classification (of this report) Unclassified	20. Security Classification (of this page) Unclassified	21. No. of Pages 221	22. Price

SI* (MODERN METRIC) CONVERSION FACTORS

APPROXIMATE CONVERSIONS TO SI UNITS					APPROXIMATE CONVERSIONS FROM SI UNITS				
Symbol	When You Know	Multiply By	To Find	Symbol	Symbol	When You Know	Multiply By	To Find	Symbol
<u>LENGTH</u>					<u>LENGTH</u>				
in	inches	25.4	millimeters	mm	mm	millimeters	0.039	inches	in
ft	feet	0.305	meters	m	m	meters	3.28	feet	ft
yd	yards	0.914	meters	m	m	meters	1.09	yards	yd
mi	miles	1.61	kilometers	km	km	kilometers	0.621	miles	mi
<u>AREA</u>					<u>AREA</u>				
in ²	square inches	645.2	millimeters squared	mm ²	mm ²	millimeters squared	0.0016	square inches	in ²
ft ²	square feet	0.093	meters squared	m ²	m ²	meters squared	10.764	square feet	ft ²
yd ²	square yards	0.836	meters squared	m ²	m ²	meters squared	1.196	square yards	yd ²
ac	acres	0.405	hectares	ha	ha	hectares	2.47	acres	ac
mi ²	square miles	2.59	kilometers squared	km ²	km ²	kilometers squared	0.386	square miles	mi ²
<u>VOLUME</u>					<u>VOLUME</u>				
fl oz	fluid ounces	29.57	milliliters	ml	ml	milliliters	0.034	fluid ounces	fl oz
gal	gallons	3.785	liters	L	L	liters	0.264	gallons	gal
ft ³	cubic feet	0.028	meters cubed	m ³	m ³	meters cubed	35.315	cubic feet	ft ³
yd ³	cubic yards	0.765	meters cubed	m ³	m ³	meters cubed	1.308	cubic yards	yd ³
~NOTE: Volumes greater than 1000 L shall be shown in m ³ .									
<u>MASS</u>					<u>MASS</u>				
oz	ounces	28.35	grams	g	g	grams	0.035	ounces	oz
lb	pounds	0.454	kilograms	kg	kg	kilograms	2.205	pounds	lb
T	short tons (2000 lb)	0.907	megagrams	Mg	Mg	megagrams	1.102	short tons (2000 lb)	T
<u>TEMPERATURE (exact)</u>					<u>TEMPERATURE (exact)</u>				
°F	Fahrenheit	(F-32)/1.8	Celsius	°C	°C	Celsius	1.8C+32	Fahrenheit	°F

*SI is the symbol for the International System of Measurement

ACKNOWLEDGEMENTS

The large-scale experiments presented in this report were funded by the Federal Highway Administration under Contract No. DTFH61-07-C-00031. Technical guidance was provided by Dr Wen-huei (Phillip) Yen (COR), Mr. Fred Faridazar (COR) and Ms. Sheila Duwadi (COR). The preparation of this report was funded by the Oregon Department of Transportation (ODOT) under Task 1 of Agreement No. 32399, “Verification of Tsunami Bridge Design Equations” awarded to University of Nevada Reno. Research coordination was provided by Jon Lazarus and technical guidance was given by Bruce Johnson and Albert Nako from ODOT.

The authors also wish to recognize Pedro Lomonaco and Solomon Yim, who assisted with the design and conduct of the experiments. Moreover, the authors wish to thank Tao Xiang, Anastasia Bitsani, Patrick Laplace, Chad Lyttle, Todd Lyttle, Tim Maddux, Alicia Lyman-Holt, James Batti, and Jeff Gent for their technical assistance during the experiments. Last but not least, the authors appreciate the assistance provided by Information Technology at the University of Nevada Reno and access to the High Performance Computing resources necessary to run the advanced Computational Fluid Dynamics and Fluid-Structure Interaction numerical analyses for the hydrodynamic design of the experiments.

DISCLAIMER

This document is disseminated under the sponsorship of the Oregon Department of Transportation and the United States Department of Transportation in the interest of information exchange. The State of Oregon and the United States Government assume no liability of its contents or use thereof.

The contents of this report reflect the view of the authors who are solely responsible for the facts and accuracy of the material presented. The contents do not necessarily reflect the official views of the Oregon Department of Transportation or the United States Department of Transportation.

The State of Oregon and the United States Government do not endorse products of manufacturers. Trademarks or manufacturers’ names appear herein only because they are considered essential to the object of this document.

This report does not constitute a standard, specification, or regulation.

TABLE OF CONTENTS

1.0	LARGE-SCALE HYDRODYNAMIC EXPERIMENTS OF TSUNAMI WAVE IMPACT ON COASTAL BRIDGES	1
1.1	BACKGROUND	1
1.2	LITERATURE REVIEW	2
1.2.1	<i>On-site surveys and experimental studies</i>	<i>2</i>
1.2.2	<i>Numerical and analytical studies</i>	<i>4</i>
1.2.3	<i>Studies focusing on the role of air</i>	<i>5</i>
1.3	OBJECTIVES OF RESEARCH STUDY	6
1.4	DESIGN OF LARGE-SCALE HYDRODYNAMIC EXPERIMENTS	7
1.4.1	<i>Bridge specimen</i>	<i>8</i>
1.4.2	<i>Facility</i>	<i>13</i>
1.4.3	<i>Flume bathymetry and bridge location in the LWF</i>	<i>14</i>
1.4.4	<i>Testing frame and installation in the flume</i>	<i>20</i>
1.5	WAVE MATRIX	23
1.6	STRUCTURAL MATRIX	25
1.7	INSTRUMENTATION	26
1.8	DATA ACQUISITION SYSTEM	29
2.0	TSUNAMI INUNDATION MECHANISM AND ASSOCIATED FORCES IN A BRIDGE WITH STEEL BEARINGS	31
	WAVE PROPAGATION AND PARTICLE VELOCITIES	31
2.2	TOTAL HORIZONTAL AND VERTICAL FORCES	34
2.3	DISTRIBUTION OF VERTICAL FORCES IN BEARINGS AND CONNECTIONS	36
2.4	OVERTURNING MOMENT	39
2.5	APPLIED TSUNAMI PRESSURES ON GIRDERS AND BRIDGE DECK	40
2.6	INUNDATION MECHANISM, ASSOCIATED FORCES AND PRACTICAL DESIGN RECOMMENDATIONS	43
2.7	EFFECT OF WAVE TYPE AND WATER DEPTH	46
2.8	APPLIED LOADING, INERTIA AND DYNAMIC AMPLIFICATION	48
2.9	REPEATABILITY AND UNCERTAINTY OF WAVE FORCES	51
2.10	SIMPLIFIED METHODOLOGY FOR ENGINEERING PRACTICE	57
3.0	THE ROLE OF STRUCTURAL FLEXIBILITY AND DYNAMIC FLUID-STRUCTURE-INTERACTION	63
3.1	INTRODUCTION	63
3.2	SELECTED RESULTS FOR DIFFERENT FLEXIBLE BRIDGE CONFIGURATIONS	64
3.3	THE ROLE OF INERTIA FORCES FOR STIFF AND FLEXIBLE BRIDGES	68
3.4	EFFECT OF BRIDGE FLEXIBILITY ON THE DYNAMIC FSI	69
3.4.1	<i>Flexibility of connections</i>	<i>69</i>
3.4.2	<i>Flexibility due to removal of shear keys</i>	<i>72</i>
3.4.3	<i>Lateral flexibility generated from substructure and removal of shear keys</i>	<i>74</i>
4.0	TSUNAMI INDUCED FORCES ON I-GIRDER BRIDGES WITH CROSS-FRAMES AND DIAPHRAGMS	79
4.1	INTRODUCTION	79

4.2	TSUNAMI EFFECTS ON AN I-GIRDER BRIDGE WITH DIAPHRAGMS.....	80
4.3	BRIDGES WITH CROSS-FRAMES VS DIAPHRAGMS: THE ROLE OF AIR-ENTRAPMENT	87
4.3.1	<i>Pressures histories.....</i>	87
4.3.2	<i>Force, moment and deck rotation histories.....</i>	89
4.3.3	<i>Maximum pressures and forces.....</i>	91
4.4	MEASURED UPLIFT FORCES VS BUOYANCY	100
4.4.1	<i>Total Forces vs Buoyancy.....</i>	100
4.4.2	<i>Increase of Uplift Forces vs Buoyancy of Trapped Air.....</i>	103
4.5	PRACTICAL RECOMMENDATIONS FOR ENGINEERING DESIGN	106
4.5.1	<i>Total Deck Uplift.....</i>	106
4.5.2	<i>Non-Dimensional Uplift Curves for Bearings and Connections.....</i>	107
4.5.3	<i>Limitations.....</i>	110
5.0	TSUNAMI PERFORMANCE OF BOX-GIRDER BRIDGES.....	113
5.1	INTRODUCTION.....	113
5.2	FORCE AND PRESSURE ON A BOX-GIRDER FOR SOLITARY WAVES AND BORES.....	114
5.3	TSUNAMI FORCES ON DIFFERENT BRIDGE SUPERSTRUCTURES: I-GIRDER VS BOX-GIRDER	118
5.3.1	<i>Connection forces and deck rotation histories.....</i>	118
5.3.2	<i>Maximum deck uplift and uplift forces in individual bearings.....</i>	122
6.0	RETROFITTING OF BRIDGES VIA THE USE OF DECK AIR-VENTS	125
6.1	INTRODUCTION.....	125
6.2	AIR-VENTS FOR AN I-GIRDER BRIDGE WITH DIAPHRAGMS	126
6.2.1	<i>Pressure, force and deck rotation histories.....</i>	126
6.2.2	<i>Comparison of maximum values.....</i>	129
6.2.3	<i>Inundation sequence for bridge case ST7.....</i>	132
6.3	EFFECT OF NUMBER OF AIR-VENTS	134
6.3.1	<i>Pressure and force histories.....</i>	134
6.3.2	<i>Comparison of maximum values.....</i>	135
6.3.3	<i>Inundation sequence for bridge case ST9.....</i>	137
6.4	AIR-VENTS FOR AN I-GIRDER BRIDGE WITH CROSS-FRAMES.....	138
6.5	EFFECTIVENESS OF AIR-VENTS IN BRIDGES WITH CROSS-FRAMES AND BRIDGES WITH	
	DIAPHRAGMS	140
7.0	EFFECT OF SOLID RAILS ON THE TSUNAMI-INDUCED FORCES AND	
MOMENTS	143	
7.1	INTRODUCTION.....	143
7.2	HORIZONTAL AND VERTICAL FORCES	144
7.3	MOMENTS	147
7.4	UPLIFT FORCES IN INDIVIDUAL BEARINGS	149
7.5	APPLIED PRESSURES – EXPLANATION OF OBSERVED BEHAVIOR.....	151
7.6	DISCUSSION AND PRELIMINARY RECOMMENDATIONS FOR DESIGN	155
7.6.1	<i>Total horizontal force.....</i>	155
7.6.2	<i>Other design parameters.....</i>	157
8.0	TSUNAMI FORCES ON A SKEW BRIDGE AND DEMAND IN INDIVIDUAL	
STRUCTURAL COMPONENTS	163	
8.1	DESCRIPTION OF SPECIMEN AND EXPERIMENTAL PROGRAM.....	163
8.2	TOTAL FORCES AND MOMENTS.....	165

8.3	TSUNAMI-INDUCED DEMAND ON BENT CAPS/ABUTMENTS.....	167
8.3.1	<i>Lateral forces</i>	167
8.3.2	<i>Vertical forces</i>	170
8.4	FORCE DISTRIBUTION IN STEEL BEARINGS.....	172
8.5	DEPENDENCE OF FORCES ON THE WAVE TYPE AND HEIGHT	176
8.5.1	<i>Total forces and moments</i>	176
8.5.2	<i>Uplift in bearings and bent caps/abutments</i>	176
8.6	COMPARISON OF TSUNAMI EFFECTS ON STRAIGHT AND SKEW BRIDGES.....	178
9.0	CONCLUSIONS AND FUTURE WORK	181
9.1	SUMMARY AND CONCLUSIONS.....	181
9.2	FUTURE WORK.....	184
10.0	REFERENCES	187
	APPENDIX A DESIGN DRAWINGS OF THE STRAIGHT BRIDGE.....	A-1

LIST OF TABLES

Table 1.1:	Summary of Bridge Characteristics.....	10
Table 1.2:	Wave Heights and Water Depths Tested in the First Stage of the Experiments.....	24
Table 1.3:	Wave Heights and Water Depths Tested in the Second Stage of the Experiments	24
Table 1.4:	Bridge Cases Focusing on the Role of the Dynamic Fluid-Structure Interaction.....	26
Table 1.5:	Bridge Cases Focusing on the Role of Air-entrapment, the Variation of Tsunami Forces Relative to the Bridge Type, and the use of Air-vents as Counter-measures against Tsunamis.....	26
Table 1.6:	Flume Instrumentation and Corresponding Locations	28
Table 2.1:	Ratio of Maximum Uplift Forces Recorded in the Bearings of each Girder Relative to the Maximum of the Total Uplift Force	39
Table 2.2:	Maximum Total, Slamming and Quasi-static Forces for Ten Runs of H=1.40m and Bridge Configuration ST1	57
Table 2.3:	Maximum Vertical Forces in the Bearings below the Four Girders for Ten Runs of H=1.40m and Bridge Configuration ST1	57
Table 2.4:	Ratios of Bearing and Column-bent Cap Connection Uplift Forces Calculated from Load Case 1 of the Improved Method to the Ones Recorded in the Experiments.....	61
Table 2.5:	Ratios of Bearing and Column-bent Cap Connection Uplift Forces Calculated from Load Case 2 of the Improved Method to the Ones Recorded in the Experiments.....	61
Table 2.6:	Ratios of Bearing Forces Calculated from Load Case 3 of the Improved Method to the Ones Recorded in the Experiments	62
Table 4.1:	Maximum Recorded Pressures below the Deck at the Overhang and in the Middle Chamber for the Bridge with Diaphragms (ST5).....	86
Table 4.2:	Maximum Recorded Pressures on the Offshore Girder G1 and on the Interior Girder G2 for the Bridge with Diaphragms (ST5).....	87
Table 4.3:	Maximum Recorded Wave Heights at wg2 and wg12	93
Table 4.4:	Maximum Total Uplift Forces for ST2 and ST5.....	96
Table 4.5:	Maximum Quasi-static Uplift Forces for ST2 and ST5.....	96
Table 4.6:	Maximum Vertical Forces Recorded in Offshore and Onshore Piers	99
Table 4.7:	Maximum Vertical Forces Recorded in Offshore and Onshore Bearings	100

Table 4.8: Maximum Vertical Forces Recorded in Bearings of Interior Girders	100
Table 4.9: Comparison of the Calculated Buoyancy Forces with the Measured Uplift Forces on the Deck with Cross-frames (ST2) and the one with Diaphragms (ST5).....	105
Table 5.1: Maximum vertical forces recorded in offshore and onshore bearings	118
Table 5.2: Maximum Uplift Forces for Bridge Types ST2, ST5 and ST6 and d=2.0m	123
Table 6.1: Maximum Total Uplift Forces for the Bridges with and Without Air-vents	131
Table 6.2: Maximum Uplift Forces in the Columns of Piers for the Bridges with a Solid Deck (ST5) and with a Vented Deck (ST7).....	132
Table 6.3: Maximum Uplift Forces in the Bearings for the Bridges with a Solid Deck (ST5) and with a Vented Deck (ST7)	132
Table 6.4: Maximum Total Uplift Forces for Different Number of Air-vents.....	137
Table 6.5: Maximum Uplift Forces in the Onshore Bearings and Column Piers for Different Number of Air-vents.....	137
Table 6.6: Total Uplift Forces for Bridge Cases ST2 and ST10	140
Table 6.7: Uplift Forces in the Columns of the Piers for Bridge Cases ST2 and ST10.....	140
Table 6.8: Uplift Forces in the Bearings for Cases ST2 and ST10.....	140
Table 6.9: Total Uplift Forces for Bridges with Cross-frames and Diaphragms.....	141
Table 8.1: Wave Heights and Water Depths Tested in the Skewed Bridge Experiments.....	165
Table 8.2: Ratios of Maximum Horizontal and Uplift Forces Recorded in the Skewed Bridge Relative to the Respective Forces of the Straight Bridge	180

LIST OF FIGURES

Figure 1.1: Damaged bridges after the 2011 tsunami in Japan: (a) Koizumi bridge on the left (source: EERI Oct. 2011) and (b) Bridge in Rikuzentakata on the right (source: EERI Sept. 2011).....	1
Figure 1.2: Damaged bridges after the 2011 tsunami in Japan: (a) Utatsu bridge on the left and (b) Tsuya railway bridge on the right (adapted from Yashinski. M 2012).....	2
Figure 1.3: Finalized rebar layout of the deck (top) and framing plan with girders and cross-frames (bottom), adapted from Reno Iron Works (Appendix C).....	11
Figure 1.4: Bridge steel components during the assembly (left) and before the concrete pouring (right).....	12
Figure 1.5: Four steel bearings connected to the bent cap (top-left), shear-key in contact with the top plate of the elastomeric bearings (top-right), and details of the connections between the girders, steel bearings, load cells and bent cap (bottom), during the pre-test assembly in the Large-Scale Structures Laboratory at the University of Nevada, Reno	12
Figure 1.6: I-girder bridge connected to the steel bent caps during the pre-test assembly (top and bottom-left) and instrumentation of cross-frames with strain gages.....	13
Figure 1.7: Large Wave Flume (LWF) facility with default bathymetry in the O.H. Hinsdale Wave Research Laboratory at OSU (source: http://wave.oregonstate.edu/large-wave-flume)	14
Figure 1.8: Full-scale CFD model of the Large Wave Flume at Oregon State University, with the adjusted bathymetry and the bridge specimen in LS-DYNA (to scale)	17
Figure 1.9: Snapshot of the contours of the fluid velocities at t=2.55sec (top), 9.51sec (middle), and t=11.43sec for two CFD models with 10cm (left) and 2.5cm (right) mesh size respectively	18

Figure 1.10: Snapshot of the contours of the fluid velocities during the wave propagation and breaking, for the CFD model with 2.5cm mesh size and a wave with $H=1.20\text{m}$ and $d=2.0\text{m}$	19
Figure 1.11: Cross-section of the Large Wave Flume (LWF) depicting the bathymetry, bridge location and flume instrumentation	19
Figure 1.12: Numerical Model of the bridge setup in CSI Bridge	21
Figure 1.13: Cross-section of the experimental setup at the bridge location depicting the major components (test frame, bridge specimen, bent caps and connecting elements)	21
Figure 1.14: Installation of the bridge with steel bearings in the LWF	22
Figure 1.15: View of the bridge specimen with the LWF empty (top) and filled with water (bottom) before the hydrodynamic tests	23
Figure 1.16: Cross-section of the experimental setup at the bridge location depicting the major components and the bridge instrumentation	28
Figure 1.17: Plan view of the experimental setup at the bridge location depicting the location of the load cells and pressure gages installed on the bridge	29
Figure 2.1: Bridge with steel-bearings connected to the bent caps during the pre-assembly in the Large-Scale Structures Laboratory at the University of Nevada, Reno	32
Figure 2.2: Surface elevation along the flume for a solitary wave with $H=0.70\text{m}$ (top) and a bore with $H=1.20\text{m}$ (bottom)	32
Figure 2.3: Theoretical and measured free-surface at $wg1$ for $H=0.55\text{m}$ (top-left), $H=0.70$ (top-right), $H=0.90\text{m}$ (bottom-left) and $H=1.20\text{m}$ (bottom-right).....	33
Figure 2.4: Theoretical and measured velocities at the bays in front of the bridge (left) and behind the bridge (right) for $H=0.70\text{m}$	33
Figure 2.5: Maximum total uplift forces measured in the bearings and piers for ST1	34
Figure 2.6: Total horizontal and vertical forces measured in the connections for $H=0.70\text{m}$ (left) and $H=1.20\text{m}$ (right).....	35
Figure 2.7: Total horizontal forces (left) and total uplift forces measured in the connections as a function of H_{input} (top) and H_{wg12} (bottom) for the bridge with steel bearing	35
Figure 2.8: Uplift forces in the steel bearings for $H=0.70\text{m}$ (top) and $H=1.20\text{m}$ (bottom)	37
Figure 2.9: Uplift forces measured in the steel bearings for several solitary waves (left) and bores (right).....	38
Figure 2.10: Maximum uplift forces measured in the offshore bearings versus the maximum total uplift for several solitary waves (left) and bores (right).....	38
Figure 2.11: Calculation of the overturning moment.....	40
Figure 2.12: Uplift forces in the offshore steel bearings, total uplift force and moment in the connections for $H=0.70\text{m}$ (left) and $H=1.20\text{m}$ (right).....	40
Figure 2.13: Pressures applied on the girders (left) and below the bridge (right) for $H=0.70\text{m}$ (top) and $H=1.20\text{m}$ (bottom).....	42
Figure 2.14: Pressures on the offshore side of the bridge for several wave heights.....	42
Figure 2.15: Pressures on the girders of the bridge wave heights	43
Figure 2.16: Pressures at different locations below the deck of the bridge.....	43
Figure 2.17: Forces, moment and normalized pressures histories	45
Figure 2.18: Tsunami inundation mechanism of coastal bridges	46
Figure 2.19: Decomposition of the total horizontal (left) and vertical (right) connection forces into slamming and quasi-static components $H=1.20\text{m}$	47
Figure 2.20: Total horizontal and uplift forces measured in the steel bearings.....	48

Figure 2.21: Maximum total (top) and quasi-static (bottom), horizontal (left) and uplift (right) forces for the tested solitary wave heights.....	48
Figure 2.22: Deck accelerations in the horizontal direction (left) and vertical direction (right) for H=0.70m (top) and H=1.20m (bottom)	50
Figure 2.23: Applied horizontal forces, forces in links and sum of inertia and links forces for H=1.20m (top), H=1.30m (middle) and H=1.40m (bottom) for ST1	51
Figure 2.24: Wave heights measured at wg2 (top-left), wg7 (top-right), wg8 (middle-left), wg9 (middle-right), wg12 (bottom-left) and uswg1 (bottom right) for the four runs of H=1.40m and the bridge with steel bearings	53
Figure 2.25: Pressure histories on the offshore girder (top) and below the overhang (bottom) for the four runs of H=1.40m and the bridge with steel bearings.....	54
Figure 2.26: Total horizontal forces recorded in links (top) and calculated from integration of pressures (bottom) for the four runs of H=1.40m and ST1	55
Figure 2.27: Total vertical forces recorded in the bearings (top) and piers (bottom) for the four runs of H=1.40m and ST1	56
Figure 2.28: Load cases for improved physics-based simplified method	59
Figure 3.1: Details of the bearings, shear keys and substructure links used to study the effect of bridge flexibility and the role of dynamic FSI.....	63
Figure 3.2: Vertical forces in bearings (left) and total horizontal and vertical forces measured in the shear keys and bearings respectively (right) for a solitary wave with H=0.70m (top) and a bore with H=1.20m (bottom).	64
Figure 3.3: Maximum uplift forces in different bearings for solitary waves (top) and bores (bottom) for a 2m water depth	65
Figure 3.4: Total horizontal forces recorded in links as a function of horizontal displacements (left) and calculated shear strains in the bearings (right) for the bridge with elastomeric bearings and no shear keys for a bore with H=1.20	65
Figure 3.5: Total horizontal forces in links (top), horizontal displacements (middle) and calculated stiffness (bottom), of the bridge with elastomeric bearings and no shear keys for a solitary wave with H=0.70m.....	66
Figure 3.6: Total horizontal and vertical connection forces for the bridge with the medium substructure springs (top), the one with the flexible springs (middle) and the one with no shear keys (bottom), for a solitary wave with H=0.70m (left) and a bore with H=1.20m (right).....	67
Figure 3.7: Applied horizontal forces, forces in links and sum of inertial and link forces for the stiff configuration ST2 (top) and flexible configurations ST11 (middle) and ST3 (bottom) for a bore with H=0.90m	69
Figure 3.8: Time histories (top) and FFTs (bottom) of total horizontal (left) and vertical (right) forces in the connections for bridge cases ST1 and ST2 and H=0.70m.....	71
Figure 3.9: Uplift forces in steel bearings (left) and elastomeric bearings (right) for H=1.20m ..	71
Figure 3.10: Total uplift force (top-left), total horizontal force (top-right), uplift force in offshore bearings (middle-left), uplift forces in bearings of girder G2 (middle-right) and uplift forces in onshore bearings (bottom) for ST1 and ST2.....	72
Figure 3.11: Total horizontal (left) and vertical (right) connection forces for H=0.70m (top).....	73
Figure 3.12: Total uplift forces (top-left), total horizontal forces (top-right) and uplift force in onshore bearings (bottom) for ST2 and ST11.....	74

Figure 3.13: Total horizontal (left) and vertical (right) connection forces for $H=0.55\text{m}$ (top), $H=0.70\text{m}$ (middle) and $H=1.20\text{m}$ (bottom)	75
Figure 3.14: Total horizontal (top) and uplift (bottom) connection forces for bridge configurations ST2, ST3, ST4 and ST11	76
Figure 3.15: Uplift forces in offshore bearings (top) and bearings of girder G2 (bottom) for bridge configurations ST2, ST3, ST4 and ST11	77
Figure 4.1: I-girder Bridge with cross-frames during the assembly in the Large-Scale Structures Laboratory at the University of Nevada, Reno	79
Figure 4.2: I-girder Bridge with plywood diaphragms during the assembly in the Large-Scale Structures Laboratory at the University of Nevada, Reno	80
Figure 4.3: Vertical forces in bearings (top-left) and piers (top-right), displacements (bottom left) and vertical forces with associated moment (bottom-right) for bridge case ST5 and $H=0.42\text{m}$	81
Figure 4.4: Pressures on girders (left) and below the deck (right) for ST5 and $H=0.42\text{m}$	83
Figure 4.5: Normalized vertical forces and pressures below the bridge deck for ST5 and $H=0.42\text{m}$	83
Figure 4.6: Normalized horizontal forces and pressures on the girders for ST5 and $H=0.42\text{m}$	84
Figure 4.7: Maximum recorded pressures at four different locations recorded below the bridge deck for unbroken solitary waves (left) and for bores (right) for the bridge with diaphragms (ST5).....	85
Figure 4.8: Maximum recorded pressures on the four girders for unbroken solitary waves (left) and for bores (right) for the bridge with diaphragms (ST5)	86
Figure 4.9: Surface elevation at the wave gage at wg1 close to the wavemaker (left) and at wg12 close to the bridge (right) for a wave with $H=0.42\text{m}$	88
Figure 4.10: Pressure on the offshore girder (top-left), below the deck at the overhang (top-right), on the 2 nd girder (middle-left), below the deck in the offshore chamber (middle-right), on the 3 rd girder (bottom-left) and below the deck in the middle chamber (middle-right), for $H=0.42\text{m}$	89
Figure 4.11: Total horizontal forces recorded in the link (left) and total vertical forces recorded in the piers (right) for $H=0.42\text{m}$	90
Figure 4.12: Bridge deck rotation (left) and moment (right) for $H=0.42\text{m}$	91
Figure 4.13: Vertical slamming (left) and quasi-static forces (right) recorded in the bearings for $H=0.42\text{m}$	91
Figure 4.14: Maximum wave heights measured in front of the bridge for $d=1.90\text{m}$ (left) and $d=2.0\text{m}$ (right)	92
Figure 4.15: Maximum pressures on interior girder G2 (left) and on interior girder G3 (right) for all the wave heights tested for a 2.0m water depth.	94
Figure 4.16: Maximum pressures below the deck in the offshore chamber (left) and in the middle chamber (right) for all the wave heights tested for a 2.0m water depth.	94
Figure 4.17: Maximum total uplift forces for all the wave heights tested for ST2 and ST5 with a 2.0m water depth.	95
Figure 4.18: Maximum vertical forces in different bearings along the abutments for bridge configurations ST2 (left) and ST5 (right) and a set of wave heights	97
Figure 4.19: Maximum vertical forces in the piers for bridge configurations ST2 (left) and ST5 (right) and waves of different height	98

Figure 4.20: Maximum vertical forces in offshore (top) onshore (bottom) columns of the piers for all the wave heights tested for a water depth of 1.90m (left) and 2.0m (right)	98
Figure 4.21: Calculated buoyancy and recorded maximum uplift forces for the deck with cross-frames (left) and the one with solid diaphragms (right), for $d=1.90\text{m}$ (top) and $d=2.00\text{m}$ (bottom)	103
Figure 4.22: Maximum normalized uplift forces in bearings (top) and columns (bottom) of the deck with cross-frames, for all the solitary waves (left) and bores (right) tested in the flume	108
Figure 4.23: Envelopes of maximum normalized uplift forces in bearings (left) and columns (right) of the deck with cross-frames (top) and the one with solid diaphragms (right)	109
Figure 4.24: Non-dimensional design curves for the elastomeric bearings and connections of open-girder decks with cross-frames (ST2) and solid diaphragms (ST5)	110
Figure 5.1: Box-girder bridge during the pre-test assembly phase in the Large-Scale Structures Laboratory at the University of Nevada, Reno	113
Figure 5.2: Assembly of the box-girder bridge in the O.H. Hinsdale Large Wave Flume at Oregon State University	114
Figure 5.3: Box-girder Bridge with attached instrumentation ready for testing in the O.H. Hinsdale Large Wave Flume at Oregon State University	114
Figure 5.4: Horizontal and vertical forces for (a) solitary waves (top) with $H=0.36\text{m}$ (left), $H=0.42\text{m}$ (middle) and $H=0.55\text{m}$ (right), and (b) bores (bottom) with $H=0.90\text{m}$ (left), $H=1.00$	116
Figure 5.5: Vertical forces in bearings for (a) solitary waves (top) with $H=0.36\text{m}$ (left), $H=0.42\text{m}$ (middle) and $H=0.55\text{m}$ (right), and (b) bores (bottom) with $H=0.90\text{m}$ (left), $H=1.00\text{m}$ (middle) and $H=1.20\text{m}$ (right) for the box-girder bridge (ST6).....	116
Figure 5.6: Pressures under the overhang and the soffit for (a) solitary waves (top) with $H=0.36\text{m}$ (left), $H=0.42\text{m}$ (middle) and $H=0.55\text{m}$ (right), and (b) bores (bottom) with $H=0.90\text{m}$ (left), $H=1.00\text{m}$ (middle) and $H=1.20\text{m}$ (right) for the box-girder bridge (ST6).....	117
Figure 5.7: Normalized pressures below the deck and normalized total vertical force in the bearing connections for a solitary wave with $H=0.55\text{m}$ (left) and a bore with $H=1.00\text{m}$ (right) for the box-girder bridge (ST6).....	117
Figure 5.8: Maximum uplift forces in the bearings for solitary waves (left) and bores (right) for the box-girder bridge (ST6)	118
Figure 5.9: Forces in bearings and links for bridge configurations ST2 (left), ST5 (middle) and ST6 (right) for $H=0.42\text{m}$ (top) and $H=0.90\text{m}$ (bottom)	119
Figure 5.10: Total vertical forces for $H=0.42\text{m}$ (left) and $H=0.90\text{m}$ (right) for three bridge types	120
Figure 5.11: Vertical forces in offshore columns of piers for $H=0.42\text{m}$ (left) and $H=0.90\text{m}$ (right)	120
Figure 5.12: Quasi-static vertical forces for $H=0.42\text{m}$ (left) and $H=0.90\text{m}$ (right) for three bridge types.....	120
Figure 5.13: Total horizontal forces in links for $H=0.42\text{m}$ (left) and $H=0.90\text{m}$ (right) for the three bridge types.....	121
Figure 5.14: Deck rotation for $H=0.42\text{m}$ (left) and $H=0.90\text{m}$ (right) for the three bridge types	121
Figure 5.15: Pressure at the middle chamber for $H=0.42\text{m}$ (left) and $H=0.90\text{m}$ (right) for the three bridge types	121
Figure 5.16: Maximum total uplift forces for bridge cases ST2, ST5 and ST6 and $d=2.0\text{m}$	123

Figure 5.17: Maximum uplift forces in offshore bearings (left) and offshore piers (right) for bridge cases ST2, ST5 and ST6 and $d=2.0\text{m}$	124
Figure 5.18: Maximum uplift forces in onshore bearings (left) and onshore piers (right) for bridge cases ST2, ST5 and ST6 and $d=2.0\text{m}$	124
Figure 5.19: Bridge deck rotation (left) and vertical translation at onshore girder (right) for bridge cases ST2, ST5 and ST6 and $d=2.0\text{m}$	124
Figure 6.1: Drilling of holes in the deck of the bridge (top-left), view of the bridge deck with air-vents (ST7) before the installation of the diaphragms, and plan view of the bridge case ST7 with 0.85% vented area (bottom-left) and bridge case ST9 with 1.70% vented area (bottom right).....	125
Figure 6.2: Surface elevation at wg1 close to the wavemaker (left) and at wg12 close to the bridge (right) for $H=0.42\text{m}$ and bridge cases ST5 and ST6	126
Figure 6.3: Pressures below the deck in the offshore chamber (left) and in the middle chamber (right) for three solitary waves with $H=0.42\text{m}$ (top), $H=0.55\text{m}$ (middle) and $H=0.70\text{m}$ (bottom)	127
Figure 6.4: Pressure on the offshore girder (top-left), below the deck at the overhang (top-right), on the 2 nd girder (bottom-left) and below the deck in the offshore chamber (bottom-right) for $H=0.42\text{m}$ and bridge cases ST5 and ST7	128
Figure 6.5: Total vertical forces for two solitary waves with $H=0.42\text{m}$ (left) and $H=0.55\text{m}$ (right)	128
Figure 6.6: Vertical forces in offshore (left) and onshore (right) bearings for $H=0.42\text{m}$	129
Figure 6.7: Bridge deck rotation for $H=0.42\text{m}$ (left) and $H=0.55\text{m}$ (right)	129
Figure 6.8: Maximum pressures in offshore (left) and middle chamber (right) for bridge cases ST5 and ST7 and different wave heights.....	130
Figure 6.9: Total uplift forces for bridge cases ST5 and ST7 and different wave heights	131
Figure 6.10: Uplift forces in onshore bearings for cases ST5 and ST7 and different wave heights	131
Figure 6.11: Snapshots of inundation of the bridge with air-vents (ST7) for $H=0.70\text{m}$	133
Figure 6.12: Pressures below the deck in the offshore (top) and onshore (bottom) chamber for three waves with $H=0.42\text{m}$ (left), $H=0.70\text{m}$ (middle) and $H=0.90\text{m}$ (right) and two venting ratios	134
Figure 6.13: Total vertical forces (top) and vertical forces in offshore bearings (bottom) for three waves with $H=0.42\text{m}$ (left), $H=0.70\text{m}$ (middle) and $H=0.90\text{m}$ (right) and two venting ratios	135
Figure 6.14: Maximum pressures below the deck in the offshore (left) and onshore (right) chamber for the two different air-venting ratios and several wave heights.....	136
Figure 6.15: Total uplift forces (right) and for two different air-venting ratios	136
Figure 6.16: Uplift forces in onshore bearings (left) and onshore pier columns (right) for two different air-venting ratios and several wave heights.....	136
Figure 6.17: Snapshots of inundation of the bridge with 36 air-vents (ST9) for $H=0.70\text{m}$	139
Figure 7.1: Bridge with solid barriers during the hydrodynamic testing	143
Figure 7.2: Cross-section of the bridge deck without (top) and with (bottom) solid rails	144
Figure 7.3: Total horizontal and vertical forces on the bridge w/o rails (left) and with rails (right) for $H=0.70\text{m}$ (top) and $H=1.20\text{m}$ (center and bottom).....	146
Figure 7.4: Maximum total horizontal (left) and vertical (right) forces on the bridge with and without solid rails, calculated at the level of the bearings	147

Figure 7.5: Overturning moment histories at the level of the bearings for the bridge w/o rails (left) and with rails (right) for H=0.70m (top) and H=1.20m (bottom)	148
Figure 7.6: Maximum overturning moment on the bridge with and without solid rails, calculated at the level of the bearings	149
Figure 7.7: Maximum uplift force in the offshore and onshore bearings for the bridge with and without solid rails	150
Figure 7.8: Total uplift force and uplift in individual bearings of the bridge w/o rails (left) and with rails (right) for H=0.70m (top) and H=1.20m (bottom)	151
Figure 7.9: Applied pressures on the offshore face of the bridge with rails for H=0.70m (top) and H=1.20m (Run 14-bottom left and Run 13-bottom right)	153
Figure 7.10: Normalized horizontal applied pressures and forces on the bridge with rails for a bore with H=1.20m (Run 14-top and Run 13-bottom)	154
Figure 7.11: Depiction of parameters affecting the hydrodynamic loads on a bridge superstructure subjected to riverine flooding (source: Kerényi et al., 2009).....	155
Figure 7.12: Ratios of maximum total horizontal force recorded in the shear keys of the bridge with rails relative to the one without rails	157
Figure 7.13: Maximum overturning moment (top-left) and deck total uplift (top-right), maximum uplift in the offshore (center-right) and onshore (center-left) bearings, and maximum downward total force (bottom-left) with the maximum downward force in the onshore bearings (bottom-right) of the bridge with rails relative to the one without rails	160
Figure 7.14: Envelopes of normalized measured uplift in sets of bearings (left) and potential design curves (right), for a bridge with elastomeric bearings, cross-frames, and with or w/o solid rails	161
Figure 8.1: Experimental setup of the skew bridge in the Large Wave Flume at OSU, including the abutments (left), deck (center) and whole system (right)	164
Figure 8.2: Skew bridge during the hydrodynamic testing (left) and a plan view of the structure showing the location of the load cells (right).....	164
Figure 8.3: Total horizontal and vertical forces on the skew bridge for H=0.70m (top-left), H=0.90m (top-right), H=1.20m (bottom-left) and H=1.40m (bottom-right).....	166
Figure 8.4: Moment histories on the skew bridge for H=0.70m (top-left), H=0.90m (top-right), H=1.20m (bottom-left) and H=1.40m (bottom-right)	168
Figure 8.5: Lateral force histories (in X direction) per abutment of the skew bridge for H=0.70m (left) and H=0.90m (right)	169
Figure 8.6: Ratios of the maximum lateral abutment forces to the total lateral force for unbroken solitary waves (left) and bores (right)	170
Figure 8.7: Lateral force histories per abutment of the skew bridge, and moment histories for an unbroken solitary wave with H=0.70m (left) & and a bore with H=0.90m (right)	170
Figure 8.8: Roll moment, total vertical force and vertical force histories in each abutment of the skew bridge for an unbroken solitary wave with H=0.70m (left) and a bore with H=0.90m (right).....	171
Figure 8.9: Ratios of the maximum uplift abutment forces to the total uplift force for unbroken solitary waves (left) and bores (right)	172
Figure 8.10: Vertical force histories in steel bearings for H=0.70m	173
Figure 8.11: Vertical force histories in the steel bearings of the left and right abutment for an unbroken solitary wave with H=0.70m (top) and a bore with H=0.90m (bottom)	174

Figure 8.12: Ratios of the maximum uplift forces in individual bearings (top) relative to the total uplift force for unbroken solitary waves (left) and bores (right)	174
Figure 8.13: Roll and pitch moments together with the vertical bearing forces for a bore with H=1.20m	175
Figure 8.14: Maximum forces (left) and moments (right) for unbroken solitary waves (top) and bores (bottom)	177
Figure 8.15: Maximum uplift forces in individual abutments (top) and bearings (bottom) for unbroken solitary waves (left) and bores (right)	178
Figure 8.16: Envelopes of the maximum uplift in individual connections relative to the maximum total uplift.....	180

1.0 LARGE-SCALE HYDRODYNAMIC EXPERIMENTS OF TSUNAMI WAVE IMPACT ON COASTAL BRIDGES

1.1 BACKGROUND

In the last two decades humanity has witnessed large magnitude earthquakes with epicenters in the ocean (Indian Ocean 2004, Chile 2010 and Japan 2011), which generated tsunami waves of significant heights that caused unprecedented damage on coastal communities. Ports, buildings and infrastructure were severely damaged and bridges were washed away, cutting lifelines and hindering the efforts of rescue team to provide help to the people in need. In the 2004 Indian Ocean Tsunami 81 bridges located on the coast of Sumatra were washed away (Unjoh, 2007). In the 2011 Great East Japan Earthquake in Japan, many bridges were able to withstand the strong shaking, however approximately 252 bridges were washed away or moved by the tsunami (Maruyama et al., 2013a). The most severe and common type of failure in these bridges was the breaking of the connections between the superstructure and the substructure, which resulted in the unseating and wash out of the bridge deck by the tsunami waves. This damage pattern was observed for different types of bridges including (a) bridges with steel-girders and cross-frames (e.g Koizumi Bridge, Fig. 1.1), (b) bridges with pre-stressed (PC) girders and diaphragms (e.g. Utatsu Bridge, Fig. 1.2), (c) box-girder bridges (e.g. Tsuya Railway Bridge, Fig. 1.2), and (d) steel truss bridges (Fig. 1.1). Another common type of damage included the scour of piers and back-walls. These unforeseen events demonstrated the vulnerability of buildings and bridges to tsunami waves and highlighted the need to study and understand their effects on structures. Advancing this understanding is essential for developing recommendations and design guidelines for tsunami resilient structures. Therefore, the main objective of this research study and particular report is to advance the understanding of tsunami wave impact on bridges via large-scale hydrodynamic experiments.



Figure 1.1: Damaged bridges after the 2011 tsunami in Japan: (a) Koizumi bridge on the left (source: EERI Oct. 2011) and (b) Bridge in Rikuzentakata on the right (source: EERI Sept. 2011)



Figure 1.2: Damaged bridges after the 2011 tsunami in Japan: (a) Utatsu bridge on the left and (b) Tsuya railway bridge on the right (adapted from Yashinski, M 2012)

1.2 LITERATURE REVIEW

The extensive damage of bridges in recent tsunamis triggered the response of the society and research world in an attempt to improve the understanding of tsunami inundation of bridges. The academic community from around the world has responded to this need and several studies have been published in recent years. These studies included (i) on-site surveys and damage analysis (Kosa, 2012; Kawashima, 2012; Kasano et al., 2012; Kawashima and Buckle, 2013) (ii) small-scale experiments in wave flumes (e.g. Hayashi, 2013; Lau et al., 2011; Maruyama et al., 2013; Seiffert et al., 2014) and (iii) numerical simulations (e.g. Hayatdavoodi et al., 2015; Bricker and Nakayama, 2014; Kataoka and Kaneko, 2013; Nakao et al., 2013; Yim et al., 2011; Azadbakht, 2014; Istrati and Buckle, 2014).

1.2.1 On-site surveys and experimental studies

On-site investigations conducted by various research teams analyzed the failed bridges and revealed that the overflow can occur either in the form of transverse drag due to large horizontal wave forces or in the form of uplift and overturning due to the combination of large vertical and horizontal tsunami forces (Kawashima, 2012; Fu et al., 2013; Kawashima and Buckle, 2013). In addition, one of the studies (Kasano et al., 2012), which investigated the bridge performance in the Tohoku area after the 2011 tsunami, revealed that concrete bridges are less susceptible to tsunami inundation than steel bridges due to their increased weight and thus inertia.

Some of the experimental studies investigated tsunami loads on flat slabs (Seiffert et al., 2014), decks with girders (Lau et al., 2011; Araki et al., 2011; Maruyama et al., 2013; Rahman et al., 2014; Hayatdavoodi et al., Part II, 2014) and box-shaped decks (Hayashi, 2013). Others examined the use of perforations in the girders and parapets as means for reducing the horizontal tsunami load, and revealed a reduction of the horizontal load approximately equal to the reduction of the projected area (Lukkunaprasit, 2008). Some of the studies simulated the tsunami waves via unbroken solitary waves, while others via turbulent bores. In most of these experiments, the researchers constructed their bridge models from acrylic, wood or steel, they either supported the deck rigidly from top/bottom of the deck or allowed the deck to move freely on the supports, and measured both pressures and forces. Furthermore, they were all small-scale experiments with scale factors ranging from 1:100 to 1:35.

In a more recent study (Hoshikuma et al., 2013) the investigators conducted experiments to study the tsunami effects on bridges at a scale of 1:20. They examined several different cross-sections, including flat slabs and decks with two or four girders, in an attempt to give insight into the forces that various types of bridges have to withstand. In this experiment the bore was created via opening of a gate and release of water (dam-break approach), specimens were made of acrylic or wood and they were connected rigidly to a pier at the middle of the superstructure. These experiments demonstrated that the offshore bearings were uplifted while the onshore were compressed meaning that there exists significant overturning moment. In addition, trapped air between girders and a rotating flow in the chambers was observed during the inundation of the bridge.

The largest-scale experiment to date was conducted by Bradner et al., 2011, where they examined the performance of a 1:5 scaled pre-stressed bridge with six girders under the impact of hurricane waves. The study found a nonlinear dependence of both regular and random wave forces on the wave height and water depth, with the former ones being also dependent on the wave period. Momentum flux was also identified as a promising parameter for the development of analytical predictive model of hurricane wave forces. This study was unique because it examined for the first time both a rigid and a flexible substructure, so that the effect of dynamic wave-structure interaction could be studied. Interestingly, the study revealed that the bridge with a flexible substructure had to withstand larger horizontal forces than the rigid substructure, for all the tested wave heights (Higgins, 2013).

Another interesting observation made by previous researchers (e.g. Douglass et al., 2004; Lau et al., 2011) included the existence of an impulsive load (called “impact”, or “slamming” in the literature) at the time of the initial impact of the wave on the bridge, followed by a slowly-varying force (also called “quasi-static”) of smaller amplitude and longer duration. Douglass et al., 2004 developed empirical equations for predicting the horizontal and vertical varying forces based on a hydrostatic reference force. The study focused on the varying loads since the impact load has a short duration compared to the response of the structure and it is often not considered important by structural engineers. However, they suggested appropriate coefficients for calculating both the varying and the impact loads of hurricane wave. For the varying loads the suggested coefficients were equal to 1 in both directions, while for the impact loads they were 3 in the vertical and 6 in the horizontal direction, which indicated how much larger the impact loads could be.

Similarly, Lau et al., 2011 developed an empirical method for predicting the loads applied on the bridge by turbulent bores, using again a reference force as was done by Douglass et al., 2004. However, for the case of bores these researchers proposed the calculation of impulsive forces only in the horizontal direction and not in the vertical one. The recommended coefficients for the slowly-varying and impulsive loads were 1 and 1.5 respectively, meaning that the latter loads could be 2.5 times larger than the former ones. It must be noted that in the aforementioned approaches the impulsive coefficients had to be added to the coefficients of the varying loads in order to calculate the impact/impulsive forces. Despite the fact that these impact loads have been observed in previous studies, their effect on structures has not been thoroughly studied or understood. Interestingly, in offshore engineering the horizontal wave slamming force has been identified to be affected by the dynamic characteristics of the deck of offshore platforms (Bea et al., 2001).

While the majority of the aforementioned studies focused on the quantification of the tsunami-induced horizontal and vertical forces, some recent studies revealed the application of significant overturning moment on bridge decks. Istrati et al, 2018, showed that this moment is generated by the large slamming loads on the offshore girder and below the offshore overhang, and increases significantly the uplift forces in the offshore connections. Given the observed significance of the tsunami-induced moments some studies (Cai et al., 2018; Xiang et al., 2020), developed simplified predictive equations, which can estimate both the forces and the overturning moment applied on coastal bridges subjected to unbroken solitary waves.

1.2.2 Numerical and analytical studies

Apart from the experimental studies, several numerical analyses have been conducted to study the tsunami effects on bridges. Some of these studies conducted Computational Fluid Dynamics analyses using FLOW 3D (Lau et al., 2011), OPENFOAM (Hayatdavoodi et al., 2014; Bricker et al., 2012), and CADMAS-SURF (Kataoka et al., 2013). In the first two cases, the researchers tried to match the CFD analyses with their experimental results. In the latter case, the researchers took the tsunami effects (stresses, forces, moments) directly from the CFD analyses, which considers the structure as a rigid boundary and calculates the forces from integration of pressures, and compared their results with the bridge capacity, in an attempt to explain the failure/survival of certain bridges during the 2011 Japan Tsunami. Another research group (Yim et al, 2011) conducted numerical studies with a FEM-based multi-physics software program called LS-DYNA and calculated the tsunami loads for a bridge made of a rigid material. The advantage of using multi-physics software like LS-DYNA, compared to pure CFD software, is that it can solve the fluid flow around the structure as well as the equilibrium of the structure and its response, while the disadvantage is generally the associated high computational cost. In order to avoid this cost the investigators modeled the structure with a rigid material and pinned supports, and calculated the total applied tsunami loads without considering the bridge flexibility and dynamics.

Murakami et al., 2012 calculated the pressures from the CFD software CADMASSURF/3D and then re-applied these pressures as external loads on a flexible bridge model, sitting on bearings represented by elasto-plastic springs. This is a more realistic approach because it includes the flexibility of the deck and the connections when it applies the external tsunami load, however, it still neglects the bridge dynamic characteristics when calculating the tsunami loads using CFD software. Istrati and Buckle, 2014 conducted advanced fluid-structure interaction (FSI) analyses in LS-DYNA using an equivalent 2D bridge model with flexible deck and flexible connections, which showed that the dynamic characteristics of the bridge can affect both the external tsunami load applied on the bridge, as well as the forces in the connections. In addition, the study showed the existence of a rotational mode during the impact of tsunami waves, which put the offshore bearings in tension and the onshore ones in compression, increasing consequently the demand on the offshore connections. These analyses revealed the significance of bridge dynamics and FSI, however, due to the simplified 2D bridge model, it was noted that further 3D FSI analyses should be conducted and the numerical results should be validated against experimental data.

More recently Motley et al., 2015, developed 2D and 3D CFD numerical models of a 1:20 scale bridge model in OpenFOAM to examine the effect of the bridge skewness. Several skew angles between 0 and 40 degrees were examined. The study simulated the bridge as a rigid boundary

and calculated the applied load from integration of pressures. It revealed that the skew bridge is subjected to pitching and spinning moments and that there exists a force normal to the abutments that could lead to unseating, however the vertical forces were not dependent on the skew angle. Another recent study (Wei and Darlymple, 2016), simulated the same 1:20 scale straight bridge as Motley et al., 2015), using the weakly compressible Smoothed Particle Hydrodynamics (SPH) method in GPUSPH. The study focused on comparison of the numerical model with the experimental results obtained by Hoshikuma et al., 2013, and on further numerical analyses for studying the possibility of mitigating the tsunami effects bridges via the use of an offshore breakwater or the existence of another bridge on the seaward side of the main bridge. Recently, Zhu et al., 2018, implement the particle finite element method (PFEM) in OpenSees to simulate tsunami impact on bridge deck and validated the methodology using again the experiments conducted by Hoshikuma et al., 2013.

Apart from the experimental and numerical studies conducted so far, analytical studies are also available in the literature. Hayatdavoodi and Ertekin, 2015 (a&b), and Lo et al., 2014, calculated analytically the wave forces on a submerged horizontal plate for waves in shallow water. The former authors used the theory of directed fluid-sheets and solved the Level I Green–Naghdi equations, while the latter ones used the linear shallow-water wave theory. Both studies compared the analytical solutions with experimental data and good results were obtained.

1.2.3 Studies focusing on the role of air

Another topic that has also attracted the attention of the researchers worldwide is the trapped air between the girders of a bridge. McPherson, 2008, studied experimentally the hurricane induced wave forces on a 1:20 scale bridge model and observed that during the inundation of the bridge water could not fill completely the chambers between the girders due to the presence of trapped air. He developed predictive force equations where he considered additional hydrostatic force-buoyancy, assuming that 50% of the volume between girders were filled with air. Some studies (e.g. Azadbakht, M., 2014), investigated numerically via 2D analyses the impact of hurricane waves on bridges, while others (Hayatdavoodi et al., 2014; Seiffert et al., 2015) investigated experimentally (1:35 scale) the impact of solitary waves on coastal bridge and all studies observed that the air-entrapment occurring between the girders can significantly alter the water flow field during the wave inundation causing a significant increase in the uplift. If the air is allowed to escape, either through the ends of the bridge or through holes in the deck then the uplift forces can be reduced significantly (Haytdavoodi et al., 2014). This seems to be in agreement with another numerical study (Bozognia et al., 2011), where it was shown that the air-vents could reduce significantly both the impulsive and the quasi-static forces, with a larger reduction of the quasi-static forces that could be up to 70%, depending on the ratio s/H , where H is the wave amplitude and s is the distance of the bottom of the girder to the still water surface.

According to Bricker and Nakayama, 2014, who conducted a numerical study of the tsunami forces induced on the Utatsu Bridge in Japan, the trapped air between the girders increased the buoyancy of the bridge deck to such a degree that if the air would have been removed then the bridge might not have failed. Moreover, an experimental study (Cuomo et al., 2009) of a bridge at 1:8 scale, revealed that the holes in the bridge deck reduces the wave pressures on the deck slab but increases the ones on the longitudinal beams. It was noted that the trapped air is compressed under the impulsive wave loads which acts as a cushioning effect and results both in

the reduction of the max impulsive load and in the increase of the load duration. Despite this reduction, this case might be more severe for the structure due to the longer duration. Last but not least, Xu et al., 2016, conducted 2D numerical work to study the effect of air venting holes in the bridge deck and concluded that such a countermeasure can reduce significantly the uplift force introduced by solitary waves, but it can also increase the horizontal force.

1.3 OBJECTIVES OF RESEARCH STUDY

As discussed in the previous section most of the experiments of tsunami effects on bridges to date have been conducted at a small-to-medium scale using very stiff bridge models that could not account for the actual bridge properties and dynamic characteristics (material, flexibility, inertia). In addition, small-scale experiments might be associated with significant scale effects since the atmospheric pressure cannot be scaled in the experiments (Martinelli et al., 2010). Especially in the case that trapped air is compressed in a chamber significant distortion of the scale can occur (Takahashi et al., 1985). These facts coupled with the fact that (a) most numerical studies to date have focused on identifying the maximum total applied tsunami forces via CFD analyses neglecting the response of the bridge, (b) most of the numerical investigations and available predictive equations of the total tsunami load have not been validated or were validated with small-scale experiments, (c) no guidance exists on estimating the individual connections forces, and (d) the effect of the short-duration slamming/impact force on bridges has not been yet thoroughly studied and understood, suggest the need for advanced large-scale hydrodynamic experiments. The main objectives of this project are to:

1. Understand the tsunami inundation mechanism of coastal bridges
2. Identify the difference in the bridge response when subjected to unbroken solitary waves and more realistic turbulent bores, and the relationship between the forces and the various hydrodynamic parameters
3. Investigate not only the total waves forces but also the distribution of these forces in the bearings, shear keys and bent cap-to-column connections in order to determine the max force that each connection has to withstand
4. Shed light on the physics of the dynamic wave-structure interaction and the role of the dynamic characteristics of the bridge, including the flexibility of the superstructure, substructure and connections, as well as the inertia.
5. Gain an insight into the role of air-entrapment and nonlinear wave-air interaction, which was seen in previous studies to occur when bridges with diaphragms were impacted by waves.
6. Determine the variation of tsunami forces for different types of bridges including I-girder and box-girder bridges, and examine which types are more susceptible to tsunami failure
7. Investigate possible mitigation strategies, such as air-vents in the deck, and provide recommendations for measures to increase the tsunami resilience of coastal bridges,

8. Develop a high quality database that can be used for the:
 - Evaluation of the accuracy of existing simplified predictive tsunami load equations
 - Validation of both computational fluid dynamics (CFD) and advanced fluid-structure interaction (FSI) analyses, which will simulate not only the applied tsunami loading but also the response of the bridge during tsunami inundation
 - Development of recommendations and design guidelines for establishing tsunami-resilient bridges.

This report is organized in several chapters, with each chapter focusing on one or more of the aforementioned objectives. In particular, Chapter 1 presents a literature review on the tsunami inundation of coastal bridges, identified research needs and objectives of this particular study. Moreover the chapter describes the large-scale hydrodynamic experiments of tsunami impact on bridges, which were conducted in the O.H. Hinsdale Wave Research Laboratory, including the design and construction of the bridge specimens, the determination of the flume bathymetry and testing program, and the instrumentation of both the flume and the bridge model.

Chapter 2 presents results from the hydrodynamic experiments of the I-girder bridge with cross-frames and steel bearings, focusing on the determination of the inundation mechanism, the horizontal and vertical forces introduced in the connections, the difference between the effects associated with unbroken solitary waves and bores, the role of the slamming component of the force, and the quality of the experimental data.

Chapter 3 focuses on the role of the dynamic fluid-structure interaction by presenting and comparing experimental results for several configurations with different flexibilities in the connections and the substructure. Detailed comparison of the applied tsunami load as well as the bridge response in terms of connection and inertia forces, moments, accelerations and displacements is included for the various bridge configurations.

Chapter 4 presents the tsunami effects on an I-girder bridge with diaphragms. Comparison of the wave effects on this type of bridge with the ones of a similar bridge with cross-frames is also included in order to determine the role of air-entrapment for both solitary waves and bores. Chapter 5 continues the investigation of the variation of tsunami forces relative to the bridge type by presenting the tsunami impact forces on a box-girder specimen and then comparing them with the respective forces witnessed by I-girder bridges. Chapter 6 examines the efficiency of air-vents in the deck as a retrofitting measure against tsunamis for two bridge types and several wave heights. The effect of the number of air-vents is also examined.

1.4 DESIGN OF LARGE-SCALE HYDRODYNAMIC EXPERIMENTS

As was stated in the first section of the chapter, the likelihood of significant scale-effects in small-scale experiments has been highlighted in previous studies. This likelihood emanates from (a) the difficulty of properly scaling the stiffness of the structure and (b) the inability to scale the atmospheric pressure (Martinelli et al., 2010), as well as from (c) the distortion of the scale when

the air is compressed by a wave (Takahashi et al., 1985). Therefore, in an attempt to advance the state-of-the-art it was deemed critical to conduct the hydrodynamic experiments at the largest possible scale. Other major reasons for conducting large-scale experiments, in addition to minimizing the scale-effects, was the fact that they will allow (i) the construction of the bridge with the same material as the prototype ones (reinforced concrete and structural steel), (ii) the use of design methods and components as used in current practice (e.g. shear studs, deck reinforcement, shear keys, cross-frames, bearings, bent caps), and (c) the simulation of the flexibility of the superstructure, substructure and connections in the most possibly realistic way.

1.4.1 Bridge specimen

For the hydraulic experiments conducted in this study a composite bridge model with four I-girders was designed and constructed at a 1:5 scale. The in-plane dimensions of the bridge deck are 3.45m length and 1.94m width. These dimensions were intentionally chosen to be equal to the ones of the bridge used in another study (Bradner et al., 2011), so that comparisons between the two experiments can be conducted. That study focused on the effects of hurricane waves on coastal bridges and it was unique because (a) it was the first study conducted at such a large scale and (b) it considered the dynamic fluid-structure interaction via the simulation of the substructure flexibility using equivalent horizontal springs. Interestingly, the aforementioned study revealed that the horizontal flexibility increased both the horizontal and vertical forces that the bridge had to withstand (Higgins et al., 2013)).

Given the in-plane dimensions the bridge and all the components were designed assuming that the structure was located on the West Coast of the US in a Seismic Zone 3 and a site class B. This was done because there is a likelihood of tsunamis inundating the west coast if a large magnitude earthquake occurs along the Cascadia subduction zone. In the preliminary phase of the design of the bridge specimen it was decided to use a composite steel bridge instead of an RC bridge with concrete girders in order to avoid possible cracking of the girders during the shipping of the bridge from Reno to Corvallis. Moreover, the steel components (girders, cross-frames, gusset plates) could be more easily modified than the concrete ones during the experiments in order to examine different configurations (e.g. adding/removing diaphragms, adding a soffit slab).

The prototype bridge was analyzed following the AASHTO LRFD Bridge Design Specifications, 2012, and the resultant forces and moments were scaled down to a 1:5 scale and were used for the design of the model bridge specimen. All the load combinations and requirements specified in AASHTO were considered in order to design a realistic bridge in accordance with the current practice. Loads considered included dead, live, wind, fatigue and earthquake among others. For the seismic design, response spectra for several cities on the west coast (e.g. San Francisco, Seattle, Anchorage) were generated using the USGS website. The chosen response spectra had $A_s=0.45g$, $S_{DS}=1.0g$ and $S_{D1}=0.33g$. Limit states for strength, constructability, service, fatigue and fracture were considered.

As shown in Fig.1-3 the bridge has four steel girders which are connected with L-shape cross-frames at the end supports and at third points. The steel girders were W8x13, and were readily available in the US market. Single angles were used at the intermediate cross-frames to satisfy slenderness ratios and prevent local buckling and lateral torsional buckling during the

construction process. At the supports double angles were used as cross-frames in order to resist the large forces during the extreme event. The detailing of the cross-frames is shown in Figure 3-2. The details of all the bridge components are shown in Appendix B.

For the shear connectors both the strength and the fatigue limit state were considered. Two shear connectors with 0.95cm diameter each and a pitch of 5.1cm were welded on the flange of each girder, in order to achieve the composite behavior with the deck. The pitch of the shear connectors was kept constant along the whole length of the girders, as shown in Figure 1.3. The deck was constructed with concrete and was reinforced with a steel wire with #3 rebar spaced at 0.10m in both directions. The reinforcement was placed at the mid-height of the concrete slab. The thickness of the slab is 5.1 cm, the haunch is 1.0 cm and height of the steel girders is 21.3cm. For the design of the slab and its reinforcement, service limit states, strength limit states and extreme events (including vehicular collision) were taken into account. In addition to the limit states specified by AASHTO, the RC bridge deck was also checked against the live load that the bridge would have to withstand during the preparation of the experiments to ensure that it will not fail when several students were standing on the bridge.

Two different bearing types were designed and used for connecting the superstructure to the substructure, including steel bearings as well as plain elastomeric bearing pads. The elastomeric bearings were designed per Method A of AASHTO, 2012, to allow for thermal expansion. The bearing dimensions were 6.5 cm diameter and 1.27 cm height, and were manufactured by Scougal Rubber Corporation, who conducted material testing to meet all the AASHTO Specifications. Shear keys were also designed to take the lateral earthquake load and transfer it to the bent caps. The shear keys consisted of steel angles L6 x 6 x (1/2) with two stiffeners 0.95cm thick each. Table 1-1 shows a summary of the main characteristics of the bridge model.

The bridge specimen was designed by UNR and was constructed by Reno Iron Works (RIW). Figure 1.3 shows the steel components of the bridge during their assembly at the facilities of RIW. The stiffeners were welded to each I-girder, while the single-angle intermediate cross-frames were welded to gusset plates, and once both components were ready then the gusset plates were bolted to the stiffeners of the girders forming the frame of the bridge. Following the completion of the assembly of the steel members, the bridge frame was moved in the yard and formwork was attached, as shown in Figure 1.4. The steel wire was installed at the mid-height of the deck before the concrete pouring.

Since the experimental setup was very complex and consisted of a large number of connecting elements and bolted connections with regular sized holes (only 1/8 in larger than the bolt sizes) it was critical for the success of the project to ensure that everything will fit together. Therefore, the two red HSS7x5 bent caps that were initially designed and constructed by Bradner et al (2010) were shipped from OSU to UNR. In order to accommodate the new bridge type the bent caps had to be modified by welding two steel plates on top of the bent caps. These plates were machined to a very tight tolerance in order to meet the flatness requirements set by the load cells manufacturer, which were attached between the girders and the bent caps. Additional connecting plates between the bent caps and the load cells as well as between the load cells and the bearings were also designed and constructed, as shown in Figure 1.4. Once the fitting process and the instrumentation of the bridge was successfully completed in the Large-Scale Structure

Laboratory at UNR –as shown in Figures 1.5 and 1.6 - all the components were disconnected and shipped separately to Oregon State University.

Table 1.1: Summary of Bridge Characteristics

Bridge characteristics	
Bridge Type	I-girder Composite Bridge
Deck Type	Reinforced Concrete
Deck Dimensions	3.45m x 1.95m x 0.05m
Deck Reinforcement	Steel wire with #3 rebar spaced at 0.10m in both directions
Girders	W8x13, height=0.21m
Girder Stiffeners	Welded steel plates, 0.635cm thick
Cross-frames	Steel angles L1x1x1/8
Shear keys	Steel angles L6x6x(1/2) with two stiffeners 0.95cm thick each
Shear Studs	2 at 5.1cm with D=0.95cm
Steel bearings	HSS 8x2x(5/16)
Elastomeric bearing pads	Circular with D=6.5cm, H=1.27cm
Bent caps	HSS 7x5, L=2.5m
Weight of bridge deck	12.62kN

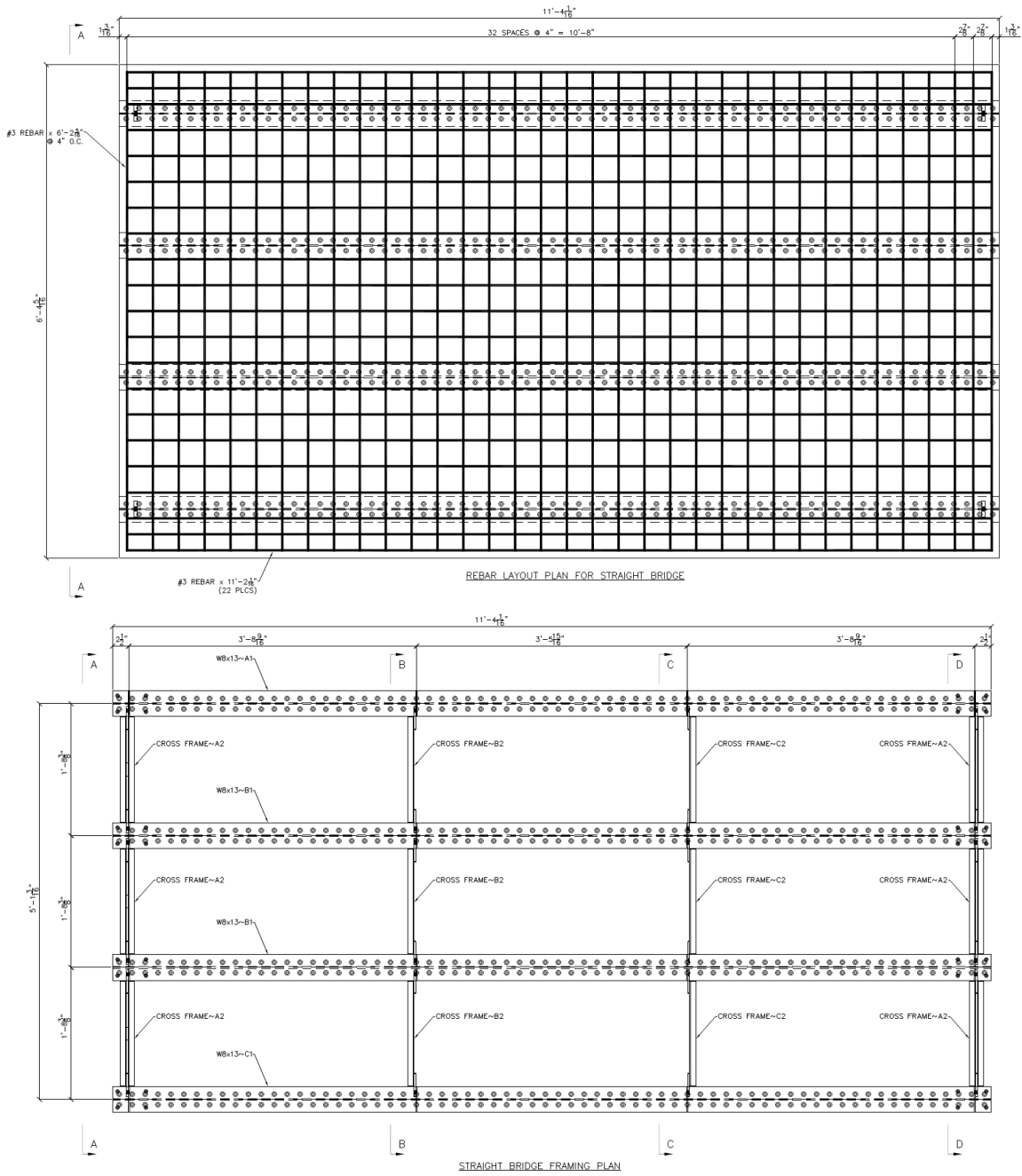


Figure 1.3: Finalized rebar layout of the deck (top) and framing plan with girders and cross-frames (bottom), adapted from Reno Iron Works (Appendix C)



Figure 1.4: Bridge steel components during the assembly (left) and before the concrete pouring (right)



Figure 1.5: Four steel bearings connected to the bent cap (top-left), shear-key in contact with the top plate of the elastomeric bearings (top-right), and details of the connections between the girders, steel bearings, load cells and bent cap (bottom), during the pre-test assembly in the Large-Scale Structures Laboratory at the University of Nevada, Reno



Figure 1.6: I-girder bridge connected to the steel bent caps during the pre-test assembly (top and bottom-left) and instrumentation of cross-frames with strain gages

1.4.2 Facility

The experiments were conducted in the Large Wave Flume (LWF) at the O.H. Hinsdale Wave Research Laboratory (HWRL) at Oregon State University. The flume is 104.24 m long, 3.66 m wide, and 4.57 m deep, and is shown in Figure 1.7. The maximum depth for tsunami-type wave generation is 2 m, and the maximum wave height for this depth is 1.40m. The LWF is equipped with a piston-type dry-back wavemaker that has a 4.2m maximum stroke hydraulic actuator, which can generate both regular and random waves, as well as solitary waves, to simulate hurricane-type and tsunami-type waves. The flume is equipped with a powered carriage spanning transversely the flume, which is supported on the flume walls and has a 6ton-capacity crane for installation of experimental specimens in the flume. Moreover, the LWF has a movable/adjustable bathymetry made of 20 square configurable concrete slabs. The flume includes a series of bolt-holes with vertical patterns every 3.66m along the flume for supporting test specimens as well as the concrete bathymetry slabs.

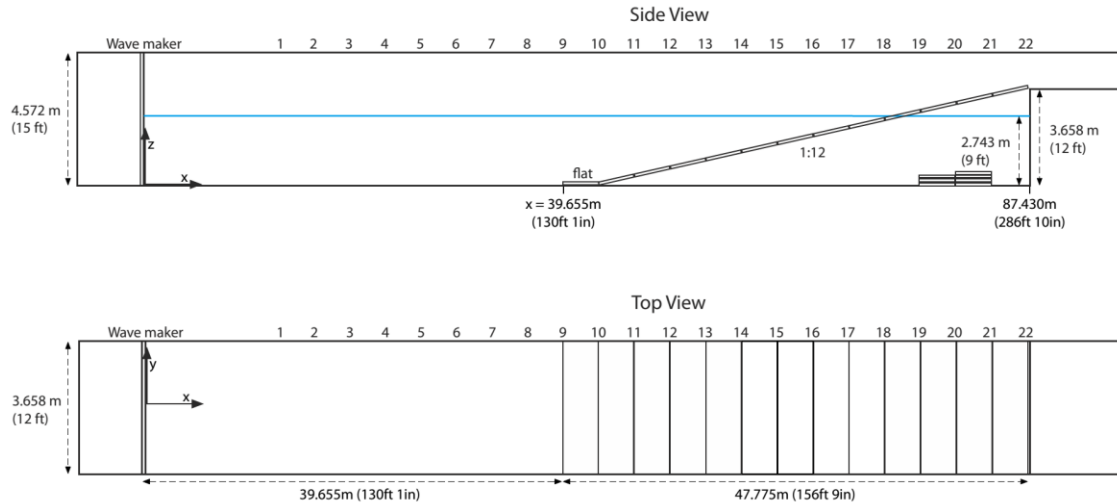


Figure 1.7: Large Wave Flume (LWF) facility with default bathymetry in the O.H. Hinsdale Wave Research Laboratory at OSU (source: <http://wave.oregonstate.edu/large-wave-flume>)

1.4.3 Flume bathymetry and bridge location in the LWF

As was discussed in the first section of this chapter several of the studies conducted to date have simulated the tsunami waves as bores, while other studies used unbroken solitary waves due to their simplicity and available mathematical description. Briggs et al., 2009, describe the tsunami waves as long gravity waves that are changing in height and shape as they reach shallow waters, due to the beach slope and bathymetry. These waves can break, ending up traveling ashore either as rising tides or bores, indicating that at the location of coastal bridges it might be more realistic to simulate the tsunami waves as bores than unbroken solitary waves. Nonetheless, one of the goals of this experiment was to use both unbroken solitary waves and bores, in an attempt to identify the differences in the tsunami forces introduced by the two different wave types.

Various studies have been conducted to study the complex phenomenon of wave breaking, (Peregrine, 1983; Ghosh et al., 2007), which presented a detailed description of the different phases encountered by a plunging wave, including the onset of wave breaking, wave overturning, plunge point, oblique splash-up, secondary plunge and multiple splash-up events. Following these multiple plunging and splash-ups events, a quasi-state bore will eventually form. Although, there exist multiple wave breaking criteria (e.g. Munk, 1949; Grilli et al., 1997) that could predict when the breaking will start, it is still unknown (a) how much time and distance will take from the onset of the breaking until the formation of the bore, and (b) how much will be the height of the bore. Determining these two unknowns was critical for the design of the hydrodynamic experiments.

To this end, several Computational Fluid Dynamics (CFD) models of the whole Large Wave Flume at OSU were developed, as shown in Figure 1.8, and extensive numerical analyses were conducted. The parametric CFD analyses examined different bathymetries with slopes of 1:12, 1:24 and 1:36, and aimed to identify:

- The appropriate combination of slopes/bathymetry that will permit the testing of a wide range of both unbroken solitary waves and bores
- The optimum distance of the bridge specimen from the wavemaker, which will be determined by the distance required for the formation of the bores,
- The elevation of the bridge specimen, which will be determined by (a) the height of the quasi-steady bores, (b) the vertical pattern of holes along the flume, and (c) the goal to inundate the bridge as much as possible, and
- The required wave matrix that will be able to impact the bridge

The CFD analyses were conducted in LS-DYNA (Hallquist, 2006) again. However, this time the new incompressible solver, called ICFD (Del Pin et al., 2014), was used instead of the compressible one. The former code has significant advantages over the latter one for problems involving water wave propagation and free-surface flow, because it is an implicit code allowing the user to specify the time-step based on the CFL condition, reducing consequently the required analysis time by an order of magnitude in some cases. The code solves the Navier-Stokes equations, uses the Level Set Method for tracking the fluid interface and includes various turbulence models, such as the Large Eddy Simulation (LES), making it therefore possible to simulate the wave-breaking.

Another useful capability of the new solver is the coupling with the mechanical solver in LS-DYNA for solving fluid-structure-interaction (FSI) problems. For the FSI coupling a partitioned approach is used meaning that the fluid and solid equations are uncoupled. Both one-way and two-way FSI coupling can be implemented. In addition, both weak and strong coupling can be achieved, depending on whether the mechanical solver runs explicitly or implicitly. The code uses an ALE approach for simulating the motion of the structure in FSI problems, allowing it to handle large displacements of the solid body during the interaction with a fluid.

In the 2D computational model of the LWF, the bridge structure was simulated as a rigid boundary, which means that the wave-bridge interaction and bridge response were not considered in order to reduce the computational time. The wavemaker was simulated using shell elements that moved horizontally with a prescribed motion. The wavemaker-water interaction was simulated via one-way FSI, meaning that the wavemaker affected the fluid but the fluid did not affect the motion of the wavemaker. Since the wavemaker had to undergo significant displacements in the model, which were in the range of 3.5m for the largest waves, special commands were used to allow the surface nodes to move with the wavemaker using an ALE approach -as was done for the volume mesh of the fluid - otherwise the analyses failed prematurely.

The prescribed motion assigned to the wavemaker in the LS-DYNA model was the actual motion that the wavemaker will undergo in the experimental tests, and this was calculated using the solitary wave generation theory. The wave generation theory used by the piston-type wavemaker in the LWF of the O.H. Hinsdale Wave Research Laboratory, is the one described by Goring and Raichlen, 1980, and Hughes, 1993. Readers are welcome to examine the derivation and all the

details of the theory by accessing the above studies. For the purpose of this dissertation only the main equations for calculating the displacement of the wavemaker are presented below:

$$X_o(t) = \frac{H}{kh} * \tanh k(ct - X_o) \quad (3-1)$$

$$c = \sqrt{(g * (H + h))} \quad (3-2)$$

$$k = \sqrt{\frac{3 * H}{4 * h^3}} \quad (3-3)$$

In the above three equations, h is the water depth, H is the wave height, g is the gravitational acceleration, c is the celerity of the wave and X_o(t) is the wavemaker displacement history. Since X_o(t) is on both sides of equation 3-1, this means that for a particular water depth and wave height the displacement of the wavemaker can be calculated numerically (e.g. in Matlab) via iterations.

CFD models with different fluid mesh sizes were developed, starting from a mesh size of 10cm and going down to 1.25cm, as shown in Figure 3.10. In addition, different time-steps were also examined ranging between 0.01sec and 0.0025sec. In a 104.24m long and 4.57m deep flume the 10cm mesh was considered a reasonable starting point. However, the results revealed that even for a large solitary wave with H=1.20m in a 1.16 water depth, breaking did not occur, despite the fact that the wave height/water depth ratio exceeded the 0.78 limit introduced by Munk, 1949. This indicated that the 10cm could not resolve accurately the free-surface of the wave, and the mesh size was reduced.

Figure 1.9 shows the contours of the fluid velocities close to the wavemaker for two CFD models, (a) one with a 10cm mesh size and 0.01sec time-step, and (b) another one with a finer mesh equal to 2.5cm and a time-step equal to 0.0025sec. Some relatively small differences can be noticed in the free-surface of the fluid. As the wave propagates along the flume and reaches the second flat section where h=1.16cm the model with the fine mesh starts breaking as expected (Figure 3.11), while the model with the coarse mesh does not break. Following the first plunging the wave in the former model keeps breaking with multiple splash-ups and plunges, while the wave in the latter model still does not break, as shown in Figure 1.9. The different models demonstrated that the wave-breaking was very dependent on the mesh size and the time-step, and most of the parametric studies were conducted using the 2.5cm mesh size. The model with the 1.25cm mesh size was also predicting the wave breaking and was capturing even more local fluctuations and details than the model with the 2.5cm mesh size, however it was computationally too expensive. Figure 1.10, shows the snapshots of the wave propagation and

breaking, with the latter one described by multiple plunges, as was observed in the experimental study (Ghosh et al., 2007).

The computational analyses were run on the High Performance Computing Cluster at UNR, using up to 100 cores per analysis. The analysis time ranged between 1 day to several days depending on the mesh size and time-step. The results of the numerical analyses showed that a 1:12 slope followed by a horizontal bathymetry 40.2m long and another 1:12 slope at the end was the most appropriate. The slope at the beginning would cause an increase of the wave height due to shoaling, and later on breaking of the wave in some cases, while the slope at the end would dissipate the energy of the wave. In addition, the optimum location for the bridge was between bays 14 and 15, in order to allow for the bore to form after the wave breaking and still inundate the bridge.

The parametric CFD analyses presented in the previous section identified the optimal bathymetry and bridge location. However, given the fact that the plunging wave-breaking is a very complex phenomenon that was seen to be dependent in the computational analyses on both the mesh size and the time-step it was decided to perform preliminary wave tests in the Large Wave Flume before the installation of the bridge. These experimental tests identified the onset of breaking point, the location of the formation of the quasi-steady bore, and its height, confirming visually the estimations found with the numerical model. Interestingly, although according to the simple solitary wave breaking criteria (Munk, 1949) the wave breaking should have happened between bay 4 and 5, it was observed in the preliminary wave tests that the onset of breaking actually happens further down, between bays 8 and 9, and the quasi-steady bore is formed after bay 12. Therefore, the bridge was installed between bays 14 and 15 and the bathymetry was a combination of two inclined sections with a 1:12 slope and a flat section, as was determined by the CFD analyses. The final bathymetry and bridge location are shown in Figure 1.11.

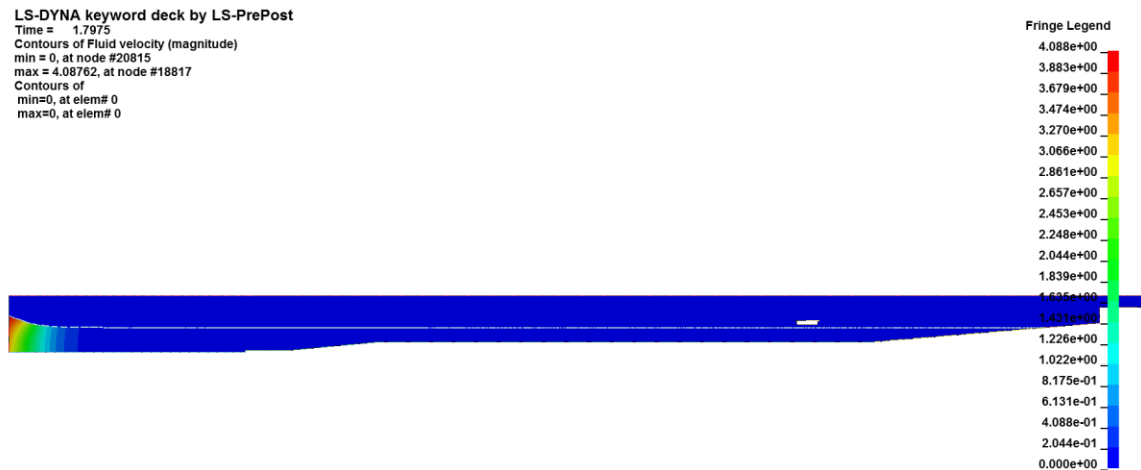
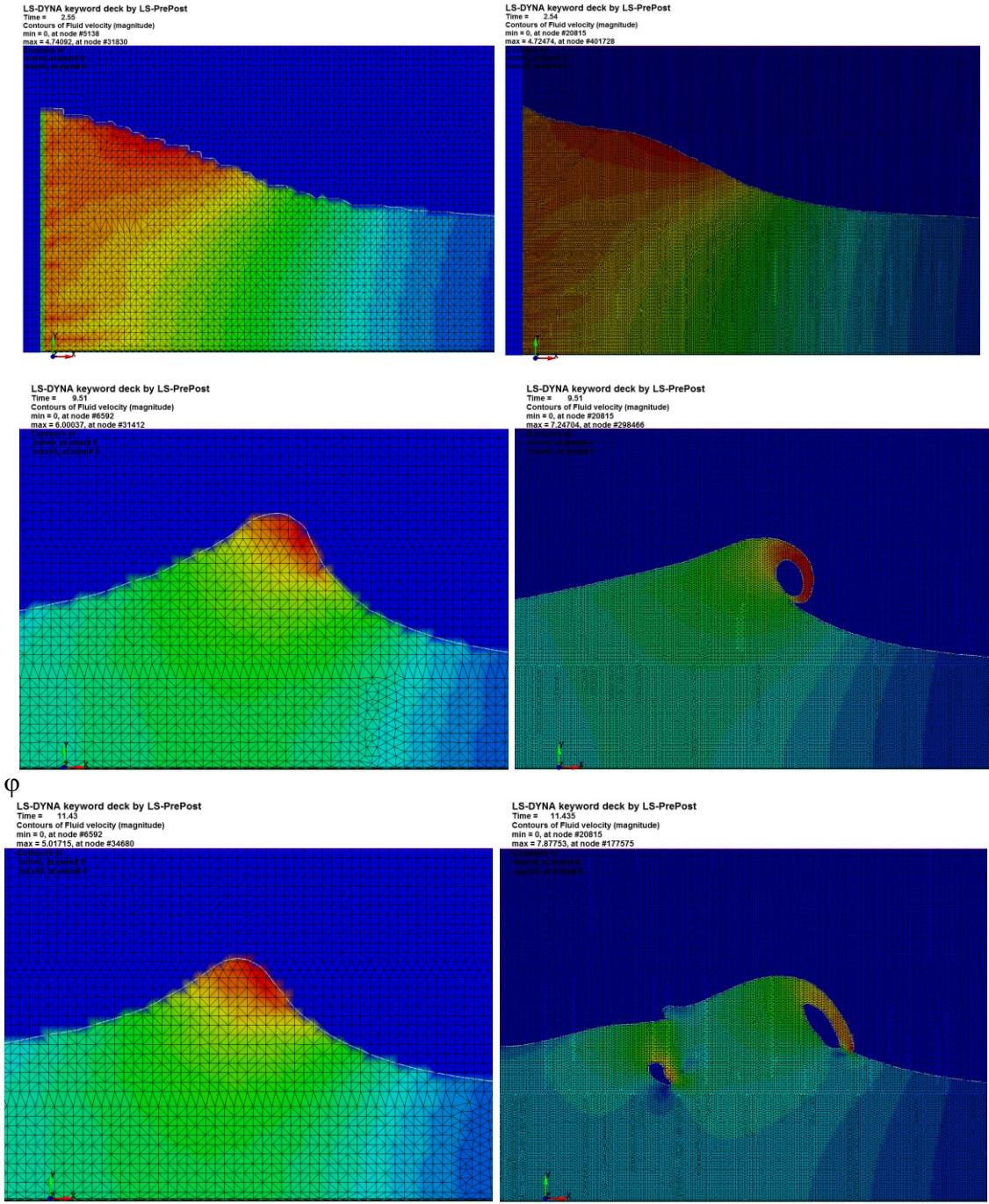


Figure 1.8: Full-scale CFD model of the Large Wave Flume at Oregon State University, with the adjusted bathymetry and the bridge specimen in LS-DYNA (to scale)



ϕ

Figure 1.9: Snapshot of the contours of the fluid velocities at t=2.55sec (top), 9.51sec (middle), and t=11.43sec for two CFD models with 10cm (left) and 2.5cm (right) mesh size respectively

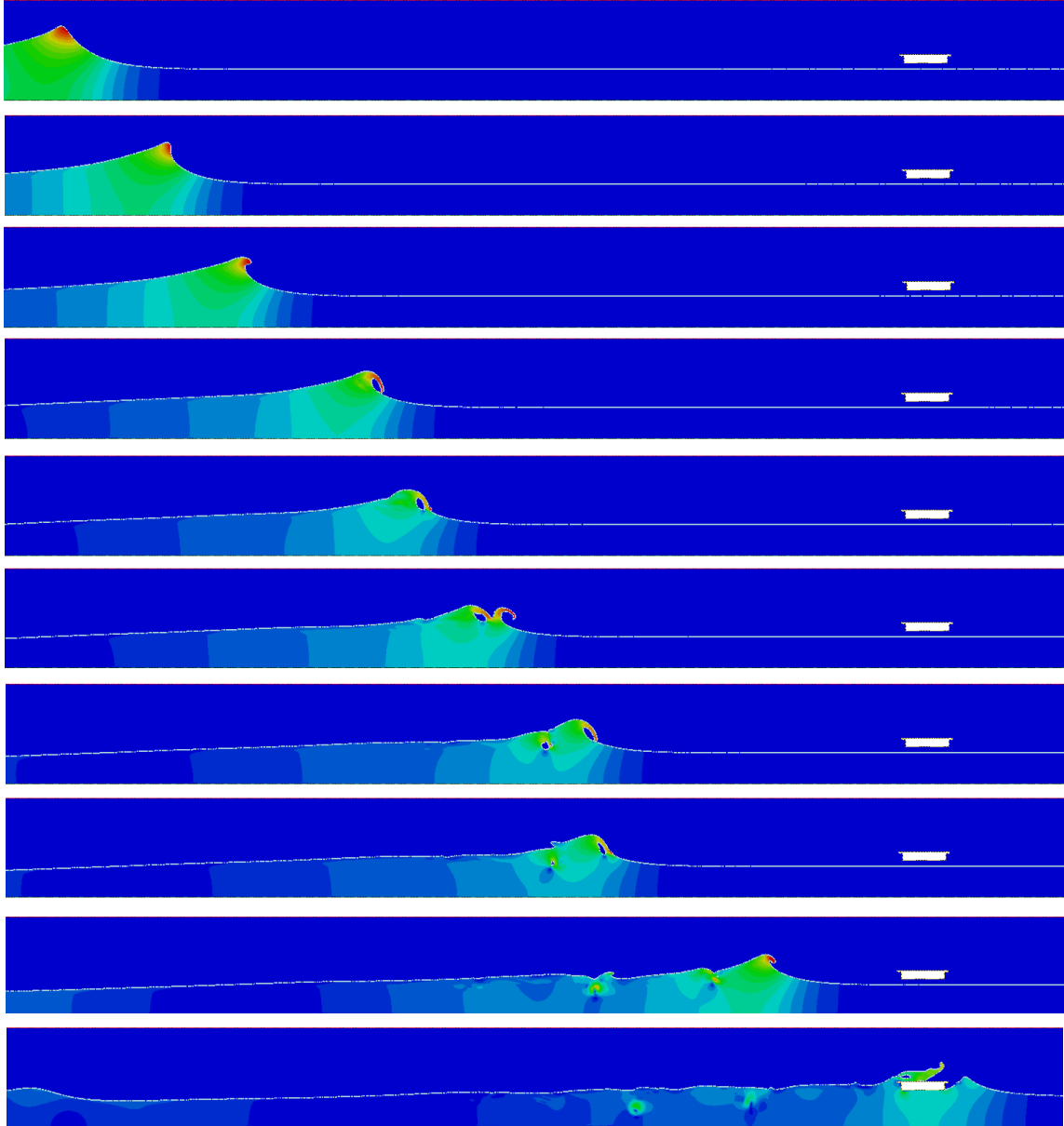


Figure 1.10: Snapshot of the contours of the fluid velocities during the wave propagation and breaking, for the CFD model with 2.5cm mesh size and a wave with $H=1.20\text{m}$ and $d=2.0\text{m}$

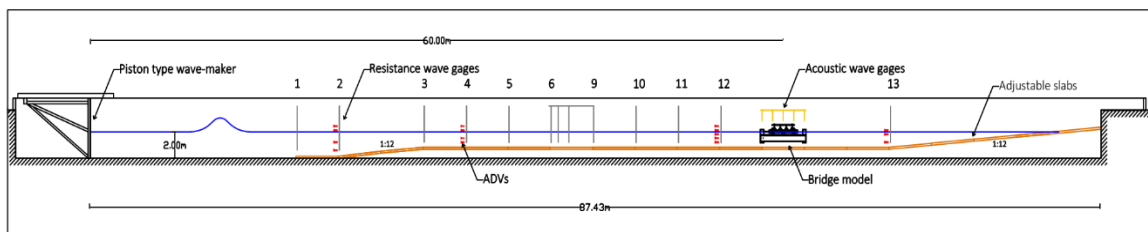


Figure 1.11: Cross-section of the Large Wave Flume (LWF) depicting the bathymetry, bridge location and flume instrumentation

1.4.4 Testing frame and installation in the flume

Steel bent caps with an HSS7x5 section were used, as in (Bradner et al., 2011). Although the bridge was not designed for tsunami loads but was instead designed according to existing guidelines and current practice, the load cells, the rails, the carriages and the connections below the bent cap had to be designed for the tsunami loads to avoid any damage during the tsunami experiments and ensure proper measurement of the parameters of interest. To this end a numerical model of the bridge with all the major components was developed in the commercial software CSI Bridge (2017) licensed by Computer & Structures, Inc, as shown in Figure 1.12. The total horizontal and vertical tsunami loads were estimated based on the available literature, and were applied on the bridge as static loads to find the distribution in each connection. These forces were multiple times larger than the forces introduced by the hurricane waves tested in (Bradner et al., 2011), which exceeded the capacity of the rails and the carriages. Therefore, the bent caps were furthermore modified by adding additional connections (carriages, load cells and steel plates) between the test-frame and the bent caps.

Figure 1.13 shows the final experimental setup at the bridge location. The main components include the test frame (W18x76), which is bolted to the walls of the flume, the rails with the rollers (carriages), the bent caps, the horizontal links/springs, the bearings (steel/elastomeric), the shear keys and the bridge deck. The rails with the rollers should not provide any resistance due to negligible friction, so that the horizontal stiffness of the substructure is represented by the horizontal springs/links attached to the bent cap. Moreover, vertical and horizontal load cells were installed both at the level of the bent caps and at the level of the girders, and are shown with yellow and green color respectively.

The load cells below the girders were added in order to capture the vertical force that each bearing and connection has to withstand, while the load cells below the bent caps were added in order to find the forces that will go into a three-column bent. The other significant reason for using load cells at both levels, was to check the quality of the experimental data and gain confidence in the obtained information. If the tsunami vertical load was a static load then the total vertical force calculated by the load cells at the two levels would be the same. Therefore, comparison of the time-histories of the recorded total vertical forces from the two sets of load cells is expected to give an insight into the dynamic effects. To distinguish between the vertical forces measured below the girders and below the bent cap, the former ones will be referred in this study as vertical forces in the “girder connections” or “bearings” while the latter one will be referred as forces in the “bent-cap connections” or “piers”. It must be noted that the actual piers and their axial stiffness was not modeled in the experimental setup. Similarly to the case with the vertical forces, horizontal forces were recorded in both the shear keys and the substructure links/springs, in order to verify that the friction at the rail-roller interface has a negligible effect, and increase the confidence in the experimental data.

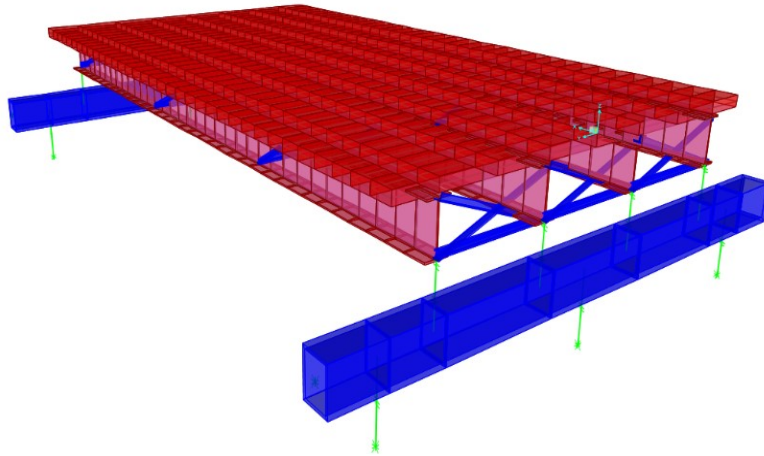


Figure 1.12: Numerical Model of the bridge setup in CSI Bridge

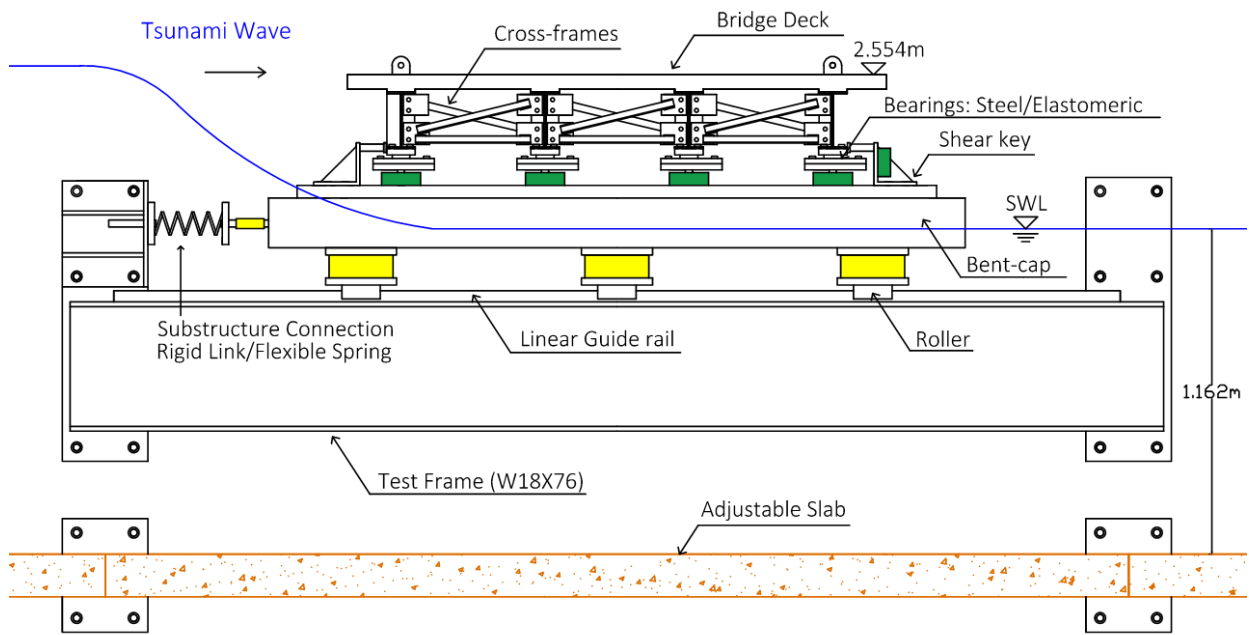


Figure 1.13: Cross-section of the experimental setup at the bridge location depicting the major components (test frame, bridge specimen, bent caps and connecting elements)



Figure 1.14: Installation of the bridge with steel bearings in the LWF

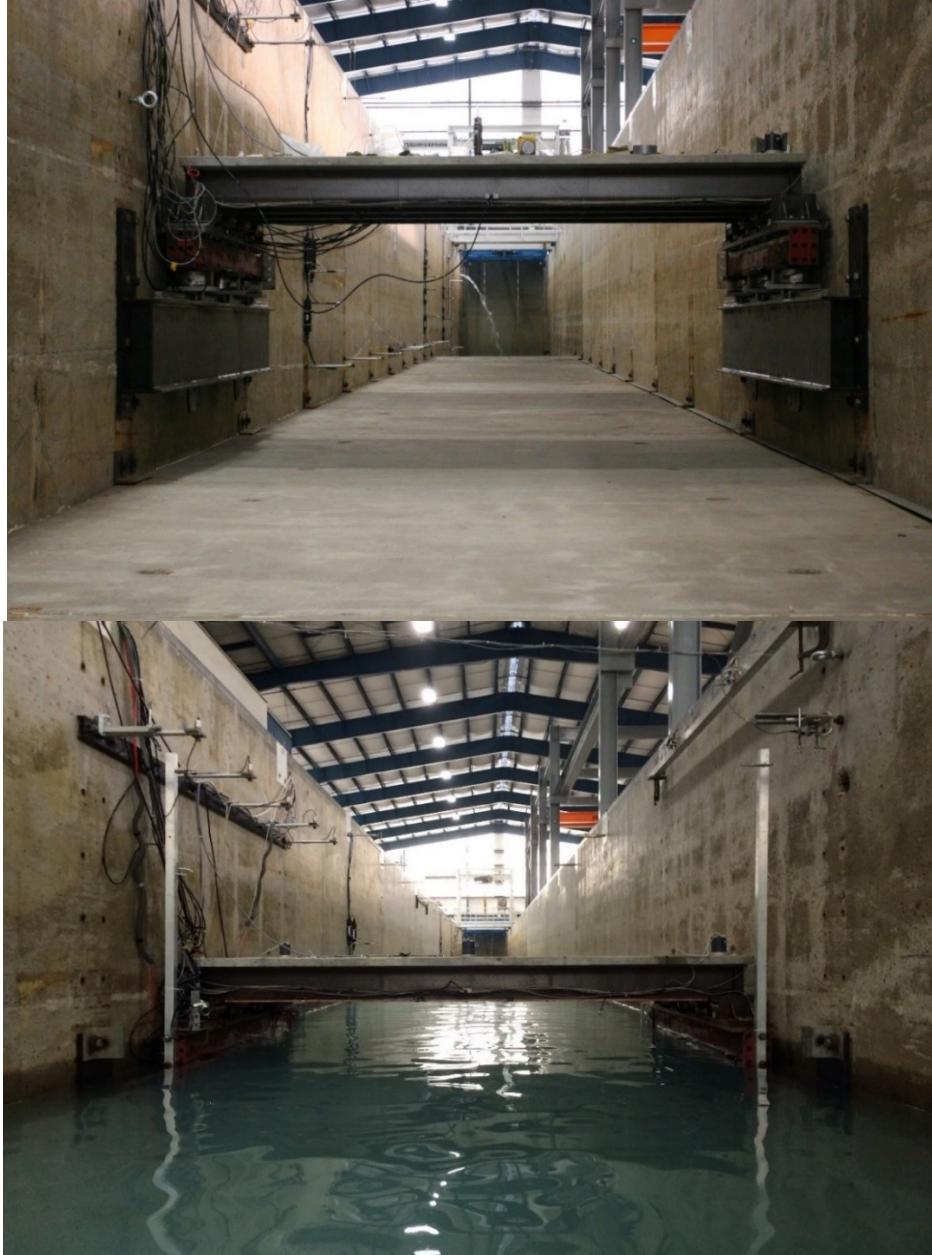


Figure 1.15: View of the bridge specimen with the LWF empty (top) and filled with water (bottom) before the hydrodynamic tests

1.5 WAVE MATRIX

In the preliminary design phase of the hydrodynamic experiments three different water depths were considered including 1.80m, 1.90m and 2.0m. However, for the finalized bathymetry (Figure 1.11) the CFD models with the refined mesh revealed that the bores could not fully inundate the bridge when the water depth was 1.80m, and consequently this case was dropped from the wave matrix. As shown in Table 1.2 and Table 1.3 two water depths were used including the 1.90m and 2.0, and a range of waves with heights between 0.36m to 1.40m.

It must be noted that the experiments were conducted in two different stages, with each stage having a different wave matrix. As shown in Table 1.2 in the first stage, two water depths and two types of waves – unbroken solitary waves and bores – with input heights between 0.36m-0.70m for the former waves and between 0.80m-1.40m for the latter ones. In the second stage of the experiments only a 2.0m water depth was examined, however three different wave types – unbroken solitary waves, a longer wave with an error function (erf=10sec), and turbulent bores – and additional wave heights were tested. In total 420 hydrodynamic tests were conducted in the LWF.

Table 1.2: Wave Heights and Water Depths Tested in the First Stage of the Experiments

Water Depth (m)	Wave height (m)	Wave Type
1.90	0.46	Solitary
	0.52	Solitary
	0.65	Solitary
	0.80	Bore
	1.00	Bore
	1.10	Bore
	1.30	Bore
2.00	0.36	Solitary
	0.42	Solitary
	0.55	Solitary
	0.70	Solitary
	0.90	Bore
	1.00	Bore
	1.20	Bore
	1.40	Bore

Table 1.3: Wave Heights and Water Depths Tested in the Second Stage of the Experiments

Water Depth (m)	Wave height (m)	Wave Type
2.00	0.36	Solitary
	0.42	Solitary
	0.50	Solitary
	0.55	Solitary
	0.62	Solitary
	0.70	Solitary
	0.80	Bore
	0.90	Bore
	1.00	Bore
	1.20	Bore
	1.40	Bore
		Unbroken with erf T=10s

1.6 STRUCTURAL MATRIX

In the current experimental study, twelve bridge configurations of a straight bridge were tested. Seven of these test cases were focusing on the effect of the bridge flexibility on the dynamic wave-structure interaction and the tsunami forces introduced in the connections. Details of these configurations are shown in Table 1.4. Both test cases ST1 and ST2 have a rigid link (rod) at the substructure level, which does not allow the bent cap to move laterally. The difference between the two configurations lies in the connection of the girder to the load cells on top of the bent caps, which in the former case is established with steel bearings while in the latter this is done with elastomeric bearings (flexible). The steel bearings in ST1 restrict all degrees of freedom, while elastomeric bearings with the shear keys in ST2 allow rotations and vertical displacements of the bridge but restrict the horizontal displacements. Comparison of these two bridge cases is expected to give an insight into the role of the flexibility of the connections during the tsunami inundation.

Test cases ST3 and ST4 are different than the two previous cases since the substructure flexibility is now modeled explicitly using a linear horizontal medium spring (flexible) and a soft spring (very flexible) respectively instead of a rigid rod, as a link between the bent cap and the bracket connected to the flume wall. These springs were first designed and used in (Bradner et al. , 2010), where the stiffness of the medium spring was selected to represent the scaled fundamental period of the prototype I-10 Bridge over Escambia Bay. The spring stiffness was 458 kN/m for the medium spring and 107kN/m for the soft spring. Last but not least, test case ST11 was similar to case ST2 however the shear keys were removed and the bridge deck was allowed to rotate and translate both vertically and horizontally, restricted only by the flexibility of the elastomeric bearings.

Bridge configurations ST2B and ST3B were conducted in the second stage of the experiments, and were similar to the configurations ST2 and ST3, respectively, of the first stage. The main difference was that in the first stage each bent cap was connected to the test frame via three load cells – representing a three-column bent– while in the second stage only 2 load cells were used below the bent-cap, representing a two-column bent. The middle connection was dropped in the second stage because the measured uplift forces were smaller than the ones predicted by the simplified predictive tsunami equations used in the design of the first stage. The second stage was also beneficial because it provided the chance to subject the bridges to additional wave heights and wave types, and to repeat previous wave heights in an attempt to check the repeatability of the measured hydrodynamic and bridge parameters.

The other five bridge configurations shown in Table 1.5, focused on the second part of the objectives presented in chapter 1, which included (a) the deciphering of the role of the air-entrapment in bridges with diaphragms, (a) the determination of the variation of tsunami forces for different bridge types, such as I-girder and box-girder bridges, and (c) the investigation of the use of air-vents in the deck as a mitigation strategy against tsunamis. Bridge configuration ST5 is similar to ST2 but in addition wooden diaphragms are attached at the location of the cross-frames. The diaphragms are sealed with caulk and are consequently expected to trap the air between the girders when the wave inundates the chamber. Bridge configuration ST6 was built based on configuration ST5 with the addition of a thick wooden slab at the bottom. This soffit slab was connected to the girders and the diaphragms, forming thus a box-girder bridge. It must

be noted that the goal for this configuration was to simulate the geometry of a box-girder, and not the exact superstructure flexibility of an actual box-girder.

Bridge configuration ST7 is similar to ST5 but this time eighteen 2.5in diameter holes were drilled in the deck. The total area of the air-vents was 0.85% of the deck area. Comparison of the data from the aforementioned configurations will shed light on the effectiveness of the air-vents in reducing the uplift tsunami forces for bridges with diaphragms. In an attempt to study the effect of the number of air-vents 18 more holes were drilled in the deck forming bridge configuration ST9. Last, in bridge case ST10 the diaphragms were removed in order to examine if the venting would have an effect on the uplift forces that I-girder bridges with cross-frames have to withstand.

Table 1.4: Bridge Cases Focusing on the Role of the Dynamic Fluid-Structure Interaction

Bridge Cases	Substructure Stiffness			Connection Type		Shear Keys	Bent-pier connections
	Rigid link	Medium spring	Soft spring	Steel Bearings	Elastomeric Bearings		
ST1	•			•		•	3
ST2	•				•	•	3
ST3		•			•	•	3
ST4			•		•	•	3
ST11	•				•		3
ST2B	•				•	•	2
ST3B		•			•	•	2

Table 1.5: Bridge Cases Focusing on the Role of Air-entrainment, the Variation of Tsunami Forces Relative to the Bridge Type, and the use of Air-vents as Counter-measures against Tsunamis

Bridge Cases	Substructure Stiffness	Connection Type	Shear Keys	Diaphragms	Soffit	Venting (%)
	Rigid link	Elastomeric Bearings				
ST5	•	•	•	•		
ST6	•	•	•	•	•	
ST7	•	•	•	•		0.85
ST9	•	•	•	•		1.70
ST10	•	•	•			1.70

1.7 INSTRUMENTATION

Since one of objectives of the current study was the development a high-quality database that could be used for validation of hydrodynamic models and CFD methods by research groups

around the world, the wave flume was heavily instrumented. Wave hydrodynamics were measured in the experiments using resistive-type wave gages, acoustic probes, pressure gages and ADVs. In particular, 13 resistive-type wave gages were installed along the length of the flume to measure the free-surface elevation and capture the propagation of the waves (shoaling) and the complex phenomenon of plunging wave breaking. Moreover, 5 acoustic probes were installed at the location of the bridge to track the overtopping process, and 16 Vectrino-II ADVs were installed at four different locations in order to measure the flow velocities and determine the velocity profile. In addition, two pressure gages were added at the same location with two velocity profiles, to measure the hydrodynamic pressure. Table 1.6 is showing the bays of the Large Wave Flume that were instrumented, the corresponding instruments and their exact location. The acoustic probes are not shown in this table because they were not installed at the exact location of a bay, but were instead installed in an array between bays 14 and 15, with two probes installed in front of and behind the bridge and the rest installed along the width of the bridge. Similarly, two wave gages are also not included since they were installed in an array between bays 8 and 9. It is worth mentioning that all the instruments were surveyed in order to identify the exact location and facilitate the comparison with numerical codes.

In addition to the extensive flume instrumentation, the bridge was extensively instrumented in order to measure both the tsunami impact pressures, as well as the bridge response in terms of accelerations, displacements, strains and forces, and obtain useful data for (a) the development of new and (b) validation of existing FSI methods. To this end, 12 pressure gages were installed on the steel girders and on the concrete deck to capture the impact pressures at certain locations, shown in Fig. 1.16 and Fig. 1.17. In addition, 3 biaxial accelerometers together with 2 vertical and 2 horizontal string pots were installed on top of the concrete deck, to capture the bridge response along the horizontal and vertical axis. The accelerometers were installed at three locations on the top surface of the bridge deck, two of which were next to the offshore and onshore lifting lugs. Vertical string pots were installed at similar locations with the two aforementioned accelerometers (offshore and onshore lifting lugs), so that both type of instruments can capture the rotation of the bridge.

The horizontal string pots were attached to stiff tubes, which were bolted to the two bent caps, to measure their displacements (Fig. 1.16). For the bridge configuration ST11 two Novotechniks displacement transducers were added between the bridge deck and the stiff tubes to measure the relative displacement between the deck and the bent caps. Moreover, 24 strain gages were installed on the steel cross-frames to get an estimation of the forces carried by each member, and understand the load path from the girders to the connections.

Furthermore, 16 submersible load cells were installed to measure the forces in certain members and connections. In particular, existing 20-kip and 50-kip load cells were used for measuring the vertical forces below the bent caps and 10-kip load cells were used to measure the horizontal forces in the rigid links and flexible springs. Additionally, 10-kip load cells were purchased and installed below each girder as well as on the shear keys. Due to the long lead time of the additional load cells, part of the experiments was conducted without the load cells at the shear keys.

Table 1.6: Flume Instrumentation and Corresponding Locations

Bay	3	4	6	7	8	9	10	11	12	13	17
Distance	17.73	21.49	28.8	32.44	36.1	39.66	43.01	47.09	50.74	54.38	68.92
Wave gauges	•	•	•	•	•	•	•	•	•	•	•
Pressure gauges	-	-	-	•	-	-	-	-	-	•	-
Elevation (m)				1.224						1.211	
ADVs	-	•	-	•	-	-	-	-	-	•	•
Elevation (m)		0.923 1.846 2.461 2.756		1.243 1.844 2.469 2.766						1.233 1.84 2.137 2.452 2.752	1.506 1.824 2.128

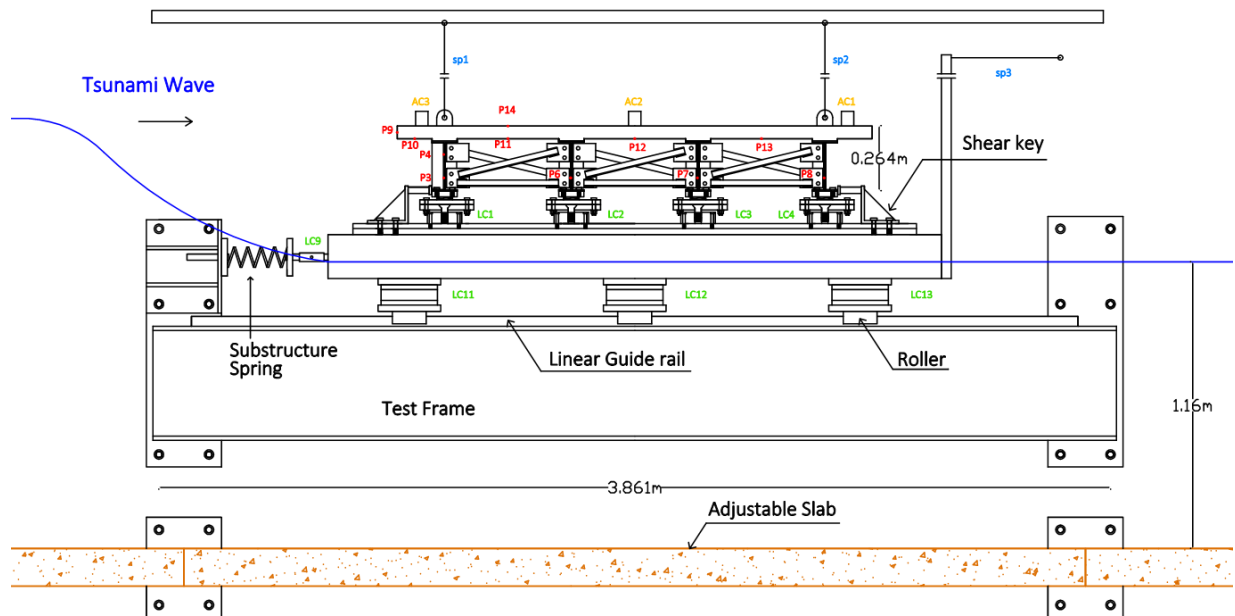


Figure 1.16: Cross-section of the experimental setup at the bridge location depicting the major components and the bridge instrumentation

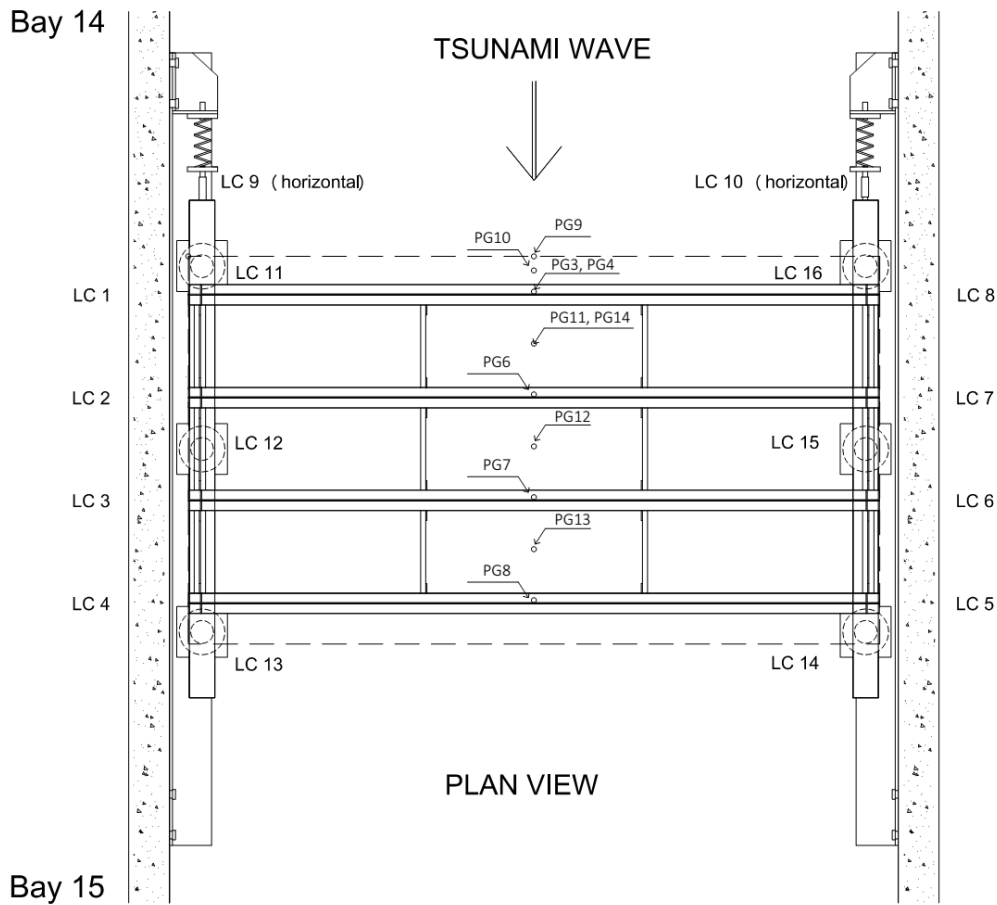


Figure 1.17: Plan view of the experimental setup at the bridge location depicting the location of the load cells and pressure gages installed on the bridge

1.8 DATA ACQUISITION SYSTEM

To accommodate the large number of instrumentation and the need to have certain parameters recorded at different rates than other ones, three different DAQ modules were utilized. Two DAQs were part of the O.H. Hinsdale Wave Research Laboratory (HWRL) equipment and the third DAQ was a portable one that was borrowed from the Earthquake Engineering Laboratory at UNR. From the two HWRL DAQs, the master DAQ was sampling at a rate of 50Hz and was storing data from the flume instrumentation (e.g. wave gages and acoustic probes), while the slave DAQ sampled at 10000Hz and stored data from the bridge instrumentation (pressures, accelerations, load cells, string pots). The UNR DAQ stored also data from the rest of the bridge instrumentation including strain gages and load cells, and sampled at a rate of 5000Hz to 6000Hz. The higher sampling rate of the bridge instrumentation was selected in order to capture the impulsive response of the bridge.

2.0 TSUNAMI INUNDATION MECHANISM AND ASSOCIATED FORCES IN A BRIDGE WITH STEEL BEARINGS

WAVE PROPAGATION AND PARTICLE VELOCITIES

The objective of this particular chapter is to advance the understanding of the tsunami inundation mechanism and associated effects on the bridge deck, bearings and bent-cap to column connections. At the same time the chapter aims to provide detailed results in terms of wave hydrodynamics, applied pressures and bridge response for validation of both numerical methods and simplified equations. To this end, both time-histories for selected wave heights and maximum values will be presented and detailed analysis of the experimental results will be conducted in the following sections. The chapter will focus on the first bridge configuration (ST1), which was the stiffest configuration among all since it had steel bearings that constrained all degrees of freedom at the connection of the superstructure to the substructure (Fig. 2.1). In addition, the configuration had a horizontal rigid link that connected the bent caps to the bracket plates minimizing therefore the effect of the substructure flexibility.

The first step towards the quantification of the tsunami effects on bridges is the understanding and characterization of the wave characteristics and its evolution along the flume as it propagates from the wavemaker towards the bridge location. Figure 2.2 shows the recorded surface elevation at certain locations along the flume for an unbroken solitary wave and bore. A continuous increase of the free-surface of all solitary waves was observed for all tested waves with a maximum increase of 33% at the bridge location. For the large waves that broke a significant reduction of the height at the bridge location was observed, which reached up to 46%. This demonstrates that the input waves at the wavemaker location and the actual waves impacting the bridge can be totally different for some wave cases meaning that the latter ones should be used for correlating the induced forces to wave parameters.

To increase the confidence in the results from the experimental work the recorded free-surface histories close to the wavemaker were compared against the theoretical values obtained from the wave generation theory (Goring and Raichlen, 1980) and good agreement was observed, as shown in Figure 2.3. Moreover, the particle velocities measured by ADVs in front and behind the bridge were compared with the theoretical velocities predicted by long wave theory (Dean and Dalrymple, 1991) and a consistently good matching was noticed as shown in Figure 2.4.



Figure 2.1: Bridge with steel-bearings connected to the bent caps during the pre-assembly in the Large-Scale Structures Laboratory at the University of Nevada, Reno

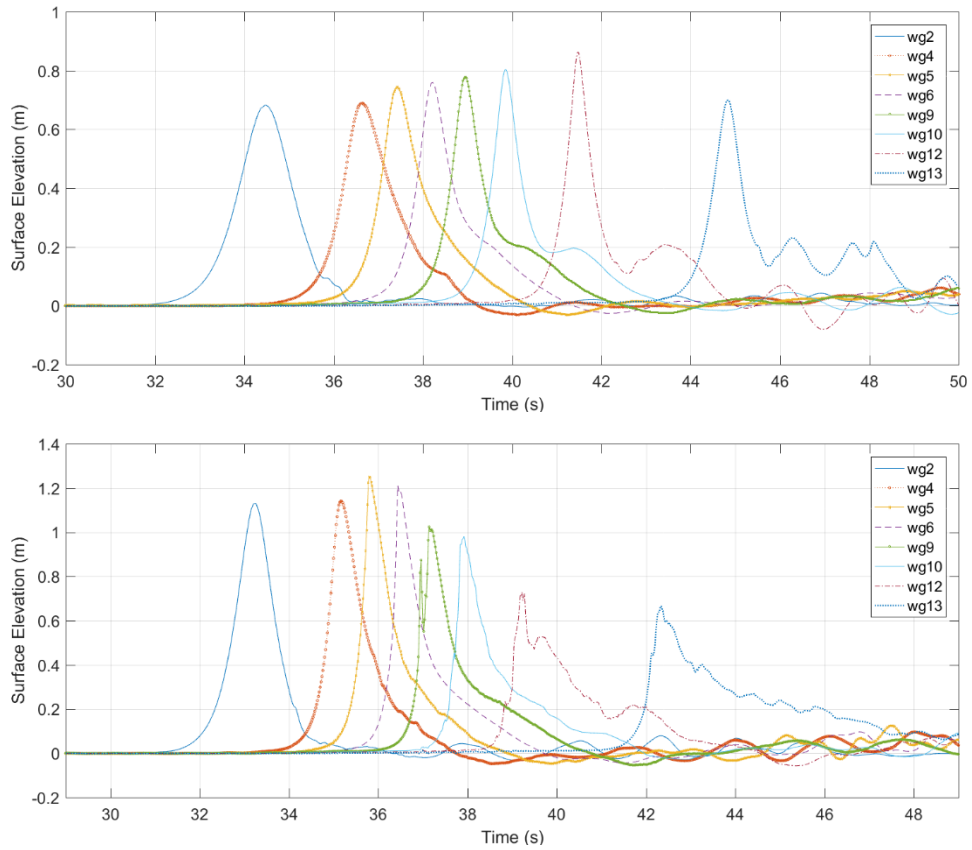


Figure 2.2: Surface elevation along the flume for a solitary wave with $H=0.70\text{m}$ (top) and a bore with $H=1.20\text{m}$ (bottom)

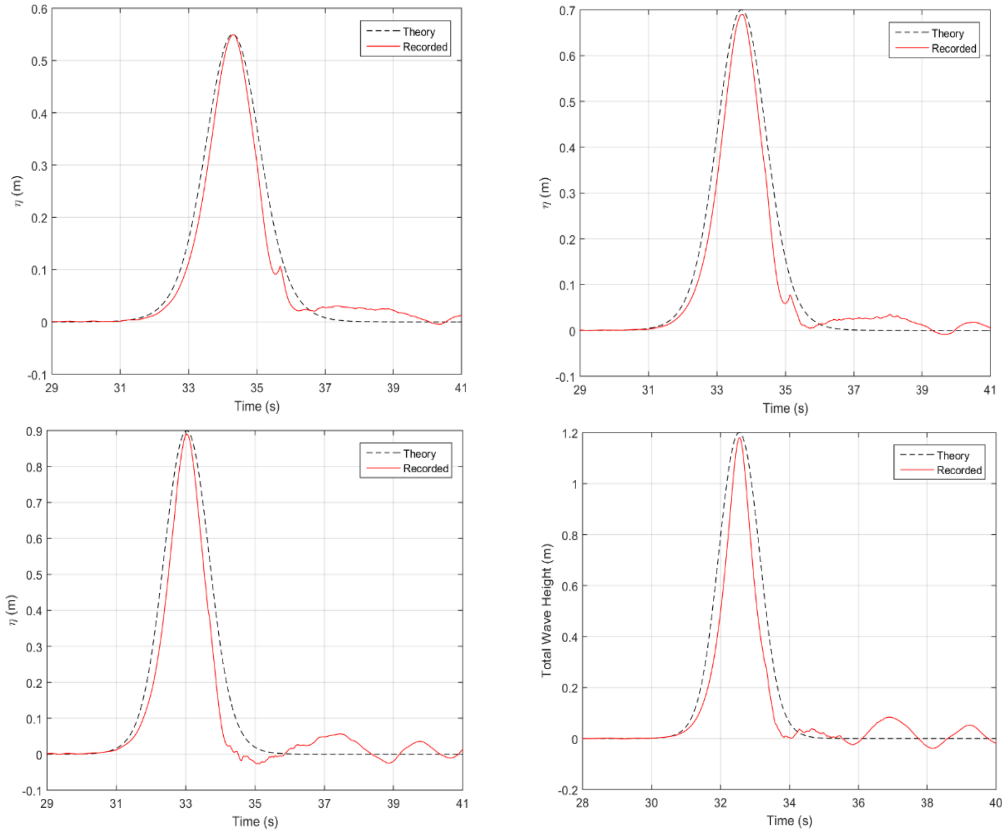


Figure 2.3: Theoretical and measured free-surface at wg1 for H=0.55m (top-left), H=0.70 (top-right), H=0.90m (bottom-left) and H=1.20m (bottom-right)

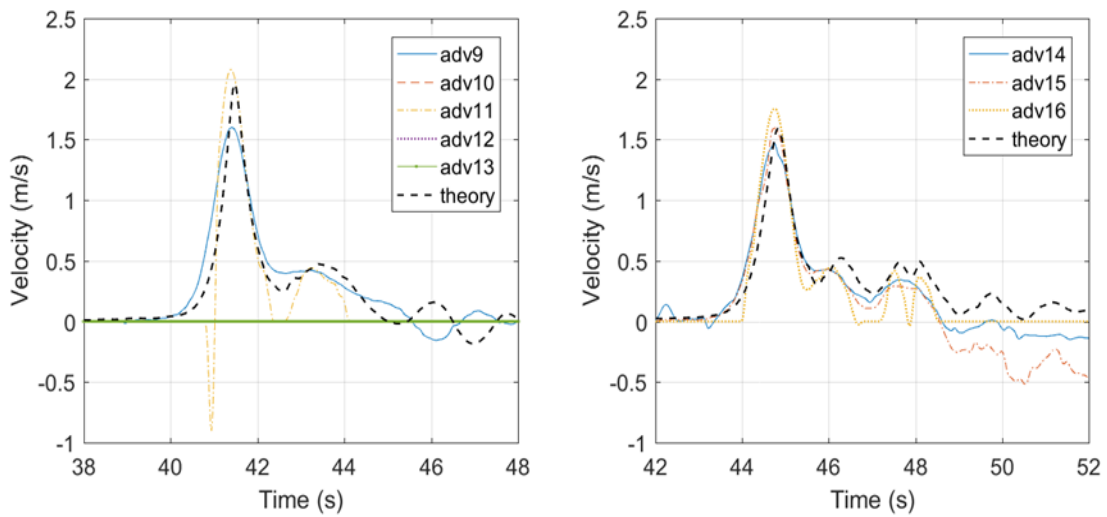


Figure 2.4: Theoretical and measured velocities at the bays in front of the bridge (left) and behind the bridge (right) for H=0.70m

2.2 TOTAL HORIZONTAL AND VERTICAL FORCES

This section will present and analyze the total forces measured in the experiments. However, before proceeding with the analysis and interpretation of the results, it is important to examine the quality of the data obtained from the bridge instruments. To this end, Figure 2.5 shows the maximum values of the total uplift forces recorded in the load cells of the piers and in the load cells of the bearings. A good agreement is observed for all the wave heights, with the piers giving uplift forces, which are higher than the ones in the bearings. This is reasonable because due to their location the bearings are taking only the uplift forces applied on the bridge deck while the piers are taking additional uplift due to the uplift pressures applied on the bent caps and all the connecting plates between the bottom of the bearings and the top of the piers.

Figure 2.6 shows the total force histories in the horizontal and vertical direction for a solitary wave and bore. Different patterns are noticed in the forces of the two wave types with the bore introducing the largest horizontal forces at the initial impact and the solitary waves introducing the largest force either when all chambers are inundated or at the initial impact, depending on the wave height. In addition, the bores seem to introduce horizontal forces larger than the vertical ones, while for the solitary waves the opposite is true. For bores both the horizontal and vertical tsunami forces consist of a short-duration impulsive component (called also ‘slamming’) that occurs at the initial impact and a longer duration slowly-varying component (called also ‘quasi-static’) as all the chambers of the bridge are being inundated.

Figure 2.7 are showing the total horizontal and uplift connection forces as a function of the input wave height and height measured at wave gage 12 (close to the bridge) respectively. The two graphs demonstrate that generally the wave height close to the bridge is a better parameter to correlate the forces to, compared to the input height. The reason for that is the significant reduction of the wave height of the bores and the significant increase of the wave height of the unbroken solitary waves, relative to the input height.

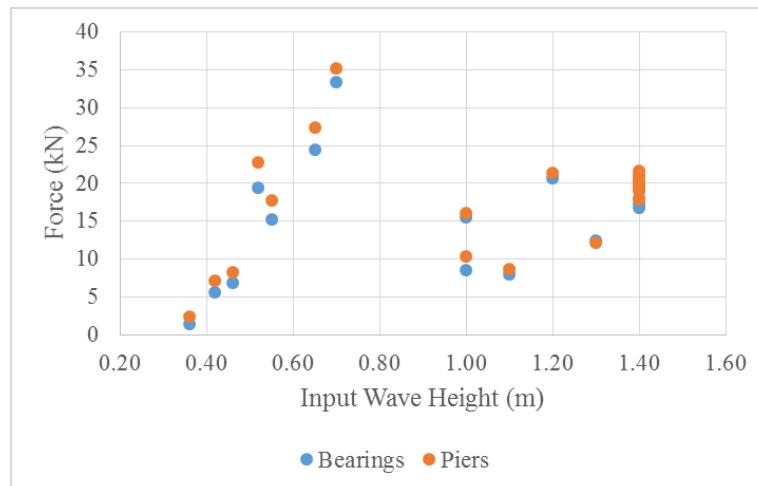


Figure 2.5: Maximum total uplift forces measured in the bearings and piers for ST1

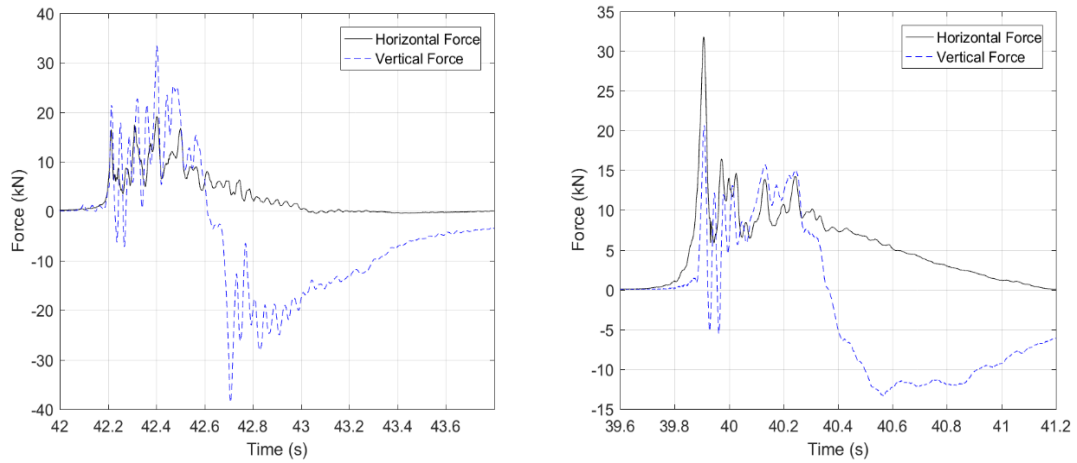


Figure 2.6: Total horizontal and vertical forces measured in the connections for H=0.70m (left) and H=1.20m (right)

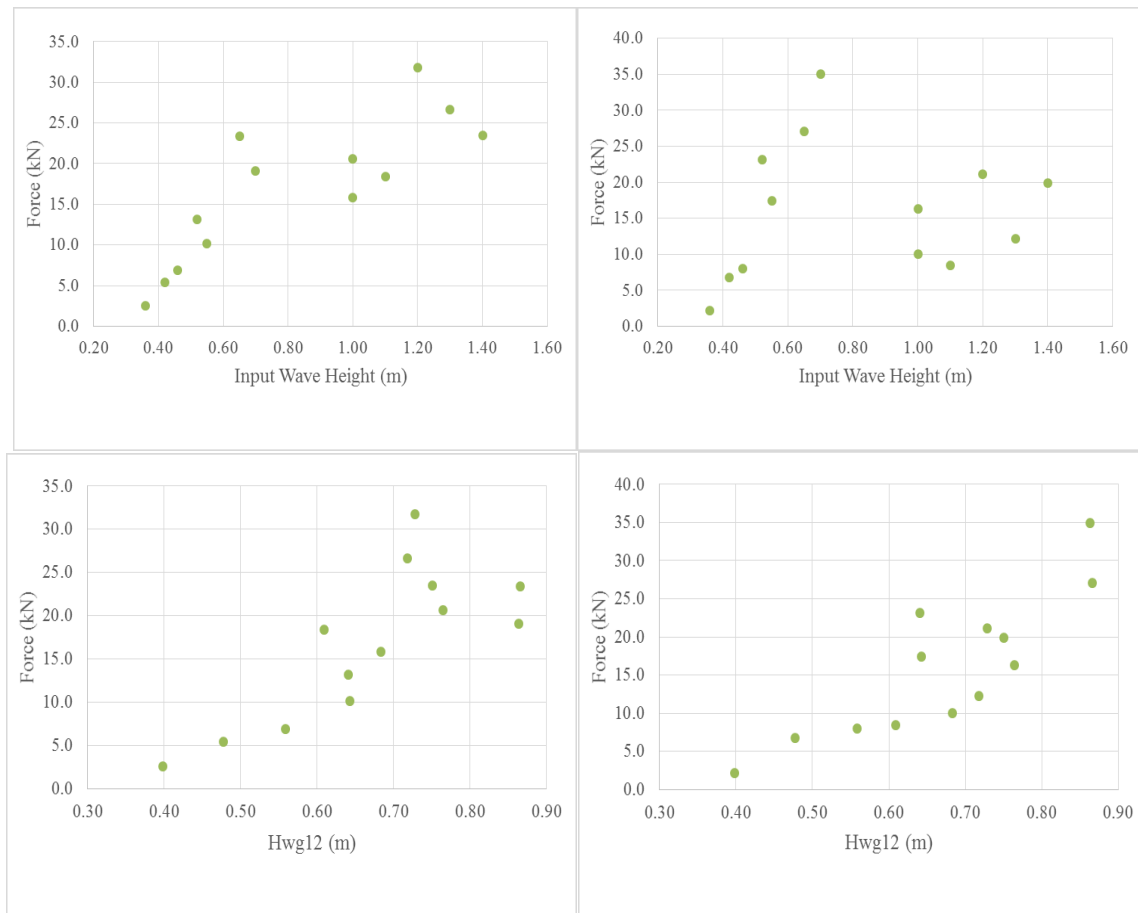


Figure 2.7: Total horizontal forces (left) and total uplift forces measured in the connections as a function of H_{input} (top) and H_{wg12} (bottom) for the bridge with steel bearing

2.3 DISTRIBUTION OF VERTICAL FORCES IN BEARINGS AND CONNECTIONS

Figure 2.8 shows the vertical forces recorded in each bearing for the aforementioned waves. For both solitary waves and bores at the initial impact the forces in the offshore and onshore bearings are out-of-phase, with the offshore bearings witnessing uplift forces and the onshore ones downward forces. However, as the inundation progresses and the chambers become inundated then all bearing witness uplift forces that are in phase, and are sharing the total uplift force indicating the existence of a vertical translational bridge mode. At the time of the initial impact the steel bearings are taking most of the uplift tsunami force with the bearings of the second offshore girder sharing also part of this force. It is interesting that for the particular waves shown in the figures the offshore bearings have to withstand significantly larger uplift forces than the rest of the bearings. This becomes clear both from the force-histories of the two waves presented in Figure 2.8, and from the maximum values for a range of waves shown in Figure 2.9. The latter figure shows the maximum uplift forces recorded in each bearing for both solitary waves and bores, for two water depths and different wave heights. As shown in this figure, uplift forces in offshore bearings were consistently significantly larger than the forces in the rest of the bearings, with solitary waves giving a ratio of the offshore to onshore bearings forces equal to a factor of 4.15 on average and 8 maximum. The two largest values (8 and 7) came from the smaller waves which could not (or could barely) reach the bottom of the deck in the chambers. If these two small waves are disregarded then the maximum factor is 4.2 and the average 2.8. For bores, the respective factors were 5.9 max and 3.2 average.

To better understand the tsunami demand on bearings Fig. 2.10 shows the maximum uplift forces measured in the offshore bearings versus the maximum total uplift for several solitary waves and bores, while Table 2.1 shows the ratios of these forces for all the bearings of the bridge. Clearly, this graph supports the previous figures that showed the offshore bearings getting larger uplift forces than the rest of the bearings. In addition, the graph shows that the offshore bearings get a large percentage of the total uplift, which could be equal up to 91% for unbroken solitary waves and 96% for bores, with the average values being 78% and 70% for the two wave types respectively. It is worth noting that if the tsunami uplift load was assumed to be a pure hydrostatic load then it could be assumed that the bearings will have to withstand uplift forces as a function of their respective tributary areas, which would yield uplift forces in offshore and onshore bearings equal to 23.3% of the total uplift load. However, this is not the case here with the offshore bearings witnessing uplift forces equal up to 96% of the total bridge uplift.

The above finding is quite significant because it demonstrates that the offshore bearings are witnessing the smallest gravity load among all bearings and at the same time the largest uplift forces, indicating that they have by far the largest probability of failure in the case of a tsunami event. Once these bearings fail then most of the tsunami load would be transferred to the nearby bearings which could fail sequentially leading to a catastrophic progressive collapse mechanism of the deck. To avoid such a damage mechanism, it is advised to design the offshore bearings for the total uplift force.

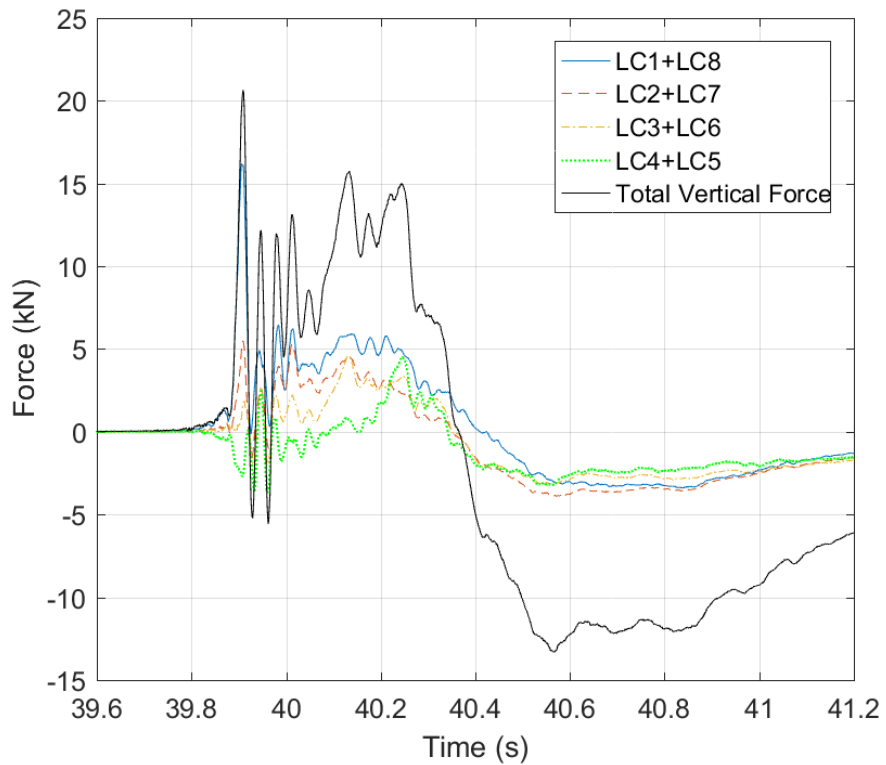
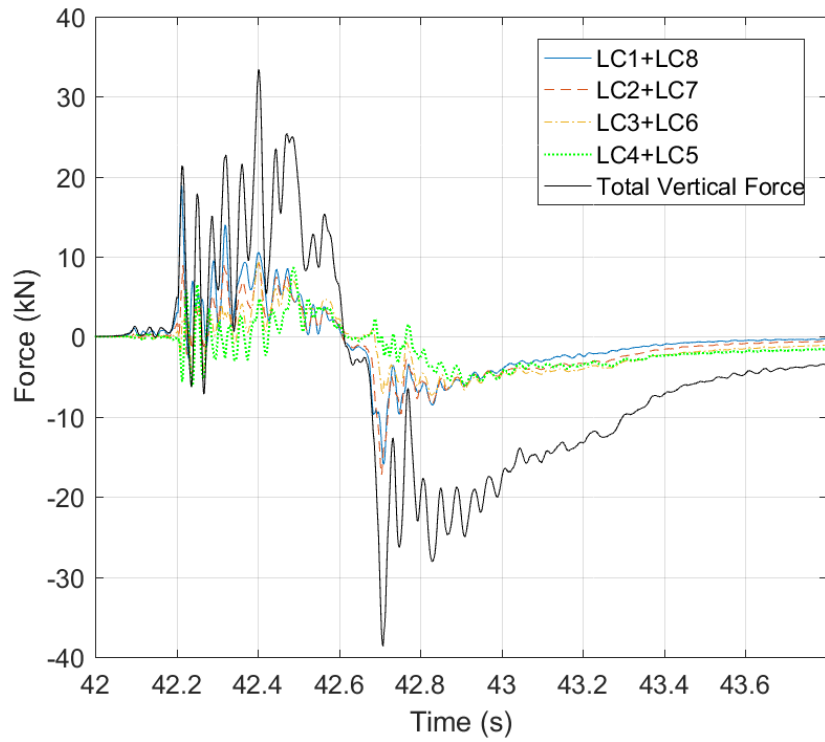


Figure 2.8: Uplift forces in the steel bearings for H=0.70m (top) and H=1.20m (bottom)

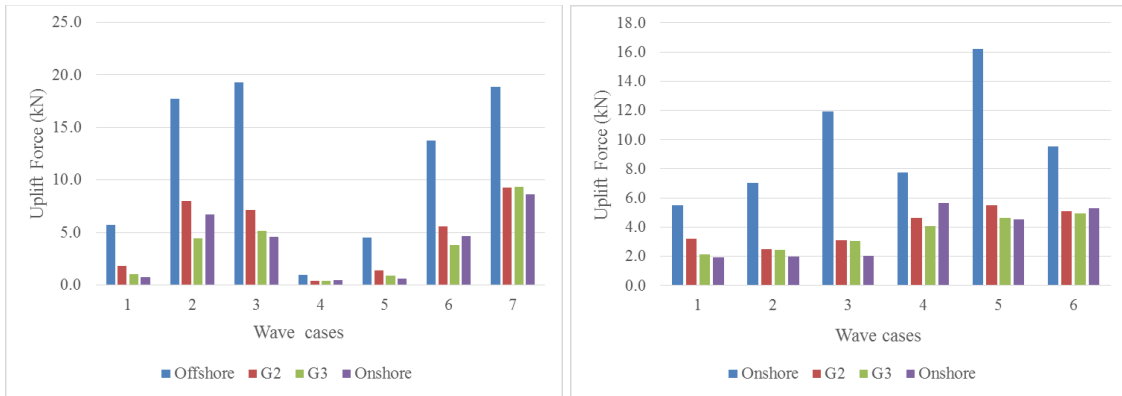


Figure 2.9: Uplift forces measured in the steel bearings for several solitary waves (left) and bores (right)

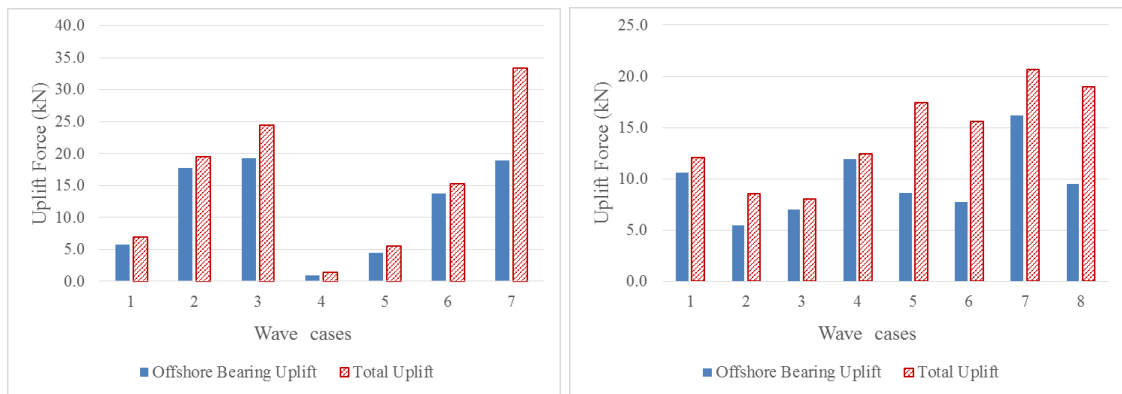


Figure 2.10: Maximum uplift forces measured in the offshore bearings versus the maximum total uplift for several solitary waves (left) and bores (right)

Table 2.1: Ratio of Maximum Uplift Forces Recorded in the Bearings of each Girder Relative to the Maximum of the Total Uplift Force

Wave Type	Depth (m)	Wave Case Num	H _{input} (m)	H/d	Fup, G1/ Fup, total	Fup, G2/ Fup, total	Fup, G3/ Fup, total	Fup, G4/ Fup, total
Unbroken solitary	1.90	1	0.46	0.53	0.72	0.23	0.12	0.09
		2	0.52	0.60	0.77	0.35	0.19	0.29
		3	0.65	0.82	0.71	0.26	0.19	0.17
	2.00	4	0.36	0.34	0.44	0.19	0.18	0.21
		5	0.42	0.41	0.67	0.21	0.14	0.09
		6	0.55	0.55	0.79	0.32	0.22	0.27
		7	0.70	0.74	0.54	0.27	0.27	0.25
Bore	1.90	1	0.80	0.80	0.86	0.23	0.20	0.21
		2	1.00	0.64	0.55	0.32	0.21	0.19
		3	1.10	0.57	0.83	0.30	0.29	0.24
		4	1.30	0.68	0.97	0.25	0.25	0.16
	2.00	5	0.90	0.73	0.47	0.26	0.27	0.31
		6	1.00	0.66	0.47	0.29	0.25	0.35
		7	1.20	0.63	0.77	0.26	0.22	0.21
		8	1.40	0.65	0.48	0.26	0.25	0.27

2.4 OVERTURNING MOMENT

The bearing force-histories presented in the previous section indicated that at the beginning of the tsunami impact the vertical forces in the offshore and onshore bearings were out-of-phase, with the former ones witnessing uplift and the latter ones downward force. This indicates the existence of clockwise overturning moment, however in order to verify if this is true, the moment was calculated directly based on experimental measurements. In particular, assuming that the tsunami load is static (neglect rotational inertia for the sake of simplicity) then the applied moment shall be equal to the reaction moment in the connections to satisfy equilibrium. This means that the applied moment at the center of mass (CM) of the deck can be calculated by using the forces and moments in the bearings or in the bent-cap connections as shown in Fig. 2.11. If it is assumed that the connection moments are negligible then the calculation of the moment requires only the horizontal forces in the links and the vertical forces in the connections, all of which are a direct output of the experiments.

Using this approach, a crude estimation of the applied moment was obtained and plotted in Fig. 2.12 for a solitary wave and a bore. Interestingly, for both wave types the moment is maximized at the initial impact of the wave on the offshore girder and overhang. Moreover, the maximum overturning moment and maximum bridge uplift do not occur at the same time for many of the tested waves in the experiment. The existence of this significant overturning moment explains why for the solitary wave of H=0.70m although the maximum total uplift force occurs when the wave has inundated all the chambers, the maximum uplift in the offshore bearings occurs at the time of the initial impact. This governing overturning moment has been neglected to date and all

the predictive equations have focused on the maximum horizontal and vertical forces. This experimental study clearly demonstrates the need of accurately capturing the overturning moment in addition to horizontal and vertical forces.

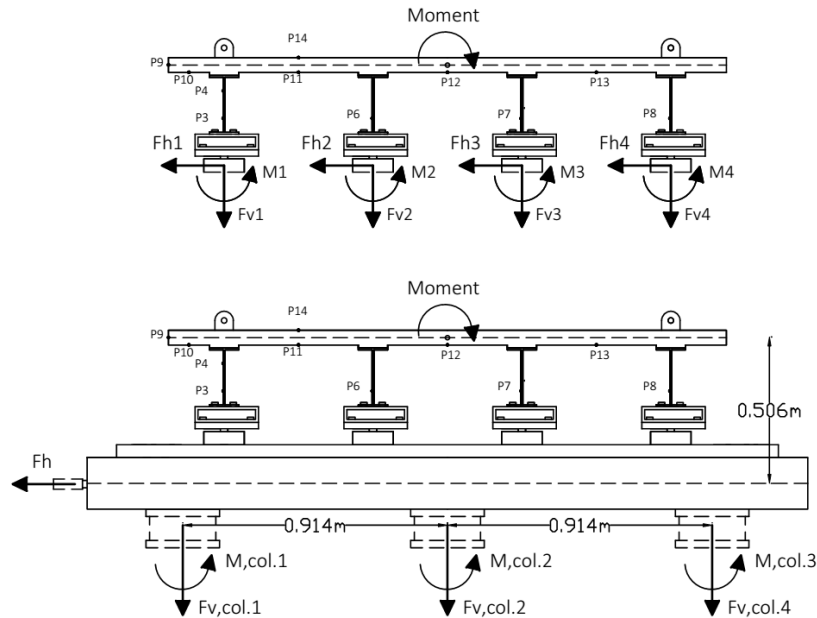


Figure 2.11: Calculation of the overturning moment

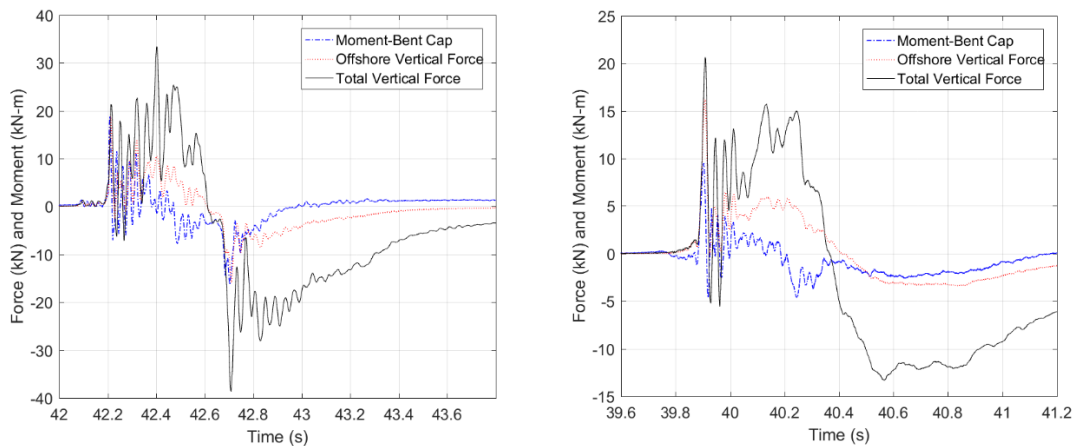


Figure 2.12: Uplift forces in the offshore steel bearings, total uplift force and moment in the connections for H=0.70m (left) and H=1.20m (right)

2.5 APPLIED TSUNAMI PRESSURES ON GIRDERS AND BRIDGE DECK

In order to gain an insight into the applied tsunami load on the different components, the pressures were recorded at different locations. The pressure histories on the four girders and below the deck at four different locations are plotted in Figure 2.13. This figure shows that the

offshore girder is witnessing significantly larger pressure than the rest of the girders for both the solitary wave and the bore. Figure 2.15 demonstrates that this observation is true for all waves examined. Actually post-processing of the experimental results revealed that for the tested waves the pressure on the offshore girder was between 1.5 and 4.3 times larger than the pressure on the onshore girder. In fact, the offshore girder has to withstand the total slamming horizontal load that is generated at the instant of the first impact of the wave on the girder, indicating that this load should be considered in the design phase of the bridge in order to avoid large lateral deformations of the girder. Especially, given the fact that at the time of the maximum horizontal slamming load there is a significant slamming uplift load that can exceed the weight of the bridge suggests that lateral torsional buckling of the offshore girder might be a possible limit state to be checked in the tsunami design of the bridge. However, further detailed FSI analyses, which will calculate the stresses in the girders, are required in order to verify that the uplift force is indeed introducing compression in the bottom flange of the offshore girder.

Similarly, to the offshore girder, the overhang of the bridge is witnessing impulsive pressures, which are multiple times larger than the pressures below the deck in the chambers. In particular, for the examined waves and a bridge with cross-frames the overhang pressure was between 2.4 to 25 (with an average of 8.8) times larger than the pressure in the middle chamber (Figure 2.16). This explains why the overturning moment is so large at the time of the initial impact. This is a major finding because it demonstrates that if the overhang were eliminated then the overturning moment and consequently the uplift forces in the offshore bearings at the initial impact would be reduced significantly.

Finally yet importantly, Figure 2.14 shows the pressures on the offshore side at three different heights ($H_{girder}/3$, $2H_{girder}/3$, $H_{deck}/2$). It can be noticed that pressures at the two lower locations were larger than the higher one, as expected.

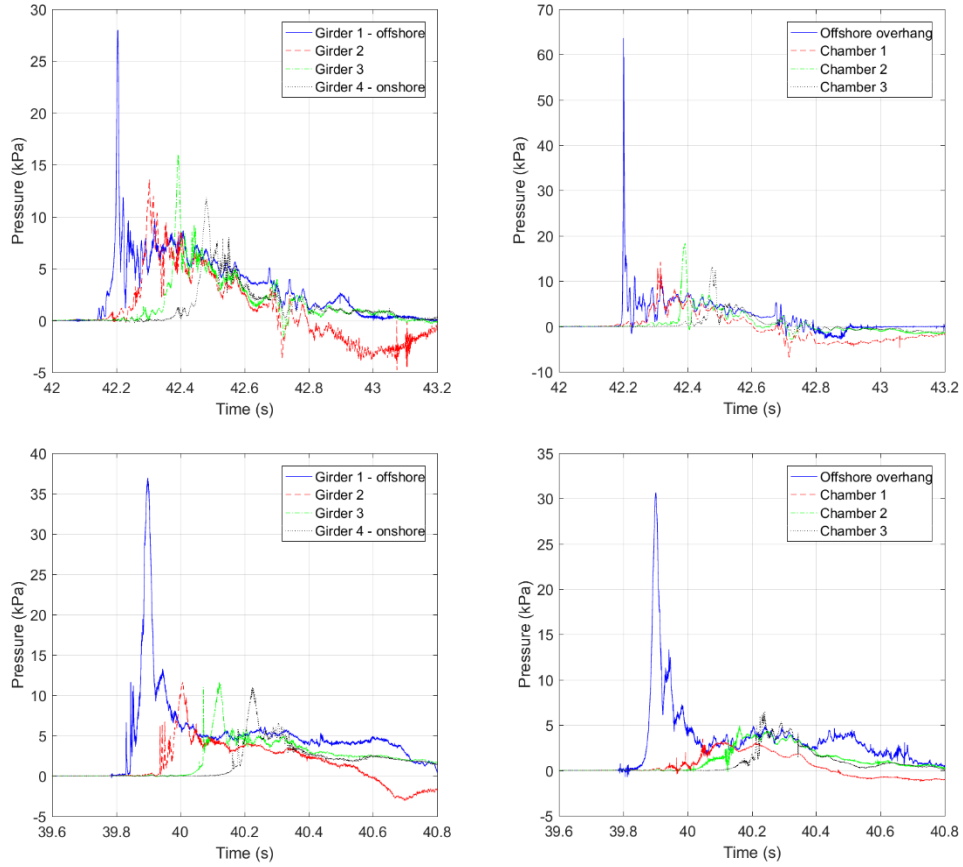


Figure 2.13: Pressures applied on the girders (left) and below the bridge (right) for $H=0.70\text{m}$ (top) and $H=1.20\text{m}$ (bottom)

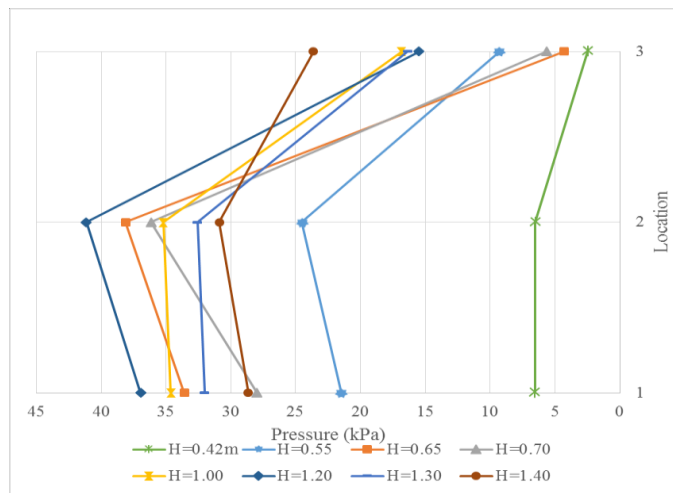


Figure 2.14: Pressures on the offshore side of the bridge for several wave heights

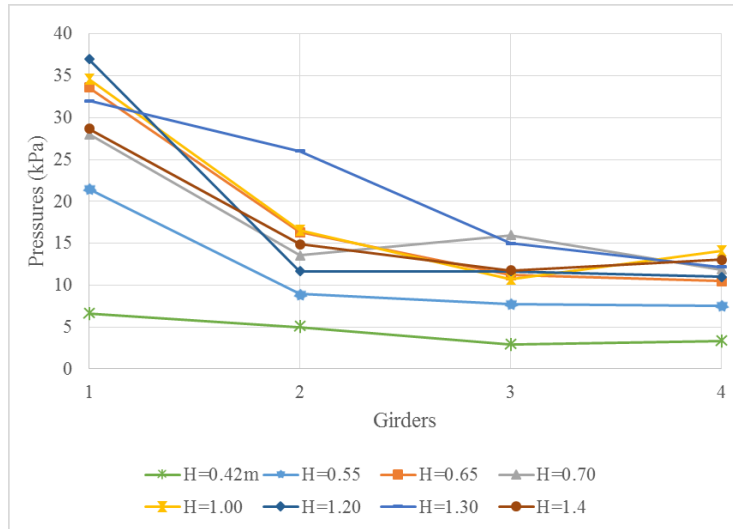


Figure 2.15: Pressures on the girders of the bridge wave heights

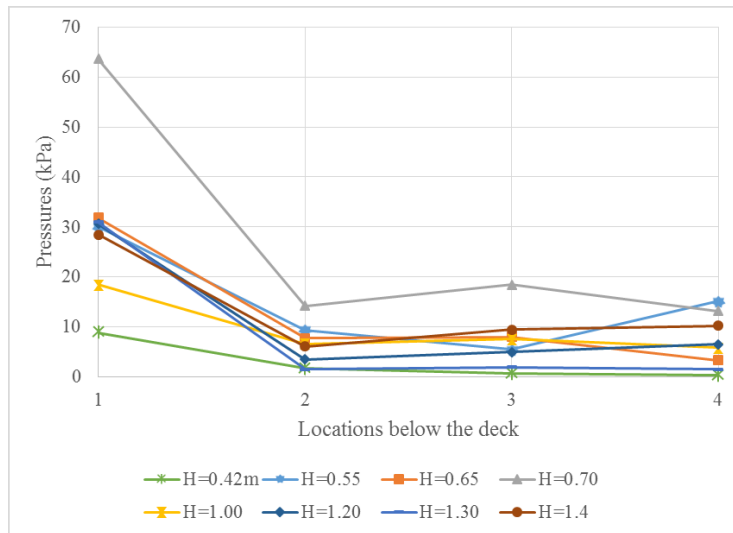


Figure 2.16: Pressures at different locations below the deck of the bridge

2.6 INUNDATION MECHANISM, ASSOCIATED FORCES AND PRACTICAL DESIGN RECOMMENDATIONS

The detailed analysis of the experimental data presented in the previous sections has demonstrated that the tsunami inundation mechanism of bridges does not consist of only pure drag or pure uplift, as hypothesized in several previous studies. To decipher the tsunami inundation mechanism and associated forces on the bridges, the force and moment histories were plotted together with normalized pressure (p/p_{max}) histories, as shown in Figure 2.17. This graph shows that there exist 4 different phases in the inundation mechanism, as described below:

- Phase 1: This is a short duration phase that witnesses significant impulsive horizontal and vertical forces and occurs when the wave hits the offshore girder and offshore

overhang. It introduced the maximum horizontal force for all bores and the maximum overturning moment in the connections for all the tested waves. Due to the simultaneously large uplift force and large moment, this phase introduces the largest uplift in the offshore bearings, meaning that it could be the most catastrophic for the offshore structural components (bearings, connections and girder). During this phase the offshore bearings are in tension and the onshore ones in compression.

- Phase 2: This is a longer duration phase that occurs when the bridge starts inundating chambers 1 (offshore) and 2 (center) of the bridge and the uplift force is applied close to the CM of the bridge deck. In this phase the moment is very small, however the bridge uplift force is very large and for some wave heights it is the maximum bridge uplift. In this phase all bearings are in phase witnessing uplift forces with the bearings of the interior girders (G2 and G3) reaching their max uplift values. For bores the horizontal force is reduced in this phase, however for certain solitary waves the horizontal force can be the maximum one.
- Phase 3: This phase occurs when the wave has reached the 3rd chamber (onshore one). In this phase the horizontal force is reduced for all wave types, the vertical force is large (can even be maximized) and there is a counter-clockwise moment, which introduces the largest uplift force in the onshore bearings. Therefore, this phase has to be considered because it's the governing one for the onshore bearings.
- Phase 4: This phase occurs after the wave was passed the onshore chamber and the wave hits the top of the bridge deck. This slamming vertical forces on the deck is so high that it exceeds the uplift force applied below the deck and introduces compression in all bearings.

The 4 phases are illustrated in Figure 2.18. Special attention should be given to Phase 1, which has been neglected to date, because it introduced the largest tension in the offshore bearings for most waves. This is of utmost significance because it indicates that if the offshore bearings exceed their tensile capacity in Phase 1 due to the significant overturning moment and get damaged then the uplift loads would be redistributed to the remaining bearings with the possibility of leading to a “progressive collapse mechanism” that will eventually result in the washout of the bridge.

As discussed in the literature review included in chapter 1 of this report, most of the studies to date have focused on total uplift forces caused by tsunamis and hurricanes. However, the large-scale experiments presented herein are indicating that the total uplift forces alone cannot sufficiently describe the effects on coastal bridges. The reason is the fact that the maximum total uplift can occur either in Phase 1 or in Phase 3, however if the maximum occurs in the former phase then the vertical force is distributed mainly to the four bearings of the first two girders (in the four-girder bridge examined herein), while if it occurs in Phase 3 then the uplift force is distributed to all eight bearings of the girders. This means that the maximum total uplift force does not necessarily correspond to the maximum tensile forces in all bearings. Therefore, the focus of future research studies should be the forces in the connections and other members of the bridge.

In order to capture the distribution of tsunami forces in all the bearings, connections and piers, different predictive horizontal and vertical force equations shall be developed for each of the three aforementioned phases. These equations shall be applied at different locations along the bridge width, with the horizontal force applied on the offshore girder and the vertical one below the overhang in Phase 1. For phase 3 the horizontal force can be applied on the girder and the vertical force below the deck, at the mid-width of the bridge cross-section (or at the CM). An alternative approach in future guidelines would be to apply the horizontal and vertical forces at the center of mass of the bridge (as currently done) for all three phases, however in this case the forces should also be accompanied by a moment (which has been neglected to date) in order to capture the correct distribution of the forces in the bearings. This method will require the development of a predictive equation for the applied tsunami moment, in addition to the forces. To the authors' view the latter approach is easier from a design point of view, however the former approach is more preferable because applying the forces at different locations of the bridge is a reminder of the complex inundation mechanism. In addition, the forces in Phase 1 will depend on different parameters than the ones in Phase 3 (e.g. in Phase 3 the uplift forces will depend on the existence of diaphragms and trapped air, while in Phase 1 not), indicating again that it might be more beneficial to separate the forces of the different phases in a design approach by applying them at different locations as observed in reality.

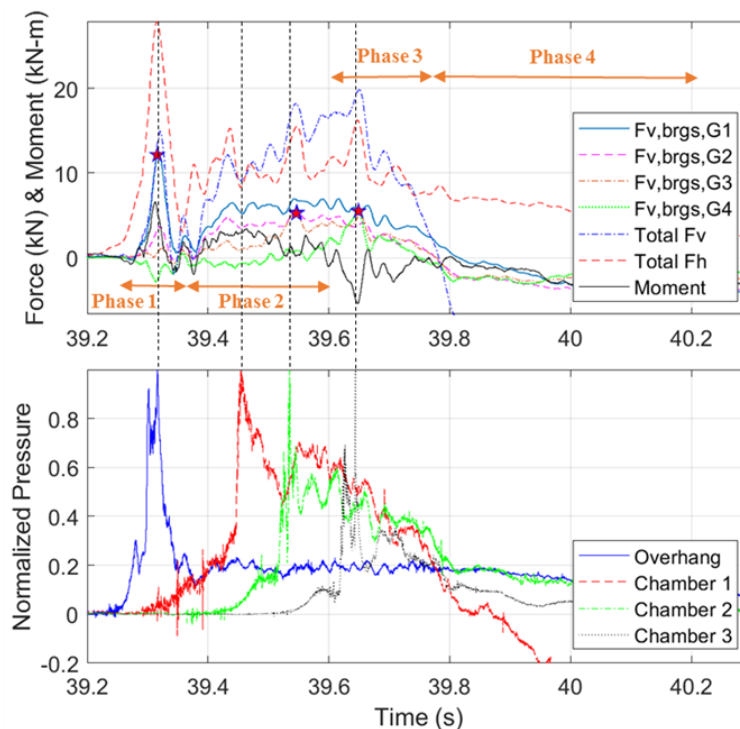


Figure 2.17: Forces, moment and normalized pressures histories

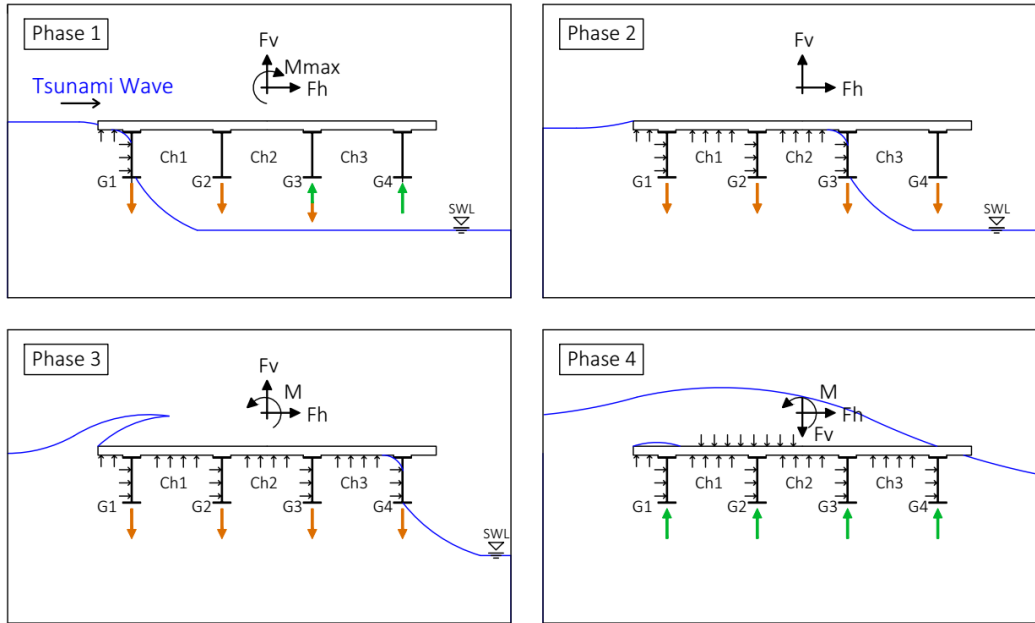


Figure 2.18: Tsunami inundation mechanism of coastal bridges

2.7 EFFECT OF WAVE TYPE AND WATER DEPTH

Figure 2.20 shows the maximum total horizontal forces against the maximum total uplift forces recorded in the connections for both solitary waves and bores. The unbroken solitary waves seem to introduce a different pattern of forces in the bridge connections than the turbulent bores. For the bores the ratio of maximum horizontal to maximum vertical force was found to be larger than 1.0 for most waves reaching a maximum value of 2.2, while for the unbroken waves this ratio was smaller than 1.0 with a minimum value of 0.54. Therefore, it is important to determine the wave type to which the bridge will be subjected, because each type introduces a different demand on the connections of the bridge and activates a different bridge resistance mechanism.

The total forces measured in the connections were separated into a slamming and quasi-static component using the Empirical Mode Decomposition Method (Huang et al., 1999). This method had been implemented for decomposing the total forces of breaking waves by various researchers (Irschik et al., 2004; Jose et al., 2016). In this report the approach followed in the latter study is implemented. In the first step of the method the total forces are filtered to remove noise in the signal. In the second step the EMD method is applied and the first intrinsic mode with the residue is obtained, representing the amplified component (due to the structural response) and the net force respectively. In the last step the net breaking force is separated into a slamming and a quasi-static via a low-pass filter. The three steps are shown in Figure 2.19.

In order to get an insight into the effect of the water depth and clearance, two different water depths equal to 1.90m and 2.0m were used in the large-scale experiments. The elevation of the bridge was kept the same when the water depth changed, meaning that the distance of the bridge from the still water (= clearance) changed accordingly. Figure 2.21 shows the maximum total connection forces in the horizontal and vertical direction, as well as the maximum values of the quasi-static component of the forces, as a function of the non-dimensional amplitude (=

measured wave height/water depth). The quasi-static forces were obtained using the Empirical Mode Decomposition Method (EMD), as described above. As shown in the figures, both the total horizontal and uplift forces are affected by the water depth however there does not seem to exist a clear trend. However, both the horizontal and the vertical quasi-static force are affected by the water depth in a consistent way, with the largest water depth introducing the largest forces in both directions. This demonstrates the significance of the water depth on calculating the recorded forces.

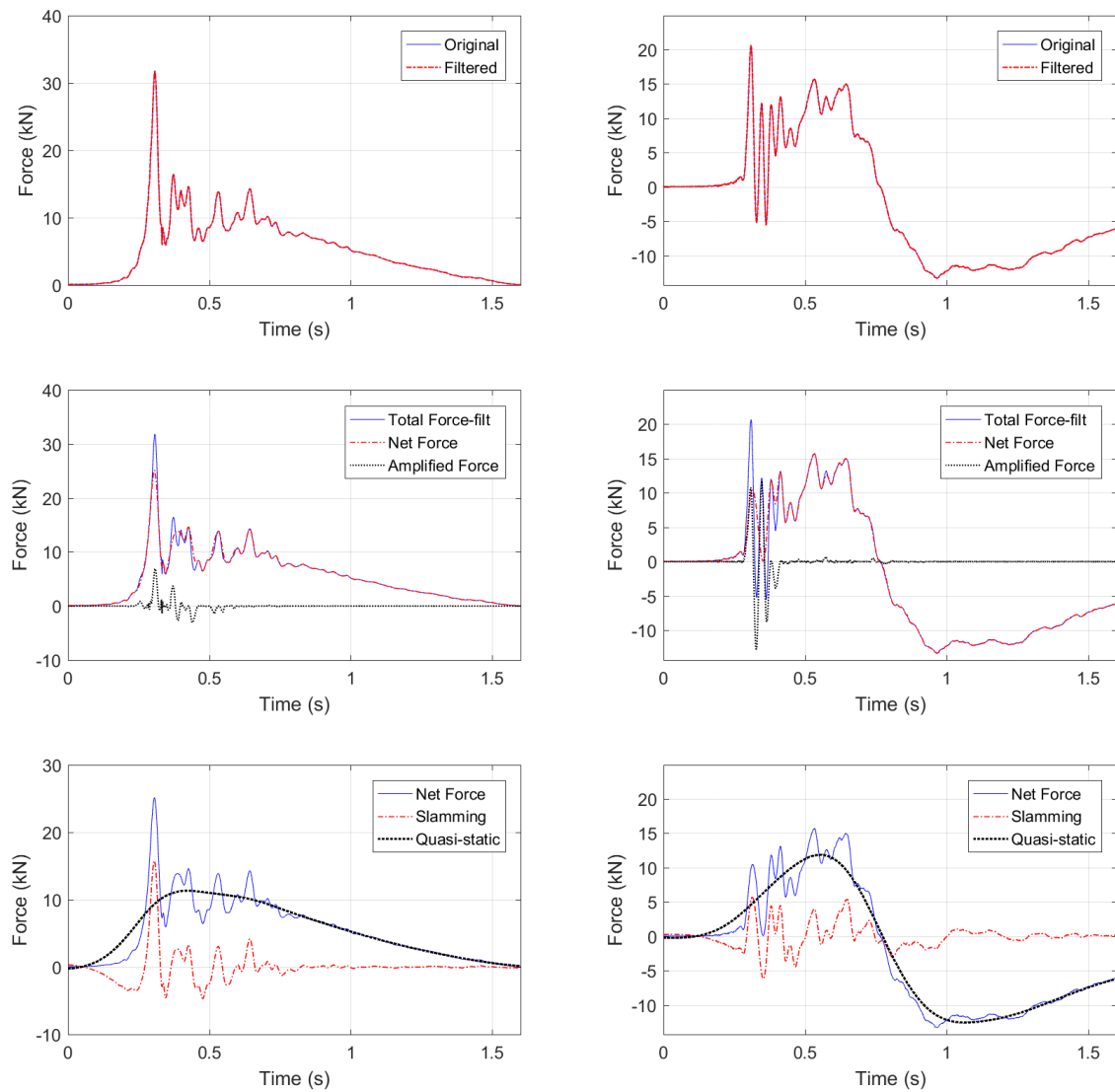


Figure 2.19: Decomposition of the total horizontal (left) and vertical (right) connection forces into slamming and quasi-static components H=1.20m

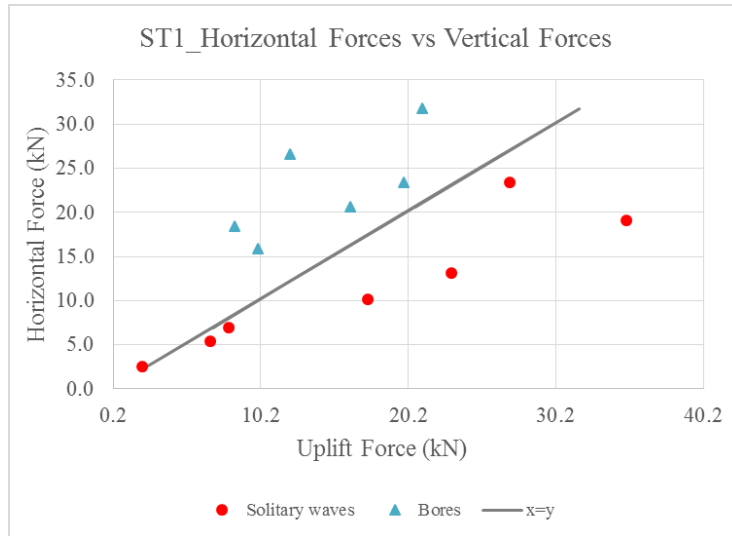


Figure 2.20: Total horizontal and uplift forces measured in the steel bearings

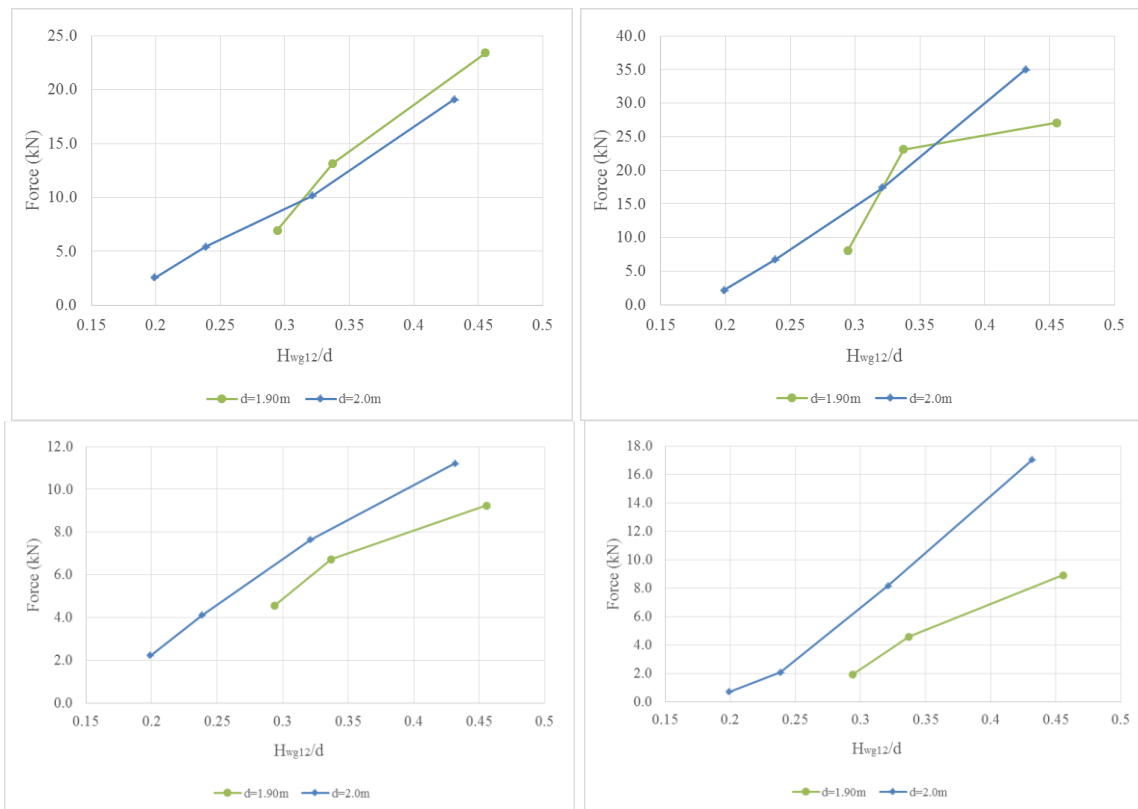


Figure 2.21: Maximum total (top) and quasi-static (bottom), horizontal (left) and uplift (right) forces for the tested solitary wave heights

2.8 APPLIED LOADING, INERTIA AND DYNAMIC AMPLIFICATION

The large-scale of the hydrodynamic experiments presented in this report has permitted the measurement of the accelerations at three different locations of the bridge. The accelerations

were measured in both x and z directions and the histories are plotted in Figure 2.22. As can be noticed, significant accelerations are introduced in the deck with the ones in the vertical direction being larger than the horizontal ones. The accelerations were measured at the offshore and onshore corners and at the center of the bridge. Notably, the accelerations at the offshore and onshore corners are out of phase at the initial impact, demonstrating again the existence of an overturning moment and giving confidence in the results obtained by the load cells.

One of the major findings of the advanced FSI analyses presented in (Istrati and Buckle, 2014) was the difference between the applied tsunami load and the forces in the connections, indicating the significance of the bridge dynamics. To examine if this finding was true, a similar comparison was conducted with the data obtained directly from the large-scale hydrodynamic experiments. The applied horizontal tsunami load was calculated via integration of the pressure measurements at different locations of the bridge and was compared with the force in the substructure links. The comparison of the two forces, plotted in Figure 2.23, revealed that the recorded forces were larger than the applied tsunami at the initial impact of the wave on the bridge. This could indicate that there exists dynamic amplification or that the tsunami load was not accurately predicted via the integration of pressure due to the small number of pressure gages. To decide which was the reason, the inertial forces were calculated based on the accelerometers installed at the three different locations on the deck and added to the connection forces to see if the dynamic equilibrium was satisfied (contribution of structural damping was not significant). Surprisingly, considering the inertia forces resulted in a good matching of the sum of connection and inertia forces with the calculated tsunami load, revealing the significance of the inertia forces and the dynamic amplification.

The above comparison showed that for bridges with a very large lateral stiffness of the substructure and the connections, the dynamic bridge properties play a major role on the horizontal forces that the connections, shear keys and substructure have to withstand. For certain bores, the natural frequencies of the bridge can coincide with the duration of the impulsive horizontal load and result in a magnification of the forces in the connections. This is a major finding because it demonstrates that for certain wave conditions, the current practice of obtaining the maximum loads from a pure CFD analysis - in which the dynamic response of the bridge is not considered - and using the maximum values for comparison with the estimated resistance of the bridge or for further static analyses might not be accurate and for certain bore heights can actually under-predict the forces in the bridge members significantly.

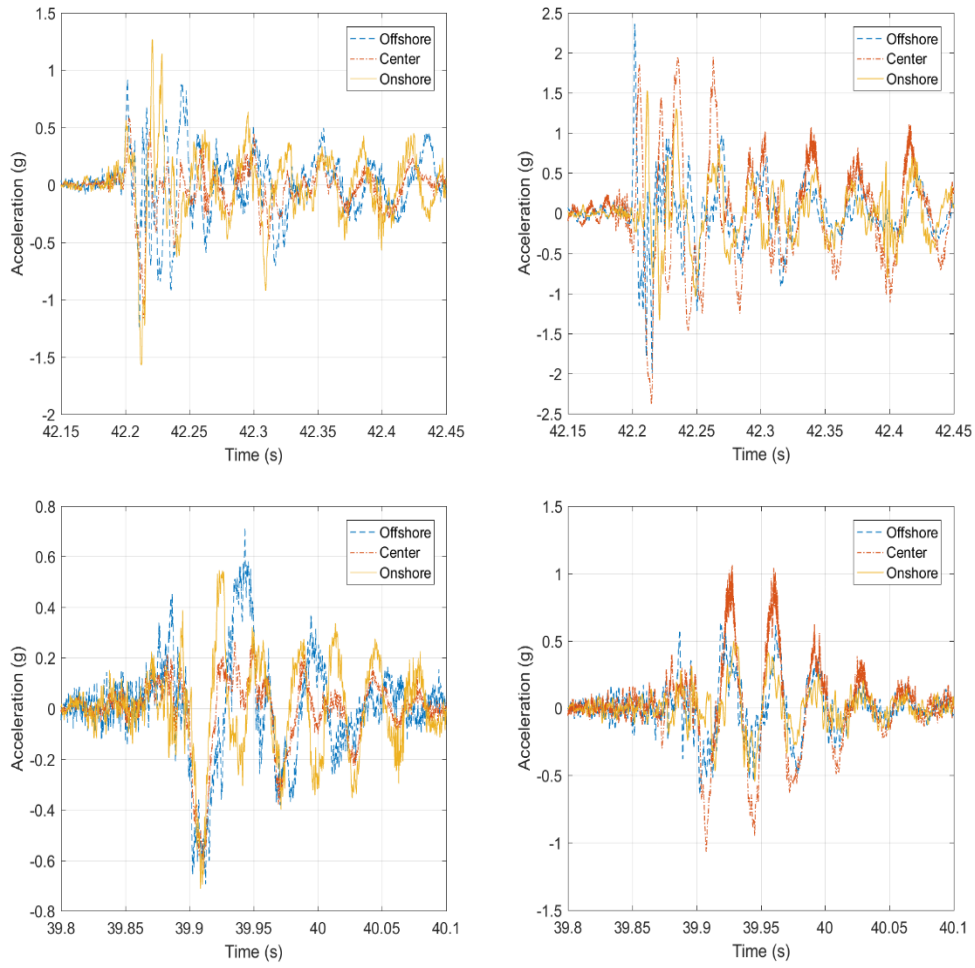


Figure 2.22: Deck accelerations in the horizontal direction (left) and vertical direction (right) for H=0.70m (top) and H=1.20m (bottom)

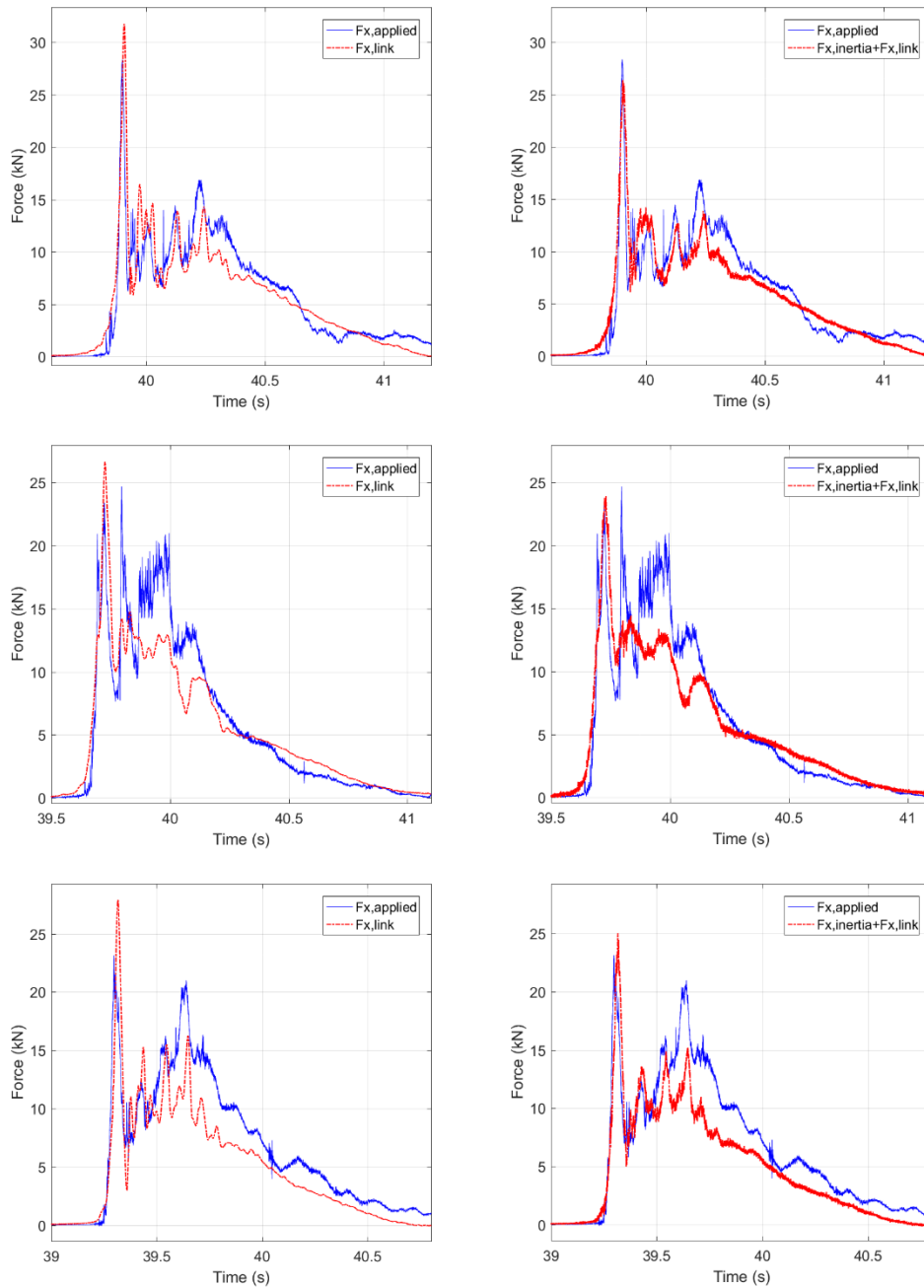


Figure 2.23: Applied horizontal forces, forces in links and sum of inertia and links forces for H=1.20m (top), H=1.30m (middle) and H=1.40m (bottom) for ST1

2.9 REPEATABILITY AND UNCERTAINTY OF WAVE FORCES

A major issue in experiments studying the impact of breaking waves, broken waves and bores on structures conducted by researchers in the field of coastal and offshore engineering (e.g. Peregrine et al., 2004; Robertson et al., 2008; Jose et al., 2016) is the high variability (in the range of 35%) of the recorded forces. This high variability has been noticed by many studies,

however as mentioned in (Jose et al., 2016) an exact explanation of this phenomenon does not exist. The previous researchers suggested that the dynamic amplification which occurs when breaking waves impact the jacket type (truss) foundation of an offshore wind turbine is a major factor for the variability. Peregrine et al., 2004, showed that the wave height and the air bubbles entrained inside in the breaker, which is a random process, are also affecting significantly the variability of the forces. Ghosh et al., 2007, demonstrated via experiments that after the plunging type breaking of a wave multiple chaotic splash-ups occur creating turbulence and vorticity.

To examine the variability of the forces introduced by the waves, the bore with the largest input height $H=1.40\text{m}$ was repeated 11 times. The repeatability of both the total forces as well as the slamming and quasi-static components (obtained from the EMD method) were examined and the results are shown Table 2.2. Interestingly, the horizontal forces present a larger variability than the vertical ones with the SD/Avg being 19.6% for the former and 5.9% for the latter. Even more interestingly, the table reveals that this variability comes from the variability of the maximum slamming force ($SD/Avg=22.1\%$), which is maximized at the time of the initial impact on the offshore girder, and not from the quasi-static component which is very repeatable. To further verify that, Table 2.3 shows the vertical forces in the bearings of the bridge for the ten runs. Clearly, the offshore bearings have a variability significantly larger than the rest of the bearings, which is 25%. The forces in the offshore bearings are maximized at the initial impact of the wave on the bridge when the slamming forces are maximized, while the rest of the bearings are maximized later on when the chambers are inundated and the quasi-static forces are maximized, verifying again that the reason for the large variability is the variability in the slamming component.

Post-processing of the data revealed that the chaotic wave-breaking process with the random entrainment of air-bubbles creates a significant variation in the pressures histories on the offshore girder and overhang resulting in an impulsive applied tsunami load of a variable shape and duration. Since the very stiff bridge configuration has a natural frequency in the same range with the duration of the impulsive peak of the slamming force (at initial impact) its response is significantly affected by both the shape and the duration of the slamming force (dynamic amplification).

Figure 2.24 shows the surface elevation at different locations along the flume for the four runs (out of the 11) that cause the smallest and largest forces on the bridge, and reveals the identical heights for all the wave gages before breaking and the introduction of significant variability after the wave breaking occurs, as noticed in the aforementioned studies. This variability in the wave height results in a significant variability in the pressure histories, histories of applied load and connection forces.

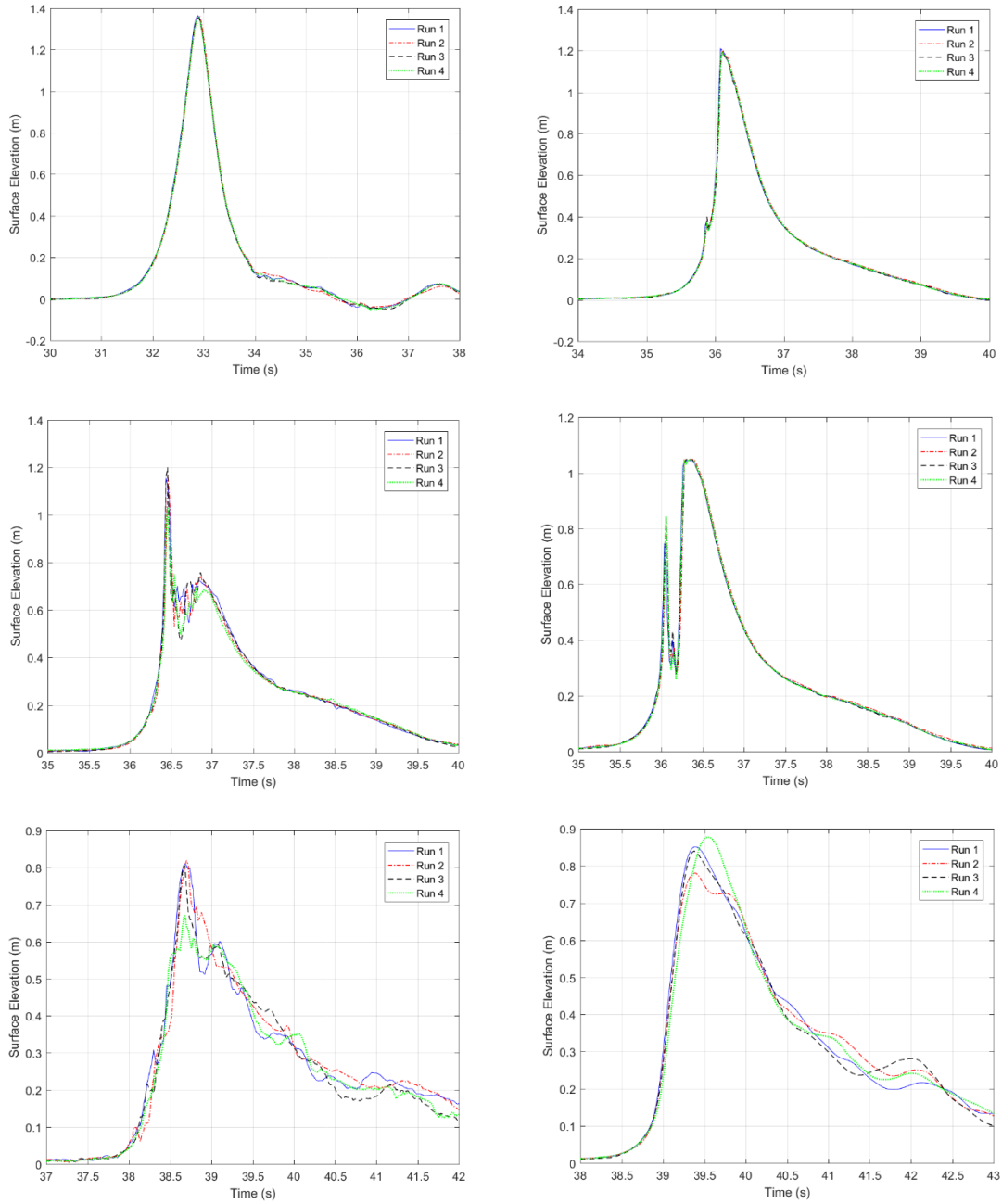


Figure 2.24: Wave heights measured at wg2 (top-left), wg7 (top-right), wg8 (middle-left), wg9 (middle-right), wg12 (bottom-left) and uswg1 (bottom right) for the four runs of H=1.40m and the bridge with steel bearings

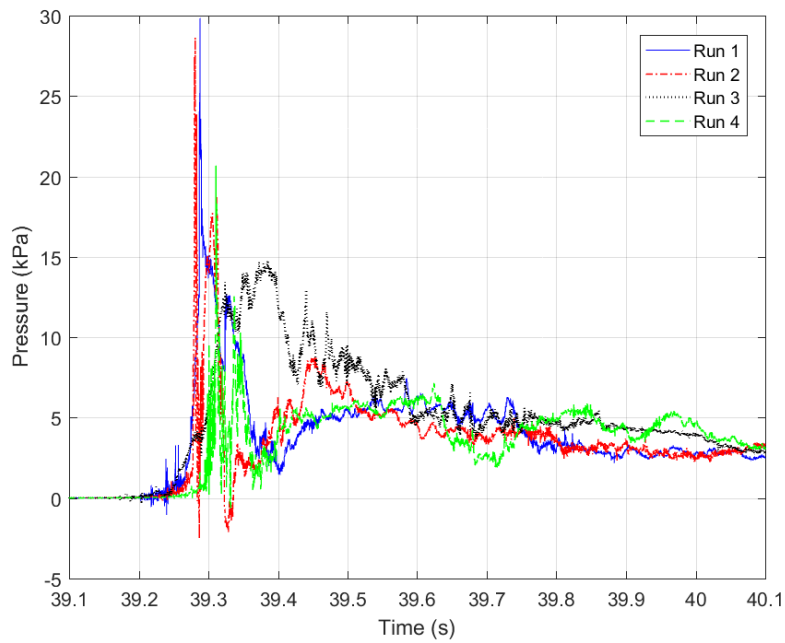
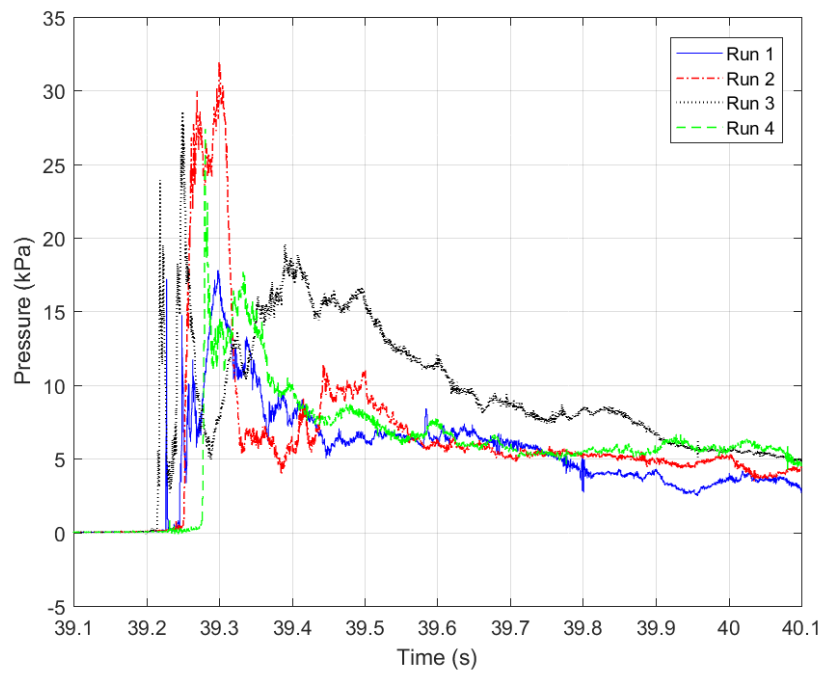


Figure 2.25: Pressure histories on the offshore girder (top) and below the overhang (bottom) for the four runs of H=1.40m and the bridge with steel bearings

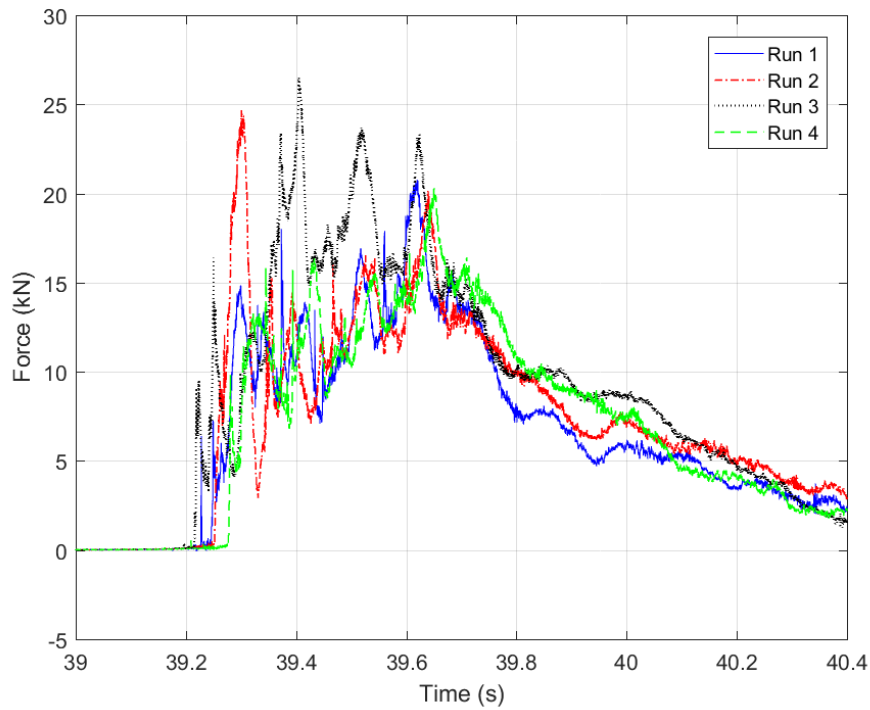
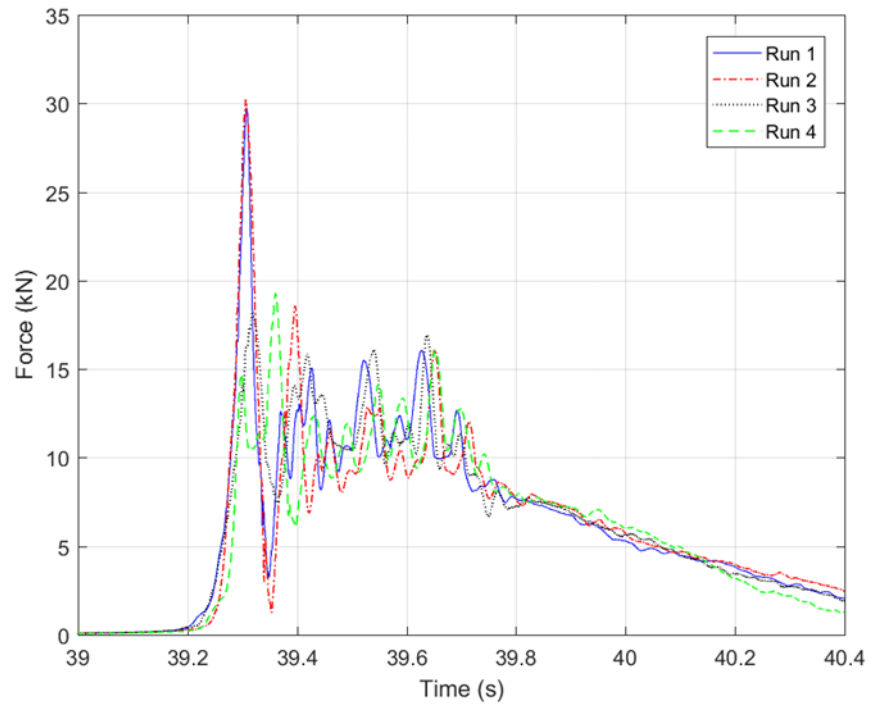


Figure 2.26: Total horizontal forces recorded in links (top) and calculated from integration of pressures (bottom) for the four runs of H=1.40m and ST1

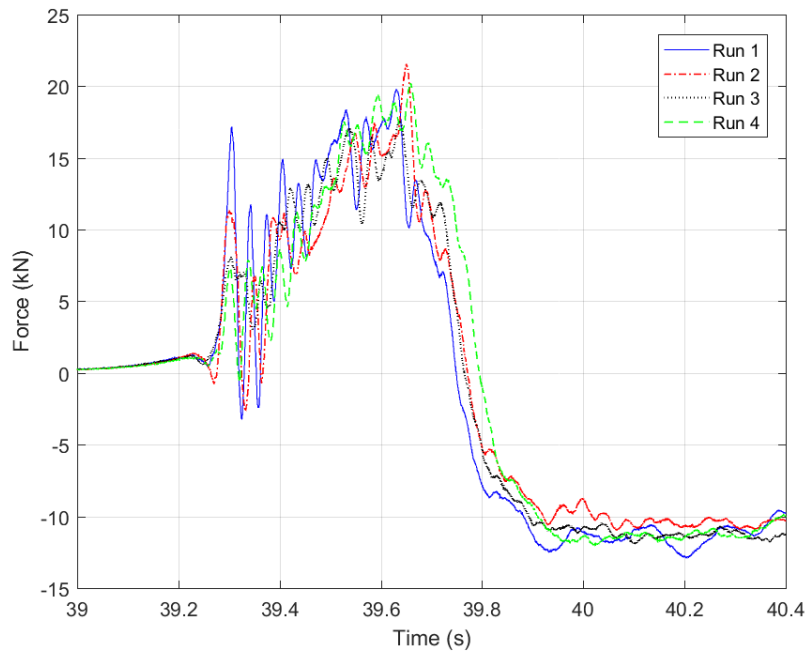
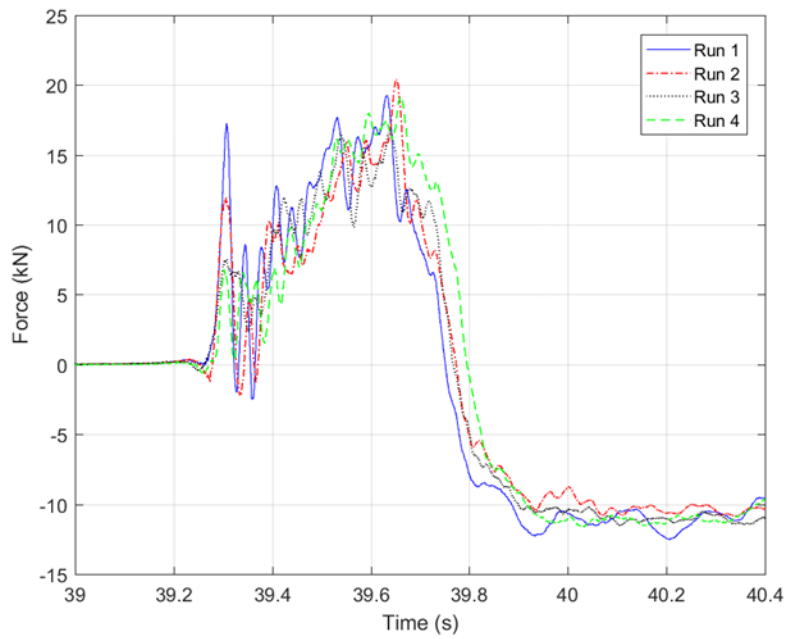


Figure 2.27: Total vertical forces recorded in the bearings (top) and piers (bottom) for the four runs of H=1.40m and ST1

Table 2.2: Maximum Total, Slamming and Quasi-static Forces for Ten Runs of H=1.40m and Bridge Configuration ST1

Run	Horizontal	Vertical	Horizontal		Vertical	
	Total Forces		Slamming	Quasi-static	Slamming	Quasi-static
1	22.70	19.08	11.28	11.84	5.65	14.58
2	19.27	20.21	6.15	11.83	5.63	16.13
3	18.24	17.59	8.90	12.56	5.25	14.15
4	20.58	19.92	11.73	11.43	7.46	15.39
5	29.74	19.78	14.40	12.21	7.39	14.62
6	27.89	20.92	12.84	11.36	7.77	15.34
7	30.19	21.54	10.16	10.60	9.43	14.03
8	26.04	20.14	10.30	11.68	7.45	14.75
9	20.56	21.13	8.77	11.79	6.52	15.77
10	19.31	18.92	9.83	12.27	6.45	14.81
Average	23.5	19.9	10.4	11.8	6.9	15.0
SD	4.6	1.2	2.3	0.6	1.3	0.7
SD/Avg (%)	19.6	5.9	22.1	4.7	18.2	4.6

Table 2.3: Maximum Vertical Forces in the Bearings below the Four Girders for Ten Runs of H=1.40m and Bridge Configuration ST1

Run	Offshore G1	Interior G2	Interior G3	Onshore G4
1	7.38	5.30	5.11	4.77
2	7.51	5.42	5.03	5.19
3	7.08	4.63	5.19	5.50
4	10.84	5.12	4.61	4.98
5	14.09	5.16	4.81	5.66
6	12.12	5.32	5.22	5.48
7	10.95	4.63	5.26	6.19
8	8.76	5.20	4.63	4.98
9	7.42	5.24	5.17	5.68
10	9.15	5.09	4.52	4.58
Average	9.5	5.1	5.0	5.3
SD	2.4	0.3	0.3	0.5
SD/Avg (%)	25.0	5.3	5.8	9.2

2.10 SIMPLIFIED METHODOLOGY FOR ENGINEERING PRACTICE

Previous sections of this report revealed the complexity the tsunami inundation mechanism and associated transient loading, which introduces a variable uplift demand on different bearings, columns and connections. One methodology to accurately capture the transient effects would be the development of time-histories of total horizontal and vertical forces as well as moment. A less sophisticated methodology would be the development of tsunami demand diagrams either

2D ones of (Fh, Fv) and (OTM, Fv) or 3D ones (Fh, Fv, OTM). This method would be less accurate and economical than developing time-histories but will require less input parameters increasing consequently its practicality. An even simpler methodology would be the determination of several sets of forces with corresponding moments (Fhi, Fvi, OTMi for set i) or with corresponding locations of application (Fhi, locFhi, Fvi, locFvi), which were seen in the experiments to be introducing the largest demand on different structural components.

This section will focus on the development of such a simple and practical methodology for predicting the tsunami induced demand on bearings, columns and connections. To achieve the highest possible accuracy the method will be based on the physics involved in the inundation process of the bridge and all the findings presented in previous sections of this paper. The method will have to be able to simulate the tsunami loading and generated overturning moment and ideally relate to the 4 phases of the inundation mechanism. Given the fact that the uplift forces in (a) offshore bearings are maximized in Phase 1, (b) bearings G2 are maximized in Phase 1 or 2, (c) bearings G3 are maximized in Phase 2, and (d) bearings G4 are maximized in Phase 2 or 3, the method will have to use different load cases. Last but not least, since the objective of the method is the direct application in engineering practice and previous research studies have already developed equations for the prediction of the maximum total horizontal load (Fhmax) and maximum uplift load (Fvmax), the ideal case in terms of simplicity would be achieved if the improved method would require only Fhmax and Fvmax as input parameters. After several iterations and examined approaches, an improved physics-based methodology that meets all the above requirements was developed herein and is shown in Figure 2.28. The method consists of 3 load cases, which are described below:

- **Load Case 1:** In this case the maximum horizontal force is applied at the mid-height of the offshore girder and the maximum vertical force is applied at the mid-width of the overhang, with the aim to represent Phase 1 of the inundation mechanism and the associated large overturning moment. This load case is expected to give the largest uplift forces in the offshore bearings, columns and connections. The experimental results demonstrated that it is more reasonable to apply the horizontal load at the mid-height of the girder, instead of the mid-height of the bridge or the CG of the deck, since as seen in (Istrati, 2017) the recorded pressures histories on the offshore girder at $H_{girder}/3$ and $2H_{girder}/3$ are simultaneously large in Phase 1, while the pressure on the offshore face of the overhang is maximized much later. It must be clarified though that this is limited only to bridges without barriers (rails) or barriers with perforations so that they do not have a significant effect on the total horizontal load. For solid barriers thing might be different and further investigation is required.
- **Load Case 2:** In this load case the maximum uplift force is applied at the mid-width of chamber 1, while a reduced horizontal load is simultaneously applied at the mid-height of girder G2. The intent for this load case is to capture the effects associated with phase 2 of the inundation mechanism during which the wave could be reaching either chamber 1 or chamber 2. Therefore, the horizontal load is reduced using a calibrated factor in order to account for the observed trends in the experimentally recorded time-histories, which showed that for all bore heights and several solitary wave heights the horizontal load was reduced after the initial impact on the offshore girder. A factor $a=0.85$ was seen to give reasonable results, however it must be noted

that this number is not intended to be conservative in terms of estimating the horizontal force for all solitary waves, since in the experiments some large solitary waves (e.g. $H=0.70\text{m}$) showed continuously large horizontal forces (close to $F_{h,\max}$) during the whole inundation process, so for such waves $a=1$ could be used. This load case will generate a smaller overturning moment than load case 1 and could possibly give a more accurate estimation of the uplift forces in bearings G2.

- Load Case 3:** For load case 3 the maximum uplift force is applied at the mid-width of chamber 3 (the onshore one) together with a reduced horizontal load. The objective of this load case is to capture the maximum uplift in bearings G3 and G4, which were seen to be governed by the reverse overturning moment for most tested wave heights. In this study three values of the reduction factor “b” were examined and particularly $b=0$, $b=0.5$ and $b=0.65$. The zero value would mean that the horizontal load is totally neglected leading to a larger counter-clockwise moment than the one generated by the other two values, and a conservative estimation of the uplift load in bearings G3 and G4.

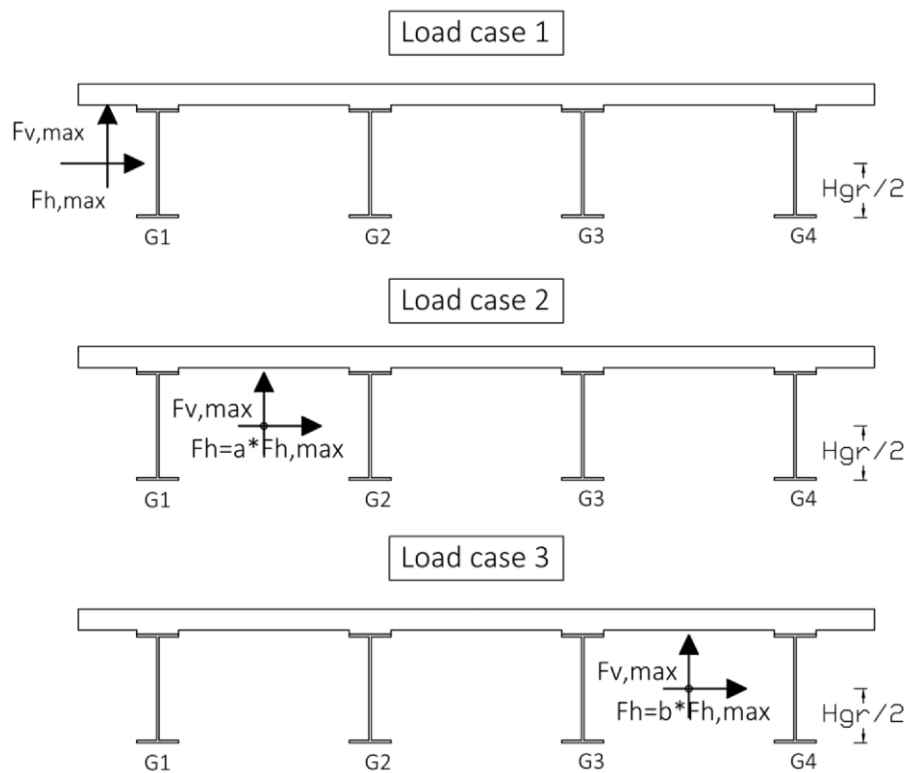


Figure 2.28: Load cases for improved physics-based simplified method

This physics-based methodology was applied using the experimentally recorded maximum total horizontal force ($F_{h,\max}$) and maximum total uplift force ($F_{v,\max}$) together with equations (6)-(9) developed in a previous section in order to calculate vertical forces in the bearings and the column-bent connections. The ratios of the calculated to the measured connection forces for Load Cases 1, 2 and 3 are summarized in Tables 2.4, 2.5 and 2.6 respectively.

As shown in Table 2.4, Load Case 1 estimates uplift forces in the offshore bearings that are conservative for all wave heights apart from two, for which however the predicted force is within 6% from the measured value. For the offshore bearings and offshore this load case gives an over-prediction of 33% on average, demonstrating that the method can conservatively estimate the demand on the offshore connections. For bearings G2 and col. 2 (center) the over-prediction is even more significant with an average value of 66% and 87% respectively. A possible reason for the larger over-estimation of the uplift forces in bearings G2 and col. 2 relative to the respective over-estimation of the offshore connections might be the rigid assumption made in the calculation, which results in a linear distribution of the uplift force in the connections, while the experimentally measured distribution is not linear at the instant that the uplift force in the offshore bearings is maximized. Therefore, future work should focus on the development of a 3D numerical model of the bridge that will simulate the actual stiffness of all bridge components and more accurately capture the distribution of the uplift in the connections. Nonetheless, the table proves that load case 1 does a good job in providing a conservative estimation of the uplift demand in bearings G1 and G2 and columns 1 and 2 but fails to capture the respective demand in the rest of the bearings and columns.

Table 2.4 shows that Load Case 2 due to the closer location of F_{vmax} to the CM of the bridge that generates a smaller overturning moment, fails to predict the uplift in the offshore bearings and columns, but it does a good job for bearings G2 and the center column (col.2). In fact this load case provides a more accurate estimation of the uplift demand in the latter bearing and column than load case 1, by over-predicting on average by 38% and 55%, instead of 66% and 87%, the uplift forces in bearings G2 and col.2 respectively. Therefore, this load case could be used for the design of bearings G2 and col.2.

None of the above two load cases could estimate the uplift in the onshore bearings and columns or in bearings G3, however as shown in Table 2.5, load case 3 can successfully achieve that. If $b=0$ then a conservative estimation of the counter-clockwise moment is made, which results in over-prediction of the uplift forces in bearings G3 and G4 and col. 3 by 52%, 156% and 111% on average respectively. Interestingly, this average value is driven by two of the smaller wave heights with $H=0.42m$ and $H=0.46m$ (over-prediction of uplift in G4 by 379% and 428% respectively), which can reach the deck but lose energy after the initial impact on the overhang and offshore girder and by the time they reach chamber 3 they do not apply significant uplift and consequently counter-clockwise moment. If these two outliers are not included in the calculation the average over-prediction is reduced. An alternative approach to neglecting the total horizontal force ($b=0$) is to consider it reduced down to $0.5 \cdot F_{hmax}$ or $0.65 \cdot F_{hmax}$. The 0.65 factor is a physics-based value and is in agreement with trends seen in the experimentally measured bore forces. Although not shown in the table, the 0.65 value yields uplift forces in bearings G3 and G4 that are closer to the measured ones, with the over-estimation being 29%, 106% and 25% for bearings G3 and G4 and col.3 respectively, however it under-predicts the uplift in the onshore columns for three waves with maximum under-prediction of 35%. Therefore, in order to reduce the under-prediction a value of $b=0.5$ was also examined and the results (Table 2-5) showed an over-estimation of 40%, 118% and 45% for bearings G3 and G4 and col.3 respectively, and an under-prediction of the uplift in the onshore columns only for two waves, which was 13% and 5%. This demonstrates that engineers could use $b=0.5$ for getting more reasonable values of the uplift demand and $b=0$ for a conservative design.

Table 2.4: Ratios of Bearing and Column-bent Cap Connection Uplift Forces Calculated from Load Case 1 of the Improved Method to the Ones Recorded in the Experiments

Wave Type	H _{input} (m)	Brngs, G1	Brngs, G2	Brngs, G3	Brngs, G4	Col. 1	Col. 2	Col. 3
Unbroken solitary	0.46	1.07	1.75	0.24	-3.79	1.12	2.12	-1.87
	0.52	0.94	1.10	0.21	-1.03	1.06	1.58	-0.62
	0.65	1.13	1.59	0.18	-2.07	1.19	1.87	-1.17
	0.36	1.46	1.72	0.01	-1.49	1.47	1.90	-0.82
	0.42	1.10	1.84	0.22	-3.40	1.12	2.43	-1.45
	0.55	0.95	1.23	0.20	-1.16	1.03	1.75	-0.67
	0.70	1.49	1.61	0.19	-1.32	1.53	1.55	-0.92
Bore	0.80	1.18	2.13	-0.06	-2.52	1.21	2.22	-3.79
	1.00	1.56	1.34	0.00	-2.19	1.46	1.87	-2.76
	1.10	1.21	1.67	-0.06	-2.22	1.22	1.69	-2.58
	1.30	1.08	2.05	-0.05	-3.29	1.20	2.03	-3.80
	0.90	1.85	1.72	0.09	-1.28	1.68	1.64	-1.36
	1.00	1.88	1.60	0.08	-1.20	1.76	1.83	-1.39
	1.20	1.22	1.83	0.06	-2.10	1.21	1.82	-2.29
	1.40	1.84	1.76	0.10	-1.51	1.67	1.77	-1.42

Table 2.5: Ratios of Bearing and Column-bent Cap Connection Uplift Forces Calculated from Load Case 2 of the Improved Method to the Ones Recorded in the Experiments

Wave Type	H _{input} (m)	Brngs, G1	Brngs, G2	Brngs, G3	Brngs, G4	Col. 1	Col. 2	Col. 3
Unbroken solitary	0.46	0.79	1.45	0.79	-1.49	0.88	2.12	-0.70
	0.52	0.68	0.91	0.56	-0.35	0.83	1.58	-0.12
	0.65	0.82	1.32	0.55	-0.80	0.93	1.87	-0.45
	0.36	1.09	1.43	0.31	-0.72	1.20	1.90	-0.36
	0.42	0.80	1.52	0.70	-1.32	0.88	2.43	-0.48
	0.55	0.69	1.02	0.51	-0.39	0.80	1.75	-0.15
	0.70	1.08	1.33	0.47	-0.42	1.18	1.55	-0.23
Bore	0.80	0.88	1.77	0.37	-1.29	0.96	2.22	-2.34
	1.00	1.16	1.11	0.35	-1.07	1.17	1.87	-1.54
	1.10	0.90	1.38	0.23	-1.16	0.97	1.69	-1.61
	1.30	0.81	1.70	0.31	-1.69	0.95	2.03	-2.37
	0.90	1.36	1.43	0.38	-0.54	1.31	1.64	-0.64
	1.00	1.39	1.33	0.40	-0.52	1.38	1.83	-0.70
	1.20	0.91	1.52	0.43	-0.96	0.95	1.82	-1.25
	1.40	1.35	1.46	0.41	-0.64	1.31	1.77	-0.69

Table 2.6: Ratios of Bearing Forces Calculated from Load Case 3 of the Improved Method to the Ones Recorded in the Experiments

Wave Type	H_{input} (m)	b=0				b=0.50			
		Brg1	Brg2	Brg3	Brg4	Brg1	Brg2	Brg3	Brg4
Unbroken solitary	0.46	-0.06	0.57	2.41	5.28	0.01	0.64	2.27	4.68
	0.52	-0.05	0.36	1.54	1.60	-0.01	0.40	1.48	1.48
	0.65	-0.06	0.52	1.65	2.93	0.01	0.58	1.56	2.61
	0.36	-0.07	0.52	1.24	1.67	0.09	0.65	1.11	1.33
	0.42	-0.06	0.60	2.12	4.79	0.01	0.68	2.00	4.26
	0.55	-0.06	0.41	1.40	1.80	-0.01	0.45	1.34	1.67
	0.70	-0.09	0.54	1.25	2.12	-0.03	0.58	1.21	1.99
Bore	0.80	-0.06	0.63	1.72	2.59	0.09	0.81	1.51	1.97
	1.00	-0.08	0.40	1.42	2.42	0.10	0.50	1.27	1.92
	1.10	-0.06	0.48	1.16	2.21	0.10	0.63	1.01	1.65
	1.30	-0.05	0.60	1.43	3.39	0.08	0.78	1.25	2.58
	0.90	-0.10	0.55	1.23	1.68	0.05	0.64	1.15	1.45
	1.00	-0.10	0.50	1.34	1.52	0.06	0.59	1.24	1.29
	1.20	-0.06	0.56	1.57	2.51	0.06	0.68	1.42	2.08
	1.40	-0.10	0.56	1.34	1.97	0.05	0.65	1.24	1.70

It must be noted that as more research studies will be conducted in the future and more information will be generated, the actual values of factors “a” and “b” used in Load Cases 2 and 3 might change so as to result in more accurate estimation of uplift demands and economical designs of structural components. Moreover, some of the assumptions made in the current methodology e.g. the application of F_{vmax} in all three phases, might also be improved and for each load case different magnitudes of the vertical force could be applied. The recommended load cases and factor values are intended for open girder bridges with cross-frames, however the framework could be adjusted for other types of bridges such as bridges with diaphragms or box-girder bridges, as well as other types of elevated coastal structures such as jetties and wharves as well as offshore platforms. Last but not least, it must be clarified that (a) engineers are expected to apply these load cases in 3D structural models that will be able to properly simulate the stiffness of all structural components, and (b) the intent of this method is to estimate the uplift demand in individual components and connections assuming that F_{hmax} and F_{vmax} are known parameters, it is up to researchers and engineers to decide how to calculate these two maximum values. Ongoing and future work of this research team will focus on evaluation and calibration of existing predictive equations for F_{hmax} and F_{vmax} and if needed development of improved equations.

3.0 THE ROLE OF STRUCTURAL FLEXIBILITY AND DYNAMIC FLUID-STRUCTURE-INTERACTION

3.1 INTRODUCTION

The previous chapter focused on the tsunami effects on an I-girder bridge with steel bearings. This chapter will present results from seven bridge configurations with elastomeric bearings and several variations in the flexibility of the connections and substructure in order to shed light on the physics of the dynamic wave-structure interaction and the role of the bridge on the forces that the bridge members will have to withstand. The results from seven bridge configurations tested in the large-scale experiments will be compared in different sections of this chapter. In particular, the bridge with steel bearings (ST1) will be compared to the one with elastomeric bearings (ST2) to identify the effect of the flexibility of the connections. Three bridge configurations with a different type of horizontal link between the bent cap and the bracket plate -ranging from a rigid link (ST2, ST2B) to a medium spring (ST3, ST3B) and a very flexible spring (ST4)- will be compared in order to study the effect of substructure flexibility. In the last bridge configuration (ST11) the shear keys were removed and the elastomeric bearings were allowed to both rotate and translate in all directions, so that the effect of the additional flexibility of the system could be studied. For all these configurations the effects of (a) the impulsive tsunami load applied at the time of the initial impact and (b) the quasi-static tsunami load, which was maximized when all chambers of the bridge became inundated, will be evaluated.



Figure 3.1: Details of the bearings, shear keys and substructure links used to study the effect of bridge flexibility and the role of dynamic FSI

3.2 SELECTED RESULTS FOR DIFFERENT FLEXIBLE BRIDGE CONFIGURATIONS

Figure 3.2 shows the histories of the uplift forces in the bearings and the total horizontal and vertical forces recorded in the shear keys and bearings respectively. It can be observed for most waves the maximum uplift forces in the bearings of the two offshore girders are maximized at the instant of the initial impact on the bridge (Phase 1), while the forces in the rest of the bearings are maximized when most of the chambers are inundated. In Phase 1 the offshore bearings and the bearings of girder G2 (girder next to the offshore one) are getting significantly larger uplift forces than the rest of the bearings and this due to significant applied moment as shown in the previous chapter. This behavior is observed for all the tested waves as shown in Figure 3.3.

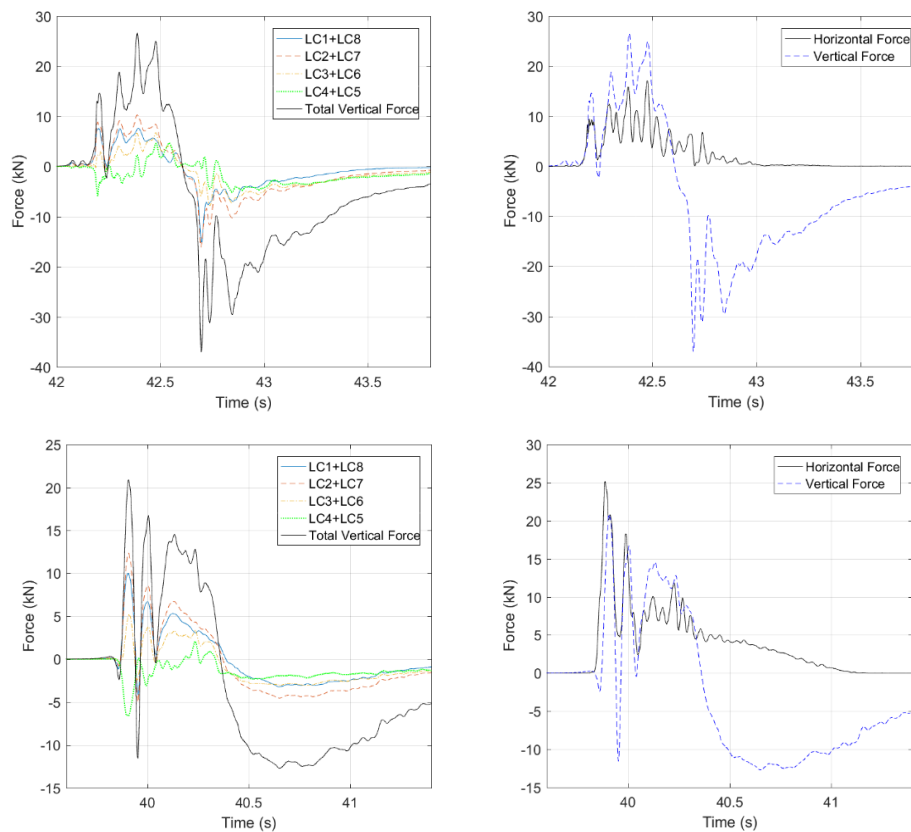


Figure 3.2: Vertical forces in bearings (left) and total horizontal and vertical forces measured in the shear keys and bearings respectively (right) for a solitary wave with $H=0.70\text{m}$ (top) and a bore with $H=1.20\text{m}$ (bottom).

Figures 3.4 and 3.5 are showing the response of the bridge with elastomeric bearings and no shear keys demonstrating the large forces, displacements and shear strains that result in the nonlinear behavior of the bearings. Figure 3.6 is showing the recorded total horizontal and vertical connection forces for three flexible specimens (ST3, ST4, ST11). In the configurations ST3 and ST4 lateral flexibility is introduced in the system by the substructure springs, while in configuration ST11 the lateral flexibility is generated by the elastomeric bearings and the

removal of the shear keys. These graphs reveal the major effect of the lateral stiffness on the horizontal forces that the bridge members and connections have to withstand. Both the amplitude of the horizontal forces in the connections and their frequency content change significantly.

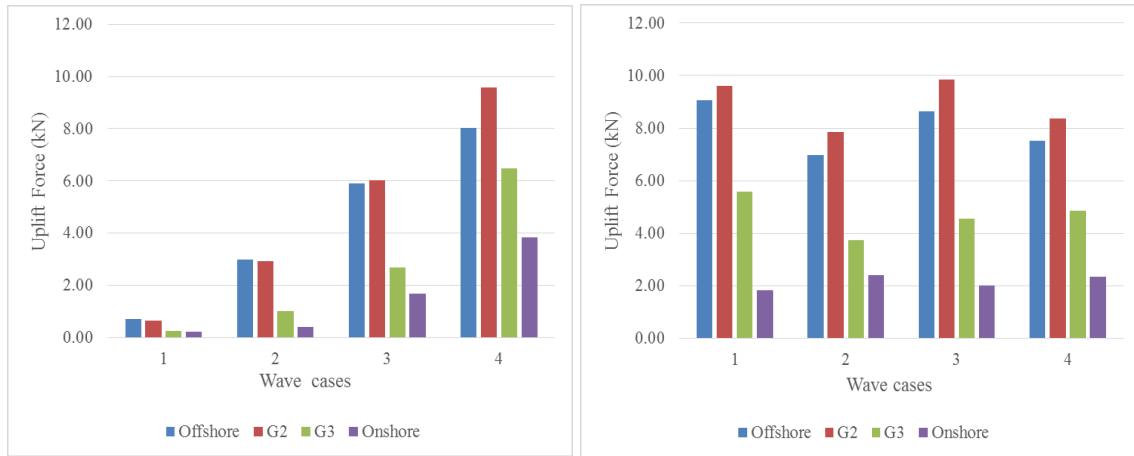


Figure 3.3: Maximum uplift forces in different bearings for solitary waves (top) and bores (bottom) for a 2m water depth

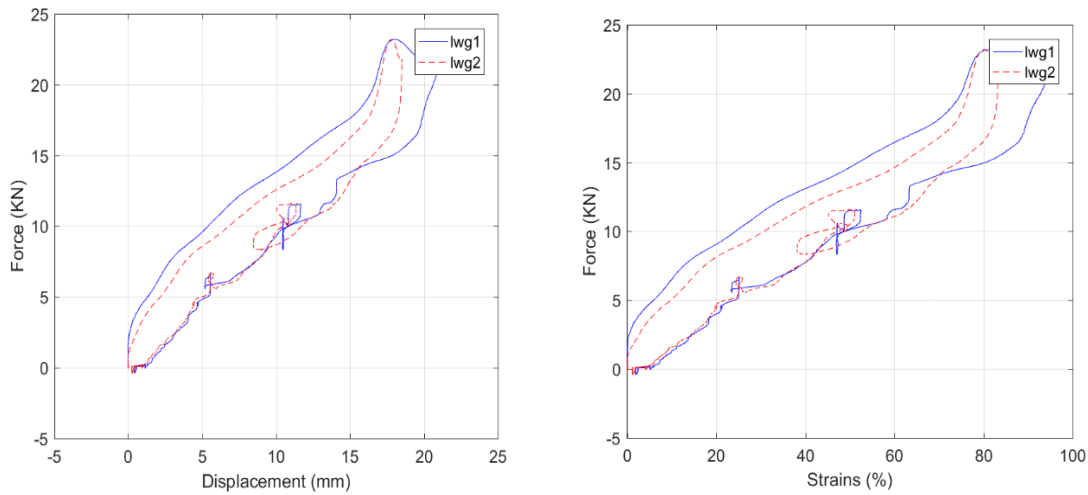


Figure 3.4: Total horizontal forces recorded in links as a function of horizontal displacements (left) and calculated shear strains in the bearings (right) for the bridge with elastomeric bearings and no shear keys for a bore with $H=1.20$

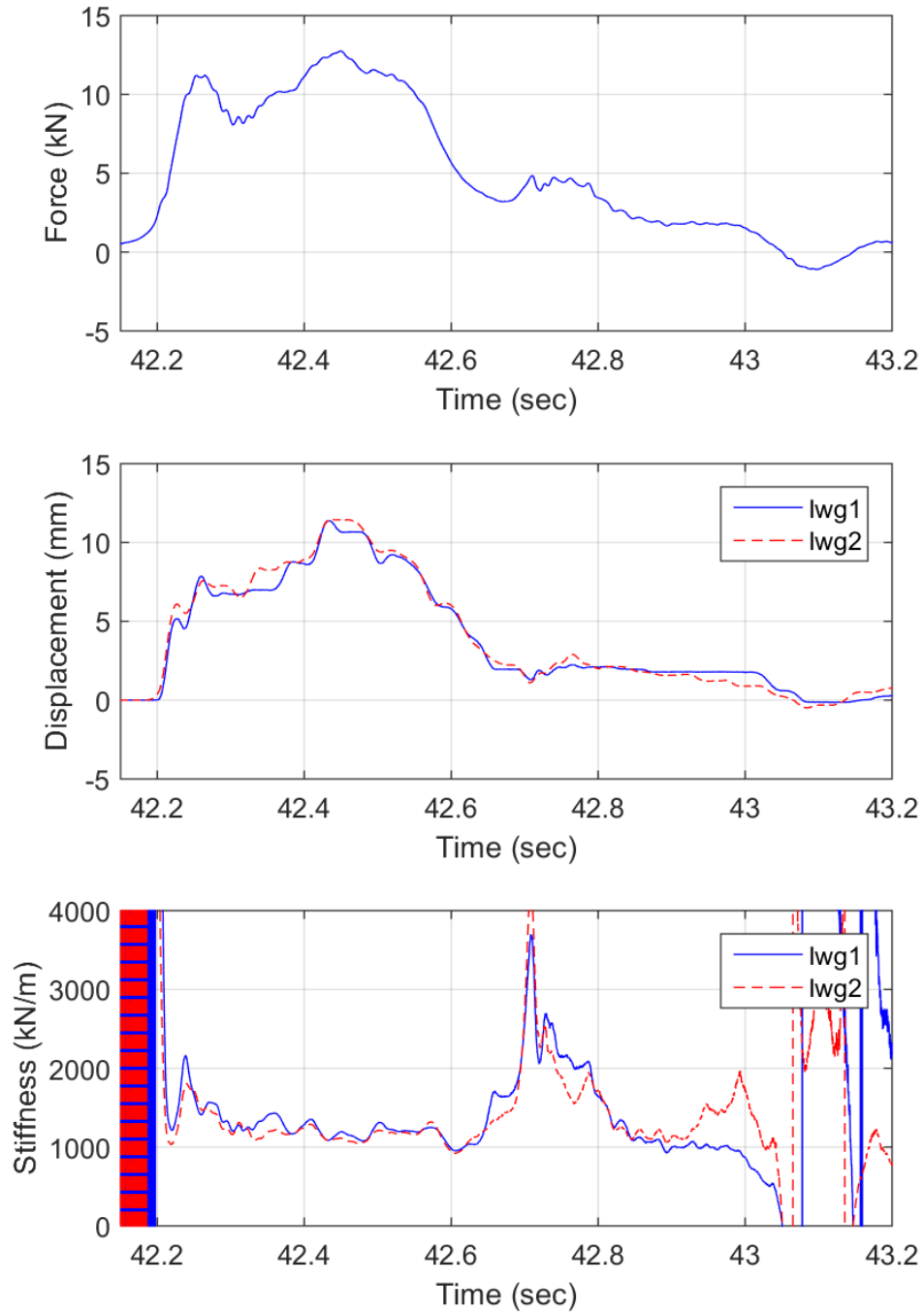


Figure 3.5: Total horizontal forces in links (top), horizontal displacements (middle) and calculated stiffness (bottom), of the bridge with elastomeric bearings and no shear keys for a solitary wave with $H=0.70\text{m}$

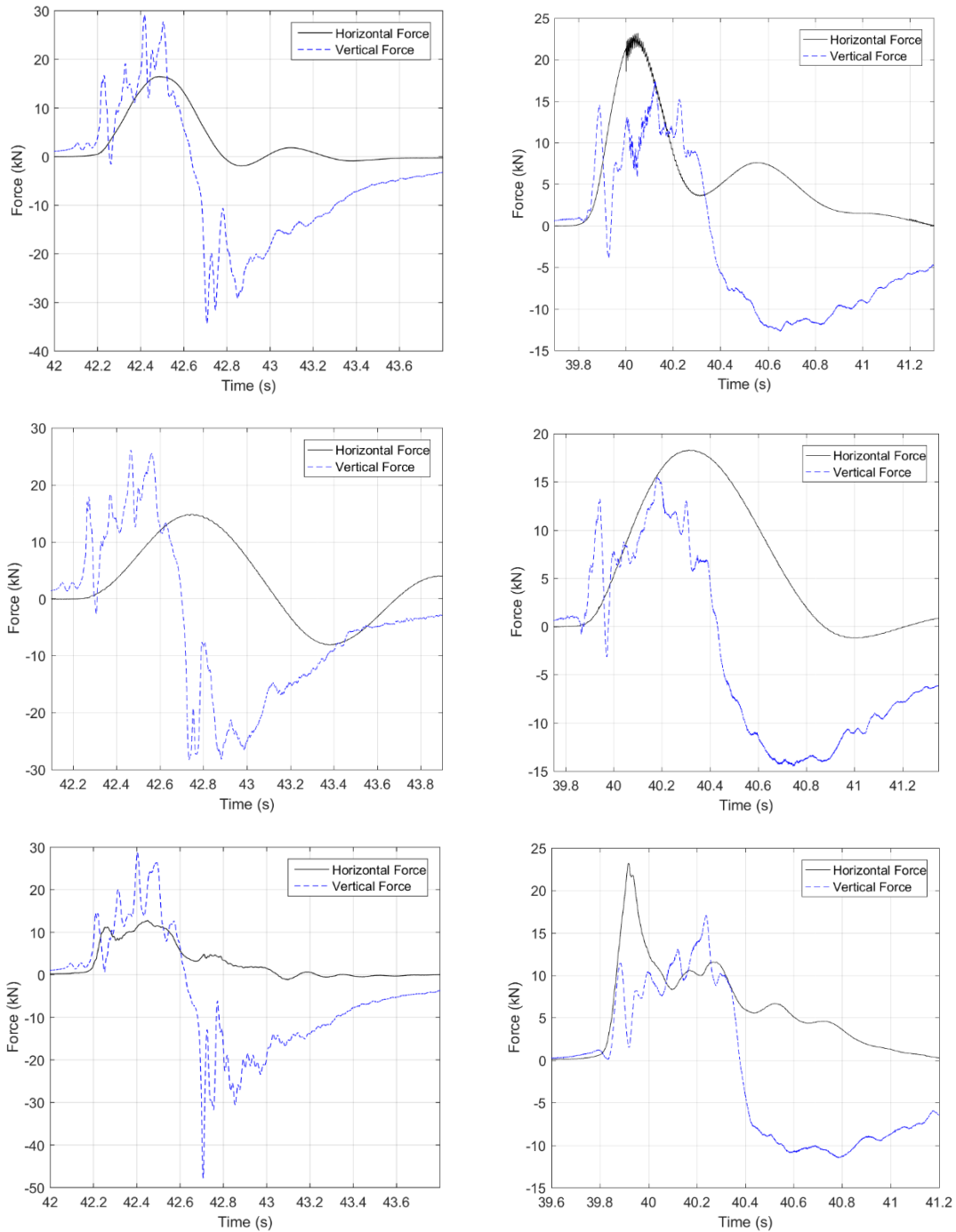


Figure 3.6: Total horizontal and vertical connection forces for the bridge with the medium substructure springs (top), the one with the flexible springs (middle) and the one with no shear keys (bottom), for a solitary wave with $H=0.70\text{m}$ (left) and a bore with $H=1.20\text{m}$ (right)

3.3 THE ROLE OF INERTIA FORCES FOR STIFF AND FLEXIBLE BRIDGES

Following the same approach as in chapter 2, the applied horizontal tsunami load was calculated via integration of the pressure measurements at different locations of the bridge and was compared with the force in the substructure links. The comparison of the two forces for (a) the very stiff configuration with shear keys and a rigid substructure link (ST2) and (b) two flexible configurations (ST3) and (ST11), is plotted in Figure 3.7 for a bore with $H=0.90\text{m}$. This figure reveals that for the former configuration the applied load and connection forces have a similar amplitude (slightly increased connection forces due to dynamic amplification) and a similar shape with a slightly increased duration of the first peak of the connection forces. For the flexible configurations the recorded forces have a totally different shape than the applied tsunami load, with the former having longer duration force peaks governed by the fundamental period of the bridge specimen. Therefore, the agreement between these two forces is very bad.

When the horizontal inertia forces calculated from the measured accelerations are added to the measured link forces, the agreement with the applied tsunami load is very good especially at the instant of the initial impact showing that the dynamic equilibrium is satisfied. This comparison revealed that for flexible bridges at the time of the initial impact a large percentage of the short duration horizontal tsunami load is taken by the inertia forces, revealing the significance of the inertial forces at that instant, however they have been neglected to date. Moreover, the comparison revealed that some flexible bridges can be totally insensitive to the short duration impulsive tsunami load due to their significantly larger natural periods.

It must be noted that in the previous figure the very good agreement between the applied tsunami load and the summation of the inertial and connection was observed at the initial impact of the bore on the offshore girder, however as the wave started inundating the chambers of the bridge the agreement was not good. This can be explained by the fact that the pressure gages were installed only on the offshore side of each girder not on the onshore one. However, as observed in the advanced FSI analyses (Istrati, 2017) there is a rotating water flow inside the chambers which applies pressures on the onshore side of the girders (opposite to the direction of propagation) reducing consequently the total tsunami load. Moreover, on the offshore face of the bridge three pressure gages were installed, however on each interior girder only one pressure gage was installed due to limited pressure gages available in the HWRL, making it impossible to accurately predict the pressure field.

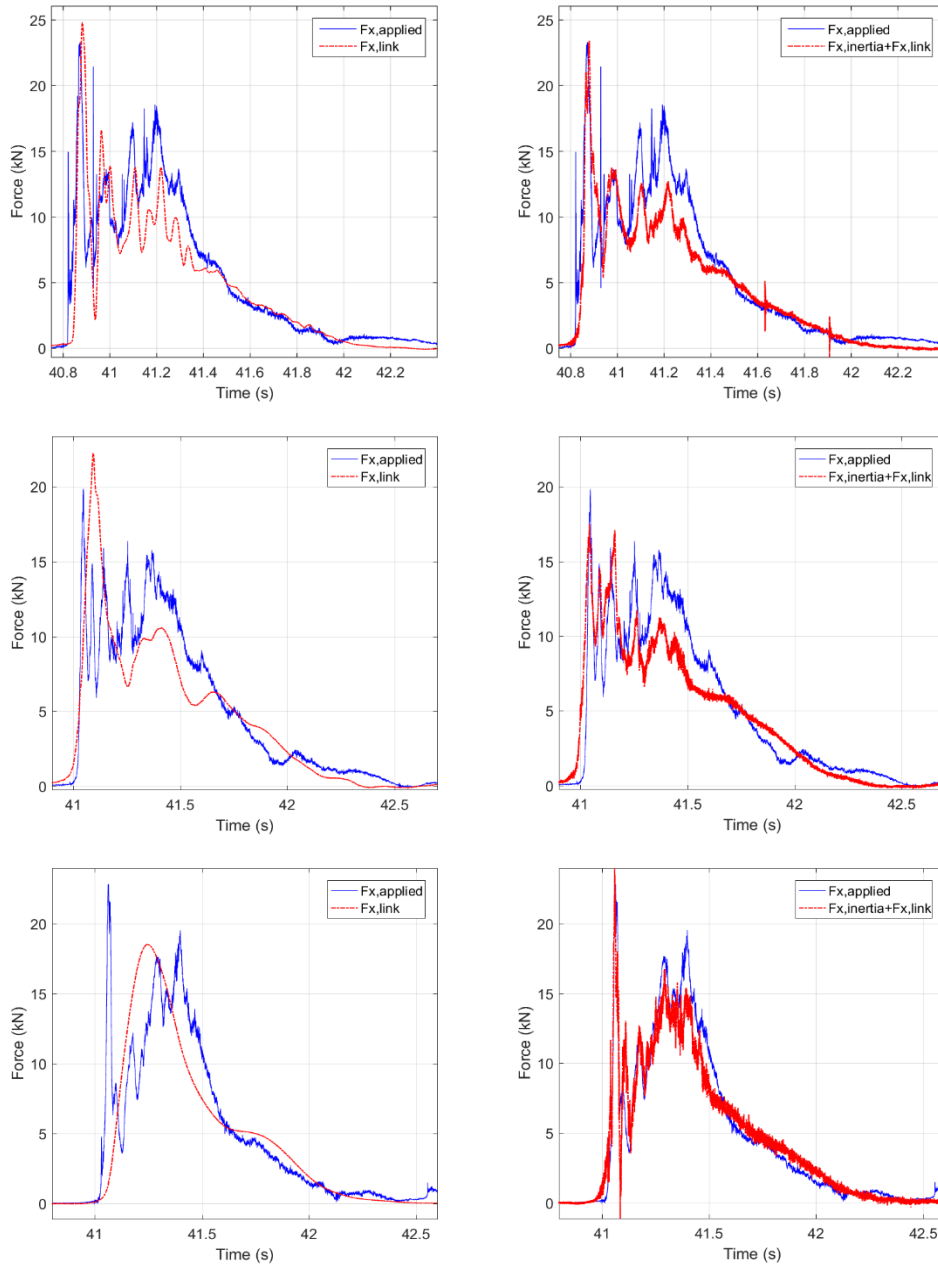


Figure 3.7: Applied horizontal forces, forces in links and sum of inertial and link forces for the stiff configuration ST2 (top) and flexible configurations ST11 (middle) and ST3 (bottom) for a bore with H=0.90m

3.4 EFFECT OF BRIDGE FLEXIBILITY ON THE DYNAMIC FSI

3.4.1 Flexibility of connections

This section will present a comparison of bridge configurations ST1 and ST2, with the former having steel bearings, which constrain all the degrees of freedom, and the latter one having elastomeric bearings and shear keys that allow the rotation of the bridge. Figure 3.8 shows the

time-histories and FFTs of the total horizontal and vertical connection forces. Both bridges have similar horizontal forces, however the bridge with the elastomeric bearings has longer duration and smoother peaks as well as smaller amplitudes.

Figure 3.9 plots the uplift forces in the bearings for the types of connections for a bore with $H=1.20\text{m}$. For both bearing types at the initial impact, the offshore bearings are out-of-phase with the onshore ones indicating the existence of a significant overturning moment. For both types of bearings, the uplift forces in the offshore connections were significantly larger than the uplift taken by the rest of the bearings. As a matter of fact, in the case of the steel bearings the offshore connections attracted most of the slamming uplift force, while in the case of the elastomeric bearings the slamming uplift force was shared among the bearing connections of the two girders impacted first by the tsunami wave. This finding is of utmost significance because it reveals that the offshore bearings and connections should be designed for larger tensile forces than the rest, and the exact amount will depend on the type of the bearings, the wave type and the height.

A further insight into the effect of the flexibility of the connections can be gained via examination of the maximum total uplift forces, total horizontal forces and forces in the bearings, shown in Figure 3.10. For several waves the elastomeric bearings are reducing the total uplift forces in the connections while for some the effect is negligible. Moreover, since the uplift force in Phase 1 is shared by the bearing connections of the two offshore girders when elastomeric bearings are used and mainly by the offshore bearings when steel bearings are used, the uplift forces in the offshore elastomeric bearings are significantly smaller than the ones in the steel bearings. This is also true for the onshore bearings but it is not true for the bearings of girder G2.

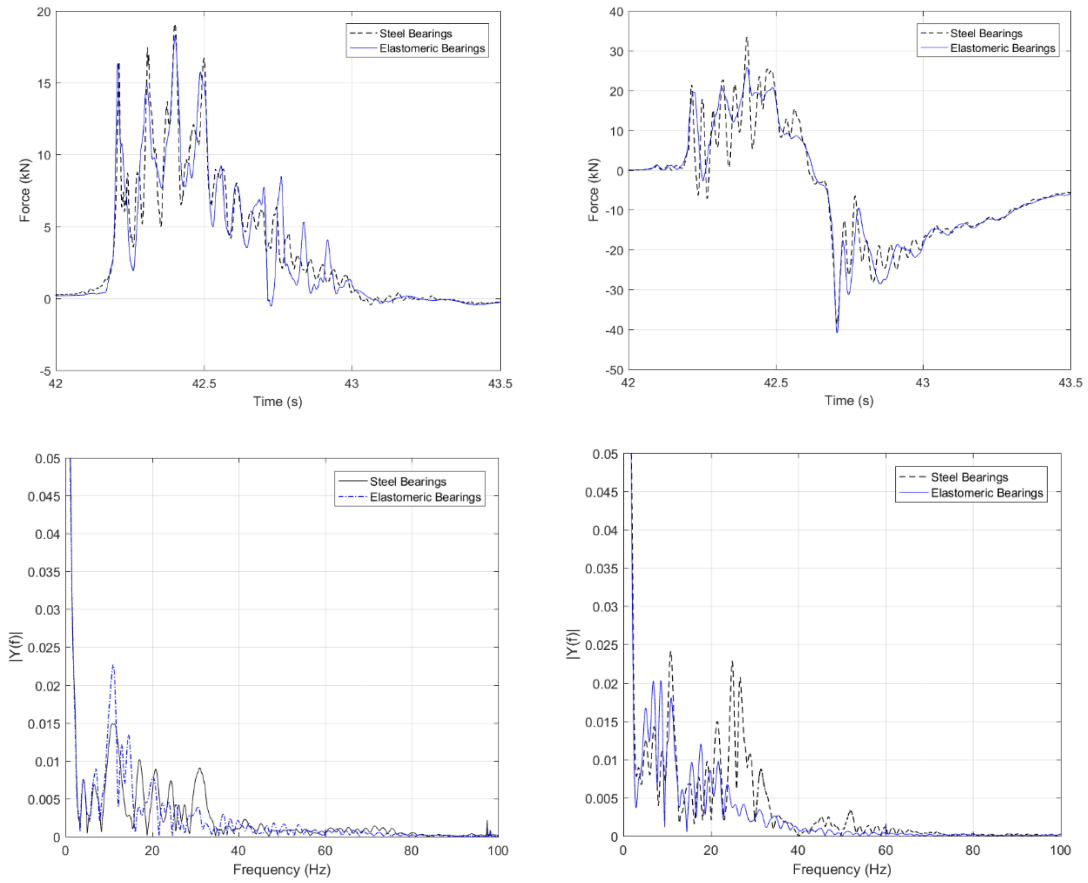


Figure 3.8: Time histories (top) and FFTs (bottom) of total horizontal (left) and vertical (right) forces in the connections for bridge cases ST1 and ST2 and H=0.70m

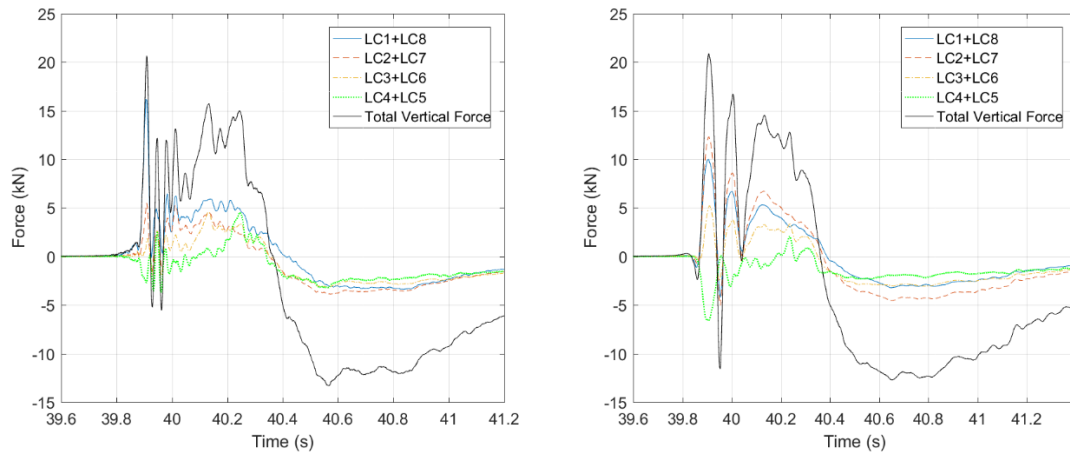


Figure 3.9: Uplift forces in steel bearings (left) and elastomeric bearings (right) for H=1.20m

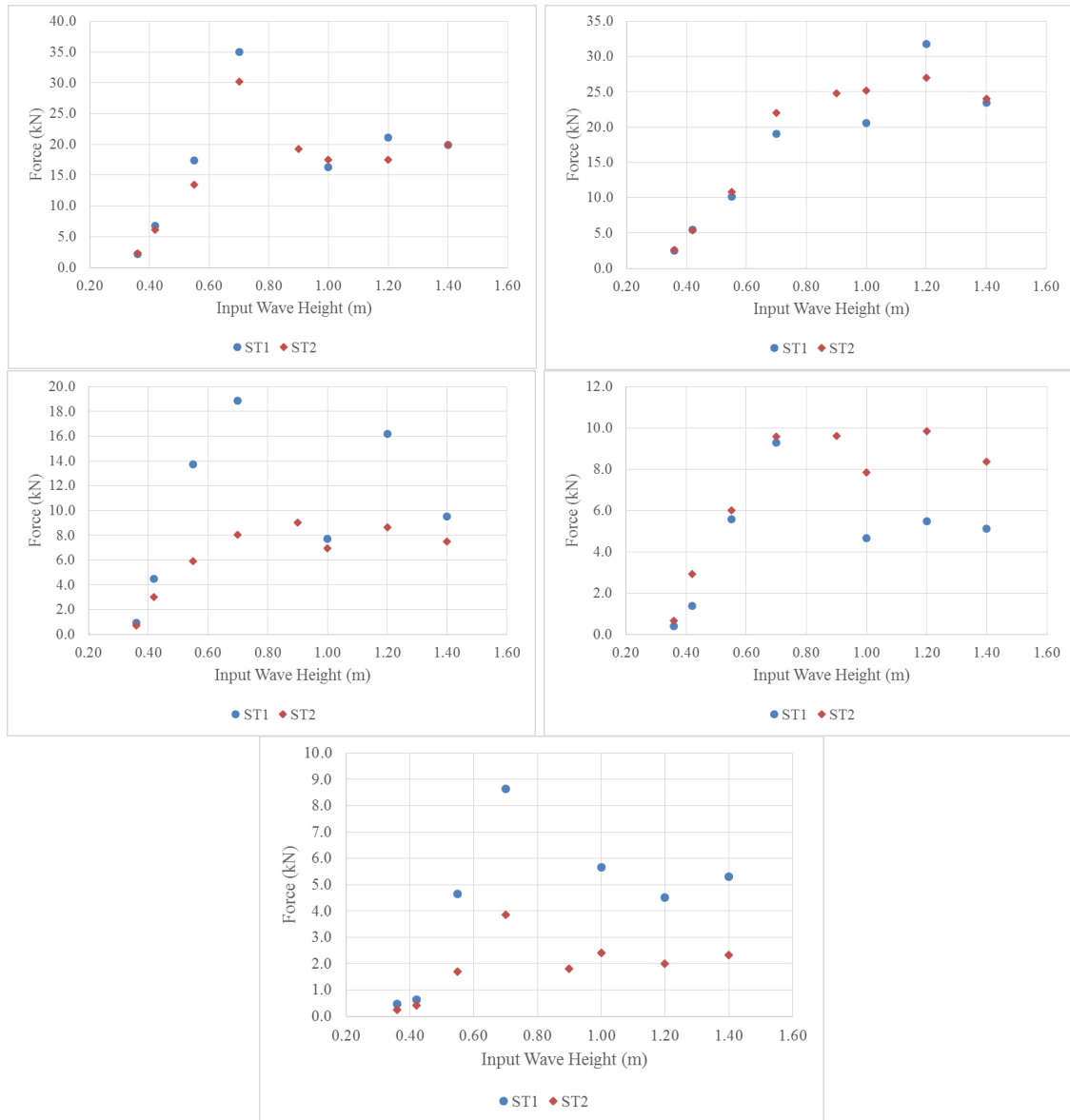


Figure 3.10: Total uplift force (top-left), total horizontal force (top-right), uplift force in offshore bearings (middle-left), uplift forces in bearings of girder G2 (middle-right) and uplift forces in onshore bearings (bottom) for ST1 and ST2

3.4.2 Flexibility due to removal of shear keys

In one of the bridge configurations with the elastomeric pads the shear keys were removed, which means that the bridge was allowed to rotate and translate both vertically and horizontally, affected only by the stiffness of the bearings. The horizontal flexibility introduced in the system by the elastomeric bearings had a minor effect on the total uplift forces and a major effect on the total horizontal forces (Figure 3.11 and Figure 3.12). In particular, the flexibility reduced the horizontal forces for most of the tested waves and it changed the pattern of the force histories. Moreover, the force peaks were smoothed out, had longer durations and were reduced in number. Instead of having four main peaks in the horizontal force histories corresponding to the instants

of the impact of the wave on each of the four girders, it has only two main peaks, with the first one occurring slightly after the initial impact and the second on occurring close to the instant at which the quasi-static horizontal force is maximized. This indicates that the bridge is responding to both the impulsive load as well as the quasi-static one.

Despite the minor effect on the total uplift forces, there was a significant effect on the forces of the onshore bearings as shown in Figure 3.12. Removing the shear keys increased significantly the uplift forces in the onshore bearings indicating that the friction generated between the girders and the shear keys during the tsunami inundation has a significant effect. This friction seems to be taking part of the uplift force reducing consequently the forces in the onshore bearings.

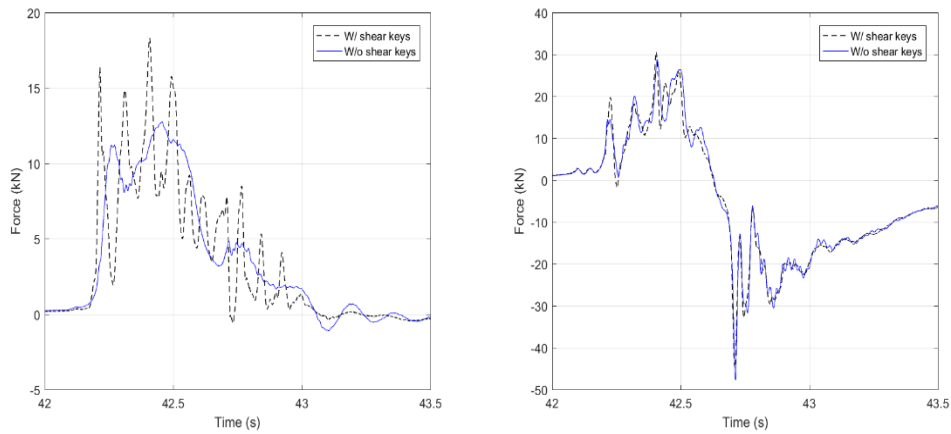


Figure 3.11: Total horizontal (left) and vertical (right) connection forces for H=0.70m (top)

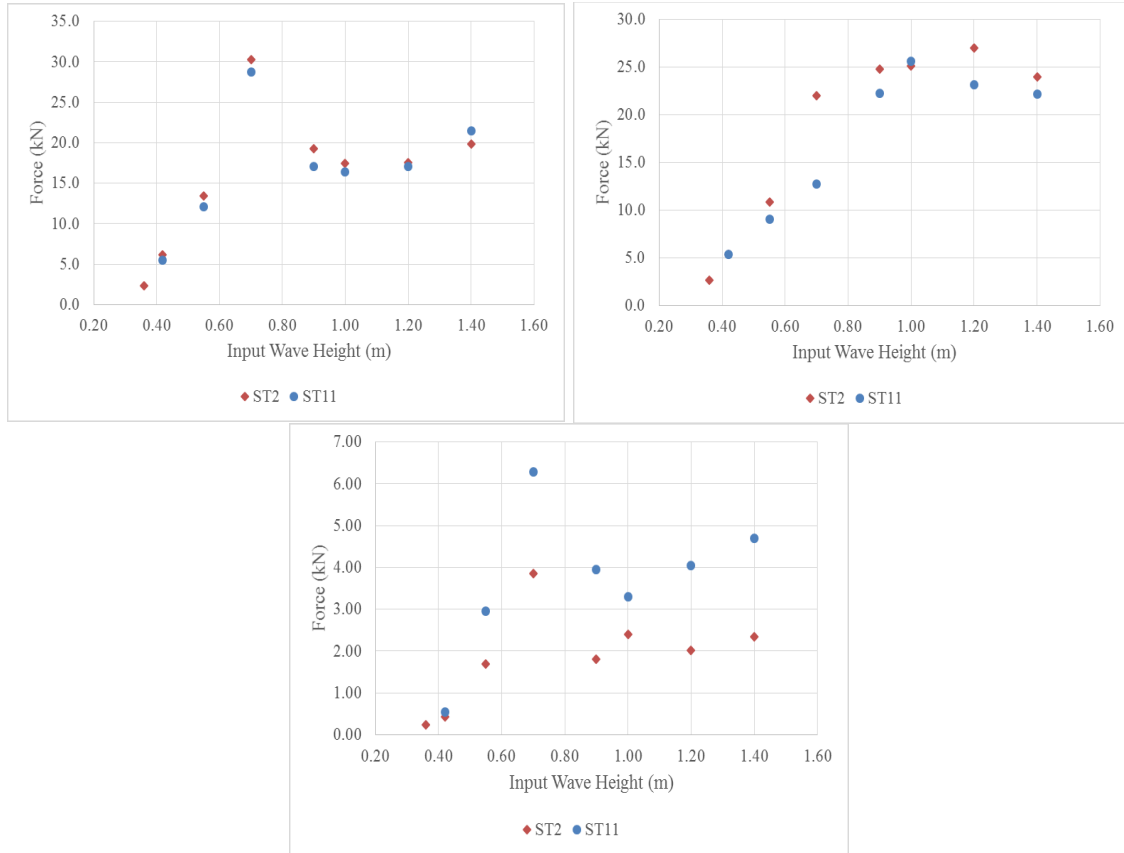


Figure 3.12: Total uplift forces (top-left), total horizontal forces (top-right) and uplift force in onshore bearings (bottom) for ST2 and ST11

3.4.3 Lateral flexibility generated from substructure and removal of shear keys

In this section four configurations will be compared. The bridge configuration with elastomeric bearings, shear keys and a rigid substructure link (ST2) will be compared with the two configurations with medium (ST3) and flexible substructure springs (ST4), and the configuration with a rigid substructure link but no shear keys (ST11). As discussed in chapter 4 of this dissertation the fundamental period of case ST11 is smaller than the ones of cases ST3 and ST4. Figure 3.13 shows the horizontal and vertical forces histories of four specimens, and although the effect of flexibility on the vertical forces is minor, the effect on the horizontal connection forces is very significant, with the introduction of flexibility resulting in significant reduction of the effect of the impulsive tsunami loads on the bridge connections.

Reducing the lateral stiffness offsets the natural period further from the duration of the impulsive load and after a certain stiffness value this load is purely taken by inertia and it is not even noticed in the connections. However, reducing the stiffness after a certain limit can worsen things because now the natural period of the bridge can coincide with the duration of the slowly-varying component of the wave load, increasing the horizontal force transferred in the shear keys and substructure (Figure 3.13 and 3-14). In addition, the lateral movement of the flexible bridge

with the wave alters the wave-structure interaction and increases the duration of the applied uplift force on the bridge, leading to a variable effect on different connections and for different wave heights (Figure 3.15). Therefore, it is critical for the design of the bridge members to identify the duration of both the impulsive tsunami load as well as the slowly-varying load.

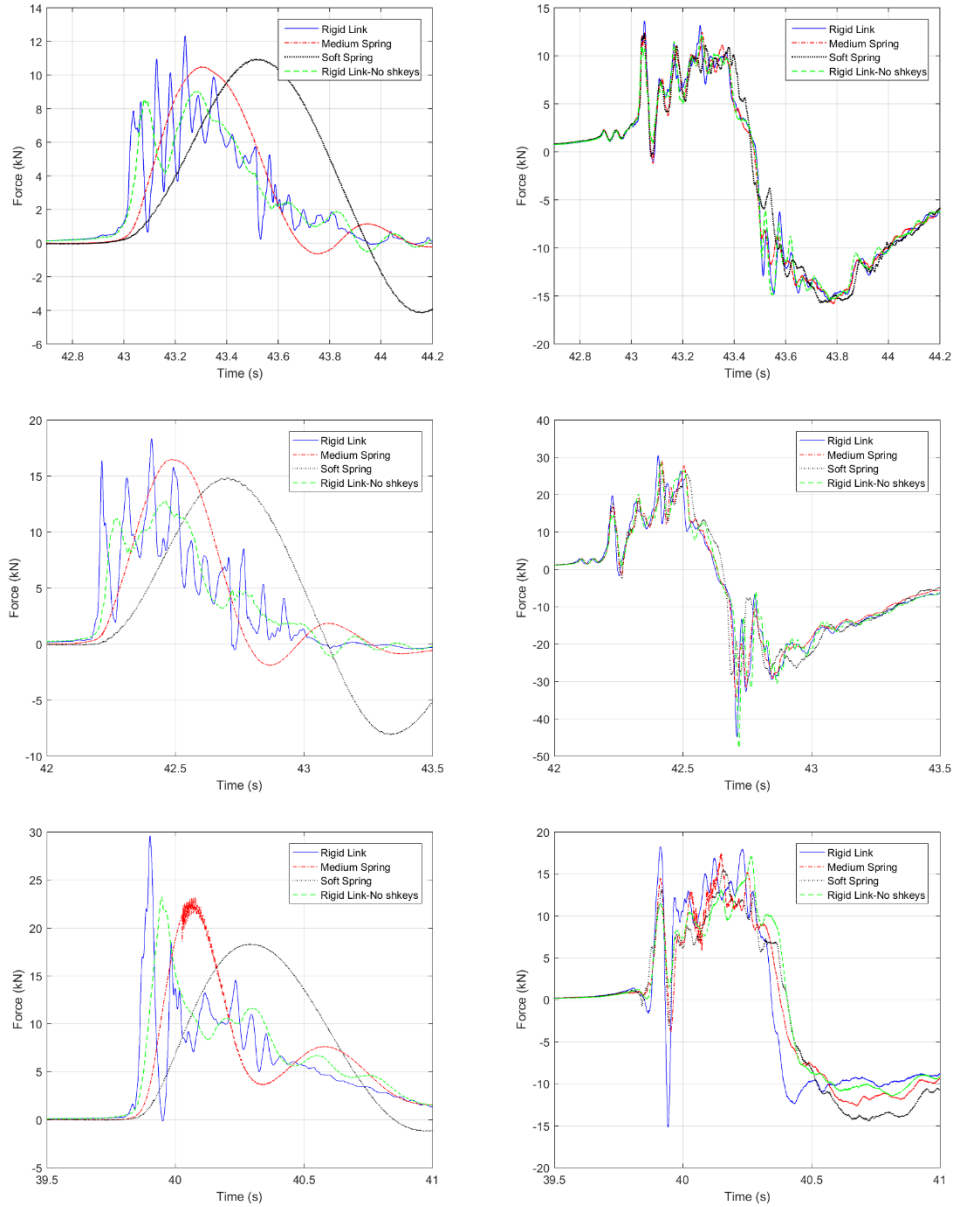


Figure 3.13: Total horizontal (left) and vertical (right) connection forces for $H=0.55\text{m}$ (top), $H=0.70\text{m}$ (middle) and $H=1.20\text{m}$ (bottom)

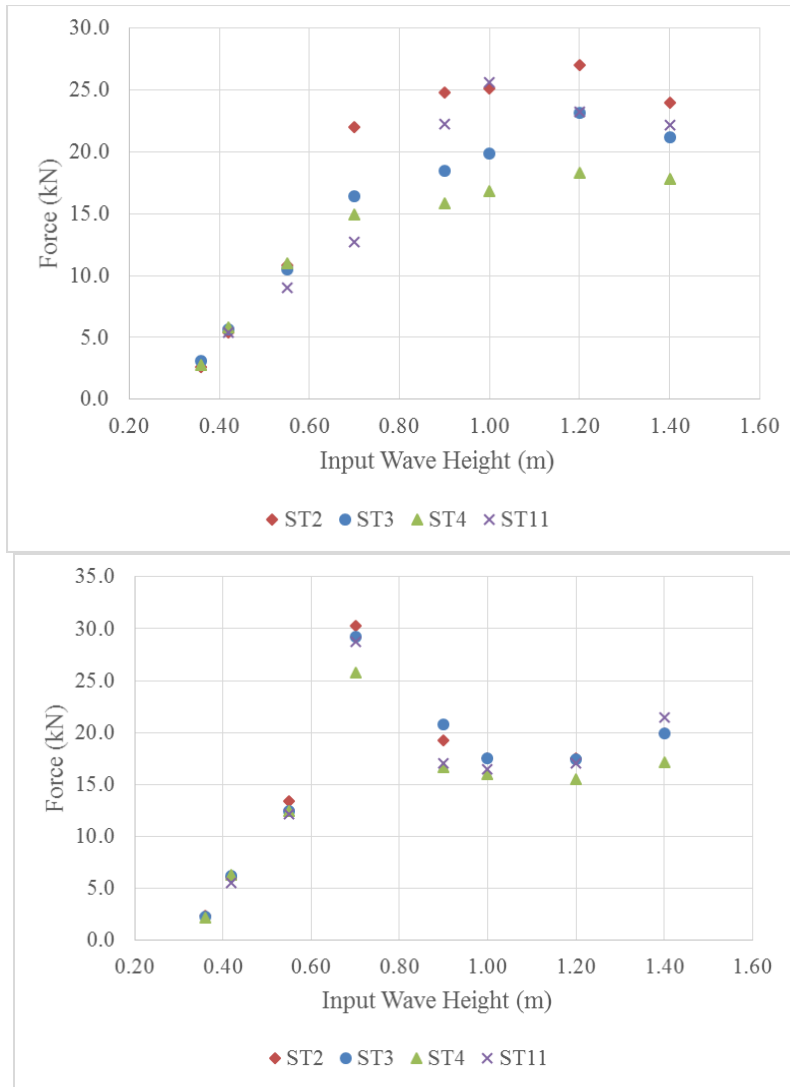


Figure 3.14: Total horizontal (top) and uplift (bottom) connection forces for bridge configurations ST2, ST3, ST4 and ST11

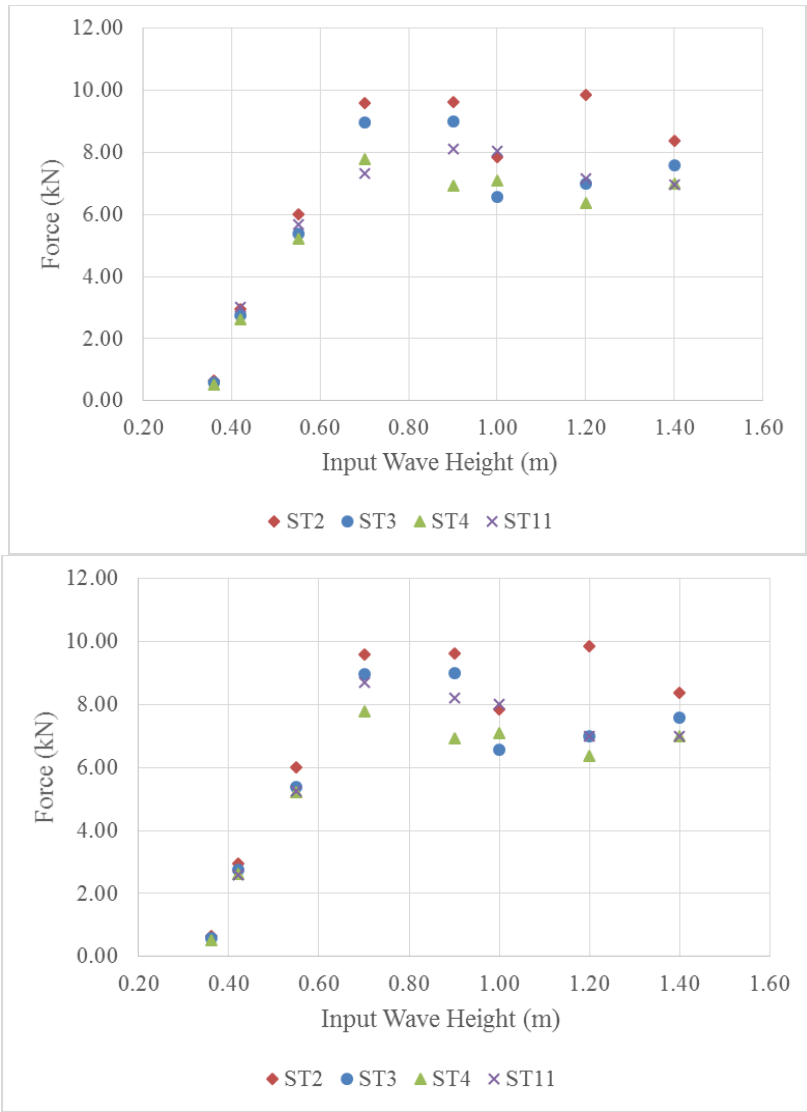


Figure 3.15: Uplift forces in offshore bearings (top) and bearings of girder G2 (bottom) for bridge configurations ST2, ST3, ST4 and ST11

4.0 TSUNAMI INDUCED FORCES ON I-GIRDER BRIDGES WITH CROSS-FRAMES AND DIAPHRAGMS

4.1 INTRODUCTION

This chapter will present detailed experimental results from two bridge types in an attempt to advance the understanding of tsunami effects relative to the air-entrapment. As was discussed in the first chapter of this report during the Great East Earthquake and Tsunami in 2011 in Japan more than 200 bridges failed due to the tsunami inundation. Among the failed bridge types were composite I-girders bridges with cross-frames, I-girder and T-girder bridges with diaphragms and box girder bridges. At first look, it seemed surprising that the bridges with concrete girders failed despite their large weight, however as hypothesized in (Kawashima and Buckle, 2013) this might have happened due to the additional buoyancy forces generated by the air trapped between the girders and the bridge deck. Recent small-scale experimental studies (McPherson, 2008; Hayatdavoodi et al., 2014; Seiffert et al., 2015) and 2D numerical studies (Azadbakht, 2014; Bricker and Nakayama, 2014) observed the air-entrapment and noted its significance on the uplift forces that a bridge has to withstand.

In order to shed light on the role of the air-entrapment for both solitary waves and turbulent bores, and determine the variation of the tsunami effects with the bridge type, two different bridge configurations were tested in the large-scale hydrodynamic experiments. The first configuration was bridge case ST2, which consisted of an I-girder bridge with steel girders and cross-frames and the second configuration was bridge case ST5, which was the same bridge with attached plywood diaphragms at both the intermediate and end-cross-frames. The plywood diaphragms were bolted to the cross-frames using pre-drilled holes and waterproof nuts, and the edges around the diaphragms were sealed with caulk to ensure that the air could not escape from the chambers. Figure 4.1 and 4-2 show the bridge configurations ST2 and ST5 respectively during their assembly in the Large Scale Structures Laboratory at the University of Nevada, Reno.



Figure 4.1: I-girder Bridge with cross-frames during the assembly in the Large-Scale Structures Laboratory at the University of Nevada, Reno



Figure 4.2: I-girder Bridge with plywood diaphragms during the assembly in the Large-Scale Structures Laboratory at the University of Nevada, Reno

4.2 TSUNAMI EFFECTS ON AN I-GIRDER BRIDGE WITH DIAPHRAGMS

In Fig. 4.3, the vertical forces in the bearings (top-left) as well as their summation, are plotted as a function of time. LC1+LC8 and LC4+LC5 are corresponding to the bearings of the offshore and onshore girder respectively. A similar graph had been plotted for bridge case ST2 with cross-frames in chapter 6 and four different phases had been observed. Phase 1 was at the time of the first wave impact when the wave reached the offshore girder and overhang, where the offshore bearings were in tension and the onshore ones are in compression while the total vertical force was upwards, indicating a large applied moment due to the applied horizontal and vertical tsunami load. Phase 2 occurred when the total vertical force became negative and the bearing forces changed signs slightly after the initial impact as the wave was moving toward the first chamber. Phase 3 had a longer duration than the first two phases and occurred when all the chambers of the bridge were inundated introducing a large uplift force and tension in all bearings and actually introduced the largest tensile forces in the onshore bearings. Last, Phase 4 occurred towards the end of inundation when the wave impacted violently on the top of the bridge deck resulting in the compression of all bearings and a downward total vertical force. For many of the examined wave heights for bridge ST2, Phase 1 introduced the largest forces in the offshore bearings, although Phase 3 introduced a larger total uplift on the bridge.

When the bridge with diaphragms is inundated by a solitary wave after Phase 1 there does not seem to exist a Phase 2 as defined for bridge case ST2 in which the bridge tends to rotate counterclockwise while the total vertical force becomes negative (downward). Instead, after Phase 1 the uplift force keeps increasing introducing tension in all bearings, maximizing the tensile forces in the offshore and nearby bearings and creating a relatively long duration uplift force. As the wave propagates through the bridge, this uplift peak is reduced and later on another uplift peak occurs in the total forces, which maximizes the tensile forces in the onshore bearings indicating that Phase 3 is taking place. Interestingly, during the formation of these two main peaks all the bearings have positive vertical forces (uplift).

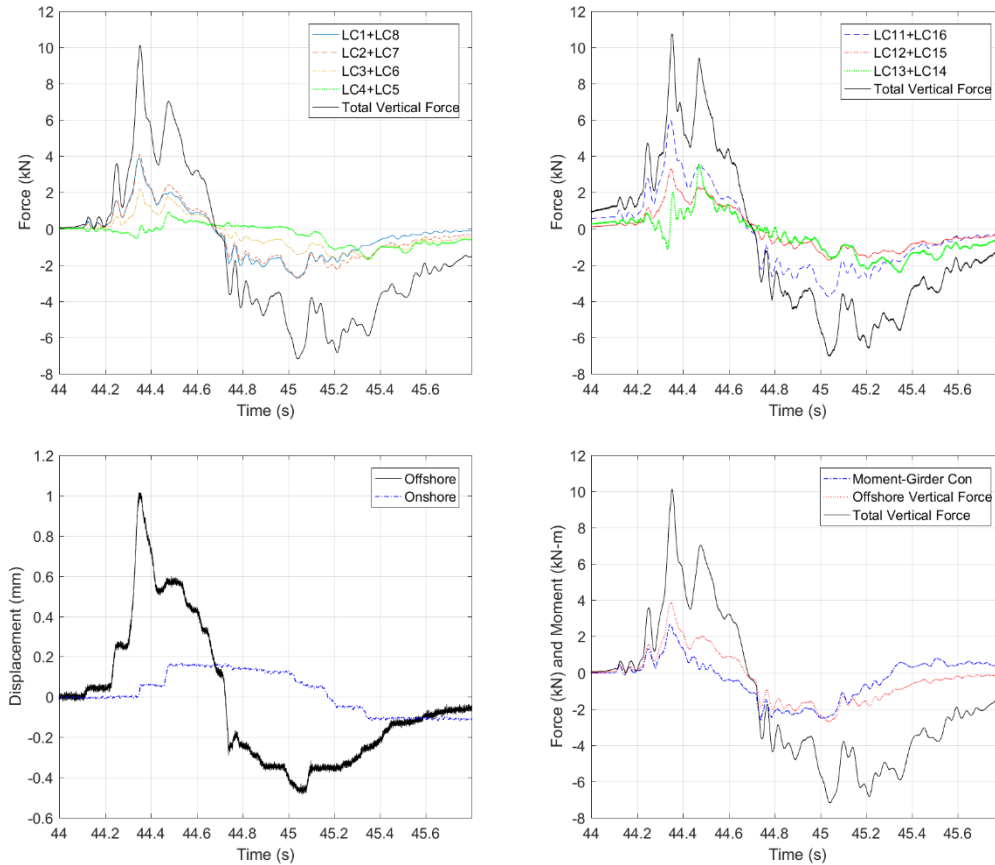


Figure 4.3: Vertical forces in bearings (top-left) and piers (top-right), displacements (bottom left) and vertical forces with associated moment (bottom-right) for bridge case ST5 and H=0.42m

This behavior can be verified by examining the forces in the piers, which are shown in Fig.4.3 (top right). In this graph, LC11+LC16, LC12+LC15 and LC13+LC14 are corresponding to the Figure 4.4 is showing the pressures applied on the girders and below the bridge deck at the location of the overhang and the chambers. Girder 1 corresponds to the offshore girder while bay 1 corresponds to the offshore chamber which is located between girders 1 and 2. The pressure histories on girders 2, 3, 4 and in the three chambers have smoother peaks than the ones on the offshore girder and overhang respectively, and this is due to the cushioning effect that was also observed in the experimental study (Cuomo et al., 2009) when a bridge was subjected to regular waves. In addition, as shown in Figure 7.7 in the case of solitary waves the pressures histories on the girders corresponding to the chambers with trapped air are witnessing two clear sequential peaks that are not observed in the pressure history of the offshore girder. Interestingly, the first pressure peaks on these girders occur before the pressure in the girder in front of it reaches its maximum and before the wave has actually inundated the respective chamber. A similar phenomenon is observed also in the pressures of the chambers below the deck, where for example the offshore chamber is witnessing significant pressure even before the solitary wave has reached the overhang. This interesting phenomenon, which to the knowledge of the author has not been discussed in the literature so far, can be explained by the existence of trapped air in the chambers, which is being compressed by the solitary wave even before the lip of the wave

has reached the chamber. The wave shape of a solitary wave has a gradual slope before it reaches the lip, meaning for example that when the lip is reaching the offshore girder or the overhang, a part of the wave has already reached the bottom of the next chamber and since the air is trapped inside, pressures are being transferred to the deck of the bridge and to the girder even before the wave actually reaches them. If the air would not have been trapped in the chamber then the wave would not have reached the deck and applied pressures on the bridge until the lip of the wave had arrived and inundated that chamber. This effect on the pressure histories of the internal chambers has been observed for all the tested solitary wave, however its significance on the total wave forces was seen to be related to the solitary wave height and length.

Examination of the pressure histories of the chambers - below the deck and on the girders – and their relationship to the existence of air-entrapment is of high significance because it can help explain the observed behavior of the bridge and the forces that are introduced in the connections. In regard to this, the pressures below the deck and the total vertical force recorded in the bearings were normalized with their maximum values and are plotted in Figure 4.5. This graph verifies that the wave applies pressure on the deck in the offshore chamber (bay 1) through the compression of the air before the pressure on the overhang is maximized, however that results only in a small peak in the vertical force histories. In addition, the graph demonstrates that the maximum uplift does not occur neither in Phase 1 (mainly rotation) nor in Phase 3 (mainly upwards translation), but it occurs in Phase 2 (rotation and upwards translation), where the impulsive pressure on overhang is reducing and the smoother pressures in the two first chambers are maximized. As expected, based on the previous discussion, at the instant of the second large peak Phase 3 occurs where the wave has inundated all the chambers and the pressures on the deck in the middle and onshore chambers are maximized.

Figure 4.6 is similar to Figure 4.5 however in this graph the normalized horizontal forces and the normalized pressures on the girders are shown. Following a similar trend as the one discussed previously for the vertical direction, in the horizontal direction the force is not maximized in Phase 1, when the pressures on the offshore girder are maximized, but slightly later when these pressures are starting to drop and the pressures on the internal girders 2 and 3 are starting to increase significantly. This demonstrates that for case ST5 where air-entrapment occurs all three first girders are contributing to the maximum horizontal force, when impacted by this particular solitary wave. Additional solitary waves will be examined in a following section in order to check if this conclusion can be generalized for all solitary waves.

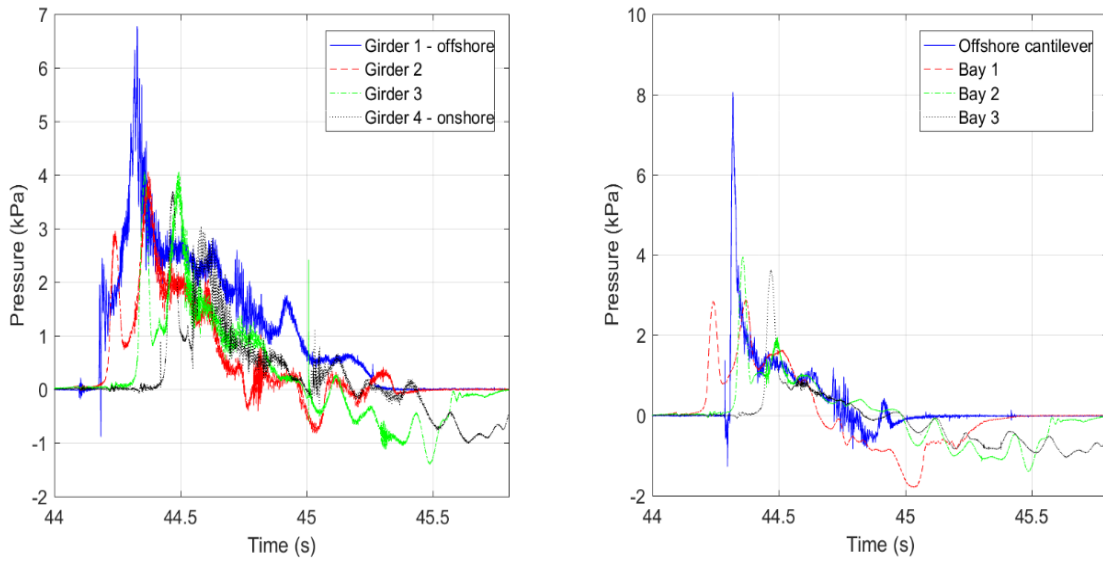


Figure 4.4: Pressures on girders (left) and below the deck (right) for ST5 and $H=0.42m$

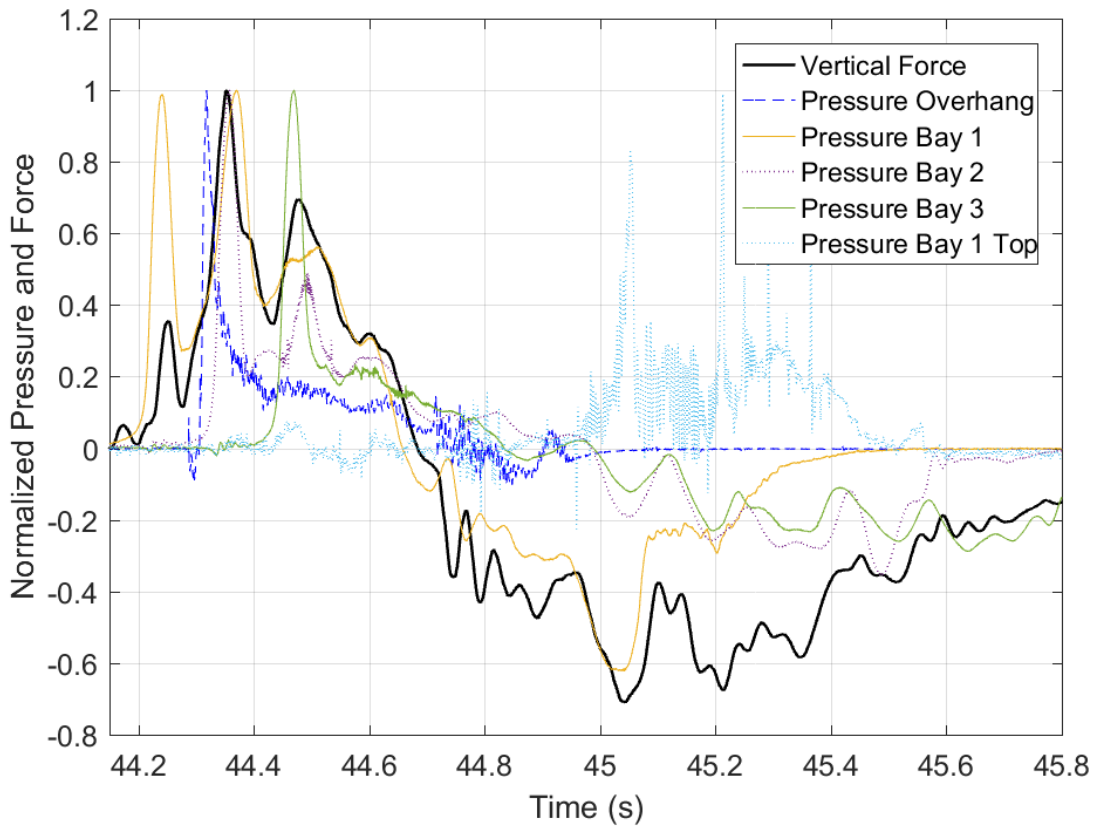


Figure 4.5: Normalized vertical forces and pressures below the bridge deck for ST5 and $H=0.42m$

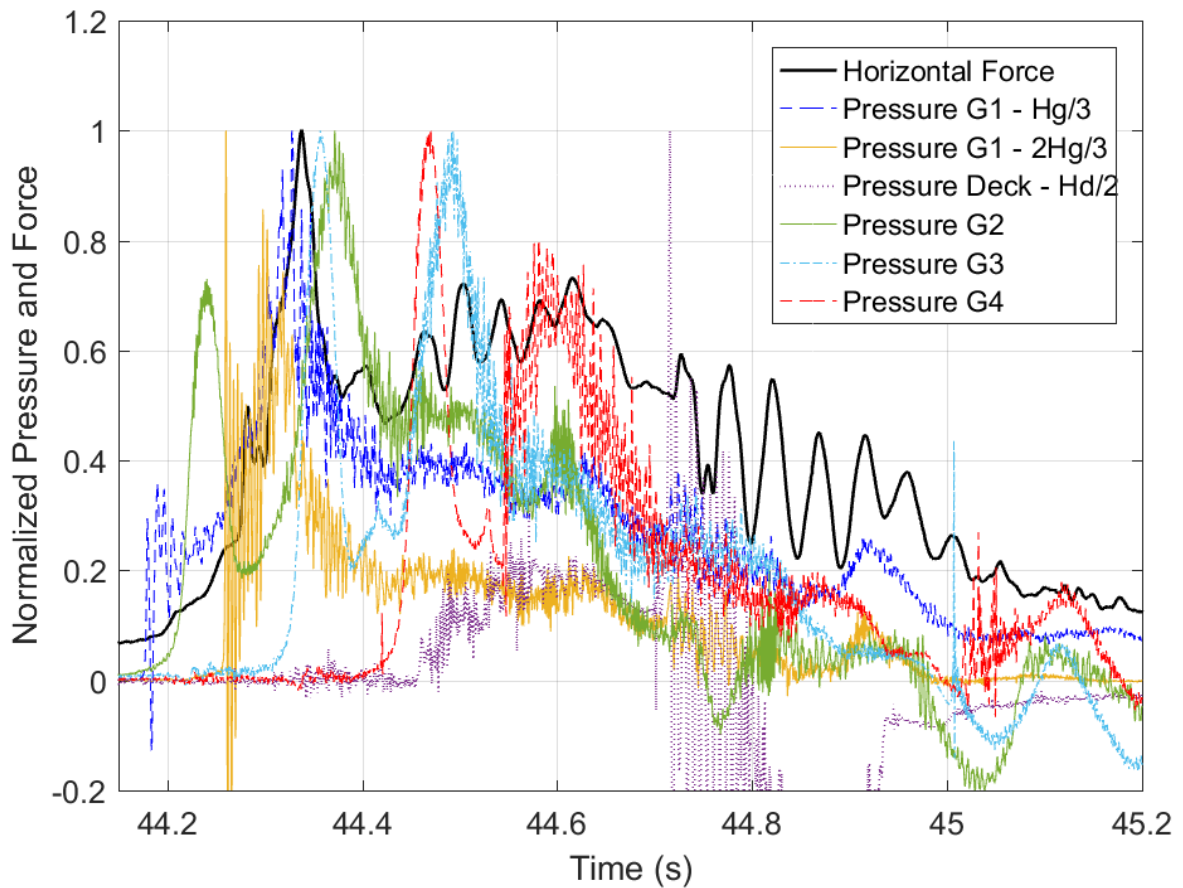


Figure 4.6: Normalized horizontal forces and pressures on the girders for ST5 and H=0.42m

Figure 4.7 is showing the maximum pressures recorded below the deck at 4 different locations, with location 1 corresponding to the overhang and location 4 to the onshore chamber. It can be noted that for both solitary waves and bores the overhang is witnessing significantly larger pressures than the chambers, justifying why the uplift force is so significant at the time of the initial impact of the wave on the bridge, determined in this study as Phase 1. In fact, as shown in Table 4.1 for solitary waves the overhang can witness pressures from 1.5 to 7.3 times higher than the pressures in the middle chamber, while for bores they are from 2.5 to 5.8 times higher. This numbers are demonstrating what a significant contribution the existence of the overhang has on the total uplift force and are indicating that if the overhang could be removed from the bridge or maybe have an optimum shape then the uplift force in Phase 1 could be reduced by a large amount.

Similarly, Figure 4.8 plots the pressures on the girders with location 1 corresponding to the offshore girder and location 4 to the onshore girder. The pressures on the offshore girder seem to be very large compared to the pressures on the internal girders for both solitary waves and bores and this is most likely due to the fact that after the impact on the offshore girder the wave loses kinetic energy and it impacts the following girders with a smaller velocity. In particular, Table

7.2 shows that the pressures on the offshore girder can be higher than the pressure on girder 2 by up to a factor of 3.5 for solitary waves and 2.4 for bores. This seems to be in agreement with previous graphs which demonstrated that at the time of the maximum horizontal force only the pressures on the offshore girder were maximized while the pressures on the other girders were negligible, meaning that the maximum horizontal force is actually applied on the offshore girder. This suggests that in the process of designing tsunami resilient bridges apart from checking the capacity of the bearing connections, which in the damaged bridges in recent tsunamis were the weak link, the engineer should also check for local failure of the offshore girder, especially if the bridge is witnessing uplift at the same time because this would put the bottom flange in compression increasing consequently the possibility of lateral and torsional buckling of steel girders. Although this failure mode has not been discussed in the literature so far, it might be worth mentioning that the Koizumi Bridge, which was swept away by the tsunami in the Tohoku Earthquake 2011, is shown in (Takeda et al., 2011) to have been overturned by the tsunami wave and laid on the ground with a laterally buckled exterior girder and buckled cross-frames and an intact interior girder, however it is not clear if this buckling occurred due the impact of the wave on the bridge or due to the impact with the ground or other objects as the bridge was being swept away by the wave.

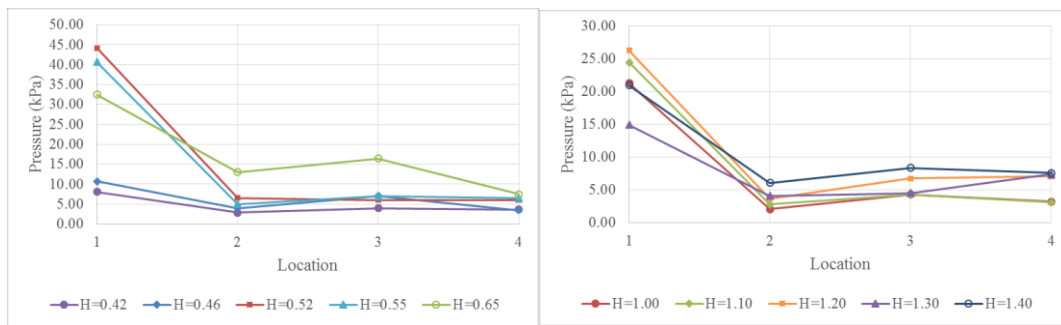


Figure 4.7: Maximum recorded pressures at four different locations recorded below the bridge deck for unbroken solitary waves (left) and for bores (right) for the bridge with diaphragms (ST5)

Table 4.1: Maximum Recorded Pressures below the Deck at the Overhang and in the Middle Chamber for the Bridge with Diaphragms (ST5)

Solitary Waves				
H _{input} (m)	Depth (m)	Overhang (kPa)	Middle (kPa)	Ratio Over/Mid
0.46	1.90	10.72	7.04	1.52
0.52	1.90	44.15	6.04	7.31
0.65	1.90	32.44	16.41	1.98
0.42	2.00	8.06	3.95	2.04
0.55	2.00	40.63	6.95	5.85
0.70	2.00	48.76	9.69	5.03

Bores				
H _{input} (m)	Depth (m)	Overhang (kPa)	Middle (kPa)	Ratio Over/Mid
1.00	1.90	21.29	4.28	4.97
1.10	1.90	24.49	4.23	5.79
1.30	1.90	14.95	4.51	3.32
0.90	2.00	26.43	7.67	3.45
1.20	2.00	26.29	6.72	3.91
1.40	2.00	20.9	8.3	2.51

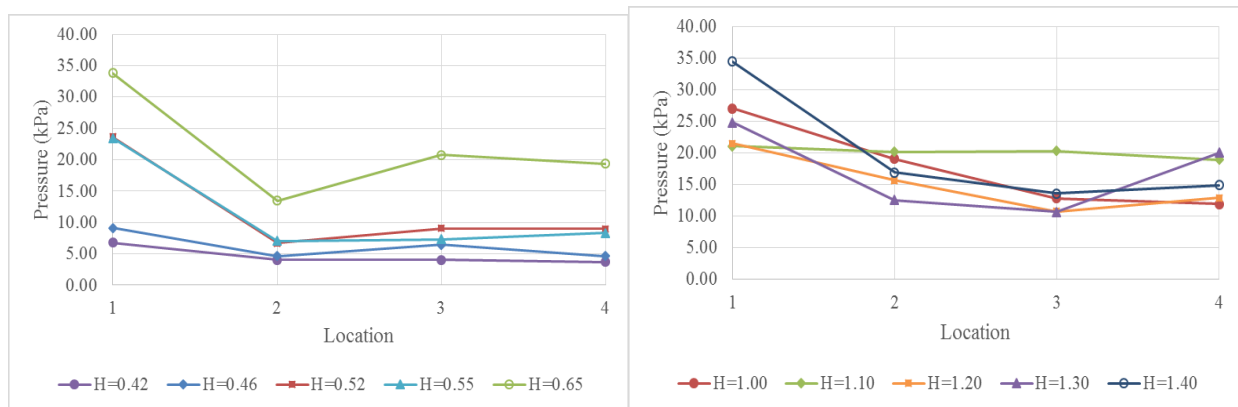


Figure 4.8: Maximum recorded pressures on the four girders for unbroken solitary waves (left) and for bores (right) for the bridge with diaphragms (ST5)

Table 4.2: Maximum Recorded Pressures on the Offshore Girder G1 and on the Interior Girder G2 for the Bridge with Diaphragms (ST5)

Solitary Waves				
H_{input} (m)	Depth (m)	Girder 1 (kPa)	Girder 2 (kPa)	Ratio G1/G2
0.46	1.90	9.09	4.63	1.97
0.52	1.90	23.65	6.69	3.53
0.65	1.90	33.85	13.50	2.51
0.42	2.00	6.78	4.05	1.67
0.55	2.00	23.47	7.08	3.32
0.70	2.00	27.36	8.90	3.07
Bores				
H_{input} (m)	Depth (m)	Girder 1 (kPa)	Girder 2 (kPa)	Ratio G1/G2
1.00	1.90	27.04	19.10	1.42
1.10	1.90	21.07	20.18	1.04
1.30	1.90	24.87	12.57	1.98
0.90	2.00	33.97	14.15	2.40
1.20	2.00	21.52	15.70	1.37
1.40	2.00	34.5	16.9	2.04

4.3 BRIDGES WITH CROSS-FRAMES VS DIAPHRAGMS: THE ROLE OF AIR-ENTRAPMENT

4.3.1 Pressures histories

In order to decipher the role of air-entrapment which occurs during the tsunami inundation of bridges with diaphragms, this section will compare experimental results from two bridge configurations ST2 and ST5, with the former having cross-frames and the latter diaphragms. The following graphs are showing results for a solitary wave with $H=0.42\text{m}$. Before proceeding with the comparison of the two bridge configurations it must be made sure that the waves are the same in both cases. This seems to be the case here, since as shown in Figure 4.9 the surface elevations at the wave-maker and one bay in front of the bridge seem to be very similar for both ST2 and ST5.

Figure 4.10 shows that the pressures on the offshore girder and the overhang are also fairly similar, which was expected since the overhang and the offshore girder are identical in both bridge cases. In contrast to the similarity of the pressures on the offshore face of the bridge between the bridge with cross-frames (ST2) and the one with diaphragms (ST5), the pressures on the internal girders and the pressures below the deck in the chambers are totally different in the two bridge types. For bridge ST5, as noticed also in the previous section, the pressures in the chambers are reaching a maximum value before they do in ST2, and this can now be attributed to the significant air entrapment between the girders, the diaphragms and the wave, which actually transfers the pressures on the girder and the deck before the lip of the solitary wave actually reaches the girder or the bottom of the deck.

Moreover, when air is trapped the pressure histories on the girders and on the deck have two distinctive peaks, which are smoother and longer in duration. When it comes to the magnitude of the pressure, the air entrapment seems to have a relatively small effect on the girder pressures and a major effect on the pressure on the deck, especially for small solitary waves that could not reach the deck. For $H=0.42\text{m}$ the pressure on the deck is approximately 3 times higher due to the air entrapment.

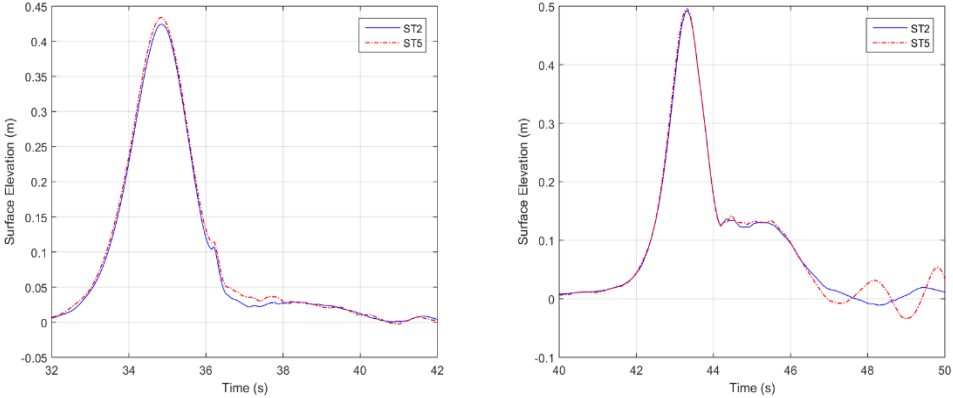


Figure 4.9: Surface elevation at the wave gage at wg1 close to the wavemaker (left) and at wg12 close to the bridge (right) for a wave with $H=0.42\text{m}$

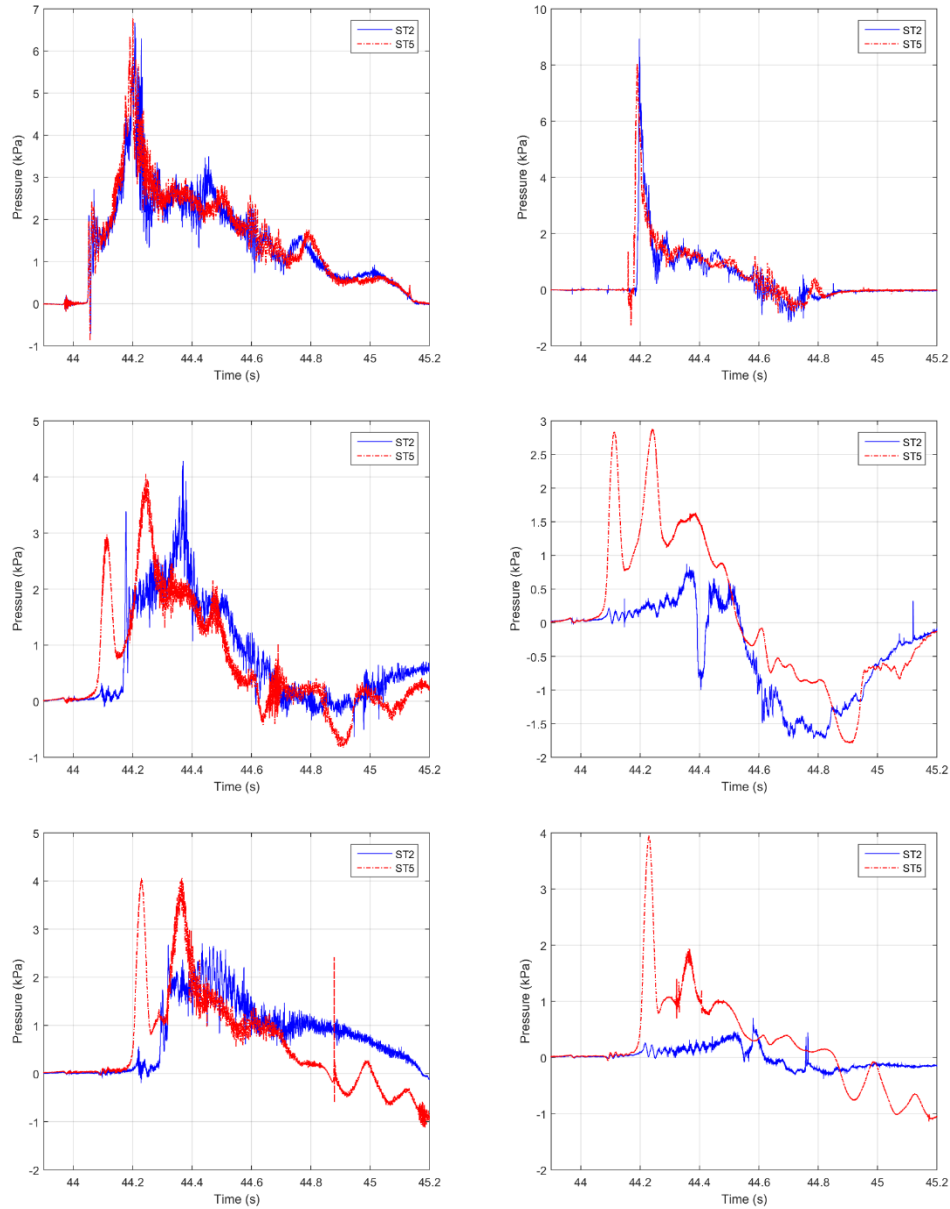


Figure 4.10: Pressure on the offshore girder (top-left), below the deck at the overhang (top-right), on the 2nd girder (middle-left), below the deck in the offshore chamber (middle-right), on the 3rd girder (bottom-left) and below the deck in the middle chamber (middle-right), for H=0.42m

4.3.2 Force, moment and deck rotation histories

Figure 4.11 shows the horizontal forces (left graph) recorded in the link and the total vertical forces recorded in the piers (right graph). Inspection of the graphs reveals that there is no significant difference in the maximum horizontal forces and this is because the maximum value occurs at the time of the initial impact, however, as the wave, inundation progresses the air entrapment and the wave-air interaction seems to alter the force history by significantly

smoothing some of the peaks. When it comes to the vertical forces, the air entrapment in the bridge with diaphragms causes a significant increase of 73% for the particular wave height and introduces two distinct peaks (uplift) in the time histories.

Figure 4.12 shows the bridge rotation calculated based on the recorded translations and the moment calculated based on the forces recorded in the piers. From this figure it becomes clear that when the bridge with the air-entrapment is inundated by a solitary wave it is witnessing a significantly larger clockwise rotation and moment. Apart from the magnitude though, the air-entrapment is also increasing the duration of the clockwise rotation and moment and this is due to the fact that the trapped air is causing a fundamentally different interaction between the solitary wave and the bridge that alters Phase 2. When the air can escape from the chambers after the initial impact in Phase 1 where the pressures on the overhang and the offshore girder are maximized causing a local maximum in the forces (horizontal and vertical) and moments, both the forces and moments are dropping until the lip of the wave arrives in the first chamber, however when air is trapped in the chambers then after the local maximum in Phase 1 the vertical forces and clockwise moments keep increasing more because additional vertical force is generated from the compression of the air in the first chamber.

Last but not least, the total vertical force histories have been analyzed using both the Empirical Mode Decomposition Method (EMD) and the FRF method -both of which are described in chapter 5 and the results from the former method are presented in Figure 4.13. Interestingly, the two bridge configurations seem to be witnessing slamming forces that have the similar maximum values and seem to occur in Phase 1, but are becoming different as the wave propagates through the bridge indicating that the presence of the trapped air has a hydrodynamic effect. In addition to this effect, the air-entrapment has a major effect on the quasi-static component of the uplift force increasing its magnitude by a factor of the 2.32. The air-entrapment also seems to alter the solitary wave as it propagates through the chambers resulting in an increase of the duration of the uplift force. A more detailed discussion about the role of air-entrapment can be found in (Istrati and Buckle, 2019). It is however noteworthy that the effect of air-entrapment on the magnitude of the uplift force has been observed also by other experimental studies (e.g. Hayatdavoodi et al., 2014; Seiffert et al., 2015) and the present study demonstrates that this increase in the total uplift force comes mainly from the increase of the quasi-static component.

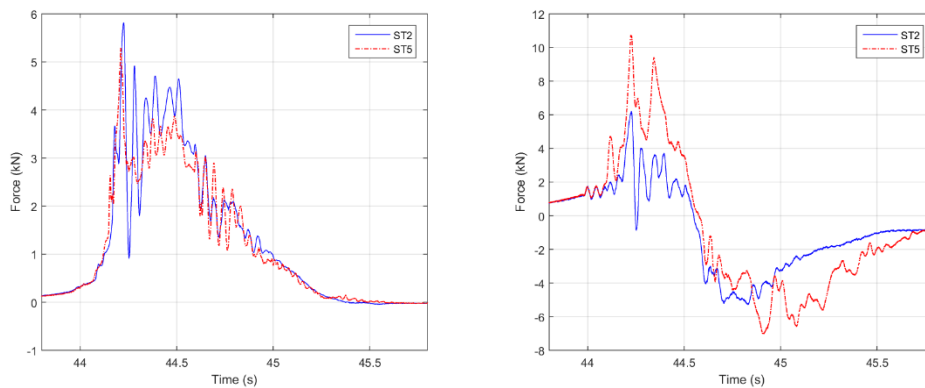


Figure 4.11: Total horizontal forces recorded in the link (left) and total vertical forces recorded in the piers (right) for H=0.42m

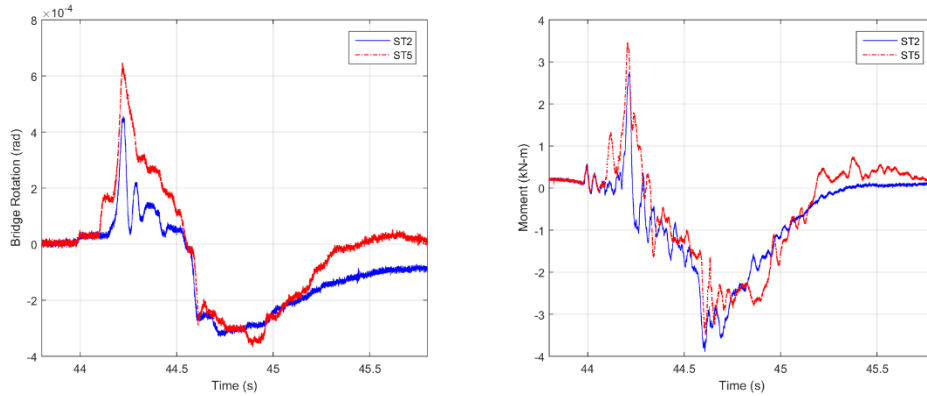


Figure 4.12: Bridge deck rotation (left) and moment (right) for H=0.42m

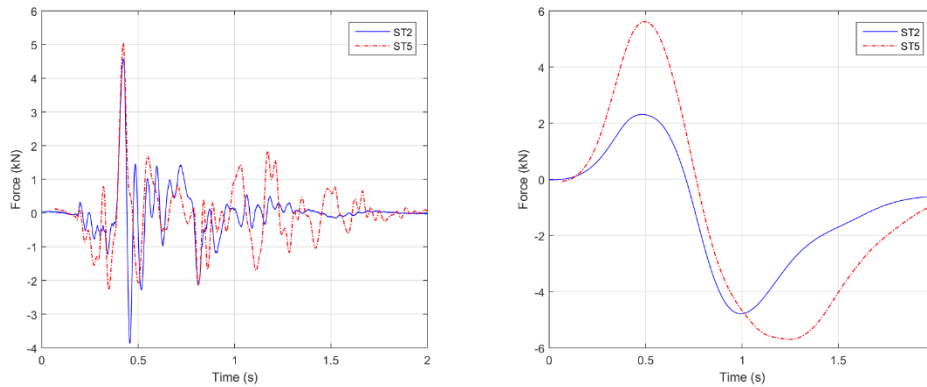


Figure 4.13: Vertical slamming (left) and quasi-static forces (right) recorded in the bearings for H=0.42m

4.3.3 Maximum pressures and forces

The two previous sections have given an insight into the effect of air-entrapment that occurs in bridges with diaphragms by comparing the time histories of pressures, forces, rotations and moments for two different waves. In an attempt to generalize the observations and conclusions reached based on two waves, this section will focus on the maximum values for a group of solitary waves and bores, which was tested for both bridge configurations ST2 and ST5. For a better correlation of the wave heights to the associated effects on the bridge structures Figure 4.20 is showing the wave heights measured by the acoustic gage uswg1 in front of the bridge for most of the tested waves. In addition, the distance Δz_{deck} of the bottom of the deck from the free-surface has also been plotted in order to check if the waves reached the bottom of the deck or not. This figure is demonstrating that most of the waves can reach the bottom of the bridge deck, apart from the 0.36m wave at 2.0m water depth and the 0.46m wave at a 1.90m water depth, both of which are lower than the deck, and the 0.42m wave at $d=2.0\text{m}$ which is barely reaching the bottom of the deck. In this figure, all the waves with an input wave height smaller or equal to 0.70m arrive as solitary waves at the bridge location, while the rest arrive as bores. Interestingly, the solitary wave heights seem to be identical for both ST2 and ST5, however this is not true for the bores, for which larger differences seems to occur.

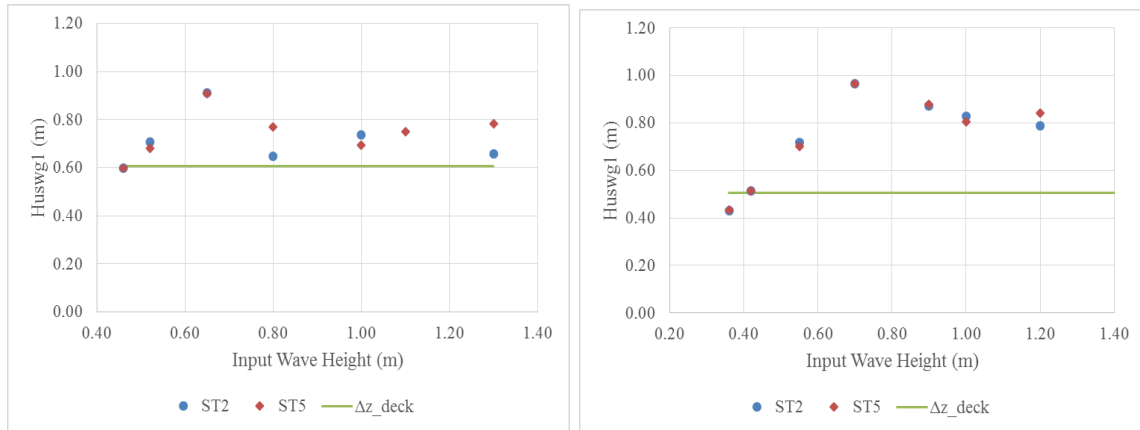


Figure 4.14: Maximum wave heights measured in front of the bridge for $d=1.90\text{m}$ (left) and $d=2.0\text{m}$ (right)

Table 4.3 is showing the measured wave heights at wg2 close to the wave-maker and at wg12 which is one bay in front of the bridge. At wg2, the wave heights of the tested waves for ST2 and ST5 seem to be very similar with an average difference of 1.7% for all waves and a max difference of 4%, which means that the waves are very repeatable close to the wave-maker. However, this is not true for the recorded wave heights at wg12, where the solitary waves have a difference of 1.7% average and 4.5% max, while the bores have a significantly larger difference equal to 9.5% average and 22% max. The main reason for seeing the considerable variability in the wave heights of the bores close to the bridge is the fact that the bores were formed after plunging wave breaking occurred, which is a very complex process consisting of multiple plunges, oblique splash-up, vertical jet, air bubble entrainment and chaotic multiple splash-up events that produce vorticity and turbulence, as described in (Ghosh et al., 2007). Therefore, the variability in the bore heights close to the bridge can be justified by the randomness associated with the plunging wave breaking process, and it should be taken into account when the responses of the two bridge configurations - with cross-frames and diaphragms- are compared.

Table 4.3: Maximum Recorded Wave Heights at wg2 and wg12

H_{input} (m)	Depth (m)	ST2		ST5		Ratios ST5/ST2	
		Hwg2 (m)	Hwg12 (m)	Hwg2 (m)	Hwg12 (m)	Hwg2	Hwg12
0.46	1.90	0.48	0.58	0.46	0.55	0.96	0.95
0.52		0.54	0.67	0.54	0.66	1.00	0.99
0.65		0.66	0.91	0.67	0.89	1.02	0.98
0.80		0.80	0.72	0.80	0.82	1.00	1.13
1.00		0.99	0.69	0.99	0.75	0.99	1.08
1.10		1.09	0.77	1.07	0.72	0.98	0.94
1.30		1.29	0.61	1.31	0.74	1.02	1.22
0.36	2.00	0.37	0.41	0.38	0.42	1.02	1.01
0.42		0.43	0.49	0.44	0.50	1.02	1.01
0.55		0.55	0.66	0.56	0.68	1.00	1.02
0.70		0.69	0.90	0.70	0.91	1.02	1.01
0.90		0.87	0.96	0.88	0.88	1.01	0.92
1.00		0.94	0.78	0.98	0.80	1.04	1.03
1.20		1.14	0.82	1.16	0.75	1.02	0.92
1.40		1.35	0.73	1.4	0.8	1.02	1.07

In order to develop a better understanding of the role of air entrapment, the maximum pressures have been plotted as a function of the wave height. In particular, in Figure 4.15 and 4-16 the pressures on the interior girders G2 and G3, and the pressures below the deck in the offshore and middle chambers have been plotted respectively, for the waves tested at a 2.0m water depth. It must be noted that as seen in the previous section for the solitary wave with H=0.42m, the pressures on the girders are indeed smoothed and the peaks consistently reduced due to the trapped air for all the solitary waves –apart from the very small ones that cannot or can barely reach the bottom of the bridge deck- however this is not true for the turbulent bores. For some bores the air-entrapment is increasing the pressure on G2 and for others it reduces it. In addition, for the same bore the air-entrapment can increase the pressure on G2 and decrease it on G3, indicating that the bore is being affected after the complex interaction with the air in the first chamber.

Similarly, for the pressures on the deck inside the chambers, although the air-entrapment increased the pressure in the middle chamber by a factor of 3 for a 0.42m wave height, this is not true for all the chambers and all wave heights, as seen in Figure 4.16. For example, in the middle chamber the pressures for all the wave heights apart from the 0.70m and 0.90m show an increase due to the air entrapment, however this trend is not the same in the offshore chamber, where the air-entrapment has a variable effect for different wave heights. This variable effect might be due to the fact that the air entrapment modifies the wave flow differently each time leading to a complex nonlinear wave-air interaction phenomenon.

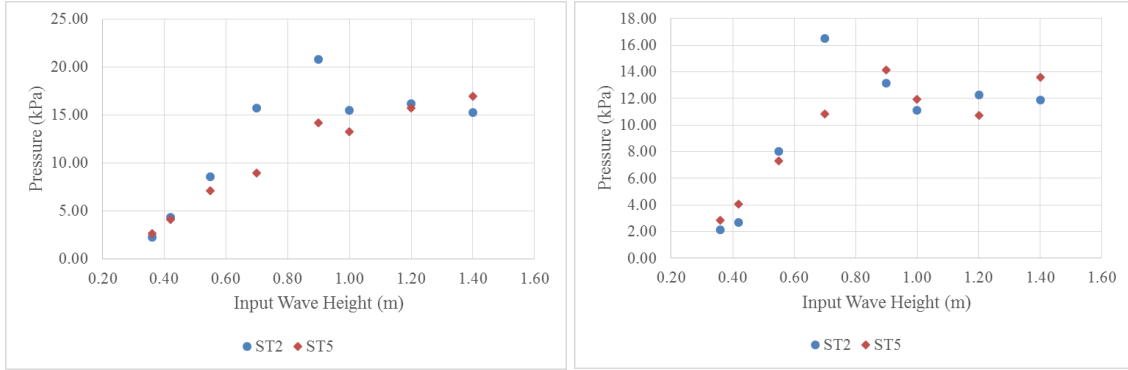


Figure 4.15: Maximum pressures on interior girder G2 (left) and on interior girder G3 (right) for all the wave heights tested for a 2.0m water depth.

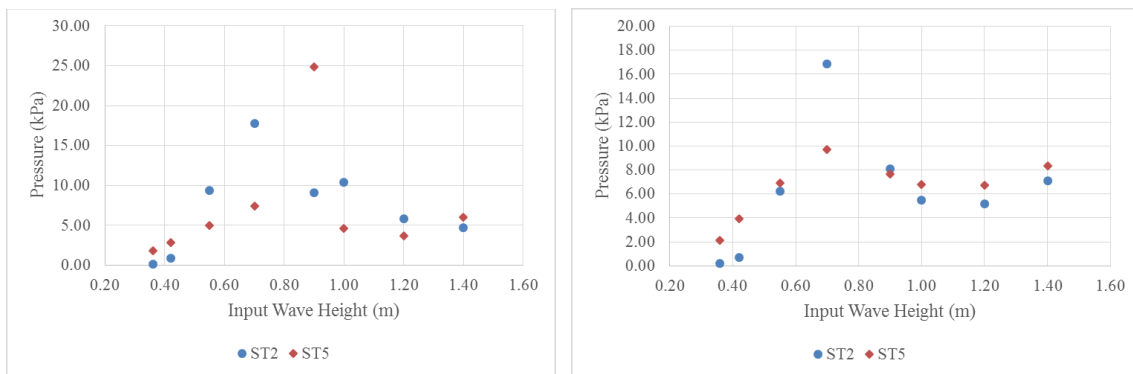


Figure 4.16: Maximum pressures below the deck in the offshore chamber (left) and in the middle chamber (right) for all the wave heights tested for a 2.0m water depth.

Figure 4.17 and Table 4.4 show the total vertical forces recorded in the bent cap-to-pier connections for solitary waves and bores of different wave heights. Interestingly the air entrapment seems to have a consistent effect increasing the total vertical forces for both solitary waves and bores. However, the exact amount of increase in the forces depends again on the wave height. The air-entrapment caused an increase of the uplift force by 40% on average with 2% minimum and 152% maximum. The largest increase was witnessed for the smaller solitary wave heights that could not reach the deck, which is reasonable because when the air is absent these waves can barely apply some pressure on the deck, while when air is trapped then the buoyancy force increases significantly and the pressures are transferred to the deck through the compressed air. For example, for the smallest solitary wave with $H=0.36\text{m}$ the total force increased by a factor of 2.5. Some waves showed a very small increase in the total uplift forces such as the 0.46m, 0.65m and the 1.0m waves (at $d=1.90\text{m}$), and the explanations for this observation is that (i) for both bridge specimens for certain waves the maximum uplift force occurs in Phase 1 where the slamming (hydrodynamic) component is governing and the air-entrapment is not affecting the results (true for $H=0.46\text{m}$), and (ii) for other waves the maximum uplift for ST2 occurs in Phase 1 while for ST5 occurs in Phase 3 (true for $H=1.0\text{m}$) where the quasi-static component is governing, making it hard to decipher the underlying physics by just examining the maximum values of the uplift force.

To improve the understanding of the physics involved, the total uplift forces measured in the bent cap-to-pier connections were analyzed using the EMD method and both the slamming and the quasi-static component have been obtained. As shown in Table 4.5, the air-entrapment increases consistently the maximum values of quasi-static forces, which occur in Phase 3, for all tested waves. The increase ranges between 15% and 157%, with the smaller value occurring for the wave with the largest inundation height in front of the bridge ($H=0.70\text{m}$) and the largest occurring for the smallest wave ($H=0.36\text{m}$). The comparison of the total uplift forces and the quasi-static uplift forces is of high importance because it demonstrated that the air-entrapment is always resulting in an increasing of the quasi-static force – which takes place in Phase 3 where all bearing connections are witnessing the uplift- but this is not always translated into an increase in the total force because for some waves the uplift force is maximized in Phase 1, which has not been considered in the literature so far.

Moreover, examination of Figures 4.15, 4.16 and 4.17 demonstrates that comparison of the pressures in a certain chamber at the mid-span (far from the end diaphragms) cannot adequately describe the effect of the escape and entrapment of the air on the total vertical forces. This indicates that the 3D effects are significant and that the pressures close to the end cross-frames or diaphragms are significantly different than the applied pressures at the mid-length of the bridge. As a result, in order to capture accurately the escape of the air 3D CFD analyses will be required despite the fact that we have a straight bridge and a 2D wave propagation.

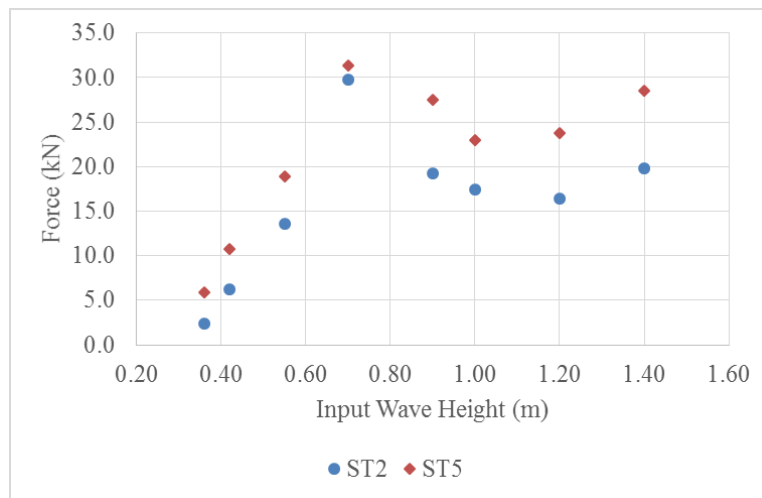


Figure 4.17: Maximum total uplift forces for all the wave heights tested for ST2 and ST5 with a 2.0m water depth.

Table 4.4: Maximum Total Uplift Forces for ST2 and ST5

H_{input} (m)	Depth (m)	ST2 (kN)	ST5 (kN)	Ratios ST5/ST2
0.46	1.90	9.02	9.18	1.02
0.52		16.69	19.88	1.19
0.65		21.55	22.91	1.06
0.80		7.98	12.36	1.55
1.00		10.54	10.89	1.03
1.10		9.00	13.49	1.50
1.30		11.34	15.52	1.37
0.36	2.00	2.33	5.87	2.52
0.42		6.23	10.74	1.73
0.55		13.61	18.93	1.39
0.70		29.79	31.39	1.05
0.90		19.29	27.48	1.42
1.00		17.45	22.95	1.32
1.20		16.43	23.79	1.45
1.40		19.83	28.49	1.44

Table 4.5: Maximum Quasi-static Uplift Forces for ST2 and ST5

H_{input} (m)	Depth (m)	ST2 (kN)	ST5 (kN)	Ratios ST5/ST2
0.46	1.90	3.15	4.94	1.57
0.52		4.55	7.59	1.67
0.65		9.00	13.10	1.46
0.80		6.64	8.94	1.35
1.00		6.82	9.55	1.40
1.10		7.56	10.02	1.32
1.30		6.24	12.26	1.97
0.36	2.00	1.53	3.93	2.57
0.42		2.81	6.52	2.32
0.55		9.06	12.93	1.43
0.70		17.52	20.16	1.15
0.90		12.81	16.97	1.32
1.00		12.87	16.62	1.29
1.20		12.09	16.98	1.40
1.40		14.26	18.83	1.32

Since in previous chapters of this study the need to examine the force in each individual bearing and column of the pier was highlighted, this part of the section will focus on the role of air-entrapment on each connection. In this regard, Figures 4.18 and 4.19 are showing the maximum recorded vertical forces in the bearings and in the columns of the piers, respectively. In the former figure location 1 corresponds to the offshore bearings, location 4 to the onshore ones, and the rest are the bearing of the interior girders. Similarly, in the latter figure location 1

corresponds to the offshore column of the pier and location 3 to the onshore one. These figures are demonstrating that both bridge types – with cross-frames and diaphragms- are witnessing similar patterns in the distributions of the forces in the bearings and the columns, with the offshore bearings and the bearings next to them, as well as the offshore column, taking significantly larger vertical forces than the rest of the connections. From these graphs it can also be observed that there is an increase of the forces in the onshore bearings and piers due to the air-entrapment.

Figure 4.20 and Table 4.6 are showing the maximum vertical forces recorded in the offshore and onshore piers for all the waves tested for two different water depths. Interestingly, the air-entrapment associated with the bridge ST5 does not seem to increase consistently the uplift forces in the offshore columns for all the wave heights, as was the case with the total uplift force, but for some wave heights can have a negligible effect or even decrease these forces. On the other hand, the uplift forces in the onshore columns are having a consistent trend and are significantly increased by the air-entrapment. The increase of the forces in the onshore columns is ranging between 8% and 292% with an average of 105% for all the tested waves. The different effect of the air-entrapment on the offshore and onshore columns can be attributed to the fact that the forces in the former columns can be maximized during Phase 1, 2 or 3, where the air-entrapment has a different effect in each phase, while the forces in the latter columns are always maximized in Phase 3 where the quasi-static force is reaching its maximum and the air-entrapment is consistently increasing the quasi-static force for all wave heights.

The previous comparison demonstrates that examining the effect of the air-entrapment on the total uplift force is not adequate because it cannot describe the complex effect it has on the forces that go in each column. The existence of the trapped air is resulting in a different wave-structure interaction for the two bridge specimens and causes a different bridge response that affects the forces that each column has to withstand.

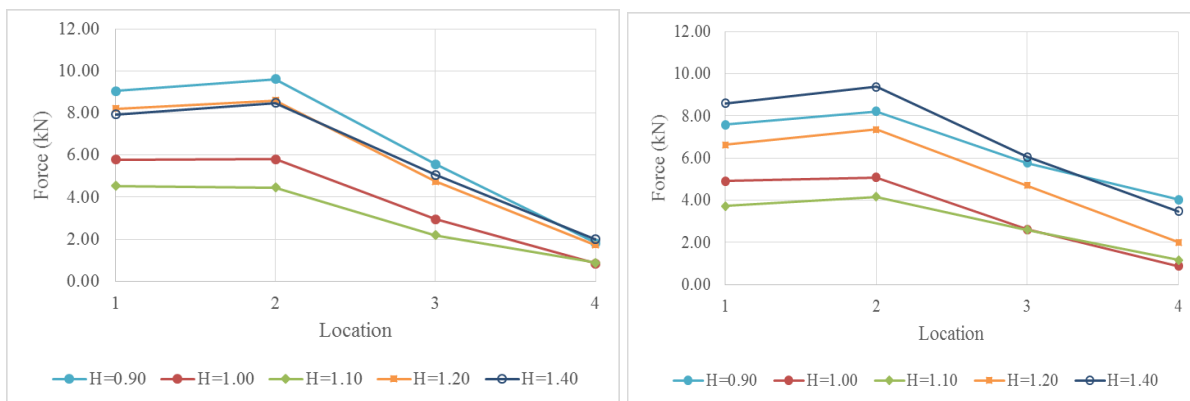


Figure 4.18: Maximum vertical forces in different bearings along the abutments for bridge configurations ST2 (left) and ST5 (right) and a set of wave heights

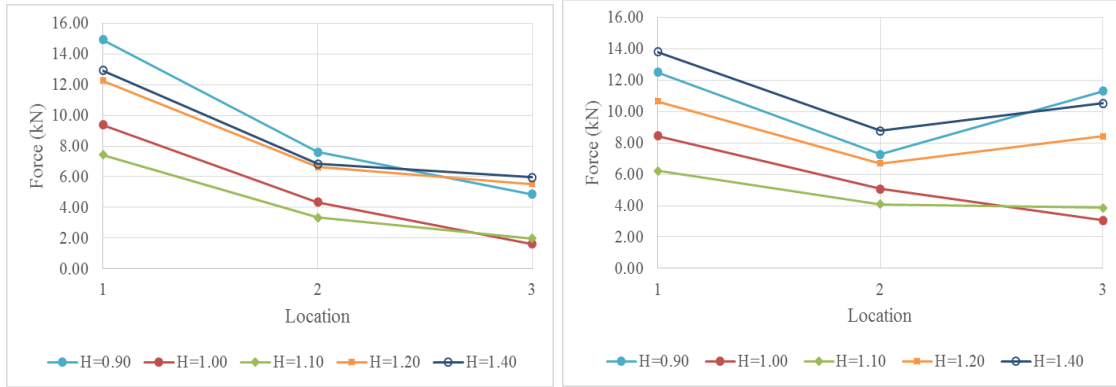


Figure 4.19: Maximum vertical forces in the piers for bridge configurations ST2 (left) and ST5 (right) and waves of different height

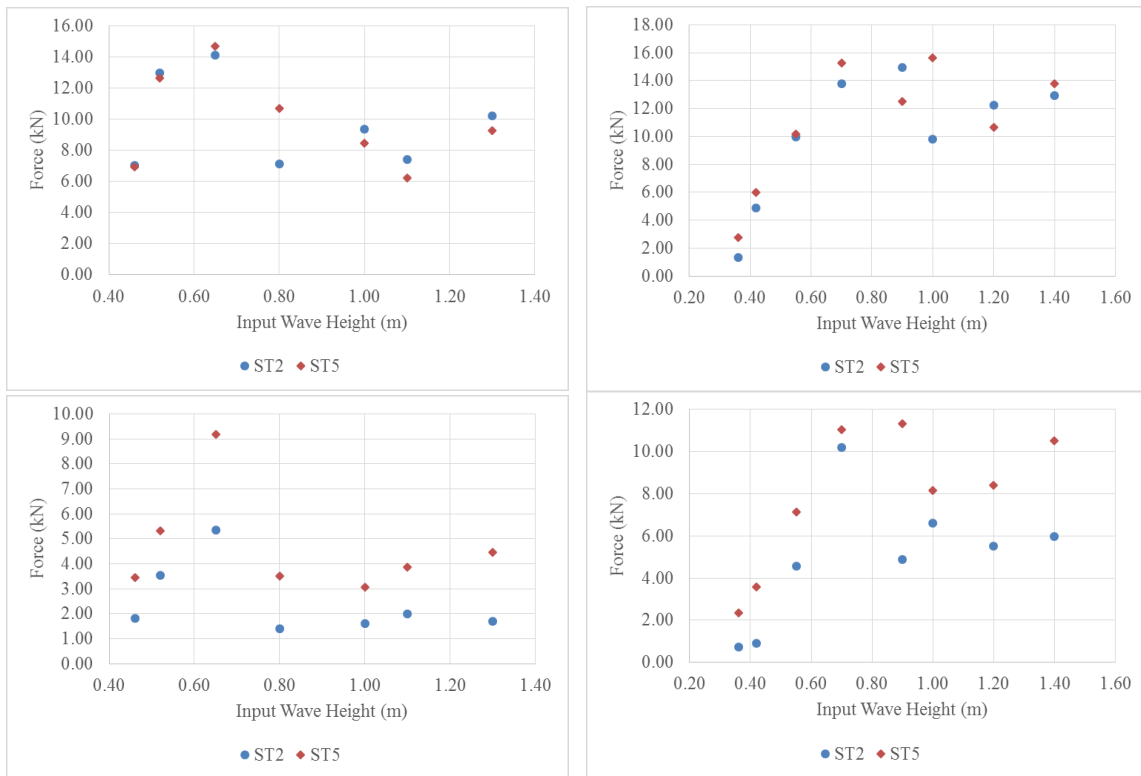


Figure 4.20: Maximum vertical forces in offshore (top) onshore (bottom) columns of the piers for all the wave heights tested for a water depth of 1.90m (left) and 2.0m (right)

Table 4.6: Maximum Vertical Forces Recorded in Offshore and Onshore Piers

H_{input}	Depth	Offshore Piers			Onshore Piers		
		ST2	ST5	Ratios ST5/ST2	ST2	ST5	Ratios ST5/ST2
(m)	(m)	(kN)	(kN)		(kN)	(kN)	
0.46	1.90	7.03	6.93	0.98	1.82	3.45	1.89
0.52		12.98	12.65	0.97	3.55	5.31	1.50
0.65		14.11	14.69	1.04	5.34	9.19	1.72
0.80		7.11	10.71	1.51	1.40	3.51	2.51
1.00		9.38	8.45	0.90	1.62	3.07	1.90
1.10		7.42	6.21	0.84	1.99	3.86	1.94
1.30		10.22	9.28	0.91	1.71	4.45	2.61
0.36	2.00	1.30	2.76	2.11	0.73	2.34	3.20
0.42		4.88	5.97	1.22	0.91	3.57	3.92
0.55		9.96	10.20	1.02	4.56	7.14	1.57
0.70		13.79	15.28	1.11	10.19	11.04	1.08
0.90		14.92	12.51	0.84	4.87	11.32	2.33
1.00		9.78	15.62	1.60	6.61	8.18	1.24
1.20		12.25	10.67	0.87	5.53	8.42	1.52
1.40		12.92	13.80	1.07	5.96	10.53	1.77

Tables 4.7 and 4.8 are showing the vertical forces recorded in the bearings. Similarly to the forces in the offshore columns, the air-entrapment seems to have a variable effect on the forces of the offshore bearings, which for some wave heights can be increased by up to 50% and for other waves can be decreased by up to 19% due to the presence of the trapped air. This variable effect is also seen in the bearings of the interior girders G2 and G3. Similarly to the onshore columns of the piers, the onshore bearings are the ones that are being affected the most by the air-entrapment and can witness an increase of 56% on average for all waves and up to 191%. Although, the air-entrapment seems to cause a consistently significant increase in the forces of the onshore columns and the onshore bearings, this is not exactly the case for the forces in the onshore bearings since for the largest solitary wave with H=0.70m the forces surprisingly decreased by 39%. Therefore, deciphering the effect of the air-entrapment on the forces of the bearings is even more challenging than the effect on the columns of the piers because the existence of the shear keys introduces a more complex response as the wave inundates the bridge and friction is generated due to the contact with the offshore and onshore girders

Table 4.7: Maximum Vertical Forces Recorded in Offshore and Onshore Bearings

H_{input}	Depth	Offshore Bearings			Onshore Bearings		
		ST2	ST5	Ratios ST5/ST2	ST2	ST5	Ratios ST5/ST2
(m)	(m)	(kN)	(kN)		(kN)	(kN)	
0.46	1.90	4.50	4.40	0.98	0.66	0.86	1.29
0.65		8.92	9.62	1.08	2.13	3.28	1.54
0.80		4.21	6.34	1.51	0.82	1.06	1.29
1.00		5.78	4.92	0.85	0.83	0.88	1.06
1.10		4.53	3.74	0.82	0.88	1.17	1.33
1.30		6.25	5.60	0.90	0.79	1.30	1.64
0.42	2.00	3.10	3.88	1.25	0.32	0.93	2.91
0.70		8.27	9.58	1.16	3.19	1.96	0.61
0.90		9.05	7.58	0.84	1.82	4.04	2.22
1.20		8.20	6.62	0.81	1.72	2.01	1.17
1.40		7.92	8.60	1.09	2.00	3.48	1.75

Table 4.8: Maximum Vertical Forces Recorded in Bearings of Interior Girders

H_{input}	Depth	Bearings of 2nd girder			Bearings of 3rd girder		
		ST2	ST5	Ratios ST5/ST2	ST2	ST5	Ratios ST5/ST2
(m)	(m)	(kN)	(kN)		(kN)	(kN)	
0.46	1.90	4.19	4.27	1.02	1.54	1.91	1.24
0.65		8.97	10.32	1.15	5.00	5.68	1.14
0.80		4.18	6.51	1.56	1.96	3.46	1.77
1.00		5.80	5.08	0.88	2.95	2.62	0.89
1.10		4.45	4.16	0.94	2.18	2.60	1.19
1.30		6.27	5.78	0.92	3.18	3.07	0.97
0.42	2.00	2.88	4.10	1.42	1.29	2.22	1.72
0.70		9.03	10.12	1.12	6.30	6.22	0.99
0.90		9.61	8.22	0.85	5.57	5.77	1.04
1.20		8.59	7.36	0.86	4.74	4.70	0.99
1.40		8.48	9.39	1.11	5.05	6.07	1.20

4.4 MEASURED UPLIFT FORCES VS BUOYANCY

4.4.1 Total Forces vs Buoyancy

One of the fundamental differences between a girder bridge with cross-frames and one with diaphragms is that the latter one will trap air underneath the deck, which will increase the buoyancy force. In order to develop a better understanding of the magnitude of the wave-induced hydrodynamic uplift forces Fig. 4.21 presents a comparison of the recorded uplift forces with the

calculated buoyancy, for both deck types. For the deck with cross-frames the buoyancy is calculated using the volume of the deck plus the other components (e.g. bearings, connecting plates etc), which gives a total of 4.67kN. For the deck with diaphragms, which is expected to trap air but the exact air quantity is unknown; the buoyancy was calculated using the following equation:

$$\mathbf{F_{b,tot} = \gamma V_{br} + n\gamma\alpha V_{ch}} \quad (4-1)$$

Where:

γ =unit weight of water,

V_{br} =is the volume of the bridge, n =number of chambers that are assumed to have trapped air,

V_{ch} = volume of one bridge chamber (created between two consecutive girders and the bottom of the deck), and

α = percentage of the volume of chamber that is filled with air.

In this study, two values of α were examined and particularly 0.5 and 1, which correspond to 50% and 100% of air-entrapment. The 50% ratio was selected following the recommendation in (McPherson et al., 2008), who found that using this assumption and considering the additional buoyancy of the trapped air the experimental data were estimated relatively well using simplified predictive equations. The 100% value was selected in order to get an upper bound for the buoyancy of a deck with diaphragms. On the other hand the coefficient “n” was assumed to be equal to 0, 1, 2 or 3 depending on the assumed scenario. Overall the total bridge buoyancy was calculated using the above equation and five different assumptions, by considering:

- only the buoyancy of the bridge $F_{b,bridge}$ which considers the buoyancy of the deck and connecting elements, assuming that all the trapped air has escaped from underneath the deck,
- the buoyancy of the bridge and the buoyancy of the trapped air assuming that 50% ($F_{b,brd+air50}$) or 100% ($F_{b,brd+air100}$) of the volume of all three chambers is filled with air, and
- the buoyancy of the bridge and the buoyancy of the trapped air assuming that 50% ($F_{b,brd+air50ch}$) or 100% ($F_{b,brd+air100ch}$) of the volume of the actual number of flooded chambers is filled with air. This is expected to be a more accurate representation because the previous section revealed that due to the complex temporal and spatial variation of the wave loading, the maximum uplift can occur anytime during the inundation process (any phase), e.g. when one chamber is flooded or when several chambers are flooded.

While the buoyancy of the bridge itself is 4.67 kN, the buoyancy coming only from the trapped air is 5.40 kN or 10.79 kN, if 50% or 100% respectively of the volume of all three chambers is filled with air. Therefore, for these cases $F_{b,brd+air50}$ and $F_{b,brd+air100}$ become equal to 10.06 kN and 15.46 kN respectively. If only the actual flooded chambers are considered then the buoyancy due to the trapped air is not constant for all wave heights, but varies between 1.80kN and 10.79 kN, with the exact values shown in Table 6, which means that $F_{b,brd+air50ch}$ and $F_{b,brd+air100ch}$ vary between 6.47 kN and 10.06 kN, or between 8.27 kN and 15.46 kN respectively.

As shown in Fig. 4.21, for the deck with cross-frames all solitary waves (apart from the smallest one) and bores tested in this study introduced a hydrodynamic uplift that exceeded the buoyancy of the bridge ($F_{b,bridge}$), by a factor of 3.01 on average and up to 6.38 maximum. For the deck with diaphragms all solitary waves and bores tested in this study introduced a hydrodynamic uplift that exceeded the buoyancy of the bridge, by a factor of 3.91 on average and up to 6.72 maximum. When 50% of the volume of each chamber is assumed to be trapped with air, the magnitude of the buoyancy force is doubled, however even in this case the measured uplift forces are larger than the buoyancy force for most waves, by a factor of 1.81 on average and up to 3.12 maximum. The largest buoyancy force is achieved when 100% of the volume of all chambers is assumed to be filled with air, in which case, the measured hydrodynamic uplift of the largest solitary waves for both water depths and all the bores tested a 2.0m water depth, still exceed the buoyancy force by a factor of 1.18 on average and up to 2.03 maximum. However, for the majority of the waves tested at 1.90m water depth and some of the smallest solitary waves tested a 2.0m water depth, the measured uplift forces are smaller than $F_{b,brd+air100}$. Therefore, although the mean value of the hydrodynamic uplift to the calculated buoyancy drops significantly and becomes equal to 1.18, this does not mean that the estimation of the buoyancy gives an accurate estimation of the wave induced uplift for all wave heights, since the coefficient of variation CV (standard deviation to mean values) was 41%.

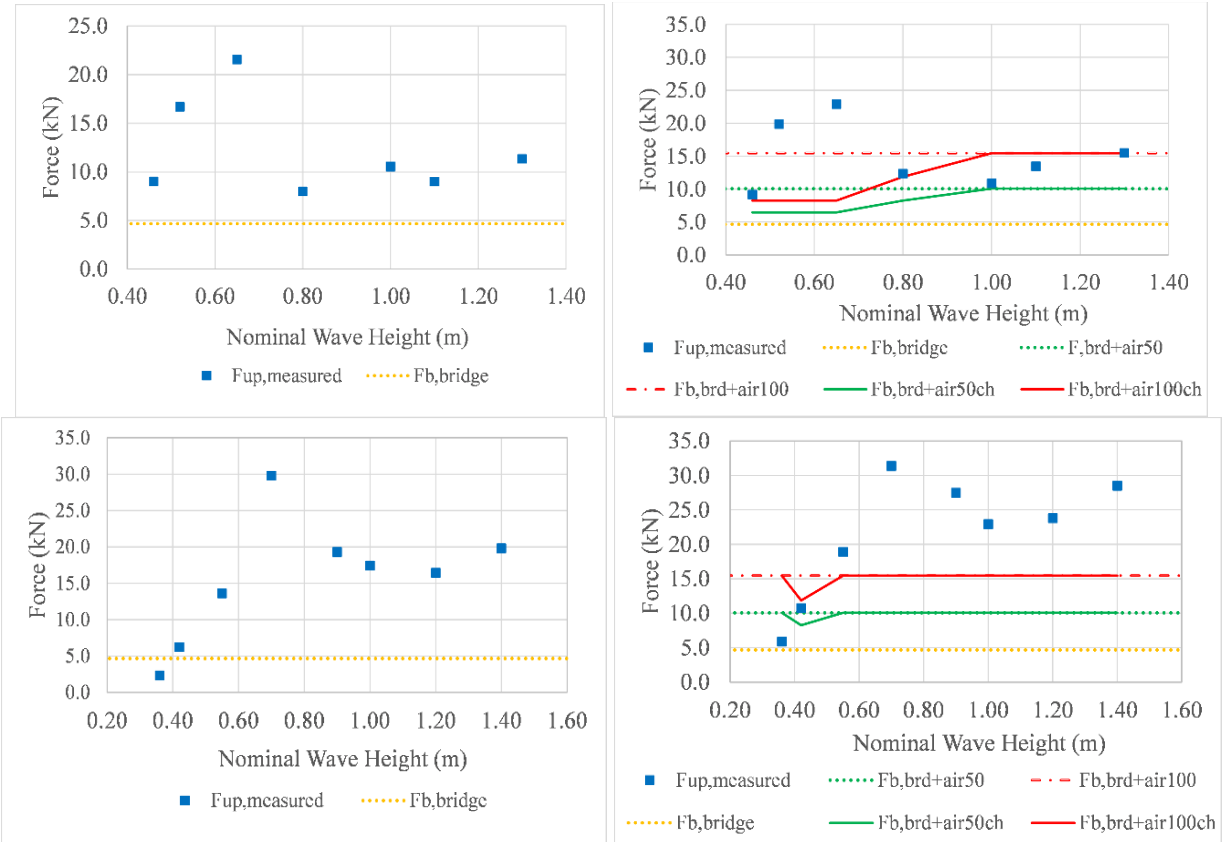


Figure 4.21: Calculated buoyancy and recorded maximum uplift forces for the deck with cross-frames (left) and the one with solid diaphragms (right), for $d=1.90\text{m}$ (top) and $d=2.00\text{m}$ (bottom)

When the actual number of the flooded chambers is used in the calculation of the buoyancy, then as shown in Fig. 4.21 (top-right) it gets closer to the measured hydrodynamic uplift for $d=1.90\text{m}$. However, the mean value of the hydrodynamic uplift to the calculated buoyancy and the CV are still high and equal to 2.04 and 41.6% respectively for the 50% assumption ($F_{b,brd+air50ch}$) or 1.41 and 45.35% respectively for the 100% assumption ($F_{b,brd+air100ch}$). This comparison verifies the inability of the buoyancy to predict the measured uplift and the importance of the hydrodynamic nature of the wave induced loading that a bridge deck has to withstand.

4.4.2. Increase of Uplift Forces vs Buoyancy of Trapped Air

Table 4.9 shows a comparison of the subtraction of the maximum total uplift between the two deck types ($F_{up,ST5}-F_{up,ST2}$) as well as of the quasi-static uplift ($F_{up,qs,ST5}-F_{up,qs,ST2}$), with the calculated buoyancy generated by the trapped air ($F_{b,air}=F_{b,50}$ or $F_{b,100}$). It must be clarified that given the fact that two of the tested wave heights give significantly larger ratios than the rest, the table presents two different values for the mean, with “Mean” considering all the tested wave heights, and “Mean2” considering all the wave heights apart from the two outliers. The major findings emerging from Table 4.6 are the following:

- Assuming that 50% of the volume of the chambers is trapped with air gives a better estimation of the increase of both the total uplift and the quasi-static one witnessed by the deck with solid diaphragms, than the 100% hypothesis. This is true irrespective of whether all three chambers or the actual number of flooded chambers at the time of maximum uplift are considered in the calculation of the buoyancy. The mean value (without the outliers) of the ratios of the uplift increase (in ST5) to the buoyancy generated by the trapped air ($F_{up,ST5}-F_{up,ST2}/F_{b,air}$) is 1.61 and 3.22 for the 50% and 100% assumption respectively.
- Using the actual numbers of the inundated chambers (at the instant that the maximum uplift occurs) in the calculation of the additional buoyancy gives closer results to the measured values than using all three chambers. Switching from the total the actual number of chambers, reduced the mean values from 1.61 to 1.26 and from 3.22 to 2.52 for the 50% and 100% hypotheses respectively. For the quasi-static uplift the respective reductions were from 1.63 to 1.37 and from 3.26 to 2.75.
- The increase of the quasi-static force ($F_{up,qs}$) is better predicted than the increase of the total uplift by the buoyancy generated from the trapped air, with the mean values (that consider the outliers) being 1.75 and 3.49 for $F_{up,qs}$ and 4.72 and 9.45 for F_{up} , for the 50% and 100% assumption respectively and all the chambers inundated. If the two outliers are removed then the F_{up} and $F_{up,qs}$ have very similar mean values, with the former showing even smaller mean values than the latter one. However even in this case the correlation of the increase of $F_{up,qs}$ with the buoyancy of the trapped air is better because than the one of F_{up} , because the coefficient of variation is 30.3% in the former case and 75.1% in the latter one. The reason behind this behavior is the fact that as discussed in previous sections, although the buoyancy of the trapped air increases consistently the quasi-static component of the uplift force, this is not always reflected in the total uplift, because it is also affected by the slamming component, which is not affected by the air-entrapment in a consistent way (can either increase or decrease).

These findings are adding to the body of knowledge regarding the role of air-entrapment. Moreover, they might prove useful for tsunami design of bridges, since they indicate that if the wave induced uplift forces on a deck with cross-frames is known then the uplift of a deck with diaphragms could be estimated by considering the additional uplift coming from buoyancy of the trapped air.

Table 4.9: Comparison of the Calculated Buoyancy Forces with the Measured Uplift Forces on the Deck with Cross-frames (ST2) and the one with Diaphragms (ST5)

H (m)	Fup ST5- ST2	Buoyancy, Fb		(Fup,ST5-Fup,ST2)/Fb				(Fup,qs,ST5-Fup,qs,ST2)/Fb			
		Actual chamb.		All chamb.		Actual chamb.		All chamb.		Actual chamb.	
		Fb,50	Fb,100	Fb,50	Fb,100	Fb,50	Fb,100	Fb,50	Fb,100	Fb,50	Fb,100
		(kN)	(kN)								
0.46	0.16	1.80	3.60	34.76	69.53	11.59	23.18	3.01	6.03	1.00	2.01
0.52	3.18	1.80	3.60	1.70	3.39	0.57	1.13	1.78	3.56	0.59	1.19
0.65	1.36	1.80	3.60	3.97	7.93	1.32	2.64	1.32	2.63	0.44	0.88
0.80	4.38	3.60	7.19	1.23	2.46	0.82	1.64	2.35	4.70	1.57	3.13
1.00	0.36	5.40	10.79	15.16	30.31	15.16	30.31	1.98	3.96	1.98	3.96
1.10	4.48	5.40	10.79	1.20	2.41	1.20	2.41	2.20	4.39	2.20	4.39
1.30	4.18	5.40	10.79	1.29	2.58	1.29	2.58	0.90	1.79	0.90	1.79
0.36	3.50	5.40	10.79	1.54	3.08	1.54	3.08	2.34	4.68	2.34	4.68
0.42	4.61	3.60	7.19	1.17	2.34	0.78	1.56	1.52	3.04	1.01	2.03
0.55	5.48	5.40	10.79	0.98	1.97	0.98	1.97	1.50	3.00	1.50	3.00
0.70	1.14	5.40	10.79	4.71	9.43	4.71	9.43	2.35	4.71	2.35	4.71
0.90	8.19	5.40	10.79	0.66	1.32	0.66	1.32	1.30	2.59	1.30	2.59
1.00	5.47	5.40	10.79	0.99	1.97	0.99	1.97	1.29	2.58	1.29	2.58
1.20	6.25	5.40	10.79	0.86	1.73	0.86	1.73	1.13	2.26	1.13	2.26
1.40	8.61	5.40	10.79	0.63	1.25	0.63	1.25	1.25	2.49	1.25	2.49
			Mean	4.72	9.45	2.87	5.75	1.75	3.49	1.39	2.78
			Mean2	1.61	3.22	1.26	2.52	1.63	3.26	1.37	2.75
			SD	1.21	2.42	1.04	2.08	0.49	0.99	0.59	1.18
			CV(%)	75.1	75.1	82.5	82.5	30.3	30.3	43.1	43.1

4.5 PRACTICAL RECOMMENDATIONS FOR ENGINEERING DESIGN

4.5.1 Total Deck Uplift

An important finding to emerge in this study is the existence of a complex interaction between the trapped air (underneath an elevated deck) with extreme waves, especially tsunami-like bores, which makes it challenging to accurately predict the effect of air on the wave induced loading on an open-girder deck and even more challenging on the individual structural components that support the deck. To decipher this complex interaction further research is necessary. In the meantime, in an attempt to provide a simple and practical approach for estimating the role of air, the previous section calculated and compared the buoyancy of the bridge with the maximum hydrodynamic uplift forces measured in the large-scale experiments. The results revealed that the buoyancy of the bridge cannot give a good estimate of the maximum hydrodynamic uplift applied neither on decks with cross-frames nor on decks with solid diaphragms. On the other hand, interestingly the additional buoyancy generated by the air that is trapped between the solid diaphragms, can give a reasonable estimate of the increase of the uplift force between a deck with cross-frames and one with solid diaphragms.

The above finding can be useful from a design point of view because it indicates that if the uplift force on a deck with cross-frames is known (e.g. from simplified predictive equations or single-phase incompressible computational fluid analyses (CFD)) then the maximum uplift on a deck with solid diaphragms can be estimated via the simple calculation of the additional buoyancy, avoiding consequently the need to conduct more complex two-phase compressible CFD analyses in order to understand the actual dynamic interaction of a bore with the air, and the induced forces. This approach can be useful during the preliminary design phase where the engineer has to decide the bridge type (e.g. composite bridge with steel girders and cross-frames or reinforced/pre-stressed concrete with diaphragms), because in reality although the decks with diaphragms are going to witness increased uplift forces due to the trapped air, they might be heavier and thus having a larger counter-acting weight. In such cases, the final decision regarding the bridge type will be made based on optimization of performance and cost, as it is usually the case with the design of such structures against other natural hazards (e.g. earthquakes).

The previous section also demonstrated that due to the complex temporal and spatial evolution of the wave loading during the bridge inundation, the maximum hydrodynamic uplift can occur at different time instants for different wave heights, where a different number of chambers has been flooded. Using the actual number of flooded chambers for the calculation of the buoyancy of the trapped air, the estimation of the increase of the hydrodynamic uplift becomes more accurate. However, since this information is not available unless CFD analyses or hydrodynamic experiments have been conducted, for design purposes it can be assumed that all the chambers of a deck are flooded and that 50% of their volume is filled with air. This percentage is recommended because it gave the best overall prediction in terms of a mean value for all the waves tested in this study, however it must be clarified that it did not give a conservative value for all wave heights. In fact for some of the largest bores, it under-predicted the uplift. For a conservative estimate, engineers could assume 100% of the volume of the chambers to be filled with air, however this case can lead to significant over-prediction of the effect of air. Therefore,

a percentage between 50% and 100% might be the optimum solution, which will be both conservative and as economical as possible.

4.5.2 Non-Dimensional Uplift Curves for Bearings and Connections

The majority of the studies conducted to date have focused on the total forces that extreme waves apply on structures, and several studies have developed simplified predictive equations for both the maximum horizontal (F_h) and uplift (F_{up}) forces. However, as discussed previously more recent research (e.g. Istrati et al., 2018)) has emphasized the need to examine the effects on individual structural components and connections, and provide guidance on the maximum forces for which these components have to be designed in order to be able to withstand extreme events such as tsunamis. To this end, it was deemed beneficial to calculate the non-dimensional ratios of the maximum uplift force measured in each bearing set ($F_{up,brngs,G_i}$) and column set ($F_{up,col,i}$) to the maximum total deck uplift ($F_{tot,up}$), and the results for the deck with cross-frames are presented in Fig. 4.22, for all the tested solitary waves and bores. It must be clarified that each set of bearings (or columns) consists of two separate bearings (or columns), corresponding to the two bent caps that support the superstructure. The figure verifies that the bearings of the offshore girders (G1 and G2) attract the largest percentage of the total uplift consistently irrespective of the wave height, with the latter one reaching about 57% of F_{up} for solitary waves and 60% for bores. This is an alarming finding because it demonstrates that the common assumption of distributing the tsunami uplift force to all the bearings –in which case each bearing set would get about 25% of the deck uplift- is not accurate. This trend is also true for the columns, with the offshore columns attracting the largest percentage of the total uplift, which reached 79% of $F_{tot,up}$ for solitary waves and 90% for bores in the hydrodynamic experiments.

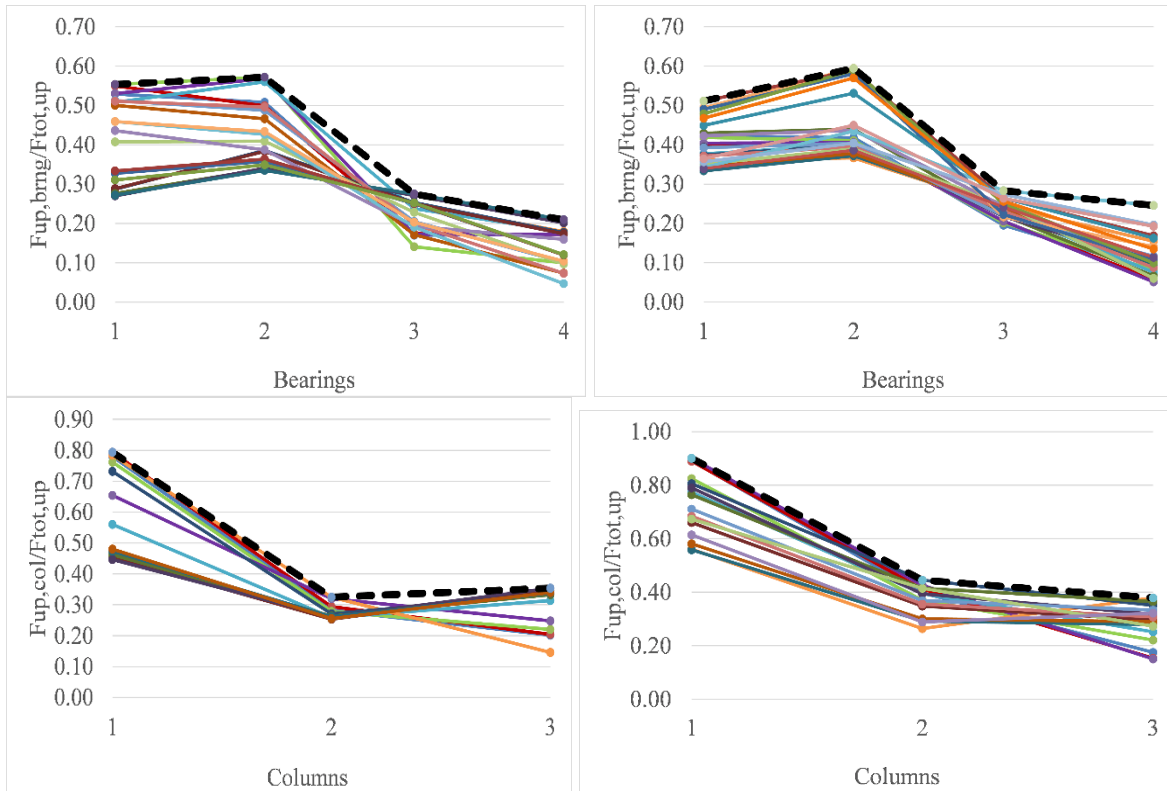


Figure 4.22: Maximum normalized uplift forces in bearings (top) and columns (bottom) of the deck with cross-frames, for all the solitary waves (left) and bores (right) tested in the flume

Figure 4.23 shows the envelopes of the ratios $(F_{up,brngs,Gi}/F_{tot,up})$ and $(F_{up,col.i}/F_{tot,up})$ for both deck types. Interestingly, despite the significant differences between the wave-structure interaction and forces introduced by solitary waves and bores, the envelopes of the two wave types are very similar for the deck with cross-frames (ST2), with the bores tending to yield larger values than the solitary waves. This indicates that from a design point of view the bearings, columns and connections could be designed for a certain level of uplift even if the exact wave type is not known. For the deck with solid diaphragms, the differences between the non-dimensional envelopes of the two wave types are more significant, and show opposite trends than the deck with cross-frames, with the bores introducing smaller percentages of the uplift forces in the offshore components than the solitary waves. The larger differences between the two wave types in the deck with solid diaphragms could be attributed to complex effect of the trapped air, which as seen in previous sections is different for solitary waves and bores. Surprisingly, although the trapped air in ST5 was seen to increase the total deck uplift ($F_{tot,up}$), it decreased the percentage of the uplift forces in the offshore bearings, which reached about 50% for the deck with solid diaphragms and 60% for the one with cross-frames.

To translate the above findings into practical information for engineers Fig. 4.24 presents normalized uplift forces for all the bearings and both deck types, which could potentially be used for design purposes. For each deck type, two different curves have been developed. In design alternative 1, all the bearings sets upstream of the center of the gravity (G1 and G2) are designed

for the same high level of uplift, which is 60% for deck ST2 and 50% for ST5, while the bearings downstream the CG are designed for a smaller percentage, which is 28% and 26% for the two deck types respectively. In design alternative 2, all bearings are designed for the same level of uplift (60% for ST2 and 50% for ST5, for each set of bearings). Although the first alternative results in a reduced bearing cost since half of the bearings will have a smaller size, the second approach is more conservative and easier from a construction point of view because all bearings will be identical. It is up to the engineer to decide the best approach, however it must be clarified that (a) the above percentages and non-dimensional design curves were developed using the measured experimental data, which means that for design purposes they should be scaled using a safety factor to account for the unknowns, and (b) the limitations described in the next section can affect the presented values, which might have to be modified depending on the bridge location and design conditions.

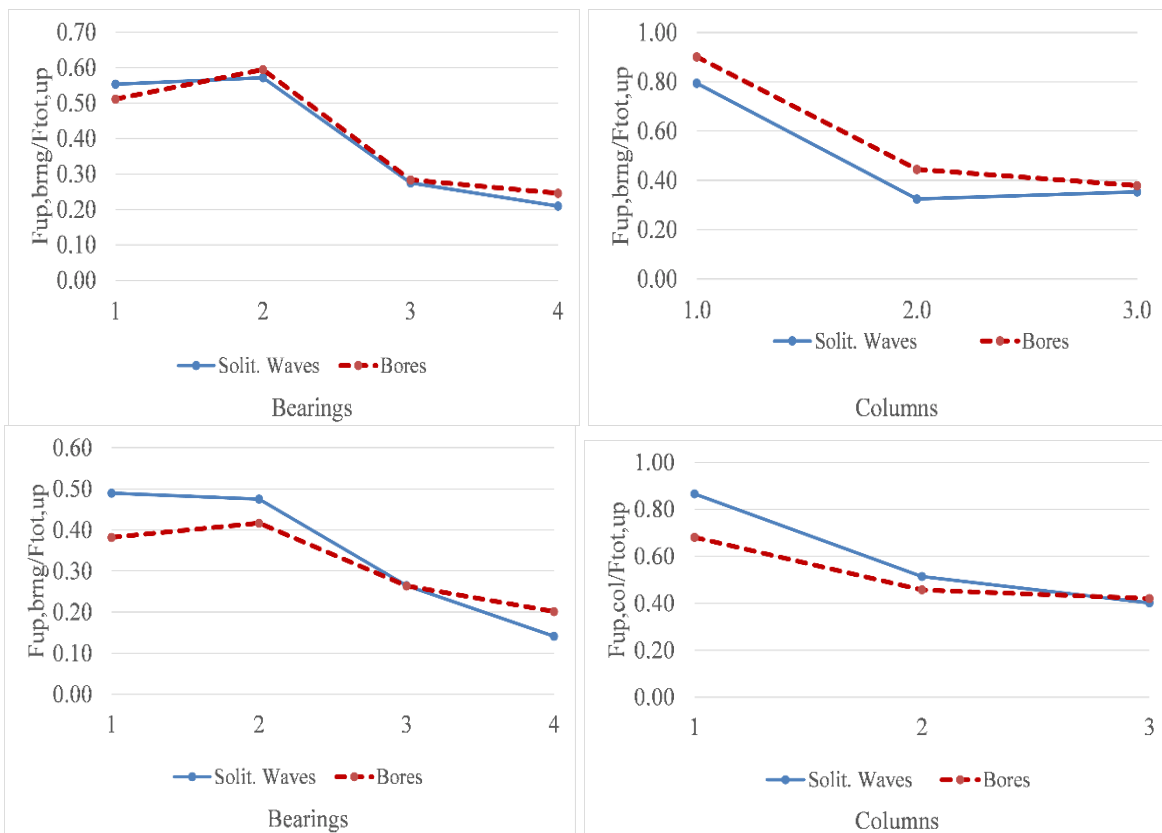


Figure 4.23: Envelopes of maximum normalized uplift forces in bearings (left) and columns (right) of the deck with cross-frames (top) and the one with solid diaphragms (right)

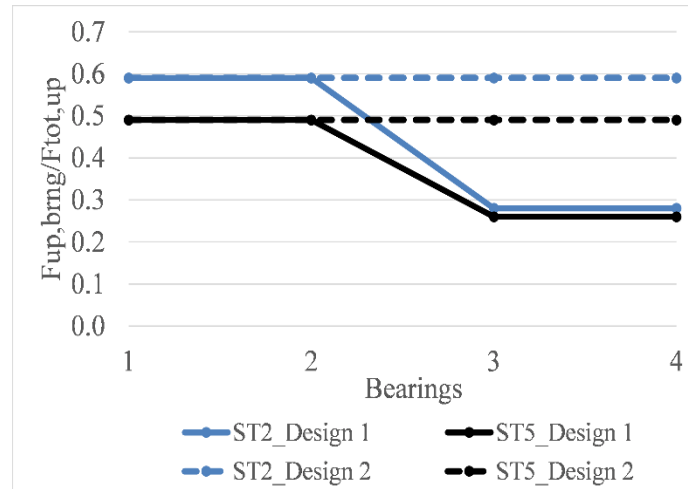


Figure 4.24: Non-dimensional design curves for the elastomeric bearings and connections of open-girder decks with cross-frames (ST2) and solid diaphragms (ST5)

4.5.3 Limitations

The current chapter has advanced the understanding of the role of air trapped beneath open girder decks and has provided practical information for engineers. However, this information and the above non-dimensional design curves are limited to:

- Elastomeric bearings. For other type of bearings (e.g. steel bearings), the readers can use the information provided in (Istrati et al., 2018).
- Bridges with four or more girders. Although in the experiments, the deck had four girders, the non-dimensional curves could potentially be used for a larger number of girders, since in this case the actual ratios are expected to be smaller.
- Deck with similar dimensions and dimension ratios (girder height to deck width, overhang width to deck width) as the one tested in the experiments, and without rails. For example, if a deck has a larger girder height or the same height but solid rails, then the moment arm of the horizontal force (F_h) will increase, which would consequently increase the overturning moment resulting in increased uplift in the offshore bearings and other structural components.
- The curves of the design alternative 1 presented in Fig. 4.24, which show reduced design values for all the bearings on the onshore side of the deck CG have been developed for the scenario in which the tsunami flows only in one direction. In reality though, the tsunami will flow in two directions, one direction when it initially impacts and inundates the coast, and the opposite direction when the tsunami retracts back to the ocean. This means that during the reverse flow the onshore bearings will witness larger uplift forces than the offshore ones, but it is unclear if they will be larger than the 28% of the $F_{tot,up}$ applied during the first impact of the bore on the offshore side of the deck. Therefore, future research should examine the effects of the reverse flow,

especially given the fact that in such a case significant debris can accumulate on the onshore side of the deck.

The findings and conclusions presented herein were reached based on (1:5) scaled experiments of tsunami impact on bridge decks, however the results might still be subjected to scale effects, which means that additional modifications might be required in order make the results applicable to full-scale bridges. Moreover, the non-dimensional design curves are applicable only to bearings and no other structural components below the bearings, such as columns and foundations. For such components the uplift demand is expected to be governed by the overturning moment generated mainly by the horizontal tsunami load, which could yield uplift forces in the members e.g. at the bottom of the offshore column or in the offshore piles, with magnitudes several times higher than the total deck uplift. Therefore, for the design of these bridge members, engineers are advised to conduct structural analyses using load cases similar to the ones described in (Istrati et al., 2018). Last but not least, in the concept of tsunami design guidelines the non-dimensional curves will have to be scaled up in order to account for possible unknowns and uncertainties generated by different sources, such as the fact that they were developed based on (i) a limited number of wave heights, (ii) results from scaled experiments, and (iii) without consideration of the effect of debris and reverse flow.

5.0 TSUNAMI PERFORMANCE OF BOX-GIRDER BRIDGES

5.1 INTRODUCTION

This chapter will focus on the experimental results for a box-girder bridge in an attempt to understand the tsunami effects on this type of bridge. In addition, the behavior the box-girder bridge (ST6) will be compared to the behavior of an I-girder bridge with diaphragms in order to see how the addition of the soffit is affecting the wave-structure interaction and the tsunami forces that the bridge has to withstand. The last part of the chapter will present a comparison of three different types of bridges – an I-girder bridge with cross-frames (ST2), an I-girder bridge with diaphragms (ST5) and a box-girder bridge (ST6) - in an effort to advance the understanding of tsunami effects relative to the bridge type.

The bridge configuration presented in this chapter - called ST6 - was built on top of ST5 (presented in the previous chapter), which had the diaphragms, with the addition of thick plywood sheets at the bottom of the girders, forming a soffit and mimicking the geometry of a box-girder. Douglass Fir Marine plywood with 0.5in thickness was used in order to ensure strength and minimal deflections during the tsunami inundation. The sheets were attached to the girders with special nails that were drilled into the girders. Waterproof nuts were used for these connections and additional foam and caulk was added between the plywood sheets and the connections to prevent the water from entering the chambers. This box-girder configuration is shown in Figures 5.1 during the pre-test assembly in the Large-Scale Structures Laboratory at UNR, and in Figure 5.2 during the set-up in the O.H. Hinsdale Laboratory at OSU. It must be noted that pressure gages had been installed inside the chambers to check if additional pressure was generated during the impact of waves on the soffit, which would indicate the penetration of the soffit by the tsunami wave. Additional pressure gages were also installed below the overhang, on the offshore girder and at the bottom of the soffit in two different locations as shown in Figure 5.3.



Figure 5.1: Box-girder bridge during the pre-test assembly phase in the Large-Scale Structures Laboratory at the University of Nevada, Reno



Figure 5.2: Assembly of the box-girder bridge in the O.H. Hinsdale Large Wave Flume at Oregon State University



Figure 5.3: Box-girder Bridge with attached instrumentation ready for testing in the O.H. Hinsdale Large Wave Flume at Oregon State University

5.2 FORCE AND PRESSURE ON A BOX-GIRDER FOR SOLITARY WAVES AND BORES

To decipher the fundamental differences between the effects caused by solitary waves and bores during the inundation of box-girder bridges, this sub-section will compare experimental results from three solitary waves and three bores. The three solitary waves have input wave heights equal to 0.36m, 0.42m and 0.65m, while the bores have wave heights equal to 0.90m, 1.00m and 1.20m. Figure 5.4 shows the total horizontal force in the link and the total vertical force in the bent cap-to-piers connections for the six waves. According to this figure, there are two fundamental differences between the forces caused by the two different types of waves when inundating a box-girder bridge. The first and difference lies in the fact that the force histories of the solitary waves have one main uplift peak, while the respective forces of the bores have two

clear peaks, one in Phase 1 and another one in Phase 3. The second difference is the fact that for solitary waves the maximum uplift occurs in Phase 2 –apart from $H=0.70\text{m}$ that occurs in Phase 3- while for bores it always occurs in Phase 3 where the wave applies pressure on the whole soffit. Figure 5.5 is also revealing that for solitary waves the maximum vertical forces in the offshore bearings take place in Phase 2 where both a rotation and vertical translation of the bridge occurs introducing tension in most bearings, while for bores the maximum occurs always in Phase 1 (at the initial impact)

Another difference between the two types of waves can be spotted in Figure 5.6 that shows the pressures applied on the overhang and on the soffit at the location of the offshore and middle chamber. Indeed, as was observed in the previous section for one particular solitary wave height and is now verified for all solitary waves, the pressures on the soffit are starting to develop before the wave reaches the overhang. This is not true for the bores and this is because the bores are have a different wave shape that the solitary waves. Interestingly, for the bores the pressures on the soffit are smaller than the pressure on the overhang, however since they are applied on a larger area they seem to result in the largest uplift force which occurs in Phase 3. This is verified in Figure 5.7, where the plot of the normalized pressures and forces is demonstrating that for solitary waves the pressures on the soffit start developing faster than for bores contributing to the total force which occurs in Phase 2, while for bores the pressures start increasing after the pressure on the overhang is maximized and therefore are introducing the max uplift in Phase 3.

Figure 5.8 is showing the maximum vertical forces recorded in the bearings of all the girders, with location 1 corresponding to the offshore girder and location 4 to the onshore one. As was observed for other bridge types and it seems to be true for box-girders as well, the offshore bearings and the bearing next to them are attracting vertical forces significantly larger than the rest of the bearings. In fact, as shown in Table 5.1 the maximum forces in the offshore bearings can be larger than the ones in the onshore bearings by up to a factor of 2.5.

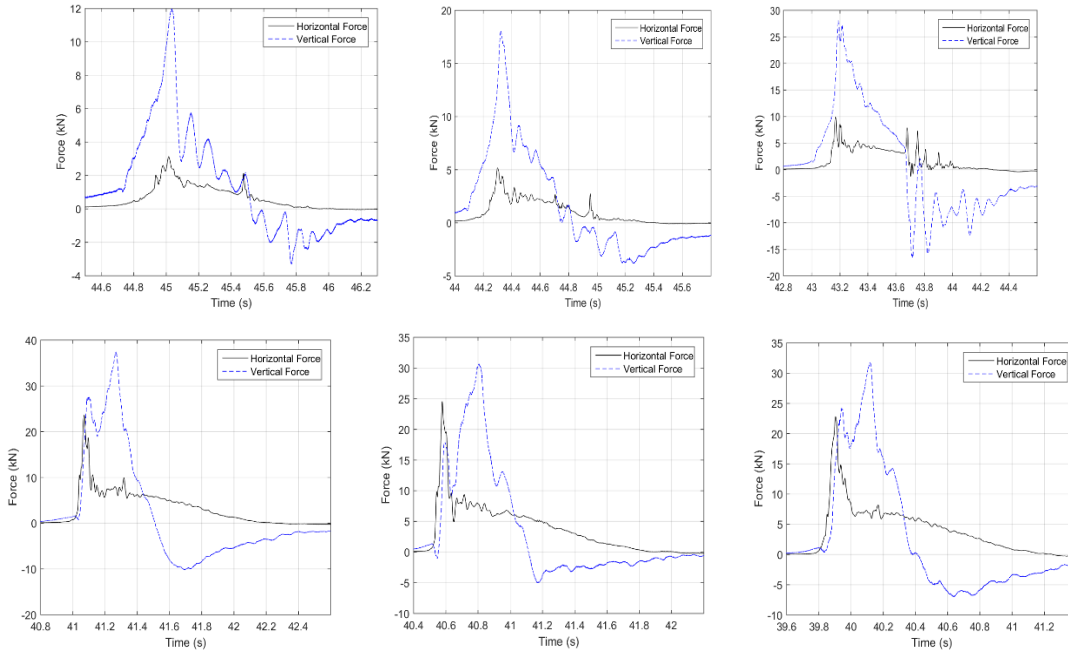


Figure 5.4: Horizontal and vertical forces for (a) solitary waves (top) with $H=0.36\text{m}$ (left), $H=0.42\text{m}$ (middle) and $H=0.55\text{m}$ (right), and (b) bores (bottom) with $H=0.90\text{m}$ (left), $H=1.00$

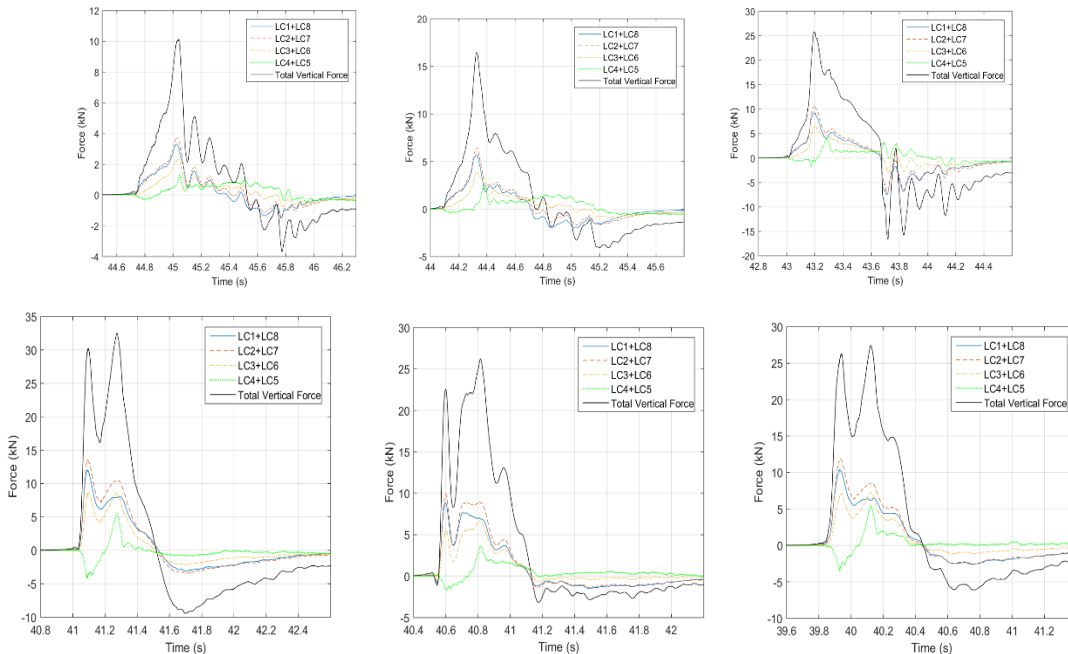


Figure 5.5: Vertical forces in bearings for (a) solitary waves (top) with $H=0.36\text{m}$ (left), $H=0.42\text{m}$ (middle) and $H=0.55\text{m}$ (right), and (b) bores (bottom) with $H=0.90\text{m}$ (left), $H=1.00\text{m}$ (middle) and $H=1.20\text{m}$ (right) for the box-girder bridge (ST6)

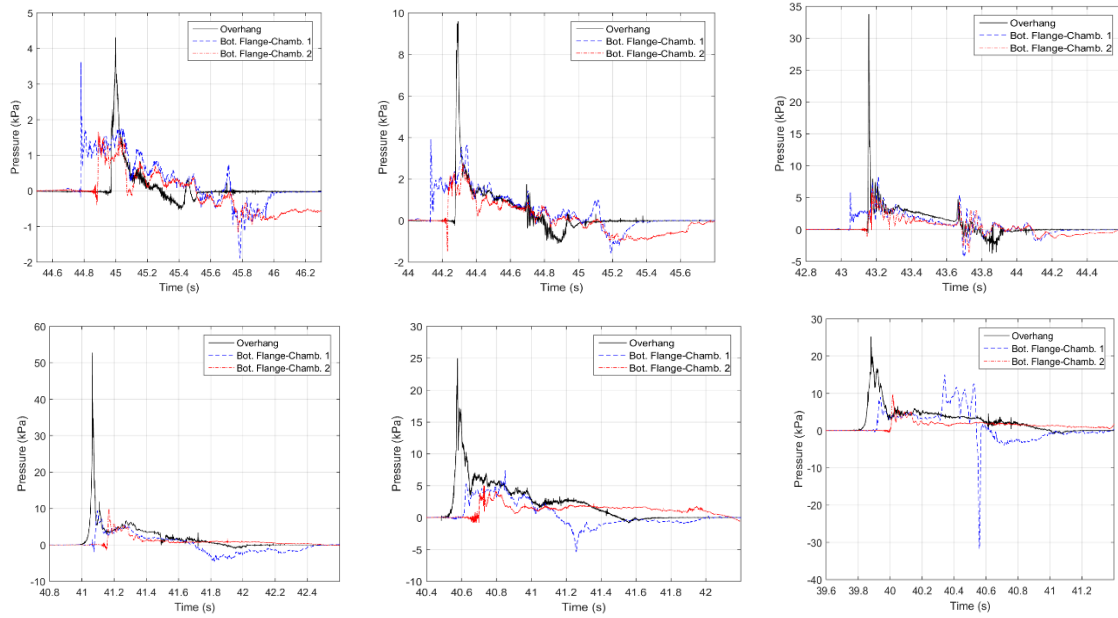


Figure 5.6: Pressures under the overhang and the soffit for (a) solitary waves (top) with $H=0.36\text{m}$ (left), $H=0.42\text{m}$ (middle) and $H=0.55\text{m}$ (right), and (b) bores (bottom) with $H=0.90\text{m}$ (left), $H=1.00\text{m}$ (middle) and $H=1.20\text{m}$ (right) for the box-girder bridge (ST6)

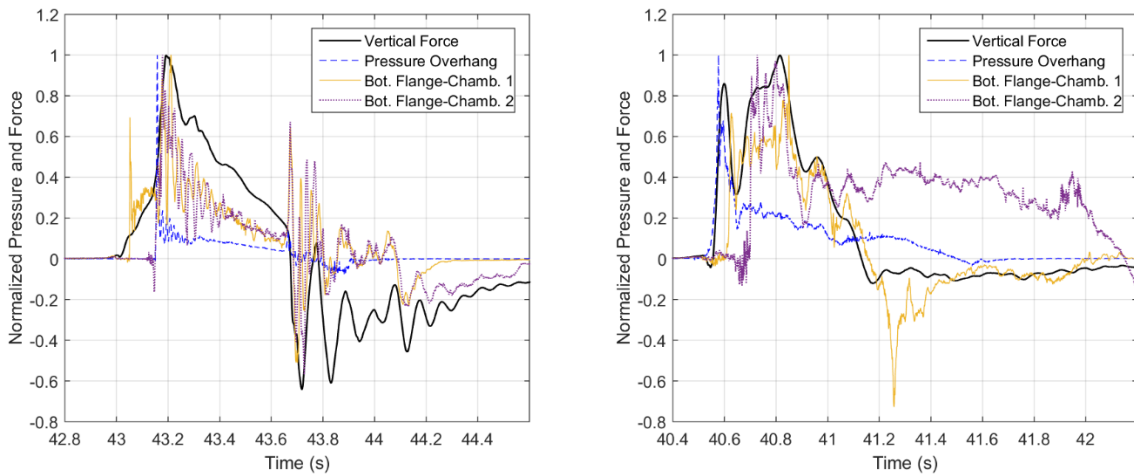


Figure 5.7: Normalized pressures below the deck and normalized total vertical force in the bearing connections for a solitary wave with $H=0.55\text{m}$ (left) and a bore with $H=1.00\text{m}$ (right) for the box-girder bridge (ST6)

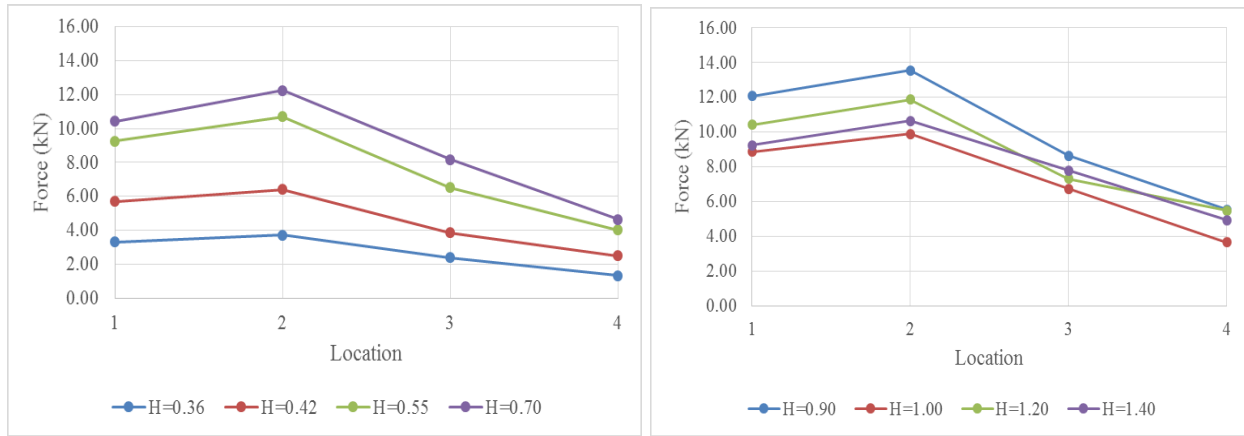


Figure 5.8: Maximum uplift forces in the bearings for solitary waves (left) and bores (right) for the box-girder bridge (ST6)

Table 5.1: Maximum vertical forces recorded in offshore and onshore bearings

H_{input}	Depth	Offshore	Onshore	Ratios Offshore/Onshore
(m)	(m)	(kN)	(kN)	
0.36	2.00	3.31	1.33	2.49
0.42		5.71	2.50	2.28
0.55		9.26	4.02	2.30
0.70		10.42	4.64	2.25
0.90		12.07	5.52	2.19
1.00		8.86	3.64	2.43
1.20		10.42	5.49	1.90
1.40		9.23	4.92	1.87

5.3 TSUNAMI FORCES ON DIFFERENT BRIDGE SUPERSTRUCTURES: I-GIRDER VS BOX-GIRDER

5.3.1 Connection forces and deck rotation histories

This section will present a comparison of all three bridge types that were presented in the previous sections. Figure 5.10 is showing the horizontal forces in the link, the vertical forces in the offshore bearings and the total vertical force in the bearings for the three types of bridges, namely the I-girder bridge with cross-frames (ST2), the bridge with diaphragms (ST5) and the box-girder bridge (ST6), both for a solitary wave with $H=0.42\text{m}$ and a bore with $H=0.90\text{m}$. This graph demonstrates that both the air-entrapment and the existence of the soffit slab associated with bridge cases ST5 and ST6 respectively, are changing the wave-structure interaction resulting in the modification of the vertical forces histories - the total ones and the ones in the bearings- and the significant increase of the uplift force. The air-entrapment in ST5 is mainly affecting Phase 2 for the solitary waves and Phase 3 for the bores, while the existence of the soffit slab in ST6 is increasing the forces mainly in Phase 2 for solitary waves and Phase 1 and 3

for bores. Among all three-bridge types, the box-girder bridge is witnessing the largest uplift force. The different vertical force patterns and the increase of the magnitudes with the addition of the diaphragms and of the soffit are also observed in the total vertical forces recorded in the columns of the piers and in the forces of the onshore columns, shown in Figure 5.10 and 5.11 respectively. Both bridge case ST5 and ST6 are witnessing larger quasi-static uplift forces than ST2 for both solitary waves and bores and longer durations, as shown in Figure 5.12, with the exact amount of elongation depending on the wave type and wave height.

Regarding the horizontal forces, shown in Figure 5.13, all bridge types seem to be witnessing similar maximum values which occur at the initial impact of the waves on the offshore girder, but different patterns after Phase 1, with the bridge with diaphragms having smoother peaks than the bridge with cross-frames due to the existence of the trapped air and its compressibility, and the box-girder bridge having the smoothest and least amount of peaks due to lack of wave impact on the interior and onshore girders.

The variation of the tsunami effects and the wave-structure interaction for the different bridge types is also documented in Figure 5.13 where the bridge response in terms of deck rotation is increased with the addition of the diaphragms and even more significantly with the addition of the soffit slab for all solitary waves and bores. In addition, for the bores the deck rotation has a total different pattern for cases ST5 and ST6.

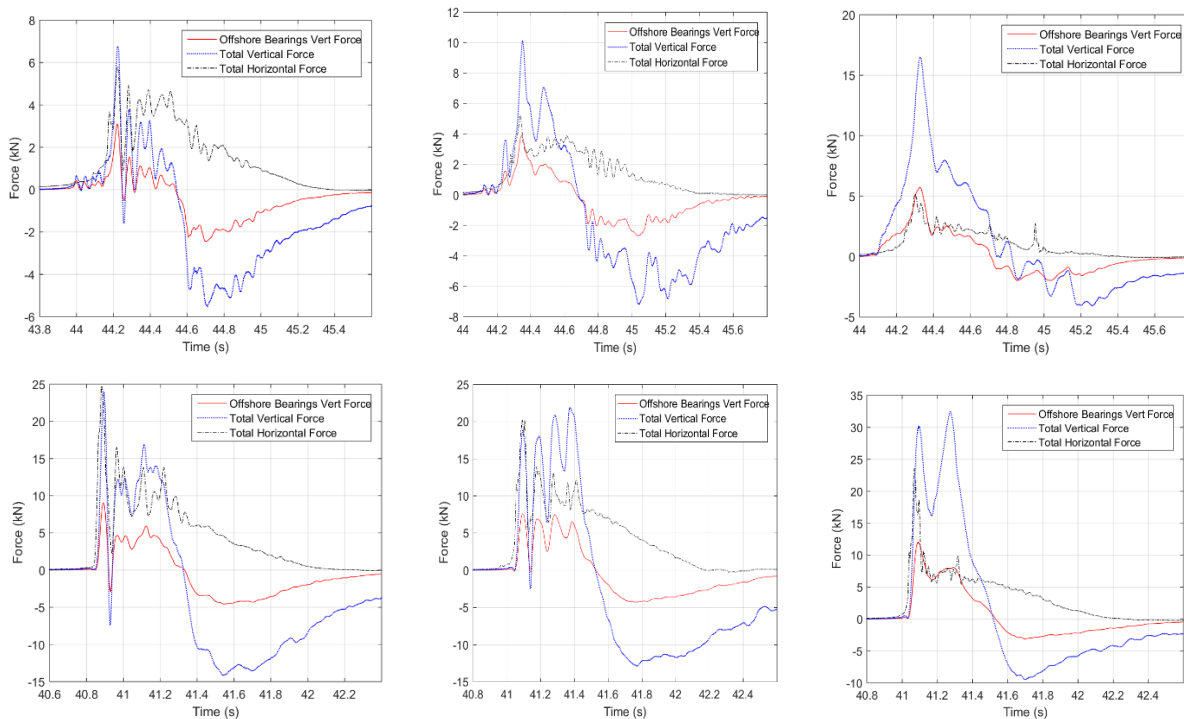


Figure 5.9: Forces in bearings and links for bridge configurations ST2 (left), ST5 (middle) and ST6 (right) for $H=0.42\text{m}$ (top) and $H=0.90\text{m}$ (bottom)

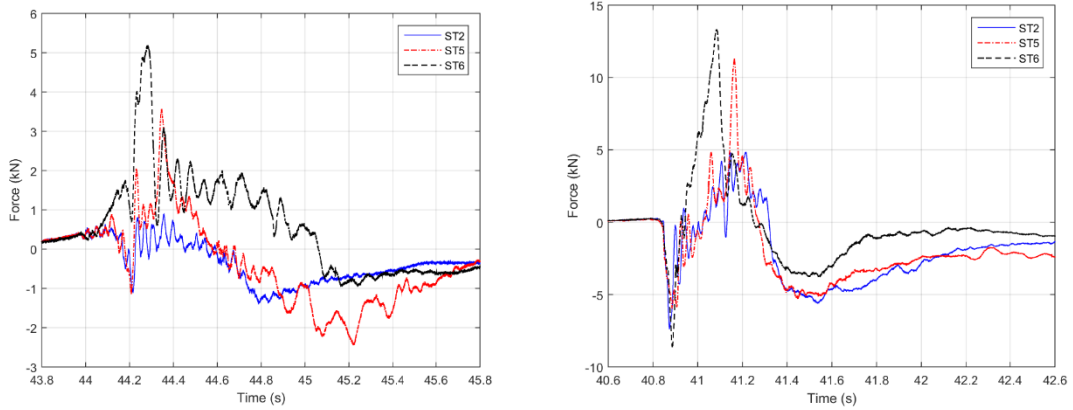


Figure 5.10: Total vertical forces for H=0.42m (left) and H=0.90m (right) for three bridge types

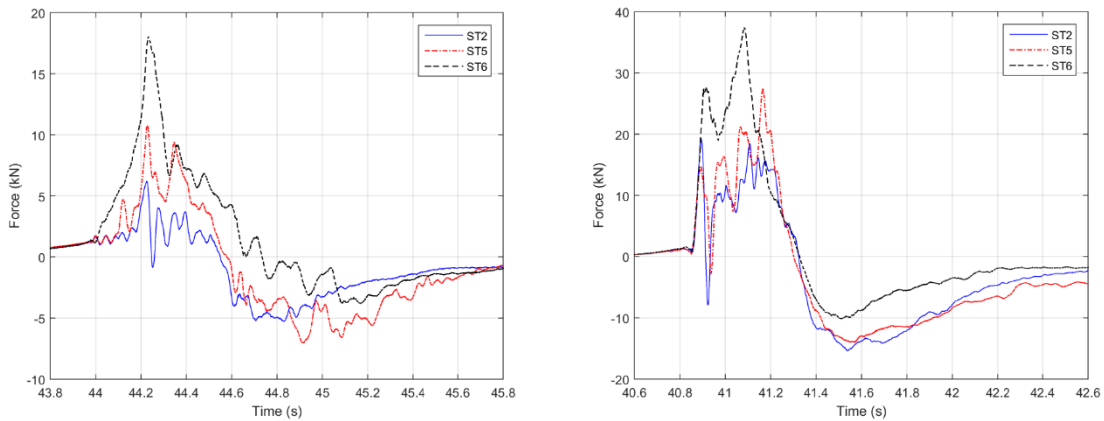


Figure 5.11: Vertical forces in offshore columns of piers for H=0.42m (left) and H=0.90m (right)

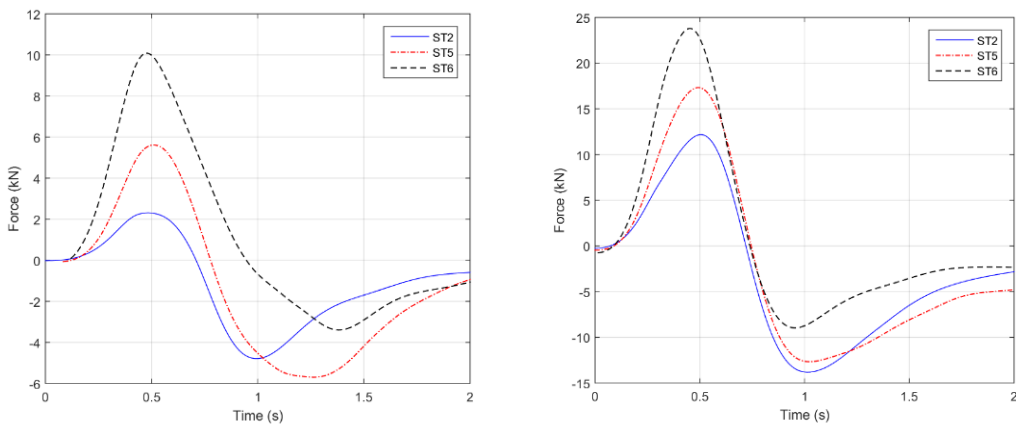


Figure 5.12: Quasi-static vertical forces for H=0.42m (left) and H=0.90m (right) for three bridge types

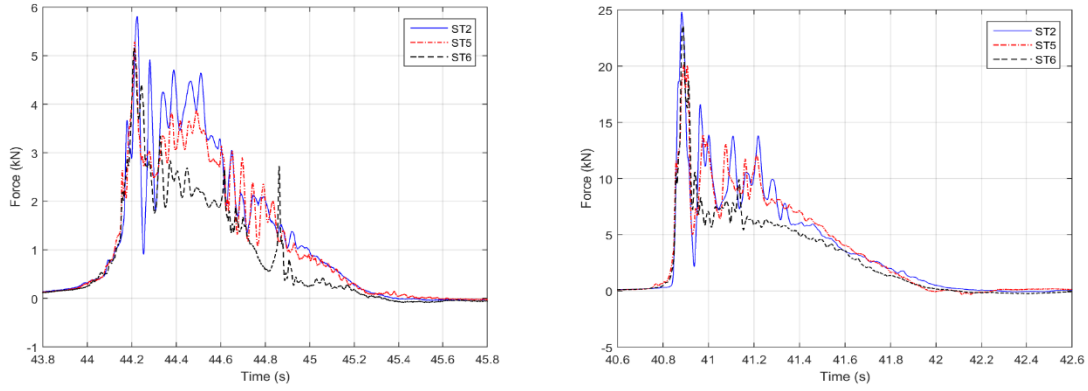


Figure 5.13: Total horizontal forces in links for H=0.42m (left) and H=0.90m (right) for the three bridge types

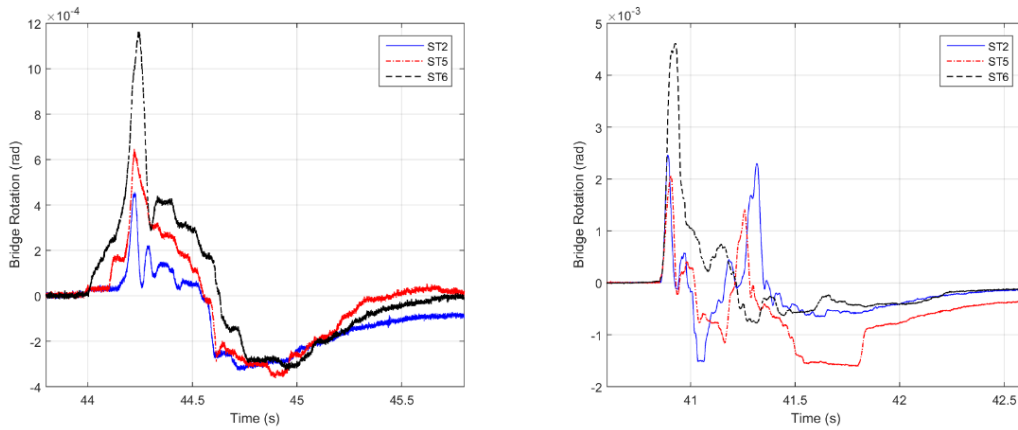


Figure 5.14: Deck rotation for H=0.42m (left) and H=0.90m (right) for the three bridge types

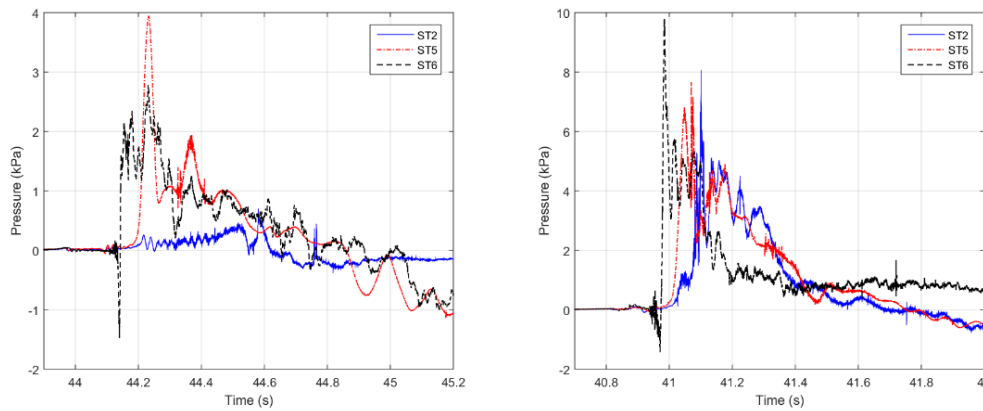


Figure 5.15: Pressure at the middle chamber for H=0.42m (left) and H=0.90m (right) for the three bridge types

Regarding the pressures applied on the bridge at the location of the middle chamber, as shown in Figure 5.15, the bridge with diaphragms is witnessing the smoothest peaks and the largest magnitude for solitary waves. For bores all three bridge types are witnessing multiple impulsive pressure peaks and the maximum pressures are witnessed either by ST5 or ST6 depending in the bore height and demonstrating the more complex interaction of the turbulent bores with the bridges compared to the solitary waves.

5.3.2 Maximum deck uplift and uplift forces in individual bearings

Figure 5.16 is showing the maximum values of the uplift forces for all bridge types, together with the weight of the bridge. For all the bores (H larger than 0.70m in the figure) and for most of the solitary waves the uplift wave force is exceeding the weight of the bridge by up to a factor of 3 for the box-girder and the largest solitary wave with $H=0.70\text{m}$ and the bore with $H=0.90\text{m}$. The bridge with diaphragms has to withstand larger total uplift forces than the one with cross-frames and the box-girder has to withstand the largest total uplift among all bridge types. As shown in Table 8.8, the bridge with diaphragms has to withstand up to 2.52 times larger uplift forces than the bridge with cross-frames and the box-girder bridge up to 5.15 times.

As shown in Figures 5.17 and 5.18 in addition to the largest total uplift forces, the box-girder bridge is witnessing also the largest forces in the offshore and onshore bearings as well as in the offshore and onshore columns of the piers –only exception is the bore with $H=1.0\text{m}$ for which bridge case ST5 gives slightly larger forces in the onshore columns than bridge case ST6. This effect is a result of the fact that the box-girder bridge is subjected to the largest rotation (moment) –which occurs in Phase 1 for bores and Phase 2 for solitary waves- and the largest vertical translation (uplift force) –which occurs in Phase 3- among the three bridge types, as shown in Figure 5.19.

Although the effect of the soffit slab is clear, the effect of the air-entrapment on the wave-structure interaction, induced forces and bridge response is much more complex, variable and harder to decipher. The air-entrapment does increase the total uplift force for all wave heights and it does consistently increase the vertical forces in the onshore columns of the piers for all waves –since it increases the maximum quasi-static component that occurs in Phase 3- however, its effect on the rest of the bearings and columns is variable and dependent on the wave type and wave height. Especially for bores the role of air-entrapment is more variable than for solitary waves. One of the most important outcomes from this comparison is that although the air-entrapment occurring in the bridge with diaphragms is increasing the total uplift forces, its effect on the forces that each bearing has to withstand is not known a priori.

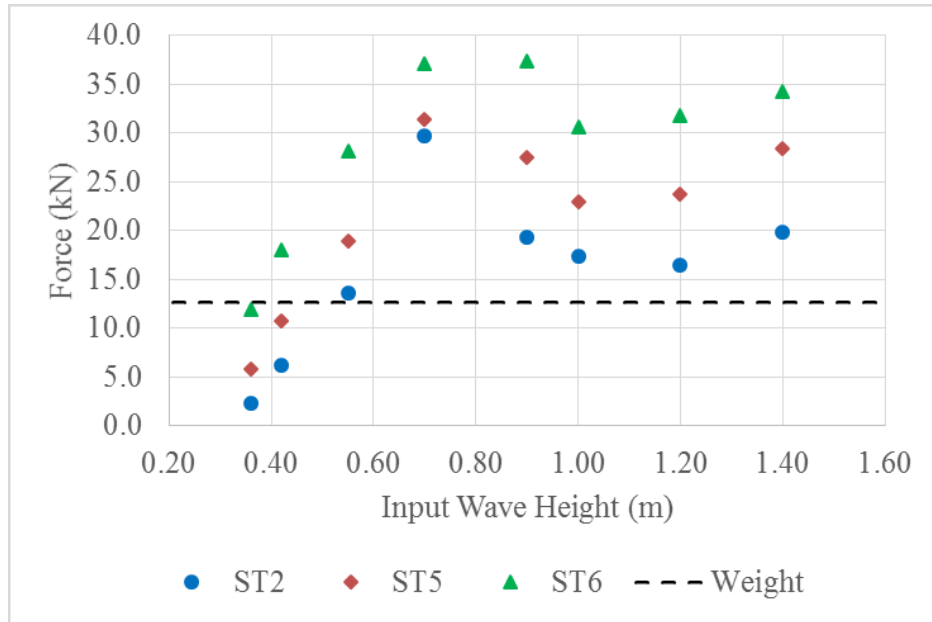


Figure 5.16: Maximum total uplift forces for bridge cases ST2, ST5 and ST6 and $d=2.0\text{m}$

Table 5.2: Maximum Uplift Forces for Bridge Types ST2, ST5 and ST6 and $d=2.0\text{m}$

Solitary waves						
H_{input}	ST2	ST5	ST6	Ratios ST5/ST2	Ratios ST6/ST2	Ratios ST6/ST5
(m)	(kN)	(kN)	(kN)			
0.36	2.33	5.87	11.99	2.52	5.15	2.04
0.42	6.23	10.74	18.04	1.73	2.90	1.68
0.55	13.61	18.93	28.13	1.39	2.07	1.49
0.70	29.79	31.39	37.15	1.05	1.25	1.18
Bores						
H_{input}	ST2	ST5	ST6	Ratios ST5/ST2	Ratios ST6/ST2	Ratios ST6/ST5
(m)	(kN)	(kN)	(kN)			
0.90	19.29	27.48	37.38	1.42	1.94	1.36
1.00	17.45	22.95	30.67	1.32	1.76	1.34
1.20	16.43	23.79	31.77	1.45	1.93	1.34
1.40	19.83	28.49	34.25	1.44	1.73	1.20

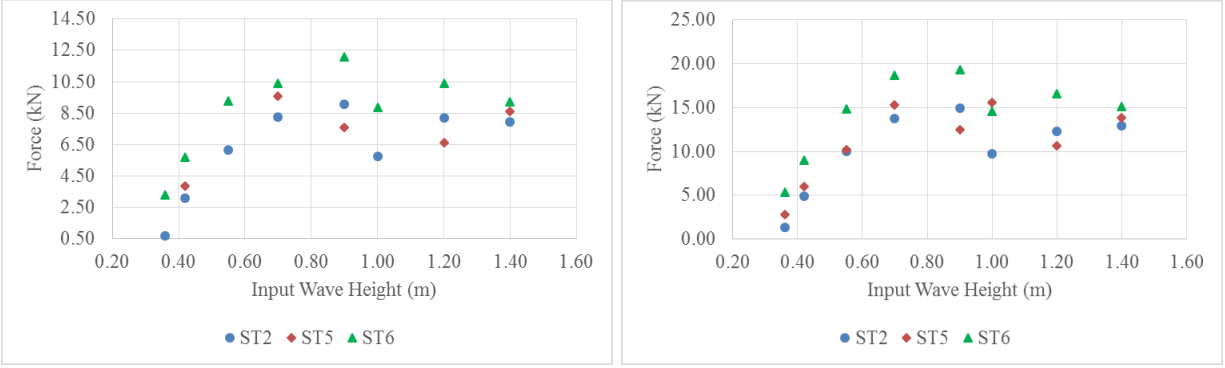


Figure 5.17: Maximum uplift forces in offshore bearings (left) and offshore piers (right) for bridge cases ST2, ST5 and ST6 and $d=2.0m$

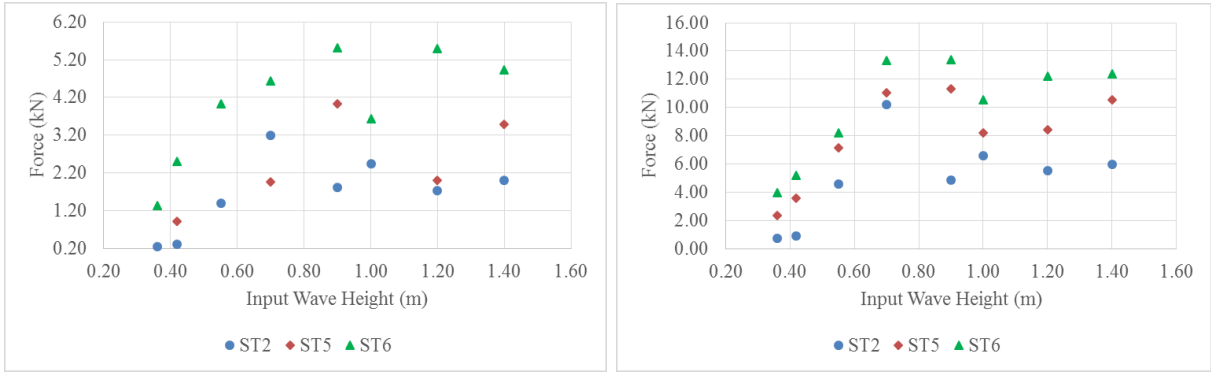


Figure 5.18: Maximum uplift forces in onshore bearings (left) and onshore piers (right) for bridge cases ST2, ST5 and ST6 and $d=2.0m$

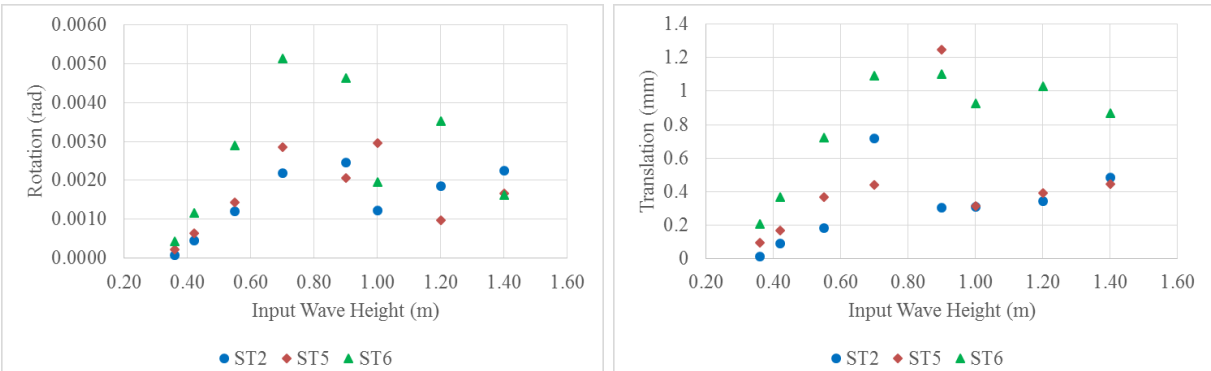


Figure 5.19: Bridge deck rotation (left) and vertical translation at onshore girder (right) for bridge cases ST2, ST5 and ST6 and $d=2.0m$

6.0 RETROFITTING OF BRIDGES VIA THE USE OF DECK AIR-VENTS

6.1 INTRODUCTION

In the previous chapters of this report, it demonstrated that the bridge with diaphragms witnessed larger uplift forces than the bridge with cross-frames due to the significant air-entrapment in the chambers. This observation indicates that there is a possibility for reducing the uplift forces by introducing air-vents in the deck of the bridge. In order to explore this possibility, 6.35cm (2.5in) diameter holes were drilled in the concrete deck to allow for venting of the air during the tsunami inundation, as shown in Figure 6.1. Two different air-vent configurations were tested with the first one (ST7) having 18 holes in the deck and a venting area equal to 0.85% of the total deck area, and the second one (ST9) with 36 holes and 1.7% vented area, as shown in Figure 6.2. The bridge specimens had 4 girders and 4 cross-frames/diaphragms between two girders, creating 3 main chambers with 3 sub-chambers in each of them.



Figure 6.1: Drilling of holes in the deck of the bridge (top-left), view of the bridge deck with air-vents (ST7) before the installation of the diaphragms, and plan view of the bridge case ST7 with 0.85% vented area (bottom-left) and bridge case ST9 with 1.70% vented area (bottom right)

6.2 AIR-VENTS FOR AN I-GIRDER BRIDGE WITH DIAPHRAGMS

6.2.1 Pressure, force and deck rotation histories

This section will focus on the comparison of the tsunami effects on an I-girder bridge with diaphragms and a solid deck (ST5), with the same bridge but 18 air-vents in the deck (ST9). Figure 6.2 plots the free-surface close to the wave-maker and close to the bridge for a solitary wave with a height of 0.42m, and it verifies that the waves are very similar for the two bridge cases, allowing us to proceed with the comparison.

The pressures on the girders and below the deck for the same solitary waves are plotted in Figure 6.4. In particular, the top graphs are verifying that both the pressures on the offshore girder and the ones below the overhang are matching in the two bridge specimens. This is however not true for the pressures on the second girder and below the deck in the offshore chamber. For the bridge with the venting, the pressure histories on the girder have a reduced first peak followed by many impulsive peaks, while the pressures below the deck have the two first peaks significantly reduced and the maximum pressure occurring later on. This behavior is observed in all the chambers of the bridge and for all the solitary waves, several of which are shown in Figure 6.3. It must be noted that although the air-venting reduces significantly the first pressure peaks and changes the pattern of the pressures by offsetting the maximum pressure to a later instant in time; it does not necessarily reduce the magnitude of the maximum pressure applied in the chambers.

The air-venting was also seen to have an effect on the total uplift forces, by reducing their magnitude both in Phase 2 & 3, with the major reduction occurring in the latter phase, as shown in Fig. 6.5. Apart from the total uplift forces, it is important to evaluate the effects of venting on the tsunami forces that each bearing has to withstand. As shown in Figure 6.6, for the particular solitary wave the air-vents reduced the uplift forces in both the offshore and the onshore bearings, with the largest reduction occurring in the onshore bearings. This phenomenon is reasonable because the maximum force in the offshore bearings occurs in Phase 3 for all waves, which was seen to be the phase that is affected the most by the venting of the trapped air. Overall the air-venting modified the wave-structure interaction and resulted in a different response of the bridge, as shown Figure 6.7.

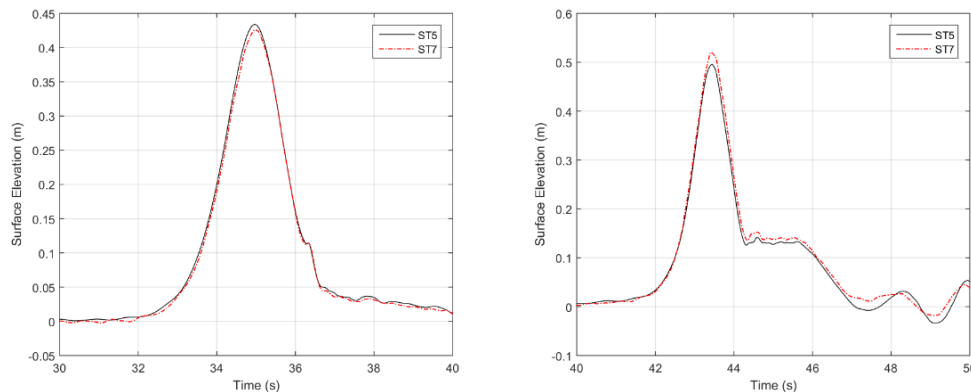


Figure 6.2: Surface elevation at wg1 close to the wavemaker (left) and at wg12 close to the bridge (right) for $H=0.42\text{m}$ and bridge cases ST5 and ST6

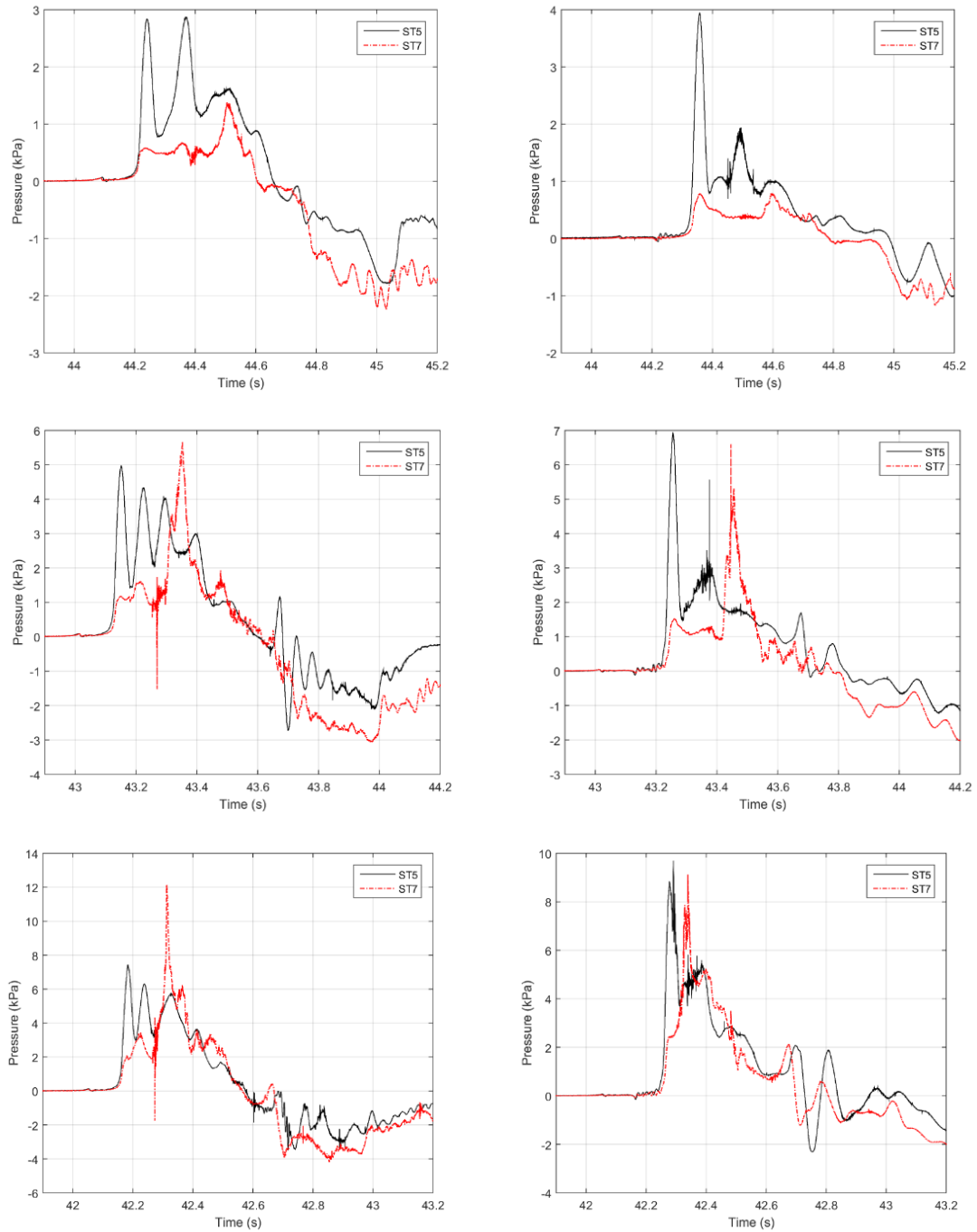


Figure 6.3: Pressures below the deck in the offshore chamber (left) and in the middle chamber (right) for three solitary waves with $H=0.42\text{m}$ (top), $H=0.55\text{m}$ (middle) and $H=0.70\text{m}$ (bottom)

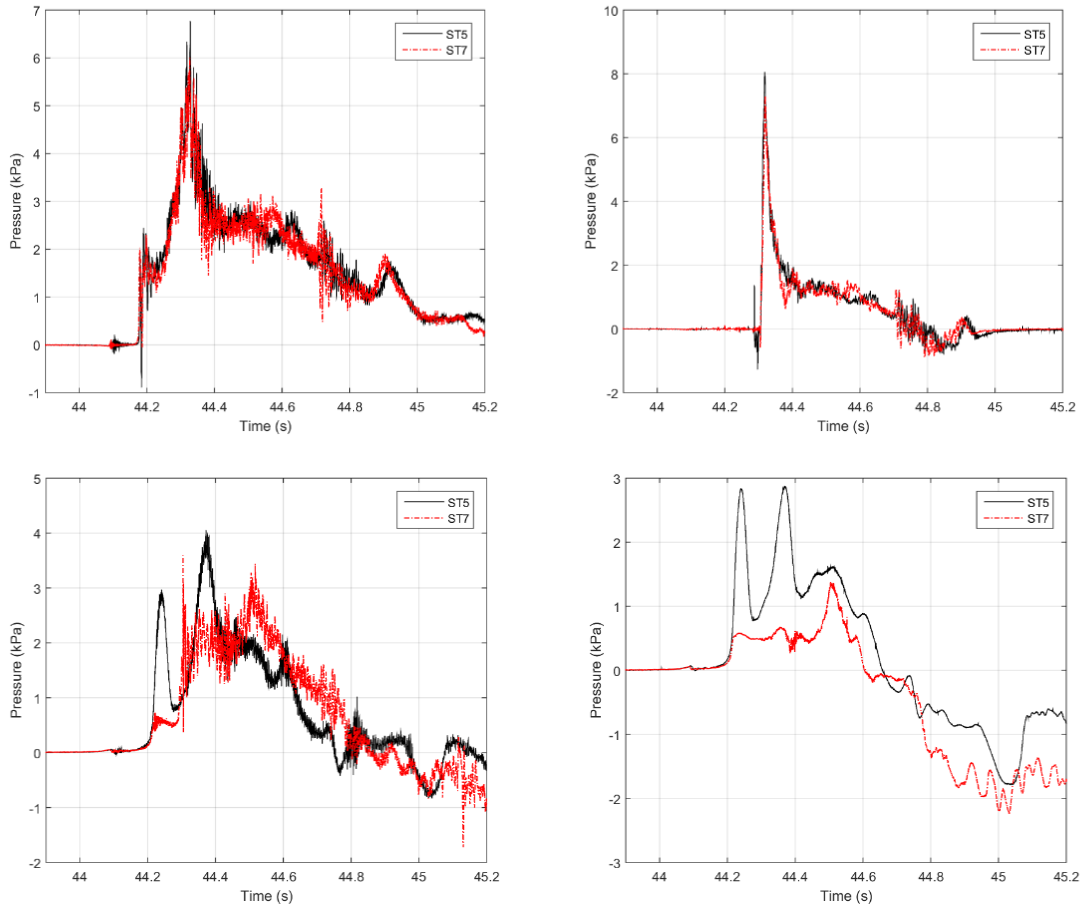


Figure 6.4: Pressure on the offshore girder (top-left), below the deck at the overhang (top-right), on the 2nd girder (bottom-left) and below the deck in the offshore chamber (bottom-right) for H=0.42m and bridge cases ST5 and ST7

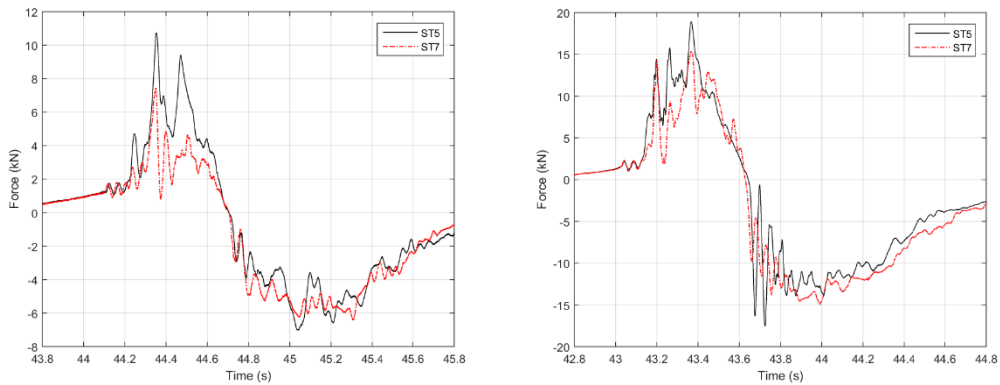


Figure 6.5: Total vertical forces for two solitary waves with H=0.42m (left) and H=0.55m (right)

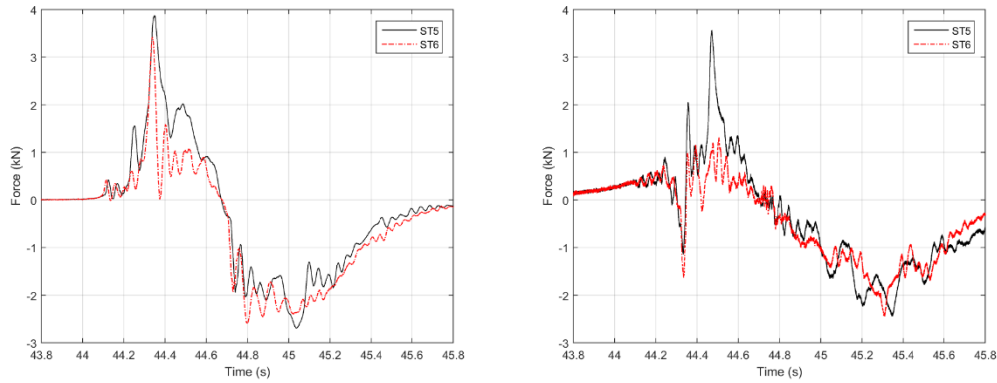


Figure 6.6: Vertical forces in offshore (left) and onshore (right) bearings for H=0.42m

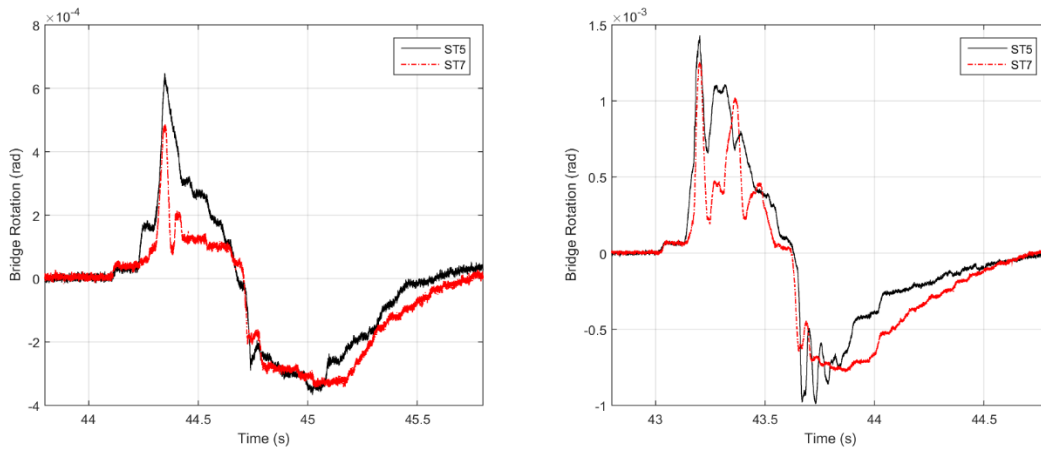


Figure 6.7: Bridge deck rotation for H=0.42m (left) and H=0.55m (right)

6.2.2 Comparison of maximum values

In order to check the validity of the conclusions reached in the previous sections based on the time histories of a few waves, this section will examine maximum pressures and forces for all the tested waves. Figure 6.8 is showing the max recorded pressures in the offshore and middle chamber. All the values shown in this graph are obtained from the raw pressure histories, apart from the maximum of the pressure in the offshore chamber for case ST5 and H=0.90, which had significant noise and was filtered at 500Hz. Examination of the graph reveals that although the venting of the air is consistently reducing the pressures in the middle chamber with a maximum reduction of 80%, it does not have a consistent effect on the pressures in the offshore chamber. For both solitary waves and bores the venting could either reduce or increase the pressure in the offshore chamber by up to 60% depending on the wave height.

A possible reason for the inconsistent effect of the air-venting on the pressures of the offshore chamber can be the two-fold role of the trapped air. On one hand, the trapped air is increasing the hydrostatic pressure applied on the bridge deck, while on the other hand -as observed in the present study and in (Cuomo et al., 2009)- it decreases the impulsive pressure peaks due to the

cushioning effect. For the small solitary waves that could not or could barely reach the bottom of the deck the venting of the air caused the largest reduction of pressures, which was 81% in the offshore chamber and 80% in the middle chamber. For the small wave heights, the waves cannot reach the bottom of the bridge deck and apply direct pressures on the deck, and in this case the pressure is transferred through the compression of the trapped air. Therefore, when air-vents are present the compression of the air is reduced significantly since the air can now escape from the holes, and therefore it transfers much lower pressures on the deck. This finding is in agreement with a previous numerical study (Azabkhat, 2013) for storm surge waves.

Despite the inconsistent effect of the air-venting on the pressures measured below the deck, its effect on the uplift forces was very consistent. For all the tested wave types and heights, releasing the trapped air resulted in a reduction of the total uplift forces, as shown in Figure 6.9. In particular, Table 6.1 shows that this reduction ranged between 6% and 55%, with the largest percentage occurring for the smaller waves. In addition to the ratios of the uplift forces between the two bridge cases, this table is also showing their subtraction, and interestingly for most of the solitary waves and bores (apart the H=1.20m and 1.40m) the absolute reduction of the uplift force is very similar with an average value of 3.53kN. This indicates that the vents are releasing a similar amount of air for all the waves with H between 0.36m and 1.00m.

The use of air-vents in the deck is also reducing the uplift forces in the bearings and piers as shown in Figure 6.10 and Tables 6.2 and 6.3. In particular, the vents have the largest effect on the forces of the onshore bearings and onshore columns of piers with an average reduction of 37% and 39% respectively. The reduction of the uplift forces in the offshore bearings and columns is very small because for most of the waves the forces in the above members are maximized in Phase 1 (time of initial wave impact on the offshore girder and overhang), where the air-venting has no effect. In this case, the small reduction emanates from the 5-10% smaller horizontal forces due to inherent variability of the bores. Last, it is worth noting that the inconsistent effect of venting on the pressures below the deck recorded at the center of a chamber compared to the consistent effect on the total uplift forces indicates that the pressures vary both along the width and the length of a chamber with possibly significant 3D effects.

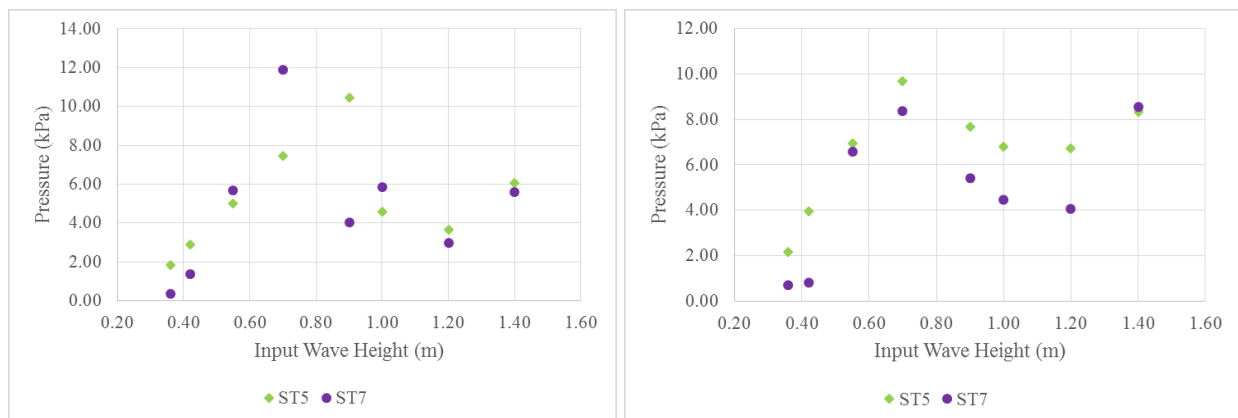


Figure 6.8: Maximum pressures in offshore (left) and middle chamber (right) for bridge cases ST5 and ST7 and different wave heights

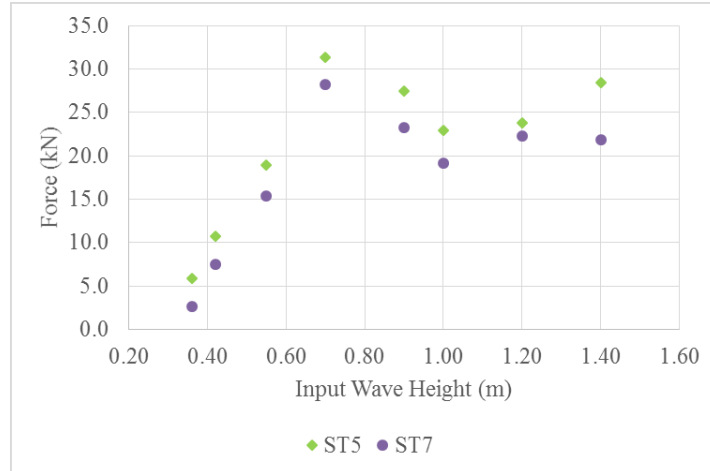


Figure 6.9: Total uplift forces for bridge cases ST5 and ST7 and different wave heights

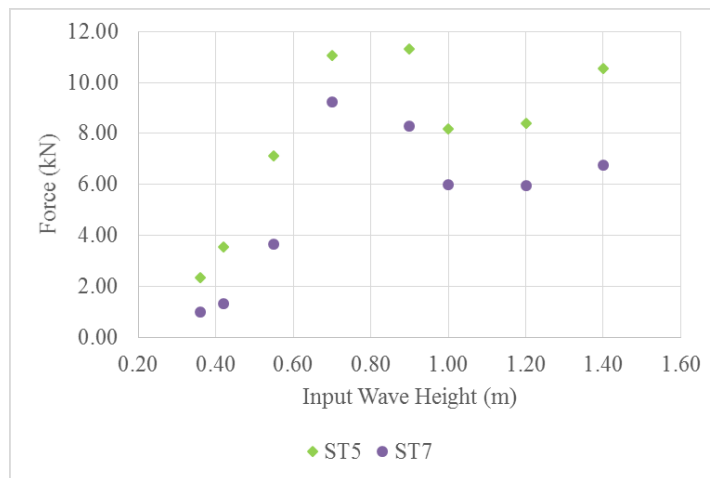


Figure 6.10: Uplift forces in onshore bearings for cases ST5 and ST7 and different wave heights

Table 6.1: Maximum Total Uplift Forces for the Bridges with and Without Air-vents

H_{input}	Depth	ST5	ST7	Ratios ST7/ST5	ST5-ST7
(m)	(m)	(kN)	(kN)		(kN)
0.36	2.00	5.87	2.62	0.45	3.24
0.42		10.74	7.49	0.70	3.25
0.55		18.93	15.37	0.81	3.55
0.70		31.39	28.24	0.90	3.15
0.90		27.48	23.25	0.85	4.23
1.00		22.95	19.21	0.84	3.74
1.20		23.79	22.32	0.94	1.47
1.40		28.49	21.81	0.77	6.69

Table 6.2: Maximum Uplift Forces in the Columns of Piers for the Bridges with a Solid Deck (ST5) and with a Vented Deck (ST7)

H_{input}	Depth	Offshore pier column			Onshore pier column		
		ST5	ST7	Ratios ST7/ST5	ST5	ST7	Ratios ST7/ST5
(m)	(m)	(kN)	(kN)		(kN)	(kN)	
0.36	2.00	2.76	1.53	0.55	2.34	1.00	0.43
0.42		5.97	5.25	0.88	3.57	1.31	0.37
0.55		10.20	9.63	0.94	7.14	3.65	0.51
0.70		15.28	13.72	0.90	11.04	9.23	0.84
0.90		12.51	10.98	0.88	11.32	8.29	0.73
1.00		15.62	13.62	0.87	8.18	5.99	0.73
1.40		13.80	12.62	0.91	10.53	6.77	0.64

Table 6.3: Maximum Uplift Forces in the Bearings for the Bridges with a Solid Deck (ST5) and with a Vented Deck (ST7)

H_{input}	Depth	Offshore bearings			Onshore bearings		
		ST5	ST7	Ratios ST7/ST5	ST5	ST7	Ratios ST7/ST5
(m)	(m)	(kN)	(kN)		(kN)	(kN)	
0.42	2.00	3.88	3.42	0.88	0.93	0.43	0.47
0.70		9.58	8.55	0.89	1.96	1.94	0.99
0.90		7.58	6.68	0.88	4.04	2.09	0.52
1.40		8.60	7.50	0.87	3.48	1.93	0.55

6.2.3 Inundation sequence for bridge case ST7

Figure 6.11 is showing several snapshots during the inundation of the bridge with 18 air-vents in the deck (ST7) by a solitary wave with $H=0.70\text{m}$. In this figure the inundation is progressing from left to right and then from top to bottom. As discussed in a previous section, in case ST7 there are three main chambers (offshore, middle and onshore) with 6 venting holes and 3 sub-chambers (end and center ones) in each. Interestingly, when the wave reaches the offshore chamber the two holes at the center are starting releasing air (and later on a mixture of air and water) before the rest of the holes. After that, the other four holes of the offshore chamber start releasing the trapped air. As the wave inundation proceeds and the wave reaches the middle chamber then again the two holes at the center of this chamber start venting air before the end holes of the same chamber. This sequence has been observed for all three chambers and it demonstrates the existence of 3D effects.

It must be noted that each of the nine sub-chambers has two venting holes. The sub-chambers at the two ends are identical; however, the sub-chambers at the center are different because their venting holes are closer to the diaphragms (7.30in) than the ones of the end sub-chambers (11.58in). This demonstrates that the distance of the holes from the diaphragms plays a major role on the air-venting and explains why the center sub-chambers started venting the air faster than the end ones. The existence of the phase lag between the sub-chambers implies that if all vents were releasing air simultaneously then a larger reduction of the uplift forces might have been achieved.

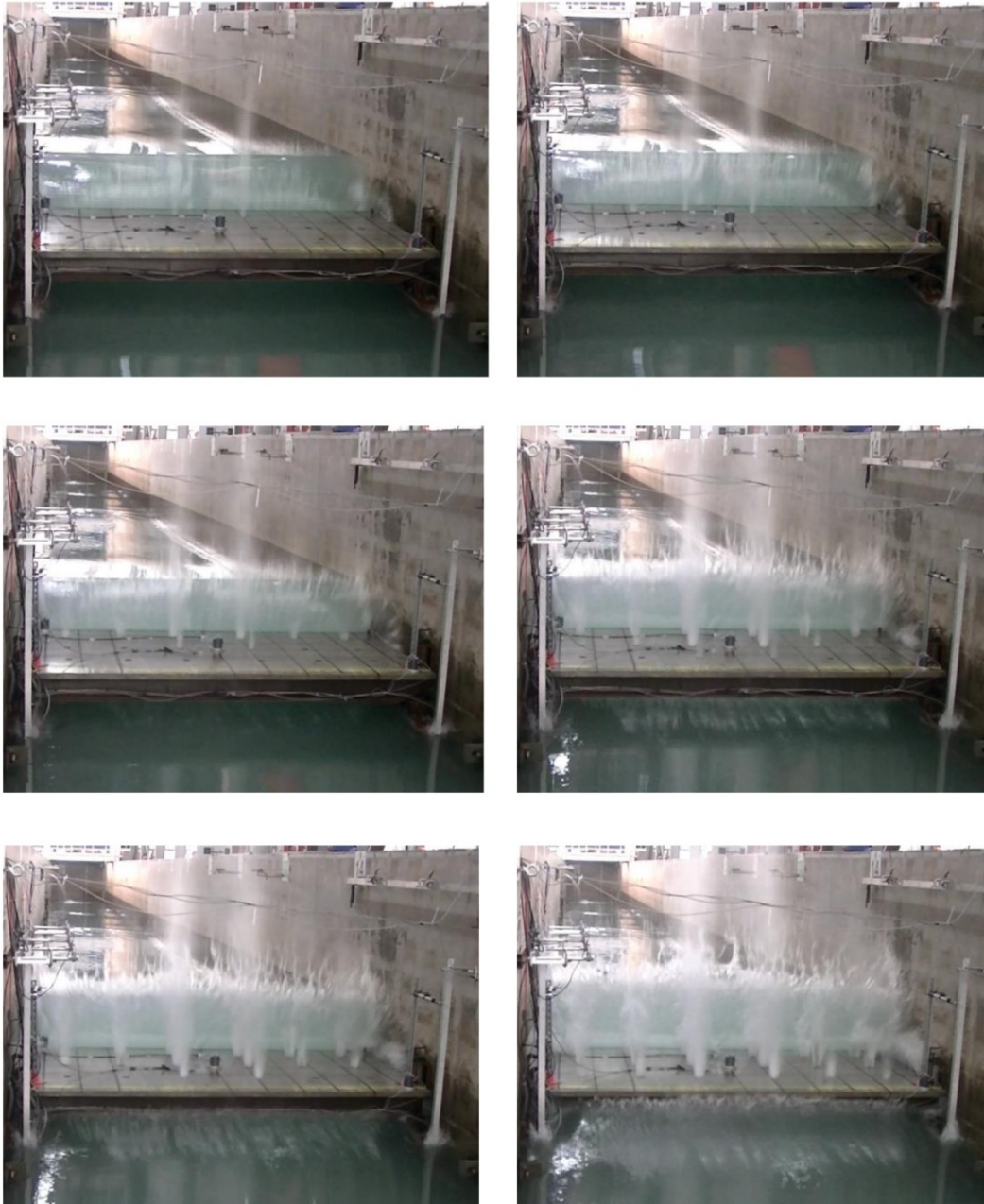


Figure 6.11: Snapshots of inundation of the bridge with air-vents (ST7) for H=0.70m

6.3 EFFECT OF NUMBER OF AIR-VENTS

6.3.1 Pressure and force histories

This section is presenting experimental results for the bridge case with 36 vents in the deck (ST9) relatively to the results obtained for the bridge case with 18 vents (ST7). As shown, in Figure 6.12 the additional vents are changing the pressure histories below the deck in both the offshore and middle chamber and are reducing the magnitude of the first pressure peaks. Despite this initial reduction, the additional vents caused an increase of the maximum pressure in the chambers for some wave heights and a decrease for other ones. Even for the same wave height (e.g. $H=0.90\text{m}$) the larger number of air-vents reduced the pressure in one chamber but increased it in another one. This variable effect demonstrates that there exists a complex air-wave-structure interaction which is affected by the air-vents in the deck. Interestingly, although doubling the number of air-vents affected significantly the pressure histories for the particular waves presented here in, the effect on the total uplift forces and on the bearings forces was minor, as shown in Figure 6.13.

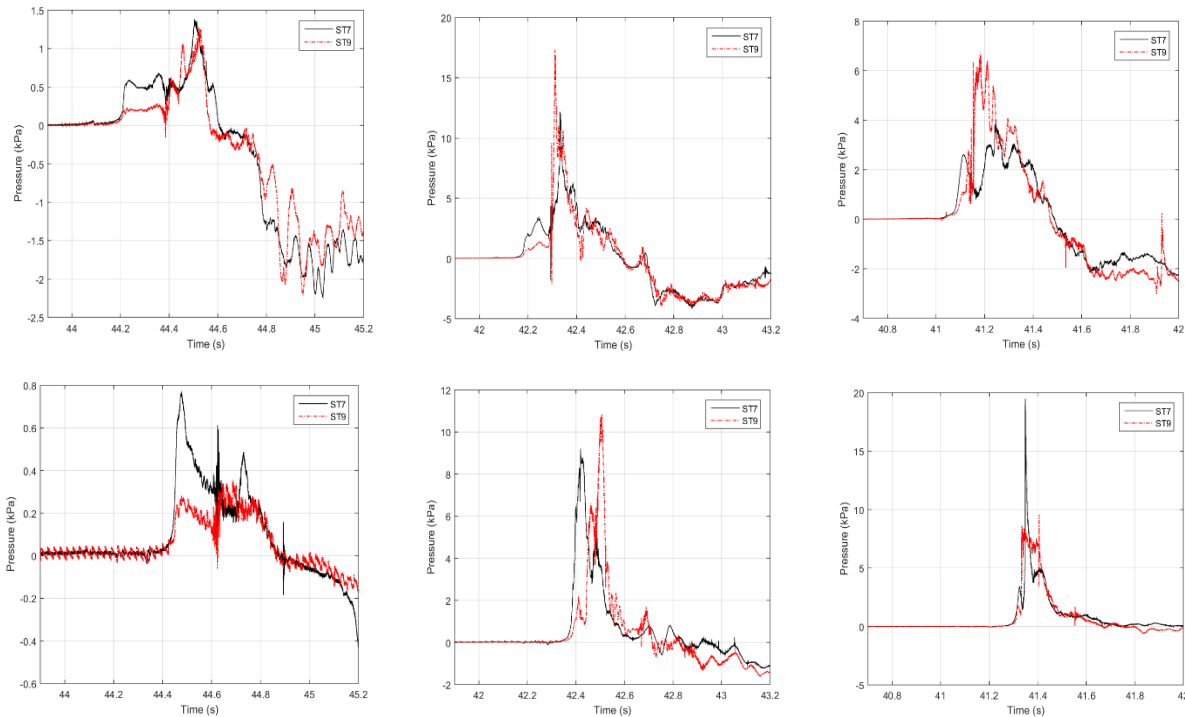


Figure 6.12: Pressures below the deck in the offshore (top) and onshore (bottom) chamber for three waves with $H=0.42\text{m}$ (left), $H=0.70\text{m}$ (middle) and $H=0.90\text{m}$ (right) and two venting ratios

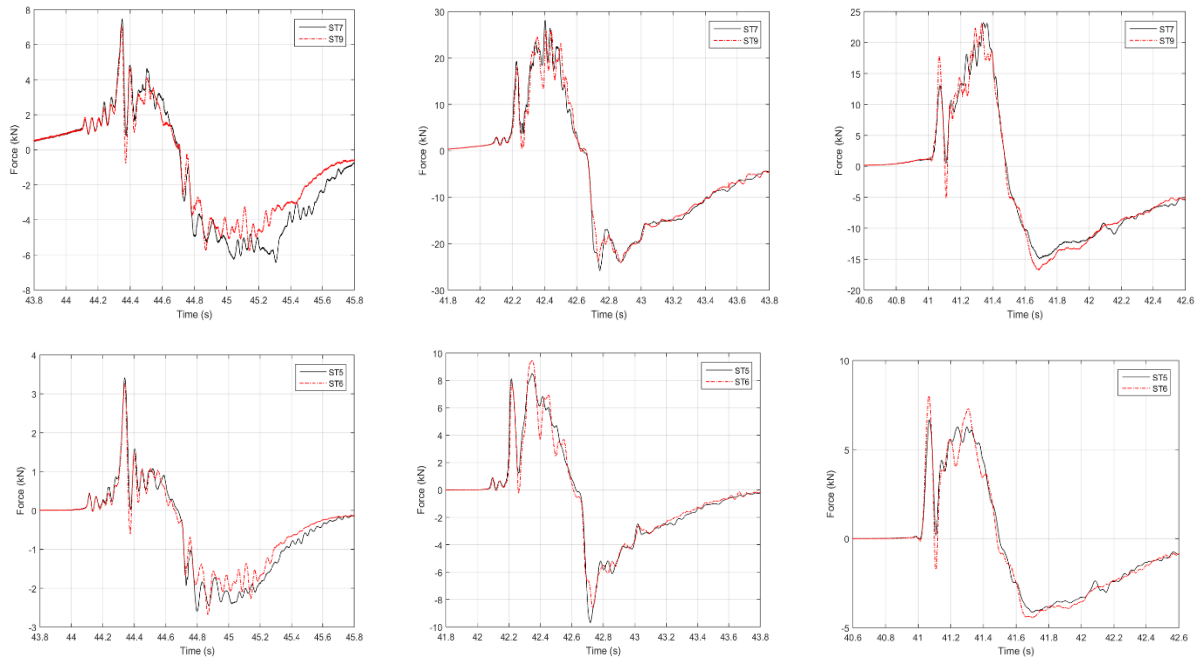


Figure 6.13: Total vertical forces (top) and vertical forces in offshore bearings (bottom) for three waves with $H=0.42\text{m}$ (left), $H=0.70\text{m}$ (middle) and $H=0.90\text{m}$ (right) and two venting ratios

6.3.2 Comparison of maximum values

Figure 6.14 is showing the maximum pressures below the bridge deck in both the offshore and middle chamber for all the tested wave heights. This figure verifies the variable, complex and significant effect of the additional vents on the pressures measured at the center of each chamber. Figure 6.15 and Table 6.4 are verifying that doubling the number of air-vents has a minor effect on the total uplift force that the bridge has to withstand, causing only a 6% reduction on average, which is an interesting finding that was not expected beforehand. Even more interesting is the fact that although the additional air-vents allowed more air to escape and reduced slightly the total uplift forces, it had an opposite effect on the forces of the onshore bearings and pier columns, as shown in Figure 6.16 and Table 6.5. In particular, for several wave heights the deck with 36 vents witnessed increased forces in the onshore bearings by up to 95% and an average value of 44% among these waves. The minor effect of the additional air-vents on the total uplift forces and the significant counter-intuitive effect on the forces of the onshore bearings and pier columns demonstrate that the venting of the air has a complex role because it modifies the wave-structure interaction resulting in a different distribution of forces in the connections. This highlights the need to evaluate the effect of retrofitting strategies not only on the total uplift forces – as has been done until now in the literature- but on the forces of each individual connection.

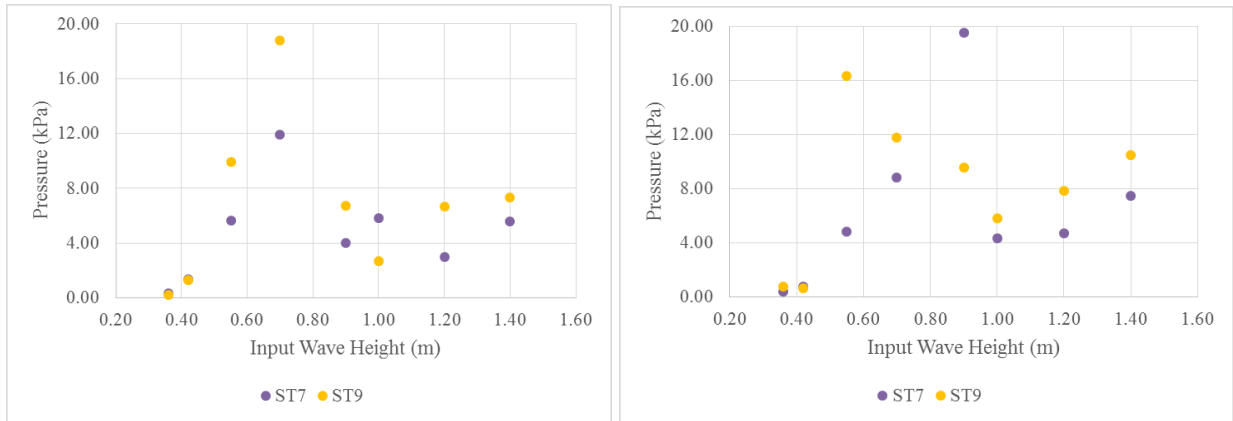


Figure 6.14: Maximum pressures below the deck in the offshore (left) and onshore (right) chamber for the two different air-venting ratios and several wave heights

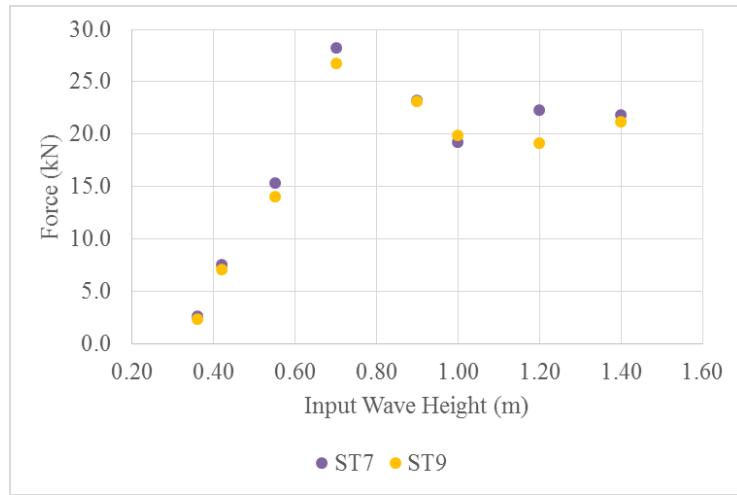


Figure 6.15: Total uplift forces (right) and for two different air-venting ratios

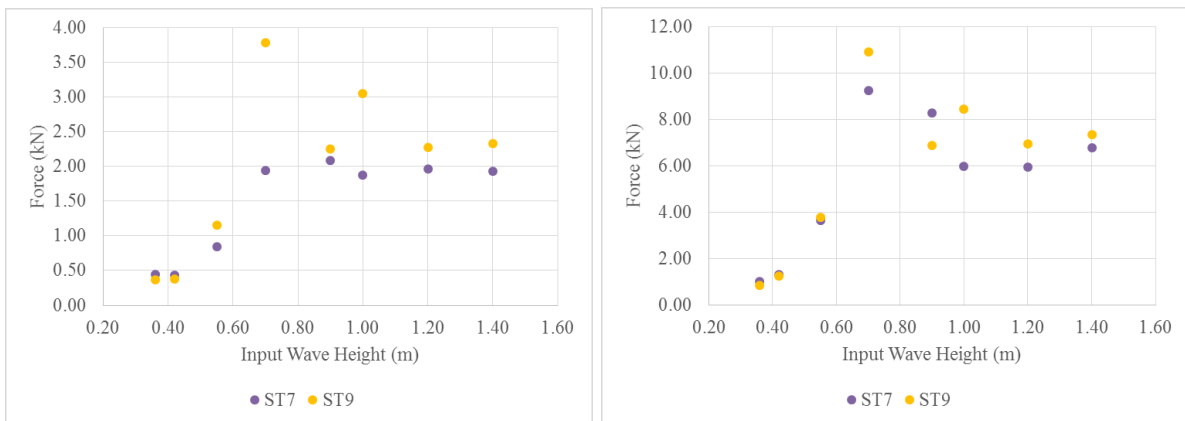


Figure 6.16: Uplift forces in onshore bearings (left) and onshore pier columns (right) for two different air-venting ratios and several wave heights

Table 6.4: Maximum Total Uplift Forces for Different Number of Air-vents

H_{input} (m)	Depth (m)	ST7 (kN)	ST9 (kN)	Ratios ST9/ST7
0.36	2.00	2.62	2.30	0.88
0.42		7.49	7.04	0.94
0.55		15.37	14.04	0.91
0.70		28.24	26.71	0.95
0.90		23.25	23.14	1.00
1.00		19.21	19.88	1.03
1.20		22.32	19.14	0.86
1.40		21.81	21.19	0.97

Table 6.5: Maximum Uplift Forces in the Onshore Bearings and Column Piers for Different Number of Air-vents

H_{input} (m)	Depth (m)	Onshore pier columns			Onshore bearings		
		ST7 (kN)	ST9 (kN)	Ratios ST9/ST7	ST7 (kN)	ST9 (kN)	Ratios ST9/ST7
0.36	2.00	1.00	0.84	0.84	0.44	0.37	0.84
0.42		1.31	1.23	0.94	0.43	0.38	0.88
0.55		3.65	3.76	1.03	0.84	1.15	1.37
0.70		9.23	10.92	1.18	1.94	3.78	1.95
0.90		8.29	6.89	0.83	2.09	2.25	1.08
1.00		5.99	8.44	1.41	1.87	3.05	1.63
1.20		5.94	6.95	1.17	1.97	2.28	1.16
1.40		6.77	7.36	1.09	1.93	2.32	1.21

6.3.3 Inundation sequence for bridge case ST9

Figure 6.17 is showing snapshots of the inundation of bridge case ST9 with 36 air-vents in the deck. In this figure the inundation progresses from left to right and then from top to bottom. As was the case with the bridge with 18 air-vents (ST7) and it is also true here, when the wave reaches a chamber the two holes of the center sub-chamber are starting venting the air (and later on a mixture of air and water) before the holes of the end sub-chambers, demonstrating the existence of 3D effects. What is interesting for this particular case, is the fact that the four holes of the center sub-chamber did not start venting the air simultaneously but the holes that are further from the wave preceded. For example, when the wave reached the offshore chamber the two holes of the center sub-chamber that were close to the 2nd girder (and further from the wave) started releasing air before the ones close to the 1st girder. This behavior was observed for all chambers. In general, as demonstrated by the snapshots, there was a gradual increase of the number of holes that were venting air as the wave propagated through the bridge, and by the time all the holes of the onshore chambers started venting air the holes of the offshore chamber were clogged by the wave that overtopped the bridge deck. This sequential release of air might explain why doubling the number of air-vents had a negligible effect on the uplift force. It must be noted

that the distance of the additional vents from the closest girder was smaller than the respective distance of the initial 18 vents from the closest girder. This means that the trapped air had to travel less before it reached the vents explaining why the new air-vents started releasing air before the pre-existing ones. These observations reveal that the efficiency of the air-vents depend on their location relative to the diaphragms and the girders, i.e. the boundaries of the chamber. This implies that the effectiveness of the vents could be optimized by choosing the appropriate number of holes and the appropriate location in order to achieve a simultaneous release of air by most -if not all- holes in the deck.

6.4 AIR-VENTS FOR AN I-GIRDER BRIDGE WITH CROSS-FRAMES

Since the air-vents were seen to reduce the uplift force in the case of the bridge with diaphragms, it was deemed useful to examine if this retrofitting approach could work for bridges with cross-frames. To this end, after the experimental tests of bridge cases ST7 (with 18 air-vents) and ST9 (with 36 air-vents) were completed, the diaphragms were removed creating bridge case ST10 that had 36 air-vents and cross-frames. In this case only a few wave heights were examined. As shown in Table 6.6, the 36 air-vents had a negligible effect on the total uplift forces of case ST10. This can be explained by the fact that the escape of the air occurs mainly from the sides, where the cross-frames are located, and not that much through the additional escape routes provided by the vents.

Although, the air-vents have a negligible effect on the total uplift force, as shown in Tables 6.7 and 6.8, they can have a negative effect of the middle and onshore pier columns, as well as on the onshore bearings, by increasing the uplift force that each of these members has to withstand. This behavior was also observed for the bridge with diaphragms and it demonstrates that the air-vents are altering the wave-structure interaction and consequently the response of the bridge. Therefore, venting the deck of a bridge with cross-frames is not recommended as a counter-measure against tsunamis.

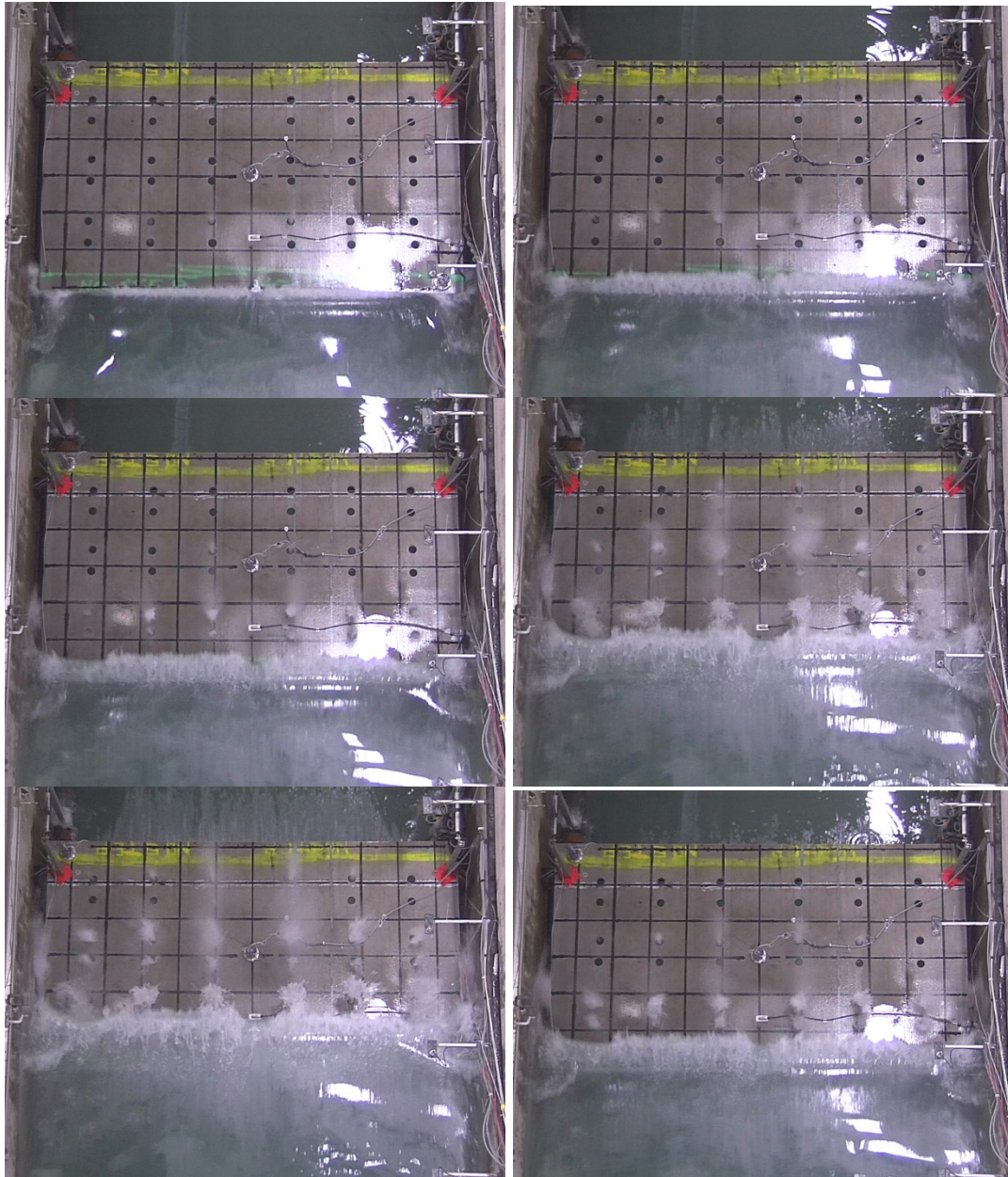


Figure 6.17: Snapshots of inundation of the bridge with 36 air-vents (ST9) for $H=0.70\text{m}$

Table 6.6: Total Uplift Forces for Bridge Cases ST2 and ST10

H_{input} (m)	Depth (m)	ST2 (kN)	ST10 (kN)	Ratios ST10/ST2
0.55	2.00	13.61	12.97	0.95
0.70		29.79	31.81	1.07
1.40		19.83	20.23	1.02

Table 6.7: Uplift Forces in the Columns of the Piers for Bridge Cases ST2 and ST10

Middle columns				
H_{input} (m)	Depth (m)	ST2 (kN)	ST10 (kN)	Ratios ST10/ST2
0.55	2.00	3.68	4.84	1.31
0.70		7.71	8.96	1.16
1.40		6.82	8.29	1.21
Onshore columns				
H_{input} (m)	Depth (m)	ST2 (kN)	ST10 (kN)	Ratios ST10/ST2
0.55	2.00	4.56	3.86	0.85
0.70		10.19	12.37	1.21
1.40		5.96	6.19	1.04

Table 6.8: Uplift Forces in the Bearings for Cases ST2 and ST10

Bearings of 2nd girder				
H_{input} (m)	Depth (m)	ST2 (kN)	ST10 (kN)	Ratios ST10/ST2
0.55	2.00	5.80	5.66	0.97
0.70		9.03	8.70	0.96
1.40		8.48	6.95	0.82
Onshore bearings				
H_{input} (m)	Depth (m)	ST2 (kN)	ST10 (kN)	Ratios ST10/ST2
0.55	2.00	1.40	1.37	0.99
0.70		3.19	4.56	1.43
1.40		2.00	2.31	1.16

6.5 EFFECTIVENESS OF AIR-VENTS IN BRIDGES WITH CROSS-FRAMES AND BRIDGES WITH DIAPHRAGMS

Table 6.9 is showing the total uplift forces recorded for four bridge configurations. The results for the solid deck are compared with the ones for the deck with 36 air-vents, for both a bridge with diaphragms (ST5 and ST9) and one with cross-frames (ST2 and ST10). As expected the air-

vents caused a large reduction of the uplift forces when the diaphragms were present, and had a negligible effect when diaphragms did not exist. This is reasonable because in the latter case the escape of the air through the sides of the bridge is governing over the escape of the air through the vents of the deck.

Table 6.9: Total Uplift Forces for Bridges with Cross-frames and Diaphragms

H_{input}	Depth	ST5	ST9	Ratios ST9/ST5	ST2	ST10	Ratios ST10/ST2
(m)	(m)	(kN)	(kN)		(kN)	(kN)	
0.55	2.00	18.93	14.04	0.74	13.61	12.97	0.95
0.70		31.39	26.71	0.85	29.79	31.81	1.07
1.40		28.49	21.19	0.74	19.83	20.23	1.02

7.0 EFFECT OF SOLID RAILS ON THE TSUNAMI-INDUCED FORCES AND MOMENTS

7.1 INTRODUCTION

This chapter focuses on the investigation of the role of solid rails for the tsunami-induced forces on straight bridges. Given the fact that in many States across the US the rails are usually perforated and therefore are not expected to obstruct the hydrodynamic flow significantly, the initial experimental tests shown in the previous chapters neglected the rails. In reality though, there are several types of rails such as, (a) hybrid rails that consist of solid concrete barriers (up to a certain height) with perforated guiderails on top of them, or (b) solid rails along the whole height, which can be found in different States. In order to cover the wide range of available rail types it was decided to repeat some of the experimental tests of the I-girder bridge with elastomeric bearings but add a solid rail, with the expectation that the two tested configurations (with and without rails) will give an upper and lower bound respectively for the horizontal forces. To that end, solid barriers were constructed using steel angles available in the market and were bolted to the offshore and onshore side of the deck, as shown in Figures 7.1 and 7.2. The gaps between the rails and the top surface of the deck generated by imperfections were sealed in order to prevent a potential fluid flow through these gaps. The height of the rails was 0.152m increasing the total deck height from 0.264m to 0.416m.



Figure 7.1: Bridge with solid barriers during the hydrodynamic testing

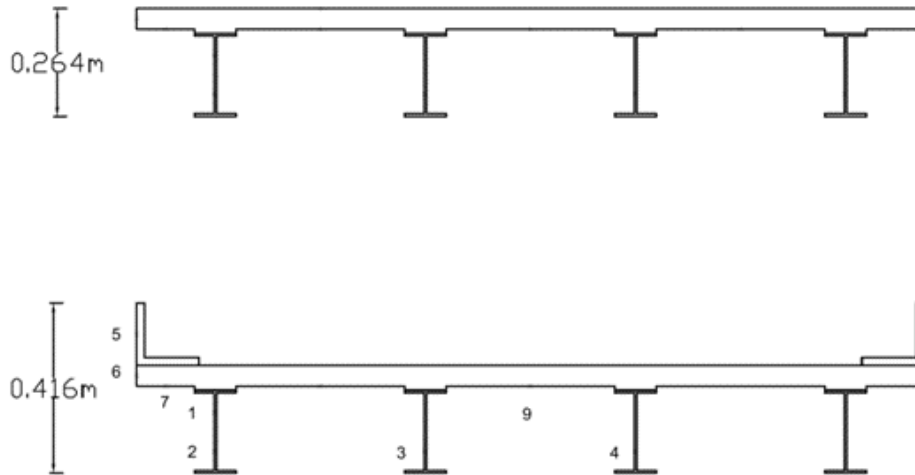


Figure 7.2: Cross-section of the bridge deck without (top) and with (bottom) solid rails

7.2 HORIZONTAL AND VERTICAL FORCES

Figure 7.3 presents the recorded horizontal and vertical forces for the largest unbroken solitary wave ($H=0.70\text{m}$) and a turbulent bore with $H=1.20\text{m}$. As discussed in Chapter 2, the hydrodynamic forces generated by bores are associated with significant variability due to the chaotic nature of the breaking process. Therefore, in order to be able to conduct a fair comparison between the forces on the bridge with rails and the one without rails, several runs of the same bore were conducted. Then some of the most representative runs were selected for the comparison of the two bridge configurations, in order to ensure that this comparison will not be skewed by the uncertainty in the tsunami loads. Therefore, Figure 7.3 shows two runs of the same bore height ($H=1.20\text{m}$), with the first one being a run that gives force magnitudes close to the average of all the repetitions, and the second one being the run with the maximum recorded force for each bridge configuration. This figure reveals that:

- For the solitary wave the addition of the rails has practically no effect on the magnitudes of the both the horizontal and the vertical forces. However, it clearly changes the pattern of the horizontal force histories by generating a second significant impulse when the deck is totally inundated (a downward force is applied) and the bore hits the onshore rail. However, this second impulse does not exceed the magnitude of the main pulse, which means that it is not expected to have a governing role in the design of the structural components that have to withstand the horizontal loading (e.g. shear keys).
- On the other hand, in the case of the bore, the rails increase significantly the magnitude of the horizontal loading. This increase is observed both in (a) the first impulsive peak and the second one, which is caused by the existence of the offshore rail, as well as, in (b) the longer duration loading, which is affected by both the offshore and onshore rails.

- Interestingly for the bore case, although the rails are vertical components that do not add to the vertical area of the bridge exposed to tsunamis, which means that the vertical forces should remain constant with the addition of the rails, this is clearly not happening. In fact, while the rails have a negligible effect on the magnitude of the uplift, they do seem to cause modifications in the pattern of the vertical force histories, especially after the first impulsive uplift peak and during the longer duration uplift. This observation indicates that the existence of the rails affects the tsunami inundation mechanism and the flow around the deck.

The above trends related to the effect of the rails on the magnitude of the forces can be generalized to all the heights of the same wave type, as shown in Figure 7.4. Clearly, the rails have a negligible effect on the maximum horizontal forces caused by unbroken solitary waves (these are the waves with H smaller or equal to 0.70m), even for the large heights that inundate the deck, while they have a major effect for bores, with increases in the horizontal force of up to 110%. Regarding the total uplift, the rails have a small and a negligible effect in the case of bores and solitary waves respectively. The above observations are important because they demonstrate that simplifying tsunami bores with unbroken solitary waves -as done in several previous studies- does not necessarily capture the same physics, wave-structure interaction and effects on the structure.

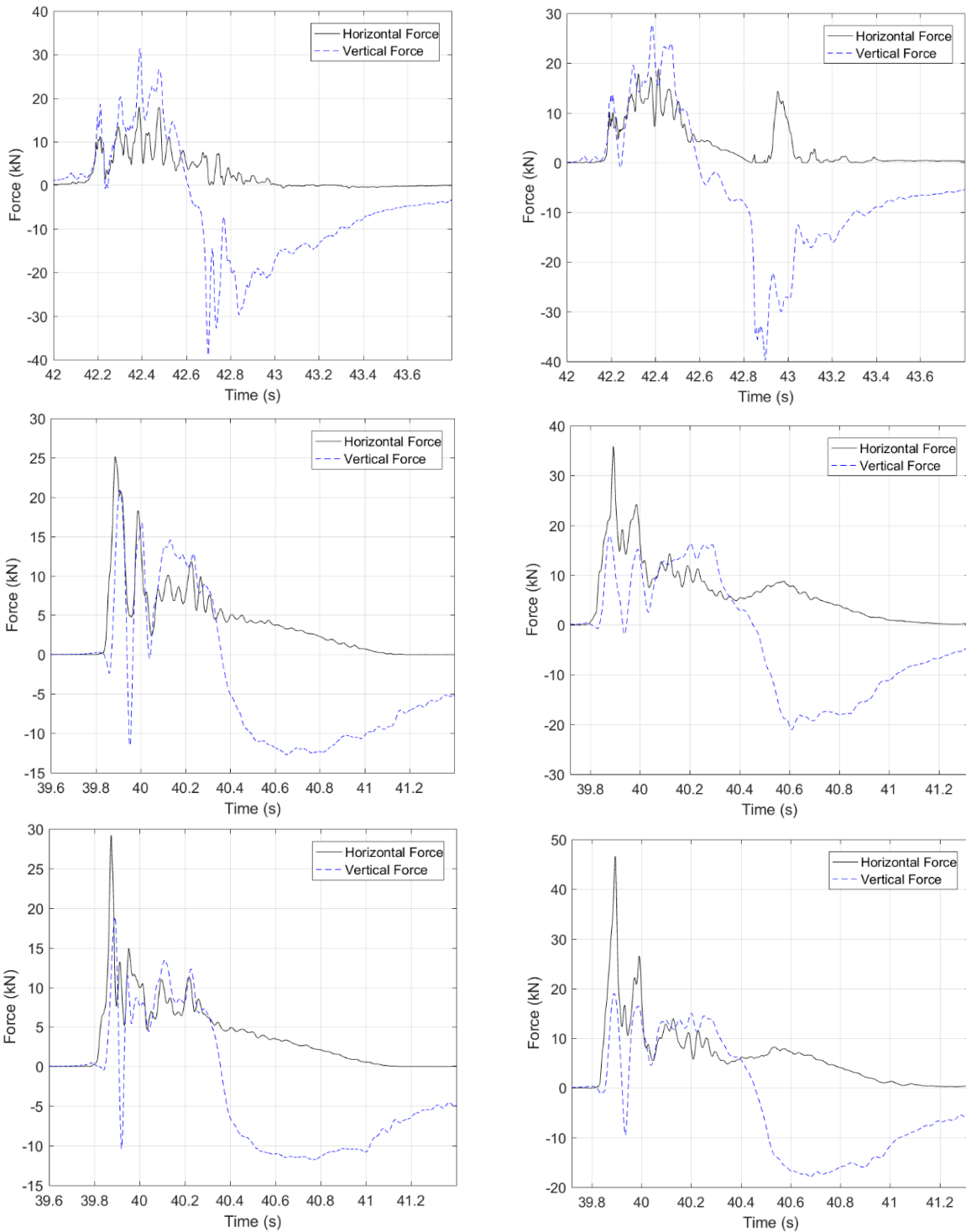


Figure 7.3: Total horizontal and vertical forces on the bridge w/o rails (left) and with rails (right) for H=0.70m (top) and H=1.20m (center and bottom)

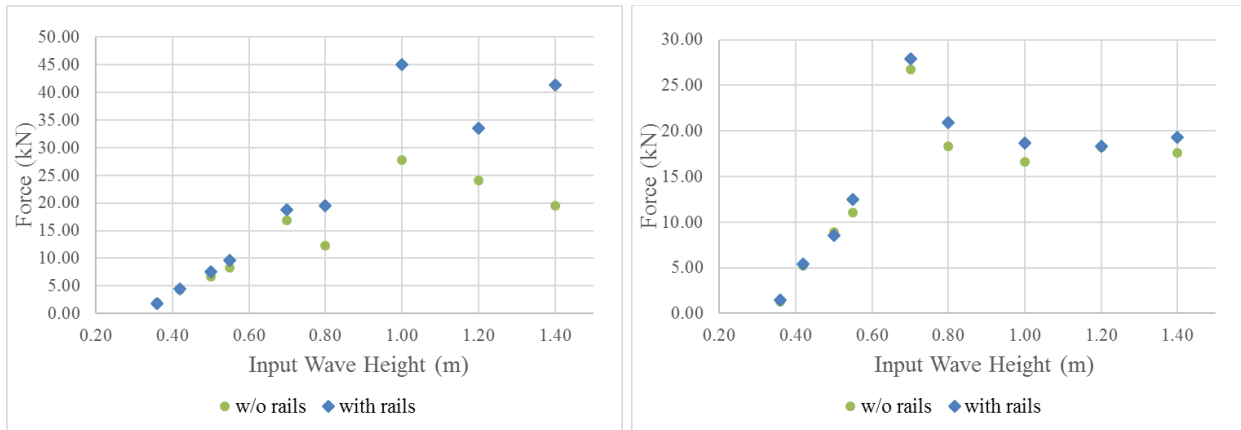


Figure 7.4: Maximum total horizontal (left) and vertical (right) forces on the bridge with and without solid rails, calculated at the level of the bearings

7.3 MOMENTS

The analysis of the experimental results in Chapter 2 revealed the significance of the tsunami-induced overturning moment for the design of the structural components of the bridge, including the bearings, bent caps and columns. Given this important role, it was deemed necessary to investigate the effect of the rails on the overturning moment. To this end, Figure 7.5 shows the moment histories for a unbroken solitary wave with $H=0.70\text{m}$ and a bore with $H=1.20\text{m}$ (for a repetition with a magnitude close to the average magnitude of all the repetitions conducted in the experiments). Note that the overturning moment (OTM) was calculated at two different levels, including the girder-bearing connections and the bent-cap-column connections, by using the force measurements from different sets of load cells. The figure clearly shows the good agreement of the OTM at the two levels, with the bent-cap-column connections witnessing slightly larger values, which is expected due their larger distance from the point of application of the horizontal load. In addition to high-quality of the experimental data the figure demonstrates that:

- For the unbroken solitary wave the rails have a negligible effect on the OTM histories from the beginning of the bridge inundation up to the point that the wave impacts the onshore rail. Once the latter impact occurs, the applied pressures on the onshore rail modify the OTM history by introducing a significant clockwise moment, which will be called “OTM2” herein. This OTM2 can be twice as large as the maximum OTM generated at the beginning of the inundation when the wave hits the offshore girder and overhang (called “OTM1”).
- Interestingly, despite the generation of such a large moment due to the addition of the rails, the OTM2 is not expected to govern the design of the vertical structural components that have to withstand significant uplift (e.g. bearings, columns) because the moment is generated when the whole deck is inundated and a simultaneously large downward tsunami load is applied on the bridge. On the other hand, this OTM2 will increase the compressive load of certain structural components (e.g. onshore bearings and columns) that are already under compression due to the downward

tsunami load. Further investigation is required in order to determine if such a load case that combines the maximum downward tsunami force with OTM2 is going to have a governing effect or not.

- Similarly to the case of unbroken solitary waves, the addition of the solid rails generates a new large clockwise moment when a bore impacts the onshore rail. This moment can exceed the magnitude of the impulsive moment generated at the beginning of the inundation (OTM1), and its exact value depends on the bore height. Contrary, however, to the unbroken solitary waves, the rails seem to affect also the magnitude of OTM1 (generated at the beginning of the inundation), as well as, the patterns in the moment histories.

The maximum values of the moment shown in Figure 7.6 demonstrate that the trends observed in the overturning moment when the rail was added, are not applicable to the smallest wave heights. While the wave with $H=0.70\text{m}$ generates a significant OTM2 when it impacts the onshore rail, this moment is not significant in the case of the smaller waves, and this could probably attributed to the fact that those waves do not have the necessary height and energy to fully inundate the bridge and generate a large amount of overtopping water that hits the onshore rail.

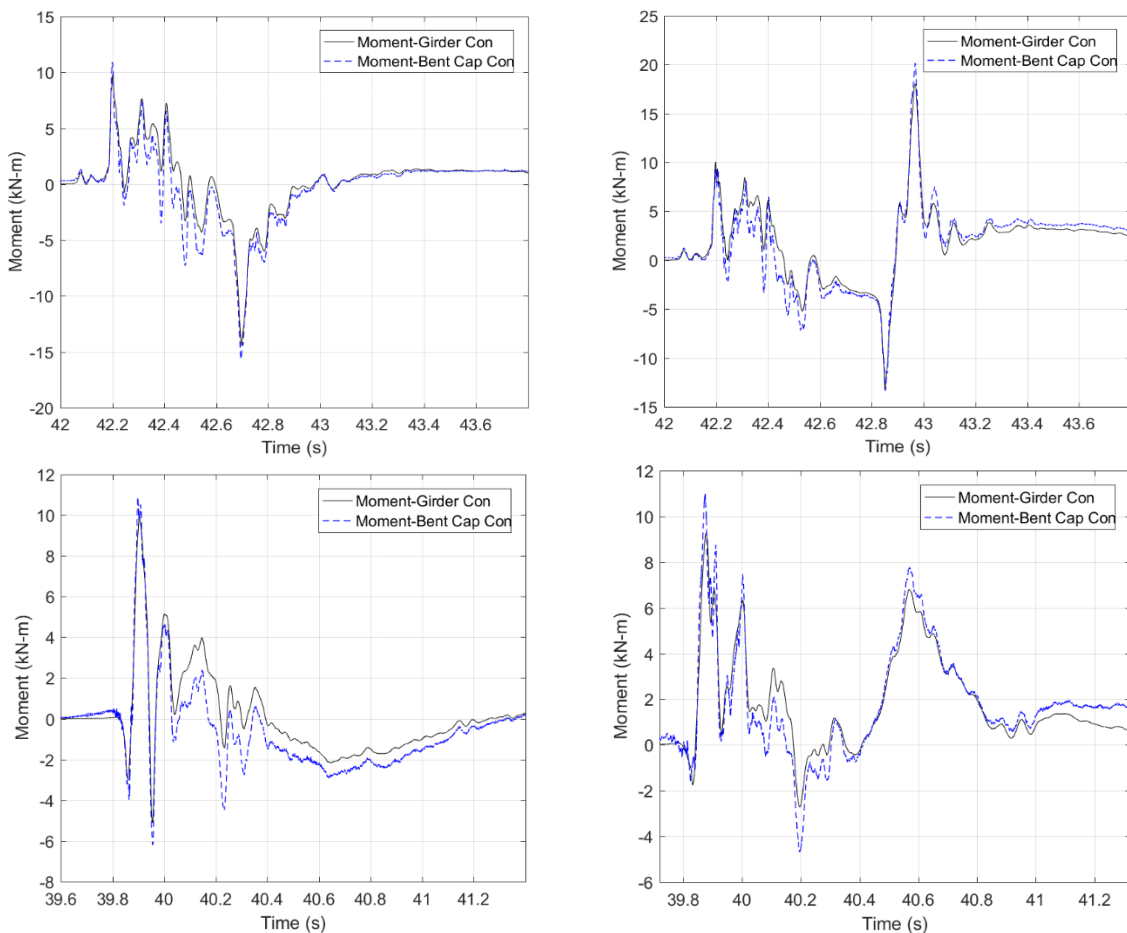


Figure 7.5: Overturning moment histories at the level of the bearings for the bridge w/o rails (left) and with rails (right) for $H=0.70\text{m}$ (top) and $H=1.20\text{m}$ (bottom)

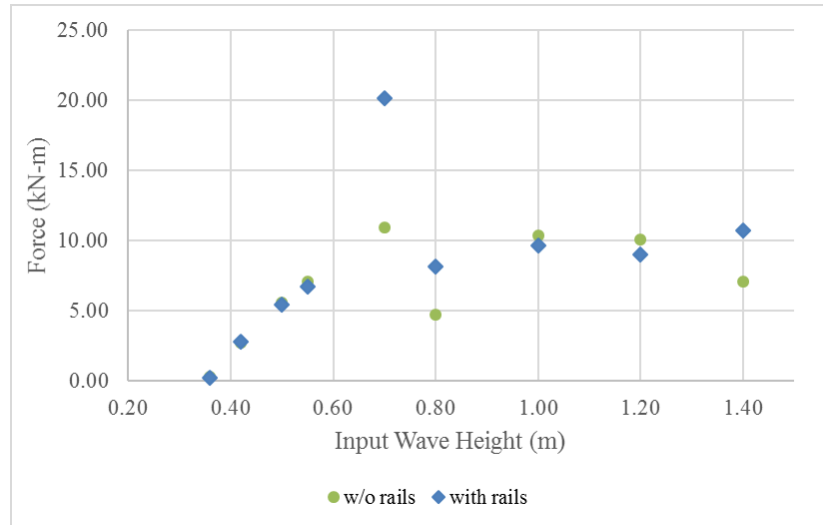


Figure 7.6: Maximum overturning moment on the bridge with and without solid rails, calculated at the level of the bearings

Regarding the bores, a significant OTM₂ is generated in all cases, however this is not necessarily reflected in the maximum values of Figure 7.6 because that OTM₂ does not exceed the already large OTM₁. For the largest bore though with H=1.40m the rails increase the maximum moment by 40%. After close investigation of the time-histories of all the repetitions of the largest bore, it was revealed that (a) this 40% is caused by the generated OTM₂ (which means that OTM₂ in the case with rails is 40% larger than the OTM₁ in the bridge w/o rails), and (b) that the addition of the rails increased also OTM₁, as well as, the follow-up peaks of the moment histories.

7.4 UPLIFT FORCES IN INDIVIDUAL BEARINGS

Since the rails were seen to modify the moment histories by introducing a new major peak (OTM₂) and by causing some noticeable increases of OTM₁, the next question is how these modifications affect the demand in structural components (e.g. bearings) and consequently their design. To provide an answer, Figure 7.7 presents the time histories of the uplift forces measured in the bearings below each girder together with the total tsunami-induced uplift, while Figure 7.8 the maximum uplift forces in the offshore and onshore bearings, for both bridge configurations (with and w/o rails). The two figures suggest that the rails:

- Have an overall minor effect on the uplift forces that the offshore bearings have to withstand. For solitary waves this effect is negligible, while for the majority of the bores is small but noticeable. This can be attributed to the fact that for open-girder bridges with cross-frames the maximum uplift demand in the offshore bearings is governed by the overturning moment at the beginning of the inundation (OTM₁), which as shown in the previous section, does not increase much with the addition of the rails.
- Increase significantly the uplift forces in the onshore bearings for most of the tested waves. This increase was 37% on average (for all the tested waves) and up to 90%, and could be explained by the combination of two factors: (i) the uplift demand in the

onshore bearings occurs when the whole deck gets inundated (not at the beginning of the inundation) and it is governed by the long duration uplift, and (ii) the existence of the rails changes the hydrodynamic flow and consequently the long duration deck uplift (differences are clearly visible in the bottom graph of Fig. 7-7) leading to increase of the uplift in the onshore bearings. Despite this significant increase, the uplift demand in the onshore bearings is still smaller than the one in the offshore bearings, which means that if all the bearings are designed for the same uplift force (governed by the offshore bearings) then the design of the bearings will remain the same.

- Have a paramount effect on the downward force applied on the bearings, which can increase by up to 254% with an average increase of 84% among the tested waves. This behavior could be attributed to two factors:
 - the increase of the maximum tsunami-induced downward (after the initial impact of the tsunami on the onshore rails the wave splashes and slams the deck with a larger momentum), which was up to 109% with an average value of 47%, and
 - the generation of a large clockwise moment (OTM_2), which increases the compression of the onshore bearings furthermore.

It must be noted that in reality when the deck is inundated by a long duration bore, it is expected that the existence of the solid rails will affect the slamming downward force but not the steady-state downward force (for the cases where the tsunami height exceeds the heights of the rails).

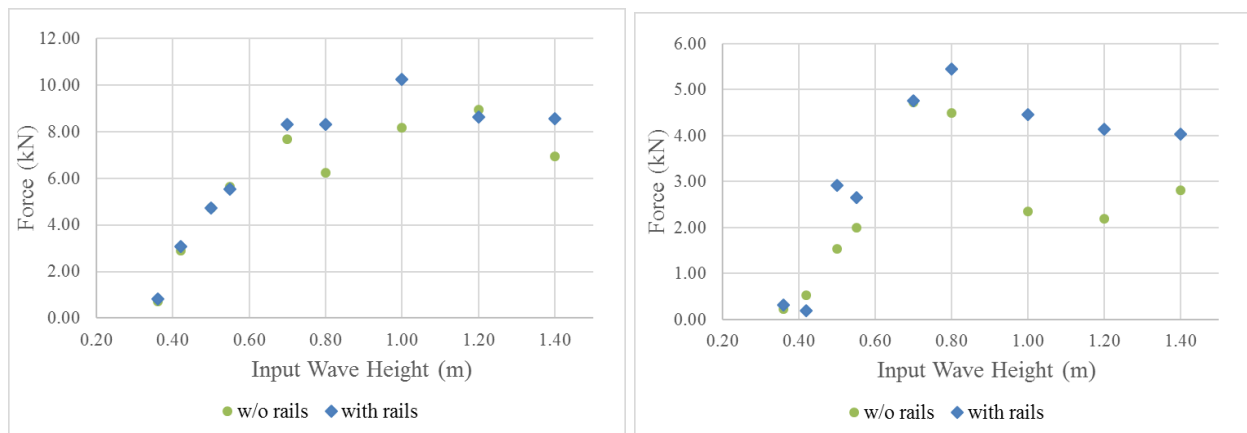


Figure 7.7: Maximum uplift force in the offshore and onshore bearings for the bridge with and without solid rails

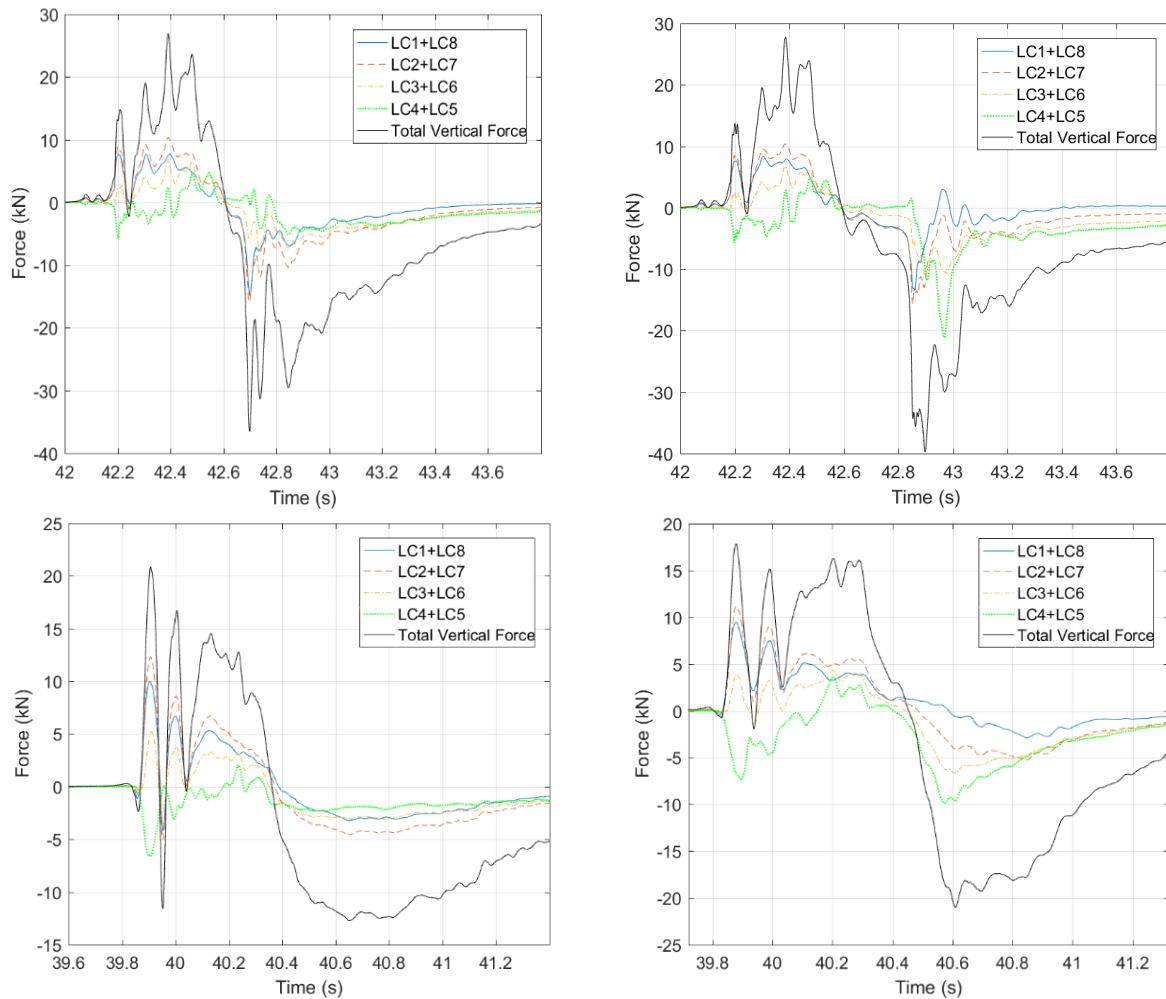


Figure 7.8: Total uplift force and uplift in individual bearings of the bridge w/o rails (left) and with rails (right) for $H=0.70\text{m}$ (top) and $H=1.20\text{m}$ (bottom)

7.5 APPLIED PRESSURES – EXPLANATION OF OBSERVED BEHAVIOR

In order to decipher the physics underlying the observed behavior and the effect of the rails on the horizontal force, one needs to investigate the applied pressures on the different components of the superstructure. To this end, Figure 7.9 presents the applied tsunami pressures on the offshore face of the superstructure, including two locations on the girder and two on the rails/concrete slab. Note that in the legend the “Pressure Deck-Hd/2” refers to the pressure on the offshore face of the concrete slab of the deck (at the mid-height of the slab), which means that the pressure gage is located at the same horizontal coordinate with the rail/barrier but at a smaller elevation. Figure 7.9 illustrates that:

- For unbroken solitary waves, the pressures on the offshore girder and the ones on the rails are maximized at different instants. Also, while the girder pressures have a major impulsive pressure peak this is not observed in the pressures on the rails.

- On the other hand, in the case of bores, the latter pressures do have an impulsive component and their magnitude is comparable to the maximum pressures on the girder. Moreover, the instants at which the pressures on the rails and the ones on the girders are maximized are relatively close to each other and in some cases the maxima occur simultaneously (e.g. Run 14 of bore with $H=1.20\text{m}$). Interestingly though, this does not happen for all the bores or even for all the repetitions of the same bore, as shown by Run 13 of the bore with $H=1.20\text{m}$ in which case the pressures on the rails are maximized when the girder pressures have been reduced significantly. These inconsistent trends indicate that the relationship between the pressures applied on the girders and the ones on the barriers is quite complex and it is dependent not only on the bore height but on additional bore characteristics (e.g. shape and velocity distribution along the height of the offshore face of the deck), which are harder to quantify. Given the fact that these bore characteristics/properties are characterized by significant aleatory variability, the relationship between the maximum girder and rail pressures becomes also variable making it impossible to quantify it deterministically.

To advance the understanding of the observed phenomenon, Figure 7.10 presents the normalized values of the horizontal pressures (on rails and girder) together with the horizontal force, for the bridge with solid rails and the two aforementioned repetitions of the 1.20m bore. Interestingly, for both runs the maximum horizontal force in the shear keys occurs when the applied pressures on the girders drop to about 50% of their maximum value. However, in Run 13 the maximum horizontal force seems to be dominated by the girder pressures (with the rail pressures being close to zero), while in Run 14 both the girder and rail pressure seem to contribute to the maximum horizontal force. In fact, in the latter case the magnitudes of the pressures on the girder and rail are similar at the instant of $\max F_h$, indicating a uniform pressure distribution along the height of the offshore face of the bridge. This finding is very significant both for understanding the underlying physics and potentially for the design of the structure, however, it should be verified with follow-up CFD analyses, which will not consider the structural dynamics (which could potentially be the reason of the time delay between the maximum pressures and the horizontal forces measured in the shear keys) in order to get a more accurate relationship between the applied pressures and the applied total load.

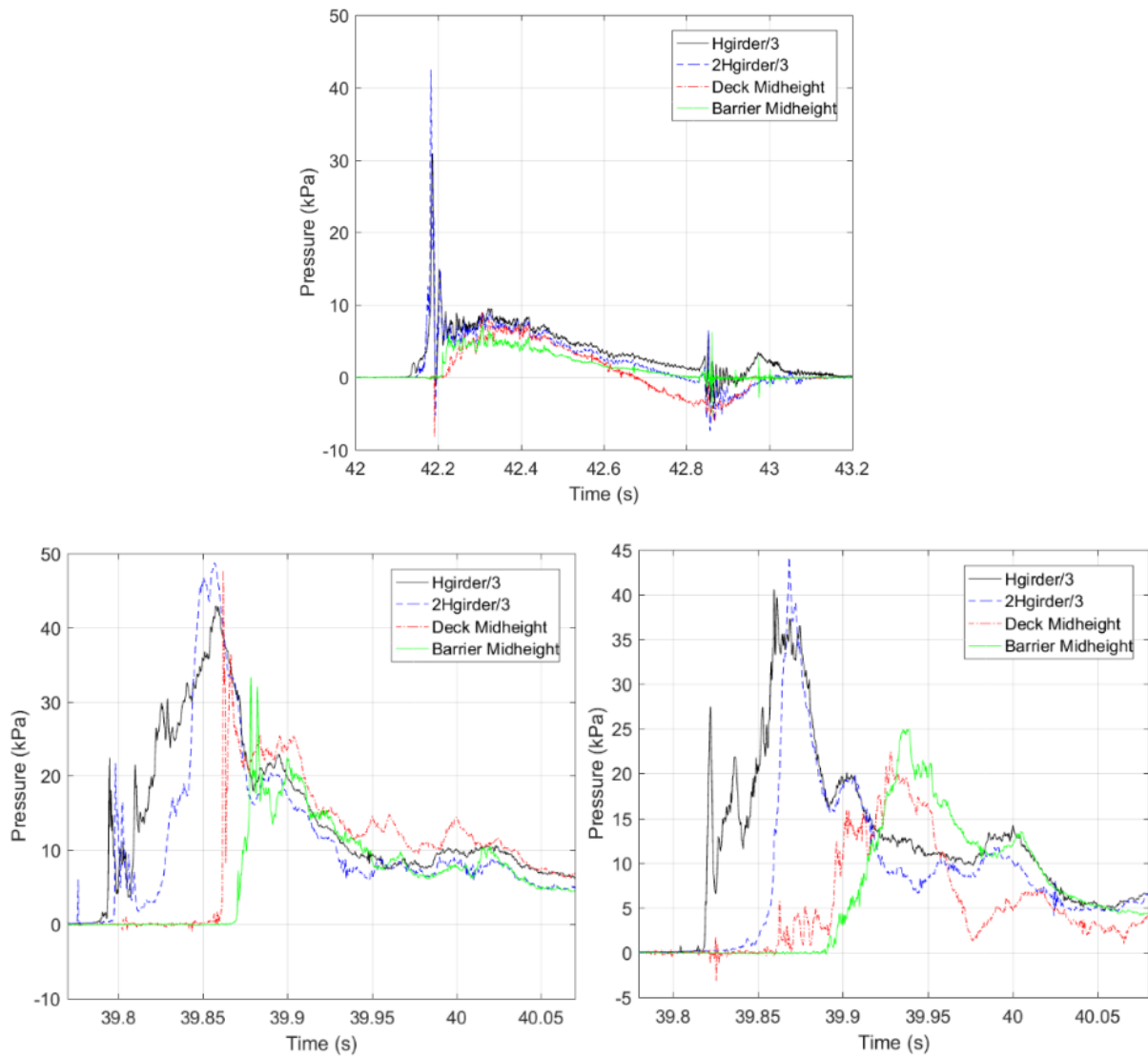


Figure 7.9: Applied pressures on the offshore face of the bridge with rails for H=0.70m (top) and H=1.20m (Run 14-bottom left and Run 13-bottom right)

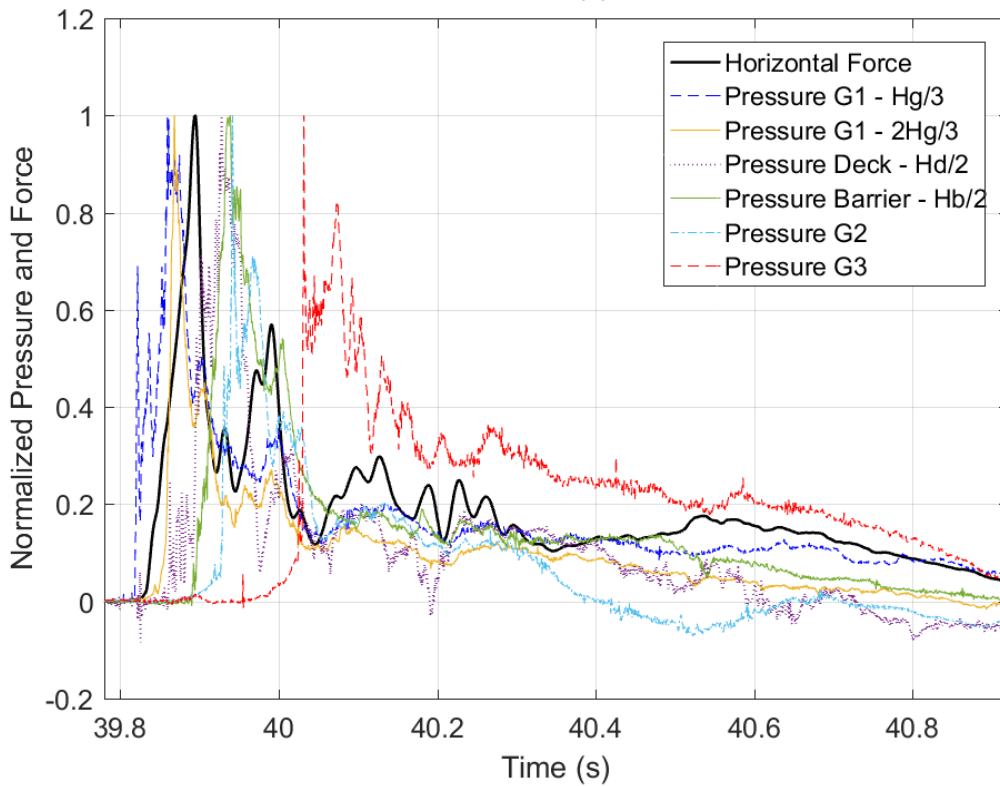
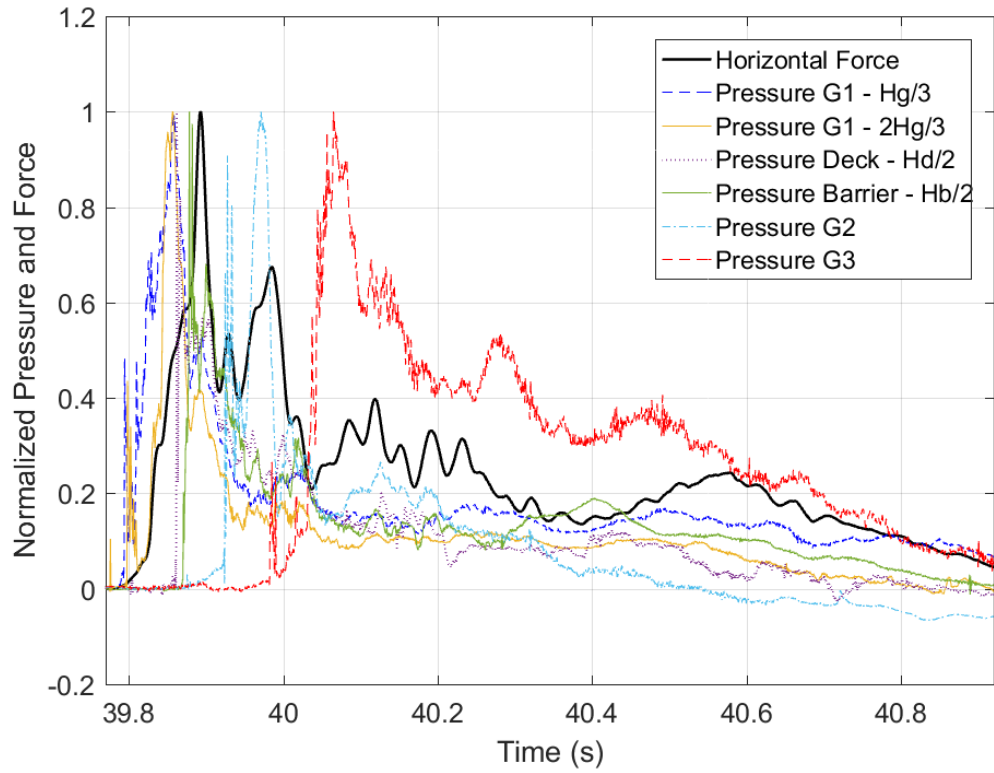


Figure 7.10: Normalized horizontal applied pressures and forces on the bridge with rails for a bore with $H=1.20\text{m}$ (Run 14-top and Run 13-bottom)

In summary, in order to determine the influence of the rails on the horizontal force two questions have to be answered: (i) how close are the maxima of the pressures on the offshore girder and on the barriers to each other in time, and (ii) what is the contribution of the pressures on the girder and on the rail when F_h is maximized. These do not have a deterministic answer, since even for the same bore the answers changes among the different repetitions due to the significant aleatory variability associated with tsunami-like turbulent bores.

7.6 DISCUSSION AND PRELIMINARY RECOMMENDATIONS FOR DESIGN

The detailed analysis of the experimental results shown in the previous sections has advanced the understanding of the role of solid rails for the tsunami-induced loads and demand in structural components. This section will utilize the experimental results in order to provide useful recommendations for the tsunami design of bridges.

7.6.1 Total horizontal force

Previous research studies (e.g. Kerényi et al., 2009), focused on the estimation of the maximum hydrodynamic loads generated by riverine flooding. This study revealed that the horizontal hydrodynamic force on the bridge is a function of the total bridge height “ s ”, as shown in equation (7-1), without distinguishing between the height of the girder and the one of the solid rails. This equation of course applies for the cases that the flooding level is higher than the rails ($h_u - h_b > s$), as shown in Fig. 7.11.

$$F_D = (1/2) * C_D * \rho * v^2 * (L * s)$$

(7-1)

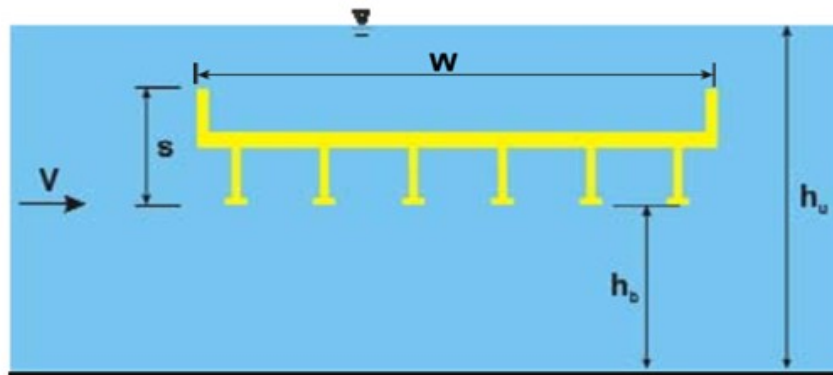


Figure 7.11: Depiction of parameters affecting the hydrodynamic loads on a bridge superstructure subjected to riverine flooding (source: Kerényi et al., 2009)

Given the complexity of the tsunami inundation mechanism of bridges and the associated loads discussed in the previous sections and chapters, it would be interesting to try and draw parallels between these loads and the ones generated by riverine flooding. If a similar equation was applicable to tsunamis then the horizontal force would be a function of the total height ($s = h_{\text{girder}} + h_{\text{rails}}$) and the increase of the total horizontal load due to the addition of the rails would

be a function of the height ratio $h_{\text{girder}+h_{\text{rails}}}/h_{\text{girder}}$ (or the area ratio, since the length of the rails and girders is the same). Figure 7.12 presents the ratios of the maximum F_h recorded in the shear keys in the bridge with rails relative to the case without rails, and compares them with the area ratio, which is equal to $0.416\text{m}/0.264\text{m}=1.575$. From the figures it becomes clear that:

- For the unbroken solitary waves the ratios of forces is much smaller than the area ratio and in fact are close to unity, which is agreement with the previous analysis showing that the rails had small/negligible effect.
- On the other hand, for three out of the four bores the ratios of $\max F_h$ (average value for all the repetitions) are surprisingly close to the area ratio. This means that:
 - despite the complex relationship between the girder and rail pressures at the time of occurrence of $\max F_h$ (discussed in section 7.5), which is dependent on the bore height and also quite variable even among the repetitions of the same bore, using the average value of the $\max F_h$ measured in all the repetitions “i” consistent trends can be observed. These trends would imply that if the rails had the same height as the girders then they would contribute equally to the total horizontal force, in spite of the differences in the lateral and vertical coordinates of the two components.
 - for design purposes it can be assumed that the pressure distribution on the offshore face of the bridge (including rails and girders) is uniform, which will consequently mean that a predictive equation similar to the one in (eq. 7-1) could be used for the whole height of the deck, without the need to consider separate hydrodynamic coefficients for the girders and the rails. Using the same predictive equation for designing different bridge configurations (with and without rails), will simplify the design process. In other words, given the known horizontal force on a bridge without rails, the force on a bridge with rails can be realistically estimated via the following equation:

$$F_{h_{w/rails}} = (h_{\text{girder}} + h_{\text{rails}} / h_{\text{girder}}) * F_{h_{\text{norails}}} \quad (7-2)$$

- for design purposes the same equation could potentially be used for the calculation of the maximum tsunami demand on each component (rails and girders). This demand should be considered in the design of the bridge, since for example (a) the applied tsunami loading on the rails could affect the design of the overhang and the connection of the rails to the overhang, while (b) the lateral tsunami loading applied on the offshore girder (and the other girders) might have to be considered in the design in order to ensure that no lateral-torsional buckling will occur when the deck is uplifted and the bottom flange of the girder is in compression. It must be clarified that before suggesting the same predictive equation for the total $\max F_h$, the $\max F_{h_{\text{girders}}}$ and $\max F_{h_{\text{rails}}}$, such an equation must be verified with follow-up CFD, which will output the applied loading separately on the rails and on the girders and

will ensure that the maximum demand on each of these components ($\max F_{h_{\text{rails}}}$ and $\max F_{h_{\text{girder}}}$) is generated when the total F_h is maximized,

It is noteworthy that the above approach of estimating the maximum tsunami-induced horizontal load on bridges with solid rails by increasing the load based only on the height (area) ratio of the rails and girders is applicable to the majority of the tested bores, but not to all of them. In fact, for the largest tested bore ($H=1.40\text{m}$) the $\max F_h$ witnessed by the bridge with rails is 112% larger than in the case without rails, which is much larger than the 57.5% increase in the area. This subsequently means that using the load estimates on a bridge without rails and adjust them to account for the whole height of the bridge with rails (girders and solid rails) is not necessarily a conservative approach, but rather a practical and empirical one justified by the experimental results for the sake of simplicity in a future design approach.

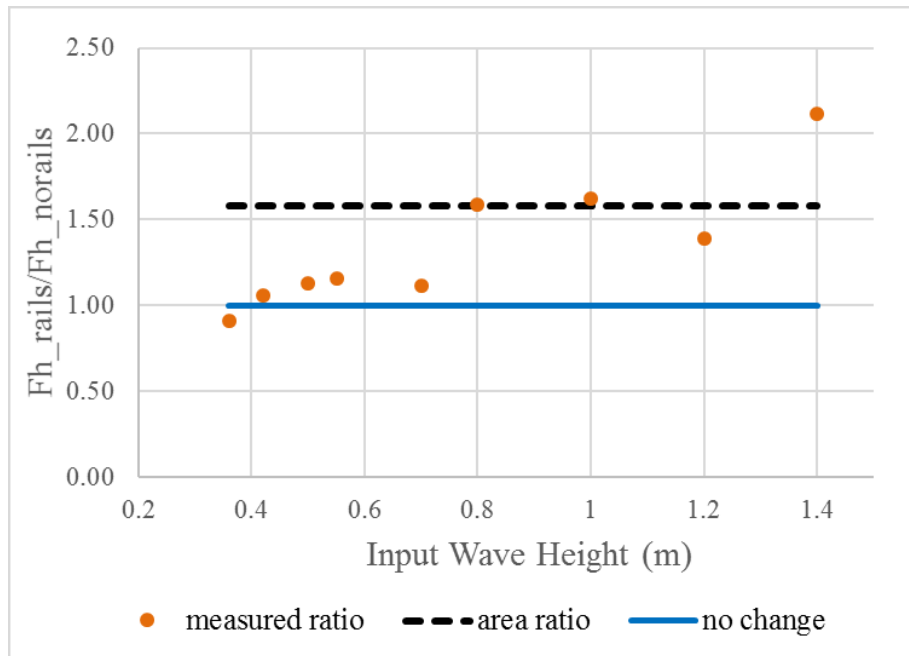


Figure 7.12: Ratios of maximum total horizontal force recorded in the shear keys of the bridge with rails relative to the one without rails

7.6.2 Other design parameters

The previous sections revealed that the addition of the solid rails affected not only the total horizontal forces (which was expected), but other parameters, such as, the vertical forces, overturning moments and demand in individual structural components (e.g. bearings and columns). The main parameters of interest are presented in Figure 7.13, in terms of ratios of the maximum forces measured in the specimen with rails relative to the one without rails. This figure highlights that the addition of the rails:

1. Has a minor effect on the total uplift forces for all the tested waves. This increase is about 7% on average, which means that it will most likely not affect the design.

2. Has a very inconsistent effect on the maximum overturning moment, with a negligible effect for some wave heights and a major effect for some other ones (e.g. for $H=1.40\text{m}$). Interestingly, for the waves that introduce a significantly larger load with the addition of the rails, this increase seems to be close to the area (or height) ratio $(h_{\text{girder}}+h_{\text{rails}}/ h_{\text{girder}})$. This indicates that increasing the max OTM of the bridge without rails by the area ratio is a reasonable assumption. In this case the maximum OTM used for the design of a bridge with rails could be:

$$\text{OTM}_{\text{w/rails}}=(h_{\text{girder}}+h_{\text{rails}}/ h_{\text{girder}})* \text{OTM}_{\text{norails}} \quad (7-3)$$

3. A potential physics-based alternative approach for the calculation of the increased moment at the beginning of the inundation (OTM_1) would be to assume that the maximum $F_{\text{w/rails}}$ (e.g. calculated from eq. 7-2) is applied at the mid-height of the bridge $[(h_{\text{girder}}+h_{\text{rails}})/2]$, while the maximum uplift force is applied below the offshore overhang (at the mid-length of the overhang). Further investigation is required in order to determine how much smaller OTMs would this approach give relatively to (eq. 7-3), as well as, the measured max OTM.
4. Causes a noticeable and a major increase in the uplift forces of the offshore and onshore bearings respectively. This increase can be up to 33% for the offshore bearings with an average increase of about 12%, while the respective increase of the uplift demand in the onshore bearings is 90% (max) and 37% (average). The increase of the uplift force in the offshore bearings can be explained by the increase of the OTM (at the beginning of the inundation), while the increase of the demand in the onshore bearings could be attributed to the modification of the hydrodynamic flow which changes the pattern of the longer duration uplift and its interaction with the moment as the inundation of the bridge progresses. The increase of the uplift in offshore bearings should be captured by the application of the increased OTM_1 , however, capturing the exact increase of the uplift in the onshore bearings is much more challenging. Luckily, despite the increase of the uplift forces in the onshore bearings, their maximum demand still remains smaller than the demand in the offshore bearings, which means that the design of the bearings (in tension) would not be affected if all the bearings were designed to have the same capacity.
5. Results in the increase of the total downward (slamming) force up to 109% and 47% on average. The maximum increase occurs for unbroken solitary waves, while for bores the increase for all the tested heights is consistently close to the area ratio. Therefore, in lack of a more sophisticated approach and assuming that the downward force on the bridge without rails is known, the downward force for the bridge with rails can be calculated via:

$$\text{Fdown}_{\text{w/rails}}=(h_{\text{girder}}+h_{\text{rails}}/ h_{\text{girder}})* \text{Fdown}_{\text{norails}} \quad (7-4)$$

6. Has the most significant effect on the downward force (compression) of the bearings and especially the onshore ones. For the latter bearings, the rails can increase the compression by up to 254% and 84% on average. This enormous increase is the result of the combination of two phenomena that occur simultaneously, including (a) the increase of the total downward force (see eq. 7-4), and (b) the generation of a previously non-existent clockwise moment (OTM_2) when the bore hits the onshore rail (see section 7.3 and Fig. 7-5). This effect on the maximum compression of the bearings could be considered in the design of the bearings via two different methods: (a) the development of normalized downward bearing forces (similar to the normalized uplift bearing demand shown in Fig. 7-14), or (b) the calculation of the bearing forces via static analyses of a bridge model where the $F_{down\ w/rails}$ and OTM_2 are applied simultaneously on the superstructure. In lack of a more sophisticated approach for the estimation of OTM_2 (generated by bores), it could be assumed that it is equal to OTM_2 . Note that this is not true for unbroken solitary waves, since for some heights (e.g. $H=0.70m$ in Fig. 7-5) the OTM_2 could be up to twice of OTM_1 .

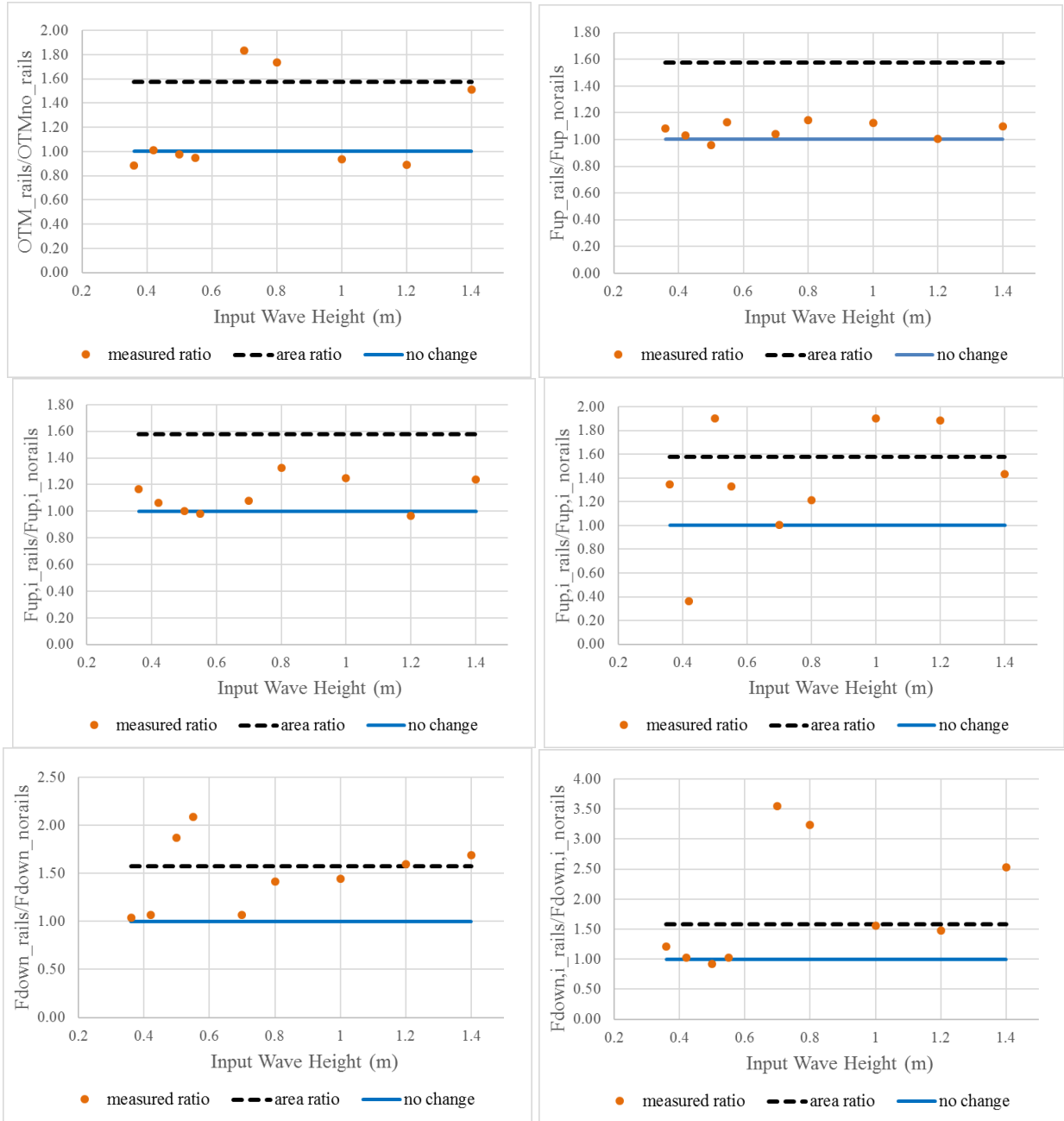


Figure 7.13: Maximum overturning moment (top-left) and deck total uplift (top-right), maximum uplift in the offshore (center-right) and onshore (center-left) bearings, and maximum downward total force (bottom-left) with the maximum downward force in the onshore bearings (bottom-right) of the bridge with rails relative to the one without rails

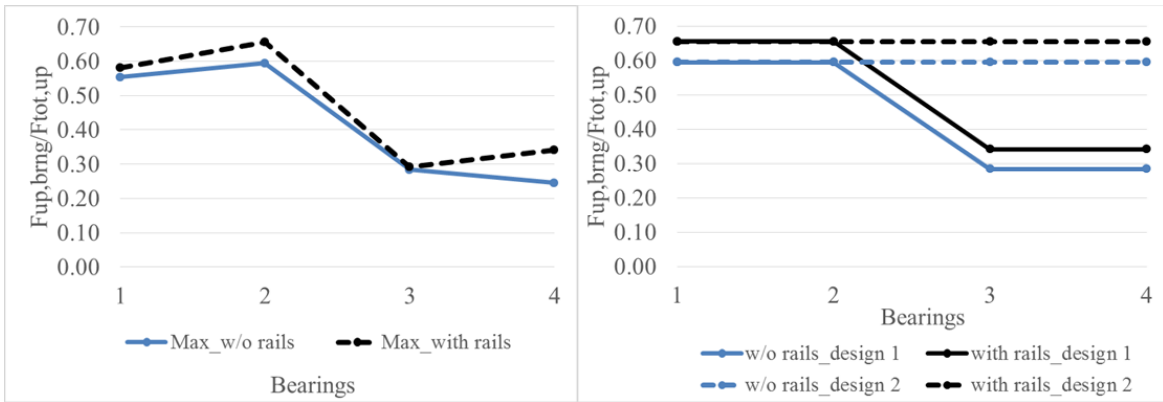


Figure 7.14: Envelopes of normalized measured uplift in sets of bearings (left) and potential design curves (right), for a bridge with elastomeric bearings, cross-frames, and with or w/o solid rails

8.0 TSUNAMI FORCES ON A SKEW BRIDGE AND DEMAND IN INDIVIDUAL STRUCTURAL COMPONENTS

8.1 DESCRIPTION OF SPECIMEN AND EXPERIMENTAL PROGRAM

Given the popularity of skewed bridges on the West Coast of the United States (e.g. in California) and the challenges/uncertainties in investigating the tsunami demand on such complex structures numerically, it was decided to conduct hydrodynamic experiments of a skewed bridge. Due to funding and time limitations, it was possible to test only one skew angle and it was selected to investigate a 45 degrees angle. The objective was to generate high-quality data that will cover the upper and lower end of the spectrum of typical bridges, so conducting experiments of tsunami impact on a straight bridge (no skew) and a 45° skew angle was expected to achieve this objective. Once computational fluid dynamic (CFD) methods and solvers are calibrated and validated for these two cases, then the remaining skew angles (within 0° and 45°) could be investigated numerically. Note that the selected skew angle was also convenient because it allowed the utilization of the existing bolt hole patterns in the walls of the flume and the same experimental setup (e.g. support beams, bent caps, bearings etc) as in the straight bridge experiments with major modifications only in the connecting elements between the bearings and the bent caps. A view of the testing setup is shown in Fig. 8.1 and Fig. 8.2.

The skewed bridge was a composite bridge model with three I-girders and constructed at a 1:5 scale. The prototype bridge was analyzed following the AASHTO LRFD Bridge Design Specifications, 2012, and the resultant forces and moments were scaled down to a 1:5 scale and were used for the design of the model bridge specimen. All the load combinations and requirements specified in AASHTO were considered in order to design a realistic bridge in accordance with the current practice. For design purposes the structure was assumed to be located on the West Coast of the US in a Seismic Zone 3 and a site class B. This was done due to the likelihood of tsunamis inundating the West Coast if a large magnitude earthquake occurs along the Cascadia subduction zone. For the seismic design, response spectra were generated using the USGS website for several cities on the west coast (e.g. San Francisco, Seattle, Anchorage). The chosen response spectra had $A_s=0.45g$, $SDS=1.0g$ and $SD1=0.33g$. Limit states for strength, constructability, service, fatigue and fracture were considered.

The width of the bridge deck was 1.94m in order to match the one of the straight bridge and its length was 5.04m. This means that the actual skew angle was 46.6° instead of the targeted 45° due to adjustments that had to be implemented in order for the structure to fit in the flume. Traditionally, the OSU wave flume had been used for 2D hydrodynamic testing, so fitting such a complex 3D structure (with steel connections that had 1/16in tolerances) required a several months-long iterative design process with careful consideration of the wave flume dimensions at the specific location. As shown in Fig.8.1 the bridge has steel girders which are connected with L-shape cross-frames at the end supports and at third points. The steel girders were W8x13 and were readily available in the US market. Double angles were used for all the cross-frames in order to satisfy slenderness ratios and prevent local buckling and lateral torsional buckling

during the construction process, as well as, to resist the large forces during the design seismic event.

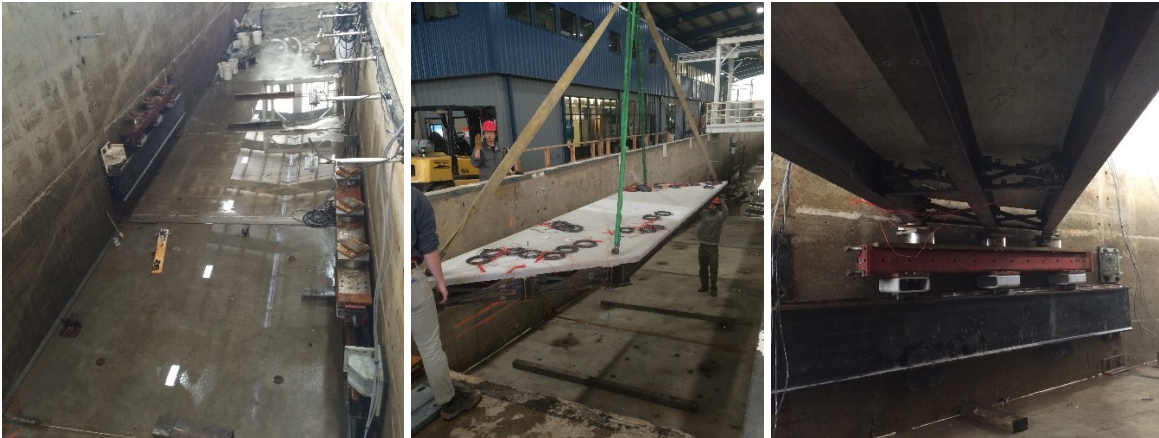


Figure 8.1: Experimental setup of the skew bridge in the Large Wave Flume at OSU, including the abutments (left), deck (center) and whole system (right)

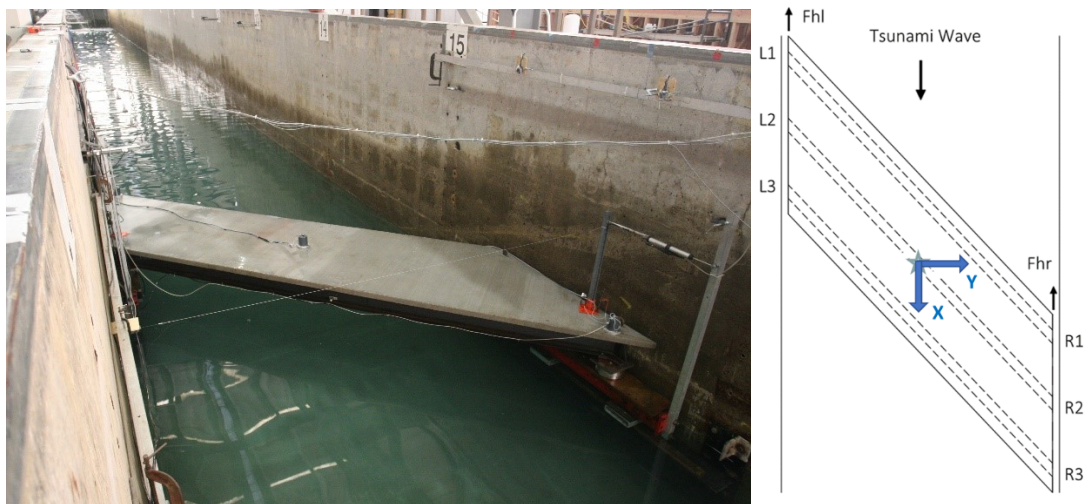


Figure 8.2: Skew bridge during the hydrodynamic testing (left) and a plan view of the structure showing the location of the load cells (right)

In the hydrodynamic experiments, extensive instrumentation was used in order to record both the wave/flow characteristics, the applied pressures and the dynamic response of the bridge (accelerations, displacements, strains and forces). The instrumentation related to the flow characteristics was the same as in the straight bridge experiments (found in Chapter 1 of this report). Pressure gages were installed at the mid-length of the bridge following a similar pattern as the one shown in Figure 1.17. In addition to that, one pressure gage was installed close the supports in order to investigate the 3D effects. Triaxial accelerometers were installed on the top face of the concrete slab at three locations, including the center of the deck and the acute corners (offshore and onshore), as shown in Fig. 8.2. Vertical string pots were installed at the locations of the lifting lungs (locations R1 and R3 in Fig. 8.2), while two horizontal string pots and two

Novotechniks displacement transducers were installed at the onshore corners (acute and obtuse) in order to record the x-displacements of the bent cap and the deck respectively. In addition, another string pot was installed at the onshore acute corner in order to record its Y-displacement.

To get a direct measurement of the demand in the structural components of the bridge, strain gages were attached on the cross-frames and eight uniaxial load cells were installed at different locations. Two of the load cells measured the horizontal force in x-direction at the two abutments, while the remaining six load cells measured the vertical force of each bearing. Utilizing the recorded bearing forces in the vertical direction it was possible to calculate the roll (M_x) and pitch moment (M_y), which will prove useful in explaining the observed behavior. Moreover, using the measured forces in the X-direction the yaw moment (M_z) was also estimated, however, it must be clarified that this is only an approximate estimate because the forces in the Y-direction, which could contribute to M_z , were not measured in the experiments due to the lack of multi-axial load cells in the lab’s inventory. Following the same approach as for the straight bridge experiments, both unbroken solitary waves and bores with a height range of 0.36m-0.70m and 0.90-1.40m respectively, were tested (see Table 8.1). However, due to time limitations only one water depth was investigated, which was 2m at the location of the wavemaker and due to changes in bathymetry it was reduced to 1.16m at the bridge location. Note that in the following sections the term “horizontal” or “lateral” force or “ F_h ” will be referring to the force in X-direction (F_x).

Table 8.1: Wave Heights and Water Depths Tested in the Skewed Bridge Experiments

Water Depth (m)	Wave height (m)	Wave Type
2.00 (at the bridge location it was 1.16)	0.36	Unbroken solitary
	0.42	Unbroken solitary
	0.55	Unbroken solitary
	0.70	Unbroken solitary
	0.90	Bore
	1.00	Bore
	1.20	Bore
	1.40	Bore

8.2 TOTAL FORCES AND MOMENTS

Figure 8.3 shows selected time-histories of an unbroken solitary wave and three bores. The skewed bridge seems to be subjected to an initial long duration uplift force with local fluctuations as the wave impacts the girders, followed by a downward force, which is larger in magnitude than the uplift one. Simultaneously it is subjected to a horizontal force F_h (in the X-direction, so this is actually F_x), which in contrast to the straight bridge does not seem to have large magnitude impulsive peaks, and therefore the F_h is not governed by the short-duration slamming component but a longer duration force. On the other hand, the force histories also exhibit characteristics that are in agreement with the straight bridge, including the fact that (a) unbroken solitary waves introduce larger uplift than horizontal forces, while the bores cause an opposite effect, and (b) the maximum F_x and F_{uplift} do not occur at the same time. In fact, for the tested skewed bridge, the uplift force tended to get maximized before the lateral one (F_x).

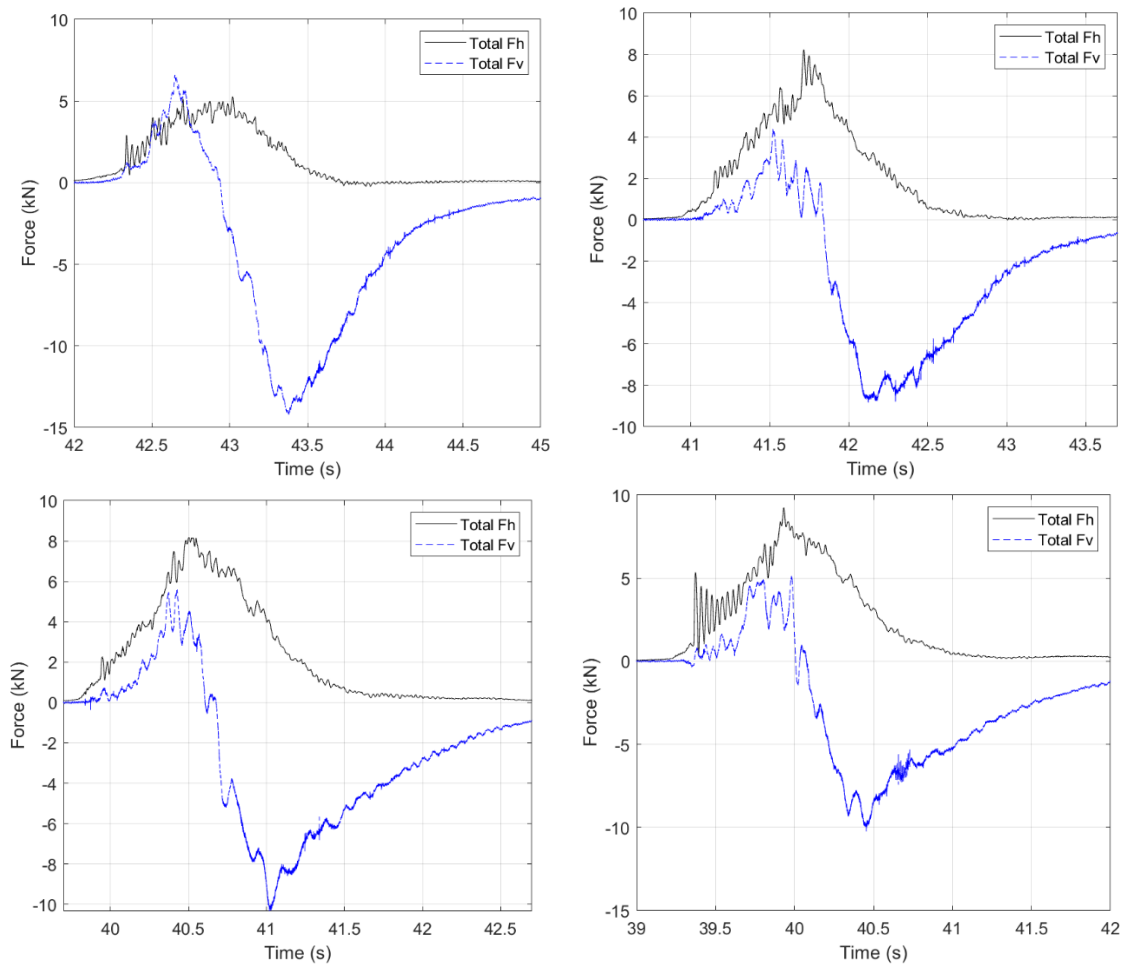


Figure 8.3: Total horizontal and vertical forces on the skew bridge for H=0.70m (top-left), H=0.90m (top-right), H=1.20m (bottom-left) and H=1.40m (bottom-right)

In addition to the horizontal and uplift forces, the experimental results of the straight bridge revealed that tsunamis generated significant overturning moment (M_y), which can have a dominating role on the demand and design of structural components. Therefore, given the observed significance of tsunami-induced moments, the pitch (M_y), roll (M_x) and yaw (M_z) moments were calculated for skew bridges and are presented in Fig. 8-4. In this figure, as well as, in the remaining figures of this chapter the moments were considered positive when they were clockwise (which means that the positive values are in the direction of $-x,+y$ and $-z$ of the respective axes). A close look at the figure reveals the following about each moment:

- **M_y :** As expected, when the wave hits the offshore acute corner it starts applying uplift pressures on the overhang, which generate a clockwise overturning moment. As the wave starts inundating the deck, the slamming force on the top of the acute corner generates a significant counterclockwise moment. Although the above trend of the tsunami applying a clockwise moment followed by a counter-clockwise one is consistent with the straight bride experiments, however, in the case of the skewed bridge there is a third major clockwise moment, which seems to be steady-state and is

generated when the whole deck becomes inundated. Interestingly, this moment seems to be having a larger magnitude than the clockwise moment applied at the beginning of the inundation when the wave hits the offshore overhang. The reduced moment of the skewed bridge at the latter instant is another fundamental difference between straight and skewed bridges.

- **M_x**: Although in straight bridges the roll moment is zero, due to a symmetric geometry and a close to symmetric flow (in reality the flow of a turbulent bore is never exactly symmetric or 2D, even if the wave hits normal to the bridge length), in skew bridges a significant roll moment is generated. The M_x histories follow similar trends with M_y, and it is characterized by three major peaks, a clockwise one at the beginning of the inundation, a counterclockwise when the wave slams the top surface, and a second longer duration clockwise moment at the end. Considering that the normal distance between the two abutments is 3.46m and the magnitude of M_x is e.g. for H=0.90m about 8kN-m, the additional uplift introduced in one of the abutments would be $8\text{kN-m}/3.46\text{m}=2.31\text{kN}$, which is 57% of the maximum total uplift of about 4kN. This is a clear demonstration of the importance of M_x for skewed bridges.
- **M_z**: As mentioned before the figures of M_z shown in this chapter are approximate due to the lack of considering the contribution of the forces in the Y-direction. Nonetheless, these approximate time-histories are going to be helpful in interpreting some of the follow-up results related to the maximum demand in individual structural components. At first sight the M_z time-histories of Figure 8.4 seem to be reasonable and consistent with the other moments, by exhibiting a counter-clockwise moment when the wave slams the offshore acute corner followed by a counter-clockwise moment as the wave propagates through the bridge and pressures are applied along the whole length of the girders. These M_z are expected to have a significant role for the horizontal demand in structural component (e.g. abutment, shear key, columns etc) similarly to the importance of M_x for the uplift demand, since the magnitudes of M_z are very large relative to the total tsunami induced horizontal load (F_x). In fact, if we repeat the same calculation for H=0.90m that we did for M_x, then the M_z would increase the demand in one abutment by about 31%. For other waves this percentage can reach 46%.

8.3 TSUNAMI-INDUCED DEMAND ON BENT CAPS/ABUTMENTS

8.3.1 Lateral forces

Although the above information on the total forces and moments advances the understanding of the tsunami-induced effects on bridges, in order to achieve a tsunami-resilient bridge design one has to know the maximum demand for each structural component. Therefore, Fig. 8.5 presents the measured horizontal forces (F_h) that each abutment has to withstand together with the total horizontal force. Interestingly, contrary to straight bridges, in the skewed bridge (i) the demand in each abutment is not maximized simultaneously and (ii) the two abutments are not sharing equally the total tsunami induced horizontal force. In fact, the time-histories reveal that the left abutment, which is the one that supports the offshore acute corner, attracts the majority of the tsunami horizontal load, which is reasonable since the tsunami pressures are applied first on the

offshore girder close to the left abutment. In addition to the almost out-of-phase maximization of the demand in each abutment (or bent-cap) another interesting finding useful for the design of the abutments is that each of them seems to be attracting more than 50% of the total horizontal force ($F_{X_{tot}}$).

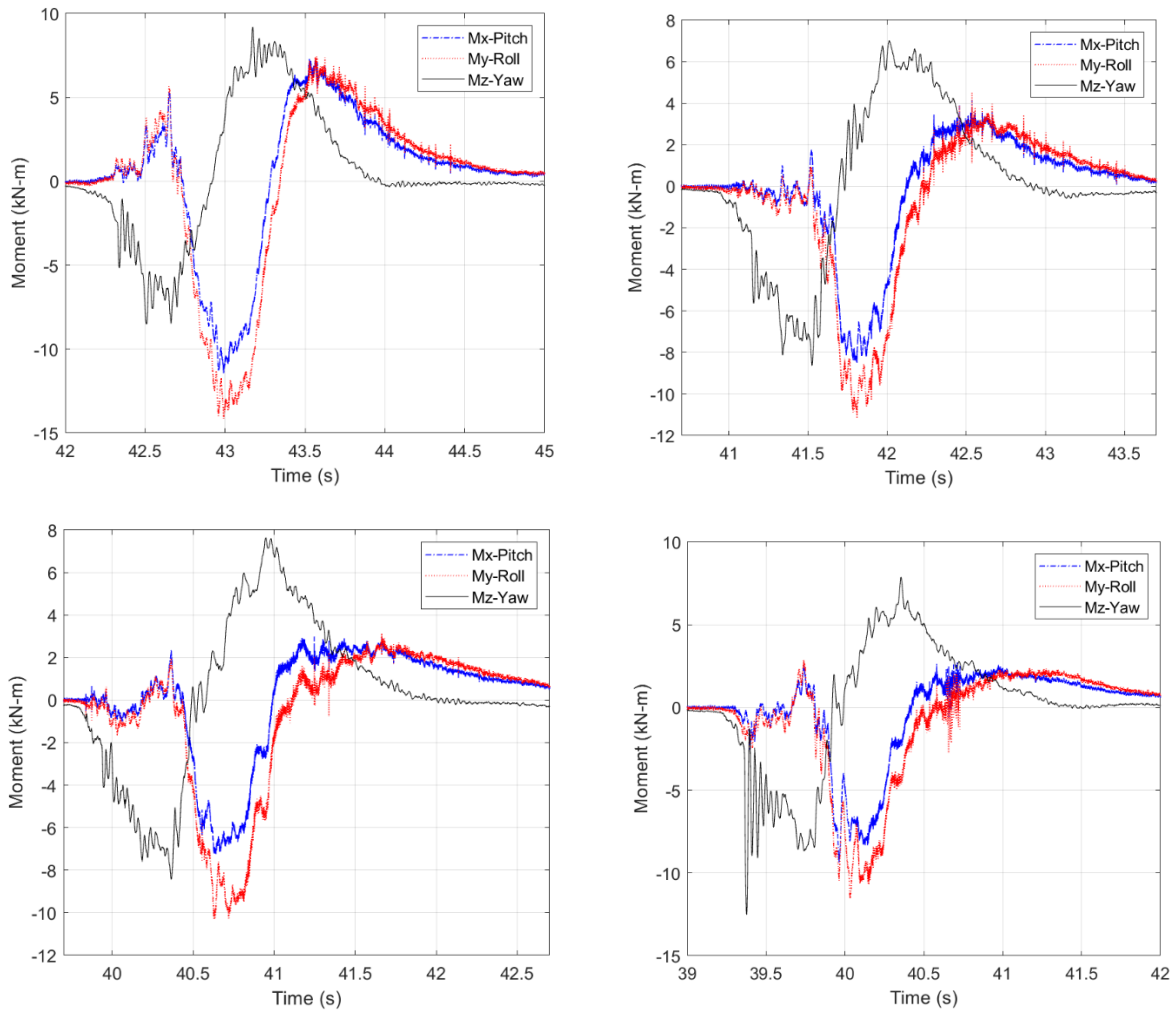


Figure 8.4: Moment histories on the skew bridge for H=0.70m (top-left), H=0.90m (top-right), H=1.20m (bottom-left) and H=1.40m (bottom-right)

To obtain a more general view of the behavior Figure 8.6 shows the ratios of the maximum force in each abutment relative to the maximum total force of the deck (the two maxima might have occurred at different instants of the inundation process) for all the tested waves. The left graph corresponds to unbroken solitary waves and the right one to bores, while in both graphs abutment 1 is the left one. This figure corroborates the previous observations and finding regarding the higher than 50%* $F_{X_{tot}}$ demand in the abutments. In fact, it reveals that:

- The maximum horizontal force (F_x) in the left abutment reach 96% of $F_{X_{tot}}$ for unbroken solitary waves, which practically means that one abutment has to be designed for the total tsunami-induced horizontal force assuming that the other

abutment is taking no force at all. On the other hand, for bores the maximum demand is 72%, which is still considerably more than the 50% an abutment of a straight bridge would have to withstand.

- For all the tested bores, the left abutment (the one that supports the offshore acute corner) attracts larger forces than the right abutment. For solitary waves though, some heights are consistent with the bores, while others show a totally opposite behavior, with the right abutment/bent-cap attracting larger horizontal forces than the left-one.

To decipher the reason behind the observed behavior, Figure 8.7 plots the time-histories of the horizontal forces in each abutment, the total tsunami-induced horizontal force and the yaw moment M_z . As expected, this moment has an important effect on the horizontal forces that each abutment has to withstand. In fact, the time-histories reveal that the maximum demand in the left abutment is actually maximized when the total horizontal force is large (but smaller than the maximum) and the counter-clockwise moment M_z is maximized. On the other hand, the demand in the right abutment (that supports the offshore obtuse corner) is maximized either at the instant of $\max F_{X_{tot}}$ or $\max M_z$ (clockwise) or in between these two instants. Predicting the actual instant at which the demand in the right abutment is maximized can be challenging due to the complex temporal and spatial evolution of the pressures applied by the bore.

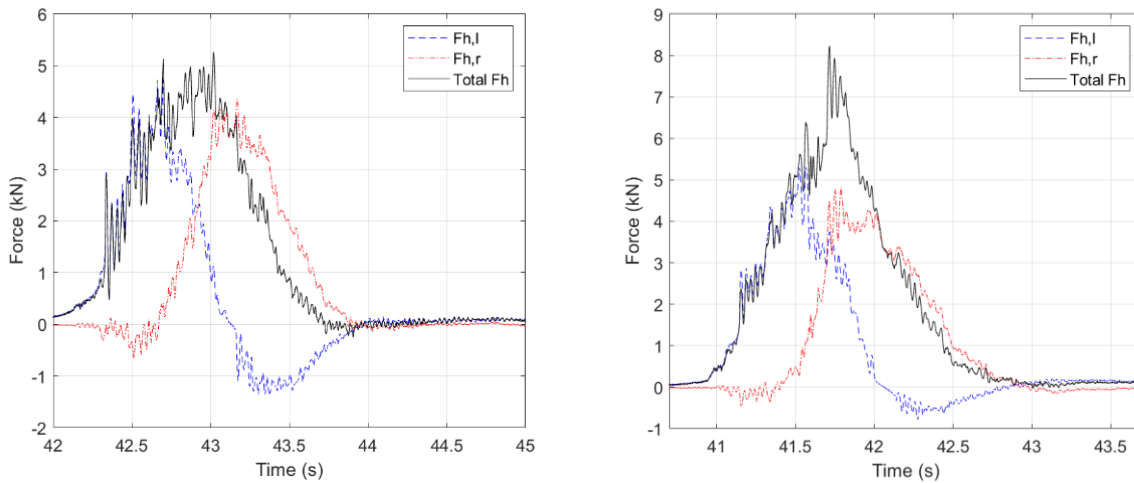


Figure 8.5: Lateral force histories (in X direction) per abutment of the skew bridge for $H=0.70\text{m}$ (left) and $H=0.90\text{m}$ (right)

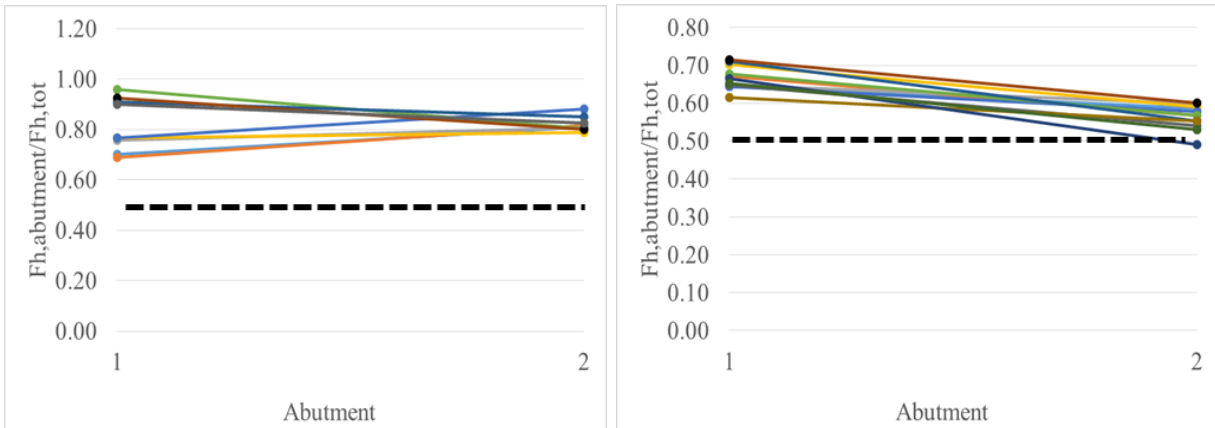


Figure 8.6: Ratios of the maximum lateral abutment forces to the total lateral force for unbroken solitary waves (left) and bores (right)

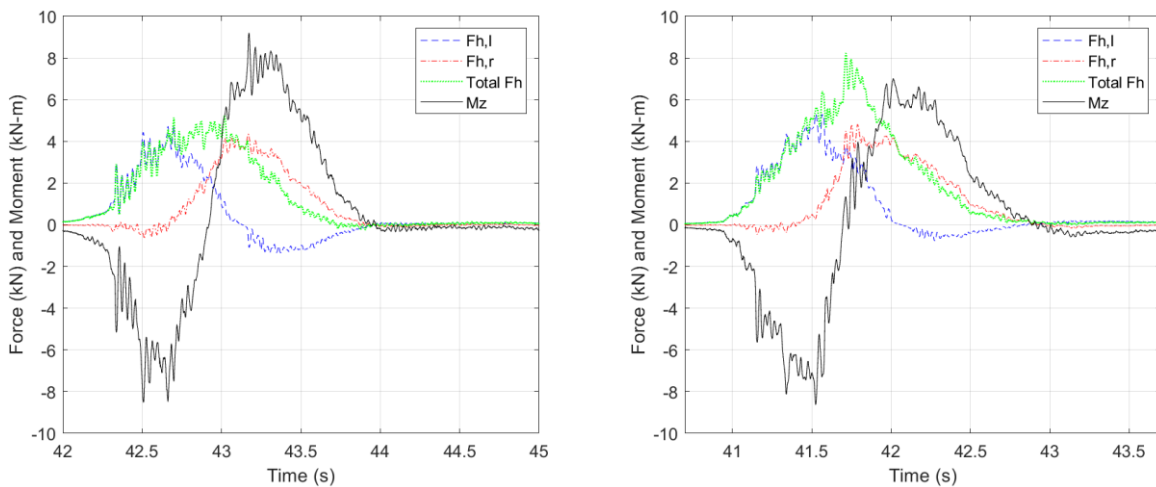


Figure 8.7: Lateral force histories per abutment of the skew bridge, and moment histories for an unbroken solitary wave with $H=0.70\text{m}$ (left) & and a bore with $H=0.90\text{m}$ (right)

8.3.2 Vertical forces

In addition to the lateral forces, the abutments and the bent caps should be able to withstand a certain amount of uplift load. Figure 8.8 presents the time histories of the vertical forces in each abutment together with the total vertical force and yaw moment (M_z) on the structure. The figure, which presents the results for an unbroken solitary wave and a bore, demonstrates that:

- Similarly to the horizontal (F_x) forces in the abutments, the vertical forces do not get maximized at the same instant in the two abutments, with the uplift force in the left abutment being maximized before the one in the right abutment, and each abutment has to withstand uplift forces larger than 50% of the total deck uplift ($\max F_{up,tot}$)
- The demand in both abutments seems to be governed by the roll moment (M_x), since the maximum uplift in the left abutment occurs when the counter-clockwise moment

reaches a large value at the beginning of the inundation and the total uplift reaches its maximum value, while the uplift in the right abutment is maximized when the M_x is maximized in the other direction. Therefore, the maximum uplift in the offshore abutment coincides always with the maximum total uplift, which is not necessarily the case for the right abutment.

Figure 8.9 shows the ratios of the maximum uplift force in each abutment relative to the maximum total uplift of the deck, for all the tested waves. The left graph corresponds to unbroken solitary waves and the right one to bores, while in both graphs abutment 1 is the left one. Moreover, the different solid lines correspond to different wave heights, while the dashed line represents the 50% ratio that each abutment would have attracted if the bridge was straight. This figure verifies the trends revealed by the time-histories, and in fact it reveals that for unbroken waves the maximum uplift force in the right abutment is 146% of the total deck uplift ($F_{up,tot}$), while for bores the respective ratio is 104%. Interestingly in the case of bores, although when it came to the horizontal abutment force the left one (which was impacted first by the wave) always witnessed the largest demand among the two abutments, this is not true for the uplift demand, which can be maximized in any of the two abutments depending on the wave height. For the design of bridges impacted by bores, a reasonable assumption would be to design each abutment for the total deck uplift, instead of distributing the total force to the two abutments.

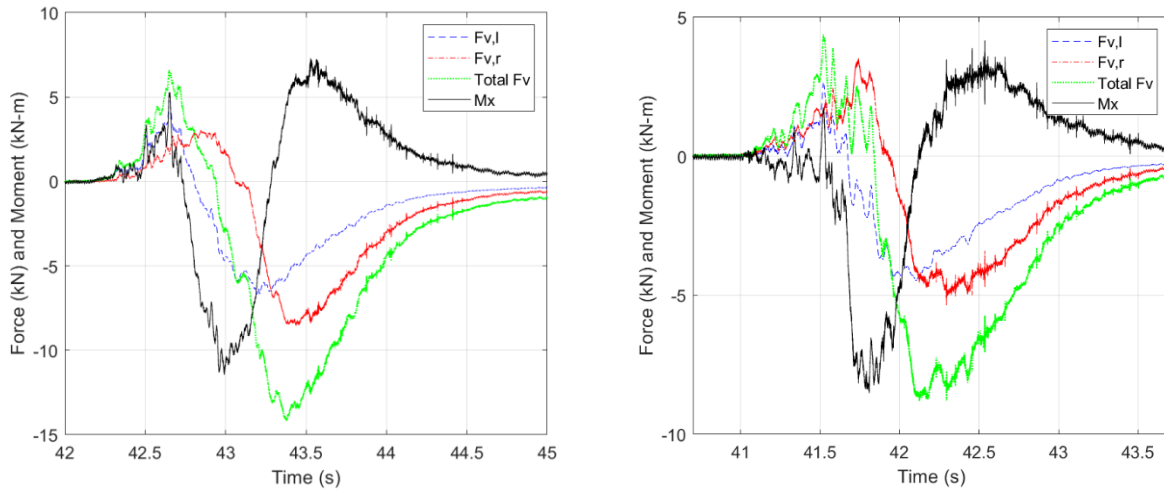


Figure 8.8: Roll moment, total vertical force and vertical force histories in each abutment of the skew bridge for an unbroken solitary wave with $H=0.70\text{m}$ (left) and a bore with $H=0.90\text{m}$ (right)

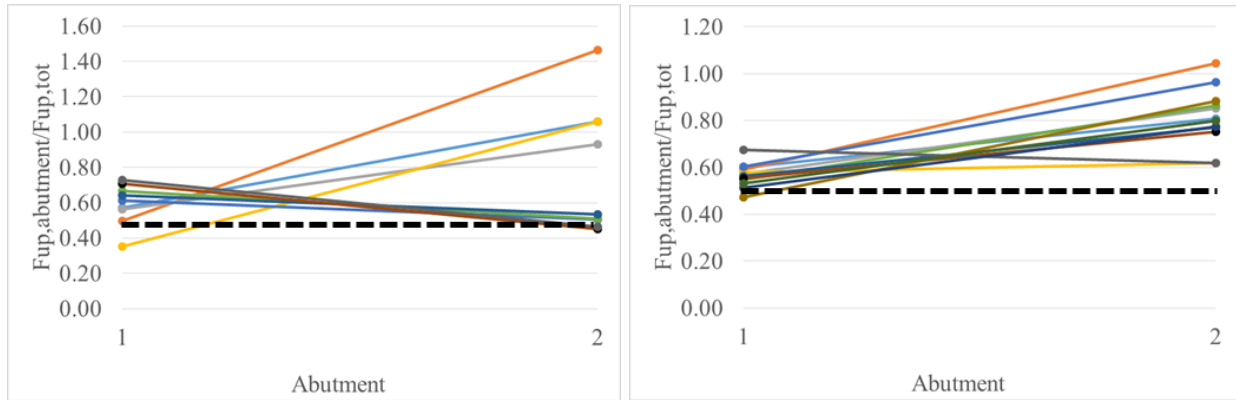


Figure 8.9: Ratios of the maximum uplift abutment forces to the total uplift force for unbroken solitary waves (left) and bores (right)

8.4 FORCE DISTRIBUTION IN STEEL BEARINGS

Given the fact that in the recent tsunami events, the majority of the failed bridges witnessed damage in the bearings or their connections to the superstructure or the substructure, it is of paramount significance to investigate the tsunami-induced demand in these components. To this end, Figure 8.10 shows the time-histories of the vertical force histories in the six bearings of the skewed bridge. In contrast to the straight bridge, where the bearings of the same girder (located at the two supports/bent-caps) witnessed identical forces, in the skewed bridge this is not the case, with the bearings of the left abutment attracting their maximum uplift before the respective bearings of the other abutment. The reason for this fundamental difference is the complex geometry of the bridge that leads to gradual application of the tsunami pressures on the girders, and the complex temporal and spatial evolution of the tsunami-induced loads during the bridge inundation. Moreover, while in the straight bridge all the sets of bearings witnessed uplift forces at some point of the inundation process, in the skewed bridge the bearings below the onshore obtuse corner tended to witness small and in some cases even zero uplift.

Figure 8.11 presents for each abutment the time-histories of the recorded vertical forces in each bearing together with the vertical force of the respective abutment. Presenting the time-histories in this way reveals the existence of similarities with the straight bridge, such as the fact that the offshore bearings of each abutment attract the largest uplift among all the bearings of the same abutment, which could be equal to the maximum abutment uplift (F_{vl} or F_{vr}). Despite the similar trends, the percentage of the uplift force that each bearing has to withstand is significantly larger than the ones in the straight bridge.

Figure 8.12 shows the maximum uplift in each of the six bearings of the bridge relatively to the total deck uplift. These ratios are then compared with a commonly used assumption in previous studies of straight bridges, according to which the total uplift could be equally distributed to all the bearings meaning that each bearing would have to withstand $1/6=16.67\%$ of $F_{up,tot}$. Given the fact that the bearing numbers 1, 2, 3, 4, 5, 6 in the horizontal axis of the figure correspond to bearings L1, L2, L2, R3, R2, R1 respectively, it can be concluded that:

- Although all the bore heights introduce similar trends in the maximum bearing forces, this is not the case for the unbroken solitary waves, which can introduce significantly different trends depending on the wave height. For example, for some solitary waves the bearing L1 attracts a larger force than L2, while for others the opposite happens. A possible reason is that fact that some of the solitary waves were relatively small and would not inundate the top deck as much as the large wave heights, causing potentially a different response and uplift distribution.
- For all the tested bores the bearings of the onshore corners have to withstand the smallest uplift among all the bearings. On the other hand, the bearing of the offshore obtuse corner attracts the largest percentage of the total uplift force $F_{up_{tot}}$ reaching 95%, followed usually by the bearing of the offshore acute corner which reaches 45%. Both of these bearings clearly have to withstand significantly larger amounts of the tsunami-induced uplift force than the 16.67% suggested by an equal distribution assumption. It must be noted that although the large uplift in the offshore bearings is expected due to the significant overturning moment, the fact that the offshore bearing below the obtuse corner (R1) attracts twice as much uplift as the acute one (L1) is surprising. A possible explanation is that when the wave hits initially the offshore girder it gets redirected towards the obtuse offshore corner, which could focus the energy of the bore on the right corner. Moreover, it is also possible that the flume of the wall next to right abutment obstructs the redirected bore flow more than the backwall of a real bridge, since in the latter case the bore could move freely in any direction after it inundated the top of the deck.

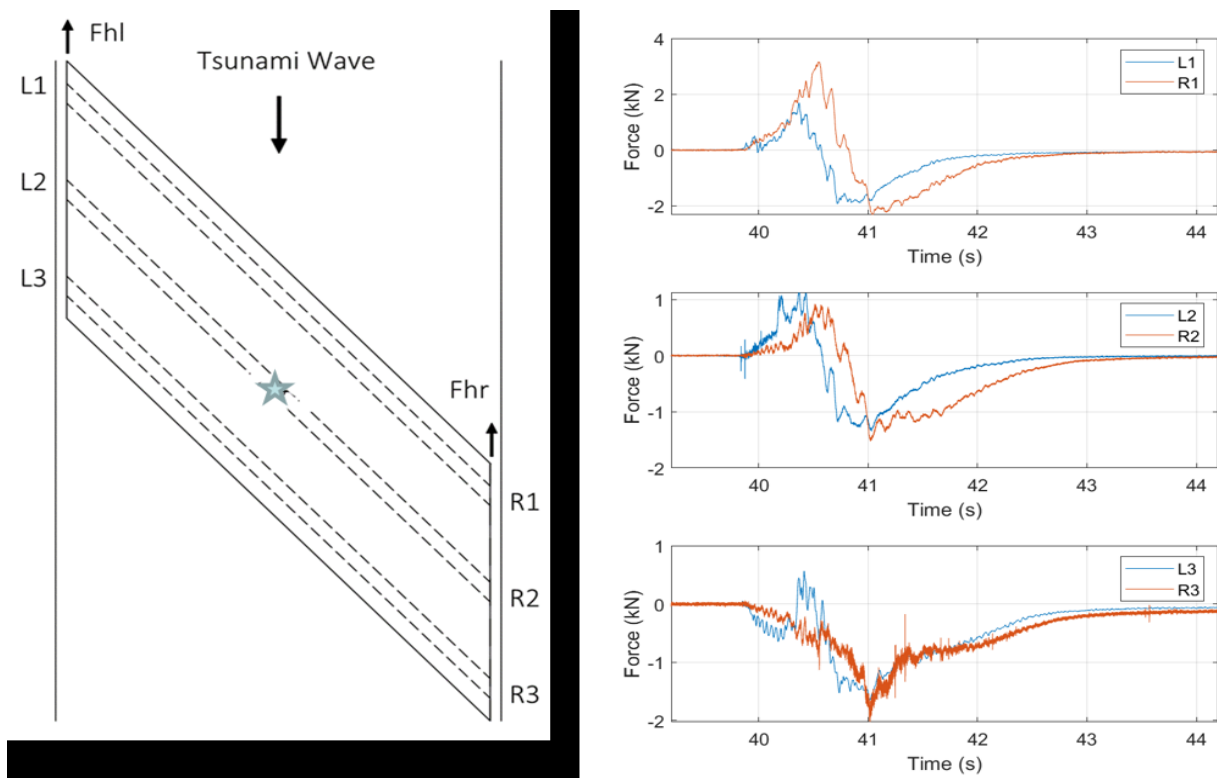


Figure 8.10: Vertical force histories in steel bearings for $H=0.70m$

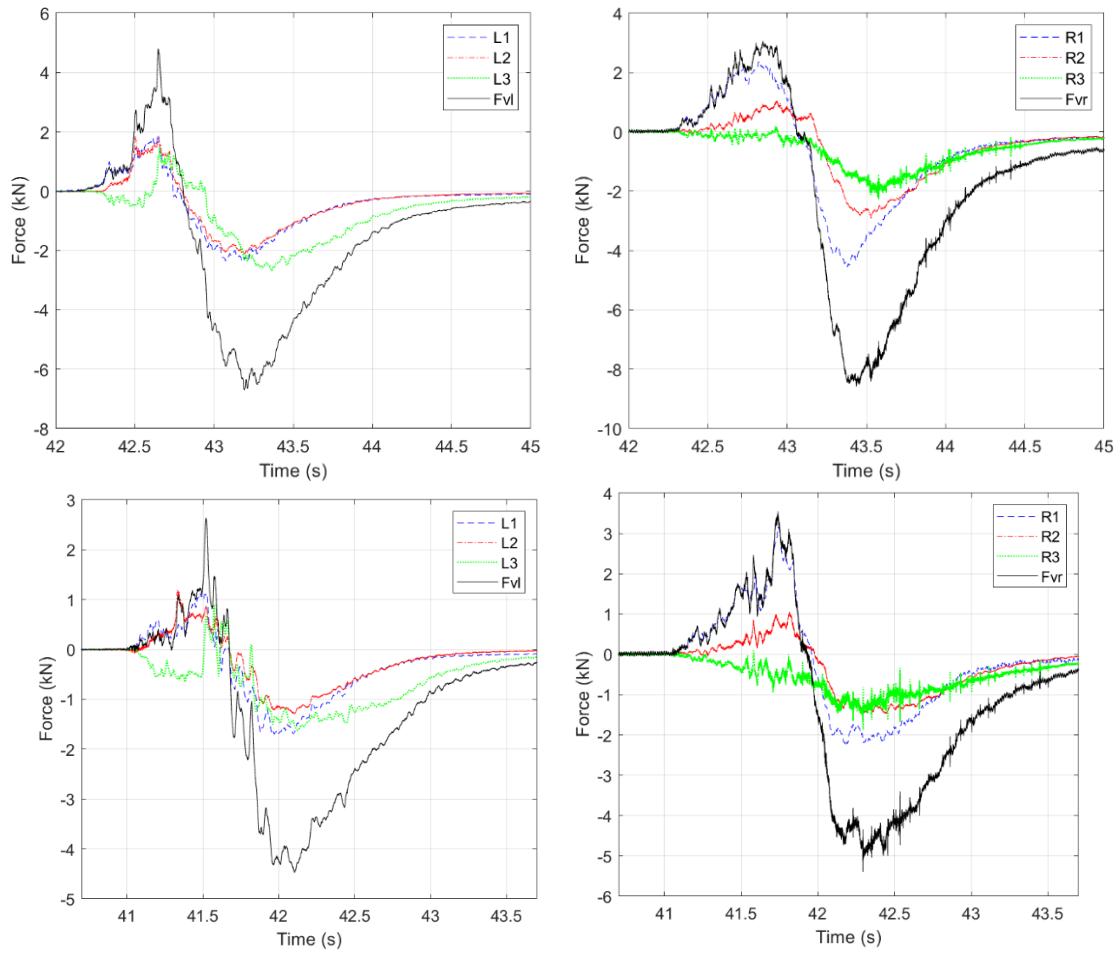


Figure 8.11: Vertical force histories in the steel bearings of the left and right abutment for an unbroken solitary wave with $H=0.70\text{m}$ (top) and a bore with $H=0.90\text{m}$ (bottom)

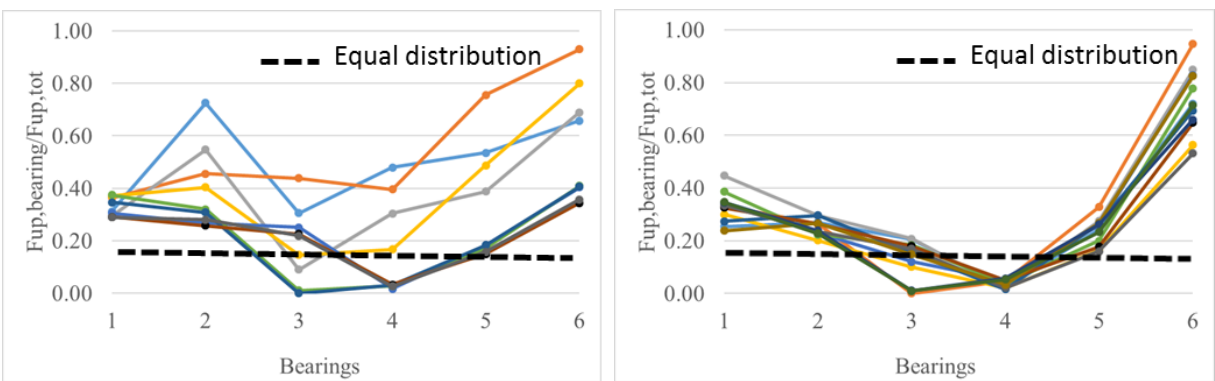


Figure 8.12: Ratios of the maximum uplift forces in individual bearings (top) relative to the total uplift force for unbroken solitary waves (left) and bores (right)

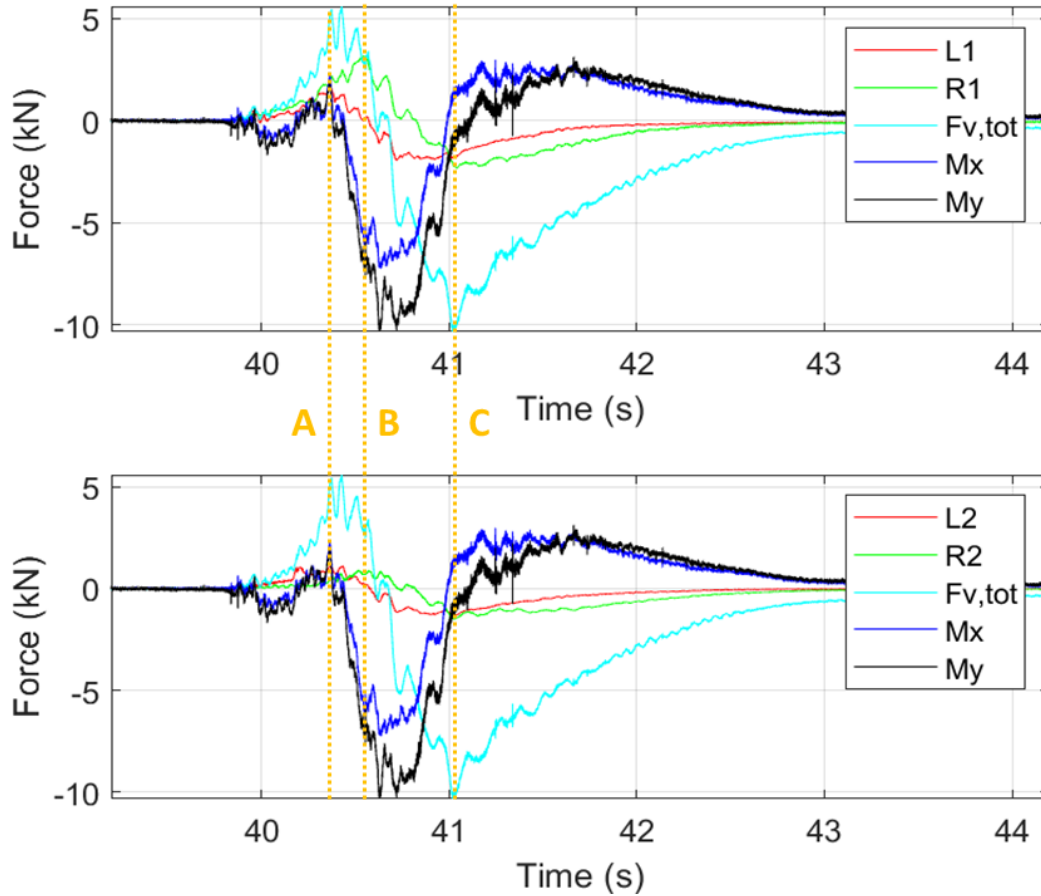


Figure 8.13: Roll and pitch moments together with the vertical bearing forces for a bore with H=1.20m

To advance the understanding of the demand in the bearings Figure 8.13 presents the time-histories of the vertical forces in the bearings L1, L2, R1, R2, together with the total vertical force of bridge and the moments Mx and My. This figure can prove useful for the development of simplified methodologies because it reveals the critical load cases and parameters that affect them. Although the figure presents the results for a selected bore height, the trends are similar for all the waves and are summarized below:

- The maximum uplift in the bearings L1 occurs when the total uplift ($F_{up,tot}$) is maximized (orange line A in the figure). At that instant the moments Mx and My exhibit the first large clockwise peaks (M_{xA} and M_{yA}). The M_{xA} introduces additional uplift in the bearings of the left abutment, while the M_{yA} peak introduces uplift in the offshore bearings, so both of them contribute to the large uplift witnessed by the bearing of the offshore acute corner L1. This means that for design purposes a load case that includes the application of $\max F_{up,tot}$, M_{xA} and M_{yA} should be considered.

- On the other hand, the maximum uplift in the onshore bearings occurs at a random instant, after the occurrence of $\max F_{up_{tot}}$ while the M_x and M_y are counterclockwise (orange line B in the figure). Depending on the wave height impacting the bridge, at this instant, the total uplift force ranges between 60%-90% of $\max F_{up_{tot}}$, while the moments M_x and M_y are in the range of 70%-100% of their maximum counterclockwise magnitudes ($\min M_x$ and $\min M_y$ in the figure).
- The last parameter of interest for the design of the bearings is the maximum downward force that each of them has to withstand. As shown in the figure, this downward force tends to be maximized when the total downward force is maximized (Line C), at which point the moments are quite small, with M_x being close to zero and M_y about 0-15% of its maximum counterclockwise moment ($\min M_y$). Given the fact that depending on the wave height the maximum downward bearing force can occur either in the offshore or in the onshore bearings, two load cases should probably be considered here, including (a) one that applies $\max F_{down_{tot}}$ and an upper bound for the counterclockwise M_y (e.g. 15% of $\min M_y$), since this would give the maximum downward force in the offshore bearings, and (b) one that applies only $\max F_{down_{tot}}$ (and the moments are zero), since this should maximize the compression of the onshore bearings.

8.5 DEPENDENCE OF FORCES ON THE WAVE TYPE AND HEIGHT

8.5.1 Total forces and moments

This section will present the maximum values of the parameters of interest as a function of the wave type and height in order to obtain an overview of the trends with the increase of the wave. To this end, Figure 8.14 plots the maximum forces and moments for both unbroken solitary waves and bores. Regarding the former wave type the horizontal force, as well as, the moments (M_x , M_y , M_z) seem to be increasing linearly with the increase of the wave height, while the uplift forces tend to exhibit a more nonlinear trend. On the other hand, the trends for the bores are not clear, and this is because the bores do not correlate directly with the input height since they break and end-up having similar bore heights close to the bridge. Another difference between the two wave types is that bores seem to consistently introduce (i) larger horizontal (F_x) than uplift forces, and (ii) larger yaw moments (M_z) than pitch and roll ones, which is not the case for unbroken solitary waves. This implies that utilizing unbroken solitary waves for investigating the tsunami-induced effects on skew bridge might lead to different trends than tsunami-like bores, and this is due to the fact that in the former wave type the ratios of the wavelength to the bridge width and to the bridge length respectively will play a major role.

8.5.2 Uplift in bearings and bent caps/abutments

Figure 8.15 plots the maximum uplift force in each abutment and bearing for all the tested waves (using the average value of all the repetitions of the same wave). It shows that for the unbroken solitary waves the maximum uplift in the abutment of the offshore obtuse corner increases linearly with the wave height, while the demand in the other abutment has a more nonlinear trend (a 2nd order polynomial fitting function gives $R^2=0.99$). While in the case of the bores the abutment (or bent-cap) of the offshore obtuse corner attracts always larger uplift than the other

abutment, this is not the case for the unbroken solitary waves, for which the governing abutment depends on the wave height. In general, the differences between the maximum uplift introduced in the two abutments ranges between 0 and about 30%, which means that for design purposes, an engineer could (a) estimate the uplift demand in one abutment (for bores use the one supporting the offshore obtuse corner) and then design the other one for the same demand, or (b) conduct more sophisticated analyses that will predict exactly the uplift demand in each abutment. The former approach is simpler with some inherent conservatism, while the second one is more complex but could yield a more economical design.

Regarding the uplift in the bearings, irrespective of the wave type and height the maximum uplift among all bearings is witnessed by the bearing of the offshore obtuse corner (R1), with the offshore acute corner (L1) attracting the second largest demand for the majority of the largest wave heights. This means that from a design point of view, one could (a) estimate the uplift demand only in R1 and design all the bearings for the same demand, (b) estimate the demand in R1 ($F_{up,R1}$) and L1 ($F_{up,L1}$) and then design all the bearings of the right and left abutment for $F_{up,R1}$ and $F_{up,L1}$ respectively, (c) or predict the exact tsunami load distribution in each bearing. The lateral approach could be very challenging since it would require an accurate representation of the tsunami-induced loading with its complex temporal and spatial variation.

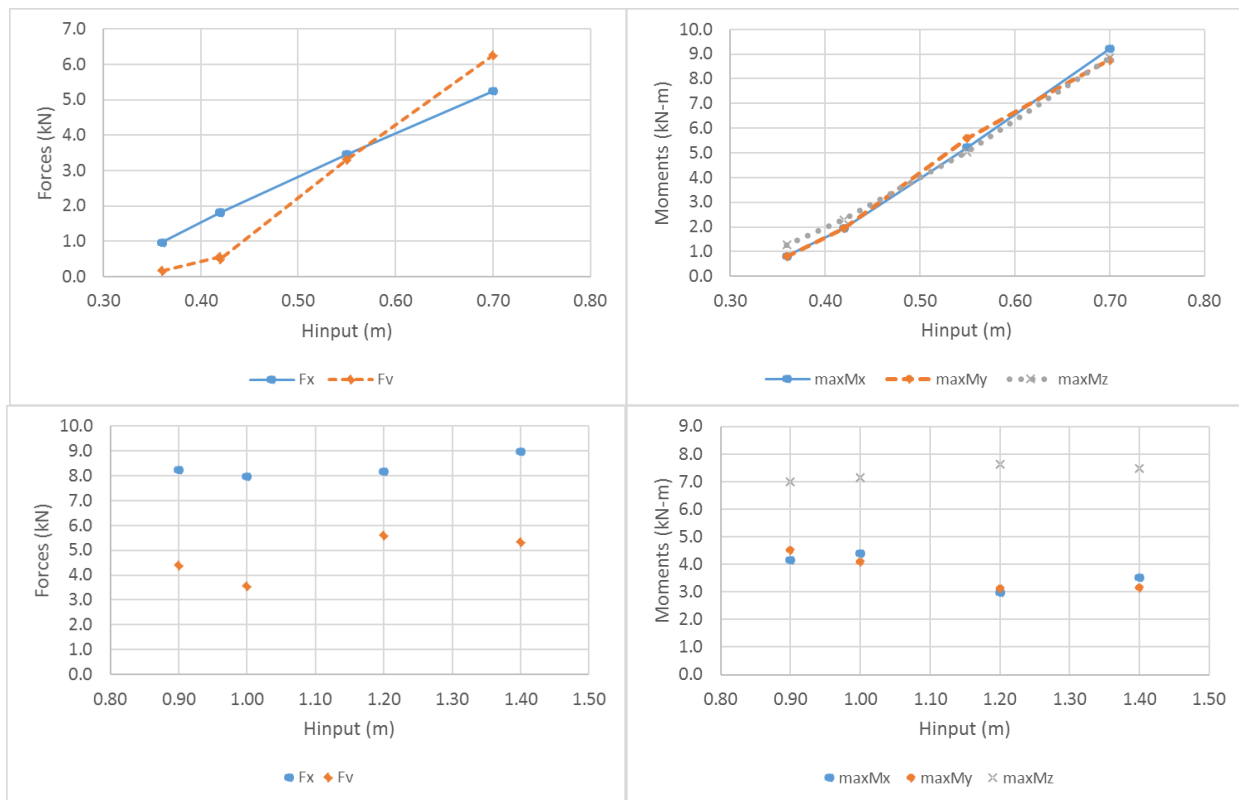


Figure 8.14: Maximum forces (left) and moments (right) for unbroken solitary waves (top) and bores (bottom)

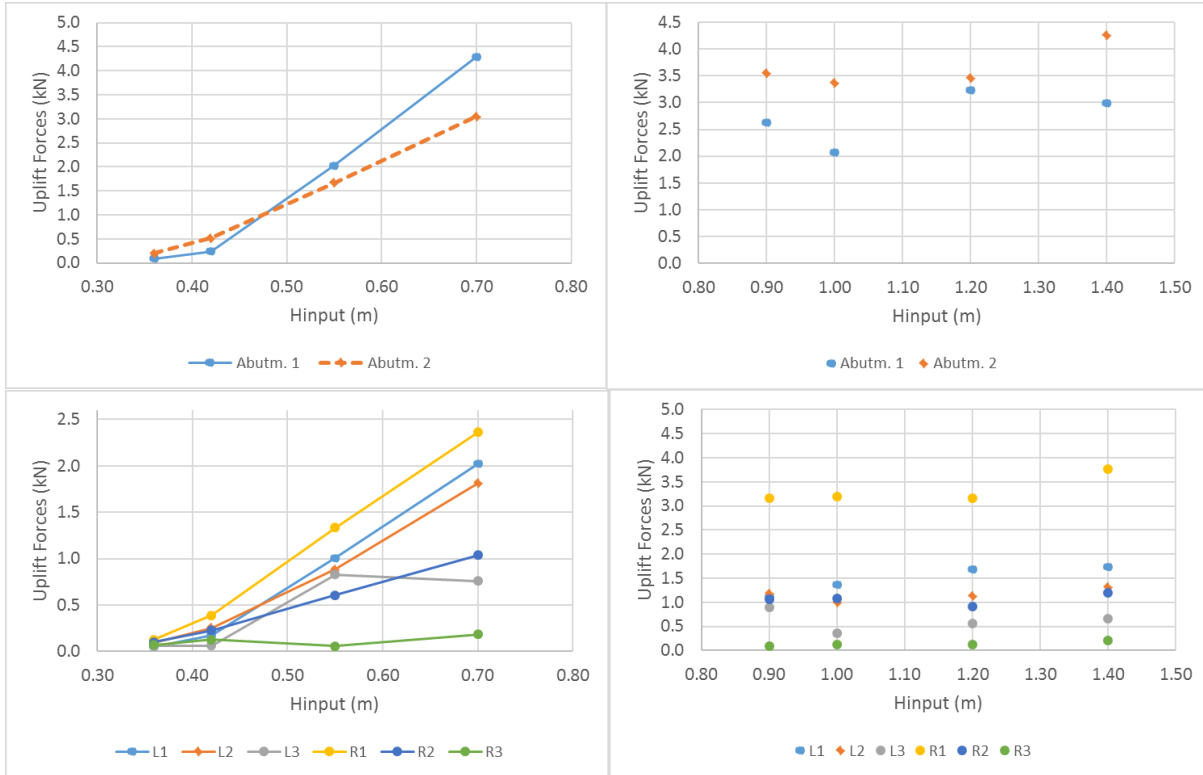


Figure 8.15: Maximum uplift forces in individual abutments (top) and bearings (bottom) for unbroken solitary waves (left) and bores (right)

8.6 COMPARISON OF TSUNAMI EFFECTS ON STRAIGHT AND SKEW BRIDGES

The last section of this chapter will focus on conducting an approximate comparison of the experimental results of the skewed and straight bridge. This comparison is approximate because the straight bridge had 4 girders while the skewed bridge had only 3 girders, however it can be justified by the fact that the two bridges had the same width, abutments/bent-caps and supports/columns below the bent caps. Also, since in the case of the bore impact on the straight bridge the horizontal force was maximized in Phase 1 at the beginning of the inundation when the tsunami slammed the offshore girder and overhang, the number of girders would arguably not make a difference for the straight bridge. On the other hand, for the vertical force histories and the overturning moments the number of girders could play a more significant role, which means that the comparison shown below might not be representative. Therefore, the following results should be taken with caution.

Table 8.2 shows the ratios of the maximum horizontal and uplift forces recorded in the skewed bridge relative to the respective forces of the straight bridge, both in terms of total forces and demand in individual abutments. Interestingly, the total forces on the skewed bridge seem to be significantly smaller than the ones of the straight bridge, reaching about 40% and 27% in the horizontal and vertical direction (for the larger waves). If accurate, this is an encouraging finding for the tsunami design of skewed bridges because it indicates that even though such a bridge has

a very unfavorable distribution of forces, which causes force and stress concentrations on specific structural components (e.g. bearing of the offshore obtuse corner), the actual demand in the components might not be necessarily larger than in the case of straight bridges. However, more work including the comparison of straight and skewed bridge with the same number of girders, is required in order to investigate the validity of the above indication.

The ratios of the maximum forces in individual abutments relative to the straight bridge are also showing reductions, however, not as much as the total forces, with the horizontal force (F_x) decreasing to 30%-62% and the uplift one to 19%-48%. Note that for the uplift load the two smallest wave heights (0.36m and 0.42m) cannot provide a representative comparison because they are very small and while they might have enough energy to reach the chambers of the straight bridge, this energy gets dissipated by the 3D geometry of the skewed bridge reducing the height of the wave by the time it reaches the chambers.

The last figure of this section (Fig. 8.16) attempts to give an insight into the effect of the skew angle on the maximum uplift in the bearings and individual connections. Unfortunately, a direct comparison of the uplift in the bearings is not feasible because the straight bridge had four girders with eight bearings and the skewed bridge had three girders supported on six bearings. However, the two bridges had the same three-column bents (where the columns were simulated axially and rotationally rigid via steel plates and load cells), and in the tests of the straight bridge the vertical forces were recorded both in the bearings (above the bent caps) and in the connections between the bent cap and the idealized columns (below the bent caps). This means that the maximum uplift forces recorded in the three bent cap-column connections (located below the bent cap) could be compared with the forces in the three bearings of the skewed bridge (located above the bent cap), noting though the different elevation of the two sets of structural components. The larger vertical distance between the location of the horizontal deck load (e.g. mid-height of girder height) and the location of the bent cap-column connection increases the overturning moment, which subsequently results in larger uplift of the offshore connections.

Neglecting the above difference, Fig. 8.16 shows a comparison of the maximum uplift forces in these connections. For the straight bridge the distribution of the uplift forces in the bearings is the same for both abutments, however, for the skewed bridge this is not the case. Therefore, for the generation of the curves in Fig. 8.16 the maximum demand in each abutment was considered and then the envelope of the two was used in the comparison, revealing the more unfavorable distribution of uplift in the connections of the skewed bridge. In fact, while in the straight bridge an offshore connection has to withstand 45% and 62% of the total uplift applied by an unbroken solitary wave and a bore respectively, the corresponding percentages for the skewed bridge are 93% and 95%.

The analysis of the experimental results presented in this chapter reveals three complex and in some case counter-acting phenomena describing the tsunami effects on skew bridges relative to straight bridges, including (a) a reduction of the total tsunami forces (F_x , F_v) and overturning moment (M_y), (b) a much more unfavorable distribution of the forces to the individual abutments, bearings and connections, and (c) generation of significant yaw and roll moments, which did not exist in straight bridges. The experimental results have given an insight into the above phenomena, however, significantly more work is required in order quantify the demand in all three directions for the critical structural components that have to transfer the tsunami load

from the deck to the earth, such as, individual bearings, connections, columns, abutments and foundations, and understand how this demand changes with the skew angle. While the findings of this chapter were based on a single skew angle (46.6deg), the authors have conducted a more rigorous numerical investigation of several skewed angles and wave conditions, which is presented in a companion report (Istrati and Buckle, 2020),

Table 8.2: Ratios of Maximum Horizontal and Uplift Forces Recorded in the Skewed Bridge Relative to the Respective Forces of the Straight Bridge

H (m)	Total forces		Forces in abutments			
	F_x/F_{xo}	F_v/F_{vo}	F_{xl}/F_{xlo}	F_{xr}/F_{xro}	F_{vl}/F_{vlo}	F_{vr}/F_{vro}
0.36	0.38	0.08	0.53	0.62	0.09	0.16
0.42	0.33	0.08	0.51	0.54	0.09	0.15
0.55	0.34	0.19	0.52	0.60	0.23	0.19
0.70	0.29	0.19	0.53	0.46	0.27	0.17
0.90	0.39	0.24	0.50	0.46	0.28	0.38
1.00	0.40	0.23	0.53	0.45	0.27	0.48
1.20	0.26	0.26	0.36	0.30	0.31	0.33
1.40	0.38	0.27	0.51	0.42	0.30	0.43

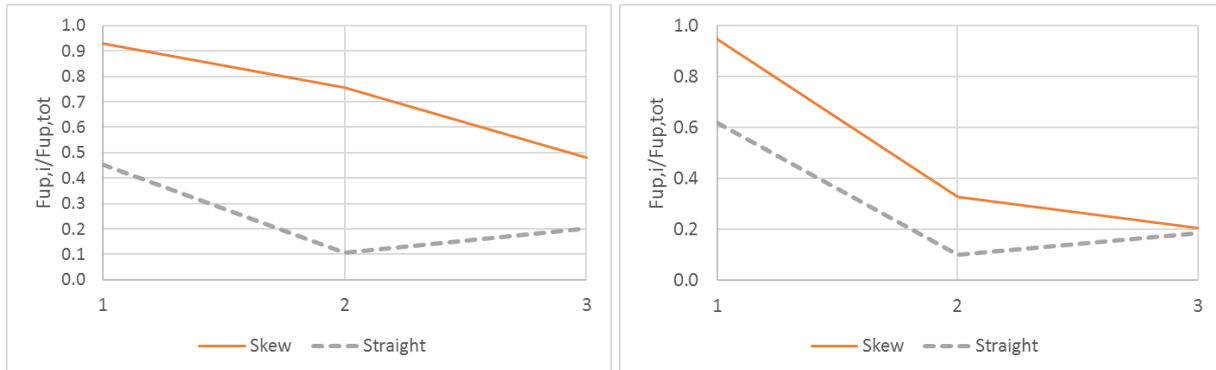


Figure 8.16: Envelopes of the maximum uplift in individual connections relative to the maximum total uplift

9.0 CONCLUSIONS AND FUTURE WORK

9.1 SUMMARY AND CONCLUSIONS

This report has presented a large-scale experimental investigation of tsunami wave impact on coastal bridges, which advances the fundamental understanding of the underlying physics and associated bridge forces, while providing preliminary but practical guidance for design. The hydrodynamic experiments included a wide range of structural configurations of a straight and a skew bridge, different superstructure types (I-girder and box-girder), two types of bearings (steel and elastomeric) and four levels of flexibility. Moreover, the testing program include two wave types, simplified unbroken solitary waves and more realistic bores, two water depths and a range of heights. Given the large-scale and test setup it was possible to design the bridge according to the latest AASHTO design guidelines and use structural components as in current bridge practice, including a composite deck with a reinforced concrete slab and steel girders, cross-frames, steel and elastomeric bearings, shear keys and bent caps. The recorded parameters included free-surface elevations, water pressures, particle velocities, applied pressures on the girders and the slab, strains in the cross-frames, forces in several components (bearings, shear keys, bent caps, and bent cap-column connections), accelerations and displacements at selected locations.

The main objectives of the study were to (a) understand the tsunami inundation mechanism of coastal bridges, (b) evaluate the accuracy of existing simplified predictive equations for tsunami loads, (c) identify the difference in the bridge response when subjected to unbroken solitary waves and more realistic turbulent bores, (d) investigate not only the total waves forces but also the distribution of these forces in each bearing and connection in order to determine the max force that each connection has to withstand, (e) shed light on the physics of the dynamic fluid-structure interaction and how it is affected by the dynamic characteristics of the bridge, (f) gain an insight into the role of air-entrapment and nonlinear wave-air interaction for bridges with diaphragms, (g) examine the tsunami forces for different types of superstructures, (h) quantify the effect of solid rails, (i) investigate possible mitigation strategies, such as air-vents in the deck, (j) decipher the tsunami-induced effects on skewed bridges, and (k) develop a high quality database that can be used by the community for calibrating and validating CFD and FSI methods, or for developing simplified design methodologies. Given the above objectives and the detailed investigation presented in the respective chapters, the major conclusions can be summarized as follows:

- The tsunami inundation mechanism of straight bridges is complex and consists of three uplift phases and one downward phase, with each phase maximizing the demand in different structural components. The slamming forces on the offshore girder and overhang play a major role, since they generate the maximum overturning moment and a simultaneously large uplift that introduces the maximum uplift demand in the offshore structural components and connections, governing their design. Despite the complex temporal and spatial evolution of the tsunami loads, it seems possible to predict the maximum uplift demand in bearings and connections using

selected load cases, and a simplified methodology has been presented in the respective chapter.

- The dynamic properties of the bridge have a significant role in the determination of the forces that the structural components have to withstand. In fact, the analysis of the experimental results revealed: (a) the need to consider the structural inertia in order to satisfy the dynamic equilibrium, (b) the possibility of dynamic amplification when the bridge is impacted by a bore that introduces an impulsive load with a duration close to the natural frequency of the bridge, and (c) the major role of structural flexibility, which can reduce/eliminate the impulsive bore loading but could potentially resonate with the quasi-static component, especially in the case of unbroken solitary waves.
- The trapped air in the chambers of the bridge with diaphragms modifies the wave–structure interaction relative to the bridge with cross-frames, introducing (a) a different pattern and magnitude of wave pressures on the superstructure due to the nonlinear cushioning effect, (b) an increase of not only the total uplift forces but also of the overturning moment, which has not been discussed in previous studies, and, (c) a variable effect on the uplift demand of structural components. Interestingly, while the trapped air causes always an increase of the total quasi-static uplift, it has an inconsistent and complex effect on the slamming component. Despite the complex role of air-entrapment, it is possible to estimate the effect of the trapped air on (i) the maximum total uplift, by considering the additional buoyancy from the trapped air that occupies a percentage of the volume in the chambers, and (ii) the maximum uplift in individual bearings, by utilizing non-dimensional demand diagrams.
- While box-girder bridges witness similar bore-induced maximum horizontal forces with open-girder bridges, their maximum uplift force was on average 134% higher. In addition, box-girder bridges were subjected to larger overturning moments and rotations than open-girder bridges for the majority of the tested wave heights. Therefore, these two combined effects result in the increase of the maximum uplift demand in all the bearings of the box-girder, with the offshore and onshore ones witnessing respectively an 84% and 245% average increase relatively to an open-girder bridge with cross-frames. The above findings suggest that box-girder bridges have to withstand significantly larger tsunami-induced loads, however, they are not necessarily more vulnerable than open-girder bridges, since they have a large weight that counter-acts the above loads.
- Solid rails increase the horizontal force as expected, with the maximum increase being 112% in the case of bores. Interestingly, despite the impulsive localized pressures on the offshore girder and the complex pressure distribution at the slamming instant of the bore on the offshore face of the superstructure (due to slight differences in the time of impact of the bore with the girder and the rails), the increase of $\max F_h$ due to the addition of the rails seems to be a function of the exposed area ratio. This in turn indicates that for design purposes a single predictive equation could be used for both bridges without rails and the ones with solid rails by just using the total height. Moreover, in addition to the expected increase in the horizontal force, the rails modified the hydrodynamic flow and caused (i) different patterns of vertical

forces and moments, with the introduction of the a new major peak when the bore impacted the onshore rail, and (ii) a significant increase in the downward slamming force. Both changes resulted in the increase of the demand in the bearings, demonstrating the need to develop additional predictive equations and modified design load cases that account for the presence of the rails

- Air-vents in the deck can be a promising mitigation strategy against tsunamis, however in order to maximize their effectiveness, the number, size and location of the venting holes has to be optimized. In the experiments two different venting hole configurations were investigated with the first one including 18 holes and the second one twice as that. Interestingly, it was shown that while the first configuration reduced the total deck uplift by up to 55%, when the number of vents was doubled there was only a 6% further reduction revealing the existence of a nonlinear effect. A close inspection of the video footage showed a sequential release mechanism of the air through the vents, which was characterized by significant 3D effects and was affected by the location of the vents.
- The complex geometry of skewed bridges and the subsequent gradual application of the tsunami pressures along the length of the deck introduce significant 3D effects that tend to dominate the tsunami loads. Due to these effects a skewed bridge (with a 46.6° skew angle) witnesses not only horizontal and vertical forces, and overturning (M_y) moments, as a straight bridge, but also significant roll (M_x) and yaw moments (M_z). The yaw moment increases the horizontal force of the abutment supporting the offshore acute corner, and in the current experiments the abutment had to withstand up to 96% of the total horizontal force, instead of the 50% associated with a straight bridge. Similarly, the M_x moment, overstressed one abutment by introducing large uplift forces, which could reach 104% of the total tsunami-induced uplift, while the combination of M_x and M_y focused 95% and 45% of the total uplift into the bearings below the offshore obtuse and acute corners respectively. The latter percentages are significantly larger than the 16.67% that each bearing would have had to withstand under an equal distribution assumption, revealing the necessity to consider all the moments (M_x , M_y , M_z) in the design of skewed bridges. Last but not least, a preliminary comparison of the total forces (F_x and F_{up}) on skew and straight bridges, revealed a reduction of the total forces down to 40% due to the skew, however, given the observed unfavorable distribution of the forces in the structural components of a skewed bridge, further investigation is required in order to quantify the exact effect of the skew angle on the design of the structure.

In summary, the experimental results presented herein provide concrete evidence about the need to shift the paradigm in the tsunami risk assessment of coastal infrastructure, by considering: (a) not only the maximum total loads applied on rigid structures, but also the distribution of this load to individual structural components (of realistically flexible structures) that are necessary for the survival of the structure, (b) the structural dynamics, which can have a major effect on the demand in structural members and connections, and (c) more realistic tsunami-like waves (e.g. bores) in addition to simplified unbroken solitary waves.

9.2 FUTURE WORK

The analysis of the experimental results has given an insight into the role of several hydrodynamic and structural parameters, advancing the understanding of the wave-structure interaction during the tsunami inundation of bridges and the associated loads. However, the findings are based on a limited number of wave conditions, bridge specimens, and levels of flexibilities, a specific number of girders, one type of rails with a particular height, and one skew angle, which means that a wider range of the above parameters should be investigated in future studies in order to determine the range of applicability of the current findings and modify them if necessary. Moreover, in addition to advancing the state-of-knowledge this study also revealed the complexity of certain phenomena and topics that also require further investigation. Therefore, future studies could focus on:

- Comprehensive parametric investigations with a larger number of wave heights of solitary waves and bores, as well as, bridge geometries (e.g. with a different number of girders or with a larger width), which would provide the necessary information for refined predictive equations and design methodologies.
- More accurate quantification of the role of bridge rails by investigating different heights and rail types (e.g. solid vs. perforated), in order to calibrate/adjust existing equations for the prediction of the horizontal force, develop new equations in order to quantify the effect of the rails on the other design parameters, and identify the critical load cases.
- The investigation of a wider range of flexibilities in the substructure and the connections in order to quantify accurately the effect of structural dynamics and develop design equations as a function of the dynamic properties of the structure.
- Different configurations of the venting holes in the deck in order to investigate further their effectiveness and identify the optimal one that will provide the largest reduction of the uplift force for the minimum venting area.
- The investigation of a range of skew angles in order to determine whether the results presented herein (for 0° and 46.6°) could bound the tsunami-induced effects. Also, in addition to the investigated parameters, follow-up studies should also look at the total and component forces normal to the direction of the tsunami propagation, since such forces could lead to the unseating of skewed bridges.

Last but not least, since in the current hydrodynamic experiments the bridge was inundated only for a few seconds by the tsunami waves (due to the large-scale of the bridge and the limitations of the wavemaker), it might be useful to conduct further numerical analyses of longer duration bores. However, given the fact that the maximum demand on straight bridges was seen to be introduced either at the instant of the initial slamming of the bore on the offshore face of the bridge or during the inundation phase of the superstructure, the steady-state loads (which are reached after the inundation of the whole deck) are not expected to govern the design of the bearings. Nonetheless, the effect of longer duration bores should still be investigated for straight

bridges, and especially for skewed ones or bridges impacted by bores with an incident angle different than 90° .

10.0 REFERENCES

- American Association of State Highway and Transportation Officials (AASHTO). (2012). *AASHTO LRFD bridge design specifications, customary U.S. units: Section 7-Index* (6th ed.). Washington, DC: American Association of State Highway and Transportation Officials.
- Aquelet, N., Souli, M., Gabrys, J., & Olovson, L. (2003). A new ALE formulation for sloshing analysis. *Structural Engineering and Mechanics*, *16*(4), 423–440.
<https://doi.org/10.12989/sem.2003.16.4.423>
- Araki, S., Ishino, K., & Deguchi, I. (2011). Stability of girder bridge against tsunami fluid force. *Coastal Engineering Proceedings*, *1*(32), 56.
<https://doi.org/10.9753/icce.v32.structures.56>
- Azadbakht, M. (2014). *Tsunami and hurricane wave loads on bridge superstructures* (Doctoral dissertation, Oregon State University, 2013). Corvallis, OR: Oregon State University. Retrieved from https://ir.library.oregonstate.edu/concern/graduate_thesis_or_dissertations/pg15bh86v.
- Bea, R. G., Iversen, R., & Xu, T. (2000). Wave-in-Deck forces on offshore platforms. *Journal of Offshore Mechanics and Arctic Engineering*, *123*(1), 10–21.
<https://doi.org/10.1115/1.1342160>
- Bozorgnia, M., Lee, J.-J., & Raichlen, F. (2011). Wave structure interaction: Role of entrapped air on wave impact and uplift forces. *Coastal Engineering Proceedings*, *1*(32), 57.
<https://doi.org/10.9753/icce.v32.structures.57>
- Bradner, C., Schumacher, T., Cox, D., & Higgins, C. (2011). Experimental setup for a Large-Scale bridge superstructure model subjected to waves. *Journal of Waterway, Port, Coastal, and Ocean Engineering*, *137*(1), 3–11. [https://doi.org/10.1061/\(asce\)ww.1943-5460.0000059](https://doi.org/10.1061/(asce)ww.1943-5460.0000059)
- Bricker, J. D., & Nakayama, A. (2014). Contribution of trapped air, deck superelevation, and nearby structures to bridge deck failure during a tsunami. *Journal of Hydraulic Engineering*, *140*(5), 05014002-1-05014002–05014007.
[https://doi.org/10.1061/\(asce\)hy.1943-7900.0000855](https://doi.org/10.1061/(asce)hy.1943-7900.0000855)
- Briggs, M. J. (2009). Physical modeling of tsunami waves. In H. Yeh & D. T. Cox (Eds.), *Handbook of Coastal and Ocean Engineering* (1st ed., Vol. Chap 39, pp. 1073–1105). Singapore: World Scientific Publishing Company. doi: 10.1142/9789812819307_0039
- Bungartz, H., & Schäfer, M. (2006). *Fluid-Structure interaction: Modelling, simulation, optimisation (lecture notes in computational science and engineering (53))* (2006th ed., Vol. 1). Berlin, Germany: Springer.

- CD-adapco. (2013). STAR-CCM+ manual (Version 8.06.005) [computer software]. Melville, NY: CD-adapco.
- Computers & Structures, Inc. (2017). CSiBRIDGE (Version 19.1.0) [computer software]. Walnut Creek, CA: Computers & Structures, Inc. Retrieved from <https://www.csiamerica.com>
- Cuomo, G., Shimosako, K., & Takahashi, S. (2009). Wave-in-deck loads on coastal bridges and the role of air. *Coastal Engineering*, 56(8), 793–809. <https://doi.org/10.1016/j.coastaleng.2009.01.005>
- Dean, R. G., & Dalrymple, R. A. (1991). *Water wave mechanics for engineers & scientists (advanced series on ocean Engineering-Vol2)*. Singapore: World Scientific Publishing Co Inc. <https://doi.org/10.1142/1232>
- Del Pin, F., Caldichoury, I., & Paz, R. (2014). LS-DYNA R7: Free-surface and multi-phase analysis for incompressible flows. In *13th International LS-DYNA Conference*. Detroit, MI: Livermore Software Technology Corporation.
- Douglass, S., Chen, J., Olsen, J., Edge, B., & Brown, D. (2006). *Wave forces on bridge decks*. US Department of Transportation Federal Highway Administration. Retrieved from <https://www.yumpu.com/en/document/view/7198095/wave-forces-on-bridge-decks>
- Earthquake Engineering Research Institute. (2011a). *Learning from earthquakes: The Tohoku, Japan, tsunami of March 11, 2011: Effects on structures*. EERI Special Earthquake Report. Retrieved from https://www.eeri.org/wp-content/uploads/Tohoku_Japan_March_11_2011_EERI_LFE_ASCE_Tsunami_effects_on-Buildings-smallpdf.com-1.pdf
- Earthquake Engineering Research Institute. (2011b). *Learning from earthquakes bridge performance in the Mw 9.0 Tohoku, Japan, earthquake of March 11, 2011*. EERI Special Earthquake Report. Retrieved from http://learningfromearthquakes.org/2011-03-11-tohoku-japan/images/2011_03_11_tohoku_japan/pdfs/East-Japan-Bridge-Performance-web.pdf
- Fu, L., Kosa, K., & Sasaki, T. (2013). Tsunami damage evaluation of Utatsu Bridge by video and 2-D simulation analyses. *Journal of Structural Engineering*, 59A, 428–438. <https://doi.org/10.11532/structcivil.59A.428>
- Fu, L., Kosa, K., Shimizu, H., & Shi, Z. (2012). Damage judgment of Utatsu Bridge affected by tsunami due to Great East Japan earthquake. *Journal of Structural Engineering*, 58A, 377–386. <https://doi.org/10.11532/structcivil.58A.377>
- Gaeta, M. G., Martinelli, L., & Lamberti, A. (2012). Uplift forces on wave exposed jetties: Scale comparison and effect of venting. *Coastal Engineering Proceedings*, 1(33), 34. <https://doi.org/10.9753/icce.v33.structures.34>

- Ghosh, S., Reins, G., Koo, B., Wang, Z., Yang, J., & Stern, F. (2007). Plunging wave breaking: EFD and CFD. In *International Conference on Violent Flows: VF-2007*. Fukuoka, Japan: Research Institute for Applied Mechanics.
- Goring, D., & Raichlen, F. (1980). The generation of long waves in the laboratory. In *17th International Conference on Coastal Engineering: Sydney, 23-28 March 1980: Abstracts-in-depth* (17th ed., Vol. 1, p. 763-783). Australia: Institution of Engineers. doi:10.1061/9780872622647.047
- Grilli, S. T., Svendsen, I. A., & Subramanya, R. (1997). Breaking criterion and characteristics for solitary waves on slopes. *Journal of Waterway, Port, Coastal, and Ocean Engineering*, 123(3), 102–112. [https://doi.org/10.1061/\(asce\)0733-950x\(1997\)123:3\(102\)](https://doi.org/10.1061/(asce)0733-950x(1997)123:3(102))
- Hallquist, J. O. (2006). *LS-DYNA theoretical manual*. Livermore Software Technology Corporation, Livermore, CA. Retrieved from http://www.lstc.com/pdf/ls-dyna_theory_manual_2006.pdf
- Hayashi, H. (2013). Study on tsunami wave force acting on a bridge superstructure. In *29th US-Japan Bridge Engineering Workshop*. Tsukuba, Japan: Public Works Research Institution.
- Hayatdavoodi, M., Seiffert, B., & Ertekin, R. C. (2014). Experiments and computations of solitary-wave forces on a coastal-bridge deck. Part II: Deck with girders. *Coastal Engineering*, 88, 210–228. <https://doi.org/10.1016/j.coastaleng.2014.02.007>
- Hayatdavoodi, M., & Ertekin, R. C. (2015a). Wave forces on a submerged horizontal plate - Part I: Theory and modelling. *Journal of Fluids and Structures*, 54, 566–579. <https://doi.org/10.1016/j.jfluidstructs.2014.12.010>
- Hayatdavoodi, M., & Ertekin, R. C. (2015b). Wave forces on a submerged horizontal plate—Part II: Solitary and cnoidal waves. *Journal of Fluids and Structures*, 54, 580–596. <https://doi.org/10.1016/j.jfluidstructs.2014.12.009>
- Higgins, C., Lehrman, J., Bradner, C., Schumacher, T., & Cox, D. (2013). Hybrid testing of a prestressed girder bridge to resist wave forces. In *29th US-Japan Bridge Engineering Workshop*. Tsukuba, Japan: Public Works Research Institution.
- Hoshikuma, J., Zhang, G., Nakao, H., & Sumimura, T. (2013). Tsunami-induced effects on girder bridges. In *International Symposium for Bridge Earthquake Engineering in Honor of Retirement of Professor Kazuhiko Kawashima*. Tokyo, Japan.
- Huang, N. E., Shen, Z., & Long, S. R. (1999). A new view of nonlinear water waves: The Hilbert Spectrum 1. *Annual Review of Fluid Mechanics*, 31(1), 417–457. <https://doi.org/10.1146/annurev.fluid.31.1.417>
- Hughes, S. A. (1993). *Physical models and laboratory techniques in coastal engineering* (Vol. 7). Singapore: World Scientific Publishing Company. <https://doi.org/10.1142/2154>

- Irschik, K., Sparboom, U., & Oumeraci, H. (2004). Breaking wave loads on a slender pile in shallow water. In *29th Coastal Engineering Conference* (Vol. 4, pp. 568-580). Lisbon, Portugal: National Civil Engineering Laboratory. doi:10.1142/9789812701916_0045
- Istrati, D., & Buckle, I. (2014). Effect of fluid-structure interaction on connection forces in bridges due to tsunami loads. In *30th US-Japan Bridge Engineering Workshop*. Washington, D.C.: Public Works Research Institution.
- Istrati, D., & Buckle, I. (2019). Role of trapped air on the Tsunami-Induced transient loads and response of coastal bridges. *Geosciences*, 9(4), 191. <https://doi.org/10.3390/geosciences9040191>
- Istrati, D. and Buckle, I., (2020). *Tsunami loads on straight and skewed bridges – Part 2: Numerical investigation and design recommendations* [Report submitted for publication] Salem, OR: Oregon Department of Transportation.
- Istrati, D., Buckle, I., Lomonaco, P., & Yim, S. (2018). Deciphering the tsunami wave impact and associated connection forces in Open-Girder coastal bridges. *Journal of Marine Science and Engineering*, 6(4), 148. <https://doi.org/10.3390/jmse6040148>
- Jose, J., Podrazka, O., Obhrai, C., Gudmestad, O. T., & Cieslikiewicz, W. (2016). Methods for analysing wave slamming loads on truss structures used in offshore wind applications based on experimental data. *International Journal of Offshore and Polar Engineering*, 26(2), 100–108. <https://doi.org/10.17736/ijope.2016.mkr05>
- Kasano, H., Oka, J., Sakurai, J., Kodama, N., & Yoda, T. (n.d.). Investigative research on bridges subjected to tsunami disaster in 2011 off the Pacific Coast of Tohoku. In *Australasian Structural Engineering Conference 2012*. Perth, Western Australia.
- Kataoka, S., & Kaneko, M. (2013). Estimation of wave force acting on bridge superstructures due to the 2011 Tohoku tsunami. *Journal of Disaster Research*, 8(4), 605–611. <https://doi.org/10.20965/jdr.2013.p0605>
- Kawashima, K. (2012). Damage of bridges due to the 2011 Great East Japan earthquake. *Journal of Japan Association for Earthquake Engineering*, 12(4), 319–338. https://doi.org/10.5610/jaee.12.4_319
- Kerenyi, K., Sofu, T., & Guo, J. (2009, May). *Hydrodynamic forces on inundated bridge decks* (FHWA-HRT-09-028). McLean, VA: Office of Infrastructure Research and Development Federal Highway Administration. Retrieved from <https://www.fhwa.dot.gov/publications/research/infrastructure/hydraulics/09028/09028.pdf>
- Kosa, K. (2012). Damage analysis of bridges affected by tsunami due to Great East Japan Earthquake. In *International Symposium on Engineering Lessons Learned from the 2011 Great East Japan Earthquake*. Tokyo, Japan.

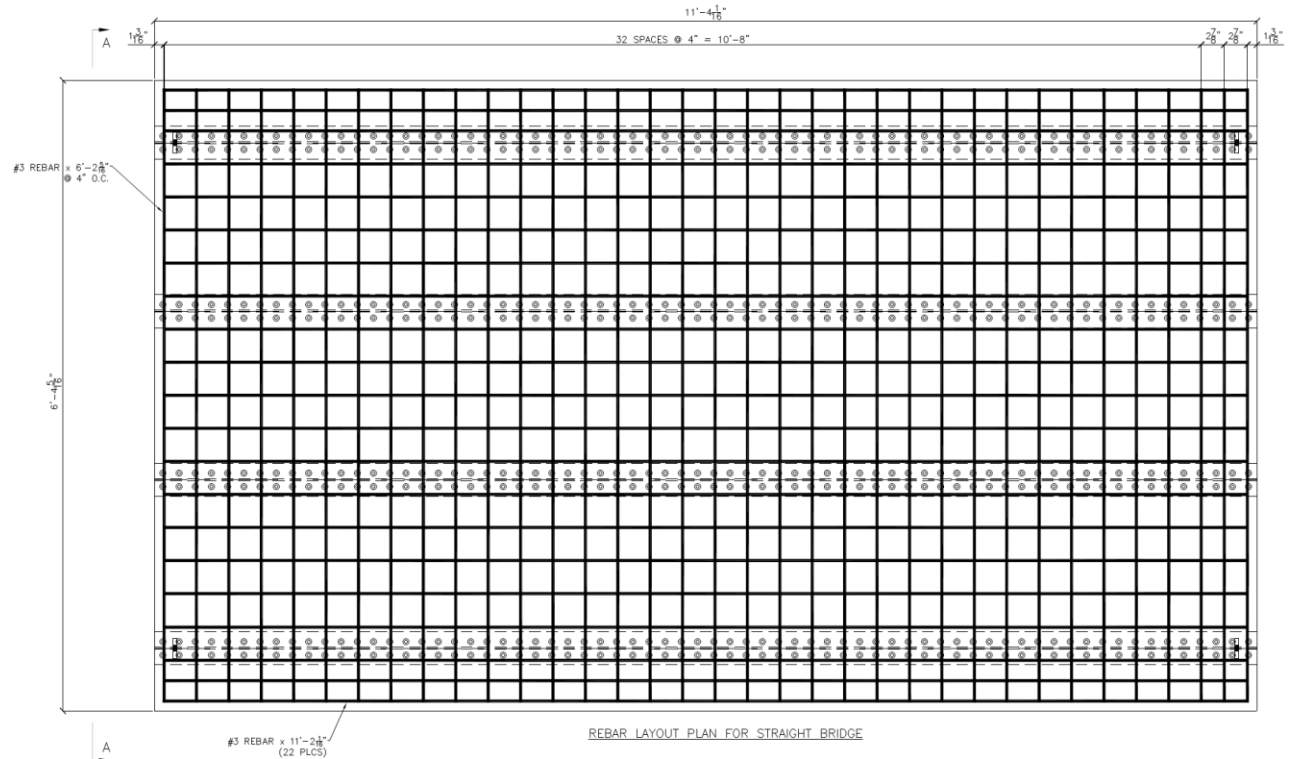
- Kosa, K., Nii, S., Miyahara, K., & Shoji, M. (2010). Experimental study for estimating tsunami forces acting on bridge girders. In *26th US-Japan Bridge Engineering Workshop*. New Orleans, LA.
- Lau, T. L., Ohmachi, T., Inoue, S., & Lukkunaprasit, P. (2011). *Experimental and numerical modeling of tsunami force on bridge decks*. Japan: IntechOpen. <https://doi.org/10.5772/23622>
- Lo, H.-Y., & Liu, P. L.-F. (2014). Solitary waves incident on a submerged horizontal plate. *Journal of Waterway, Port, Coastal, and Ocean Engineering*, *140*(3), 04014009. [https://doi.org/10.1061/\(asce\)ww.1943-5460.0000236](https://doi.org/10.1061/(asce)ww.1943-5460.0000236)
- Lukkunaprasit, P., Lau, T., Ruagrassame, A., & Ohmachi, T. (2008). Tsunami wave loading on a bridge deck with perforations. In *14th World Conference on Earthquake Engineering, October 12-17, 2008, Beijing, China: Innovation, practice, safety*. Beijing, China: World Conference on Earthquake Engineering.
- Lum, D., Riggs, R., & Robertson, I. (2011). *Assessment of the vulnerability of Oahu's coastal bridges to storm waves and tsunami inundation* (UHM/CEE/11-06). Hawaii Department of Transportation. Retrieved from <http://www.cee.hawaii.edu/wp-content/uploads/UHM-CEE-11-06.pdf>
- Martinelli, L., Lamberti, A., Gaeta, M., Tirindelli, M., Alderson, J., & Schimmels, S. (2010). Wave loads on exposed jetties: Description of large-Scale experiments and preliminary results. *International Conference on Coastal Engineering* (Vol 1, No. 32). doi:10.9753/icce.v32.structures.18
- Maruyama, K., Tanaka, Y., Kosa, K., Hosoda, A., Arikawa, T., Mizutani, N., & Nakamura, T. (2013a). Evaluation of tsunami force acting on bridge girders. In *Thirteenth East Asia-Pacific Conference on Structural Engineering and Construction (EASEC-13)*. Sapporo, Japan.
- Maruyama, K., Tanaka, Y., Kosa, K., Hosoda, A., Mizutani, N., & Nakamura, T. (2013b). Evaluation of tsunami force acted on bridges by Great East Japan Earthquake. In *Tenth International Conference on Urban Earthquake Engineering*. Tokyo, Japan.
- McPherson, R. L. (2008). *Hurricane induced wave and surge forces on bridge decks* (Master's thesis, Texas A&M University, 2008). College Station, TX: Texas A & M University.
- Motley, M. R., Wong, H. K., Qin, X., Winter, A. O., & Eberhard, M. O. (2015). Tsunami-Induced forces on skewed bridges. *Journal of Waterway, Port, Coastal, and Ocean Engineering*, *142*(3), 04015025. [https://doi.org/10.1061/\(asce\)ww.1943-5460.0000328](https://doi.org/10.1061/(asce)ww.1943-5460.0000328)
- Munk, W. H. (1949). The solitary wave theory and its applications to surf problems. *Annals of the New York Academy of Sciences*, *51*(3), 376–424. <https://doi.org/10.1111/j.1749-6632.1949.tb27281.x>

- Murakami, K., Sakamoto, Y., & Nonaka, T. (2012). Analytical investigation of slab bridge damages caused by tsunami flow. In *33rd Conference on Coastal Engineering 2012: Santander, Spain, 1-6 July 2012* (Ser. 33). Los Angeles, CA: International Conference on Coastal Engineering. doi:10.9753/icce.v33.structures.42
- Nakao, H., Zhang, G., Sumimura, T., & Hoshikuma, J. (2013). Numerical assessment of tsunami- induced effect on bridge behavior. In *29th US-Japan Bridge Engineering Workshop*. Tsukuba, Japan.
- Malaysian Rubber Producers' Research Association. (1987). *Natural rubber engineering data sheet*. Hertford, England: Malaysian Rubber Producers' Research Association.
- Peregrine, D. H. (1983). Breaking waves on beaches. *Annual Review of Fluid Mechanics*, 15(1), 149–178. <https://doi.org/10.1146/annurev.fl.15.010183.001053>
- Peregrine, D., Bredmose, H., Bullock, G., Obhrai, C., Muller, G., & Wolters, G. (2004). Violent water wave impact on walls and the role of air. In *Coastal engineering 2004: Proceedings of the 29th International Conference* (4th ed., Vol. 1, pp. 4005-4017). Lisbon, Portugal: World Scientific Publishing. doi:10.1142/9789812701916_0323
- Rahman, S., Akib, S., & Shirazi, S. M. (2014). Experimental investigation on the stability of bridle girder against tsunami forces. *Science China Technological Sciences*, 57(10), 2028–2036. <https://doi.org/10.1007/s11431-014-5628-8>
- Robertson, I., Riggs, H., & Mohamed, A. (2008). Experimental results of tsunami bore forces on structures. In *Proceedings of the 27th International Conference on Offshore Mechanics and Arctic Engineering--2008: June 15-20, 2008, Estoril, Portugal, USA* (pp. 509-517). New York, NY: American Society of Mechanical Engineers.
- Seiffert, B., Hayatdavoodi, M., & Ertekin, R. C. (2014). Experiments and computations of solitary-wave forces on a coastal-bridge deck. Part i: Flat plate. *Coastal Engineering*, 88, 194–209. <https://doi.org/10.1016/j.coastaleng.2014.01.005>
- Seiffert, B. R., Cengiz Ertekin, R., & Robertson, I. N. (2015). Effect of entrapped air on solitary wave forces on a coastal bridge deck with girders. *Journal of Bridge Engineering*, 21(2), 04015036. [https://doi.org/10.1061/\(asce\)be.1943-5592.0000799](https://doi.org/10.1061/(asce)be.1943-5592.0000799)
- Souli, M., Olovsson, L., & Do, I. (2002). ALE and Fluid-Structure Interaction capabilities in LS-DYNA. In *7th International LS-DYNA Users Conference: May 19-21, 2002, Dearborn, Michigan*. Livermore, CA: Livermore Software Technology Corporation.
- Souli, M., & Benson, D. J. (2010). *Arbitrary Lagrangian-Eulerian and Fluid-Structure interaction: Numerical simulation* (1st ed.). Wiley-ISTE. <https://doi.org/10.1002/9781118557884>
- Takahashi, S., Tanimoto, K., & Miyanaga, S. (1985). Uplift wave forces due to compression of enclosed air layer and their similitude law. *Coastal Engineering in Japan*, 28(1), 191–206. <https://doi.org/10.1080/05785634.1985.11924415>

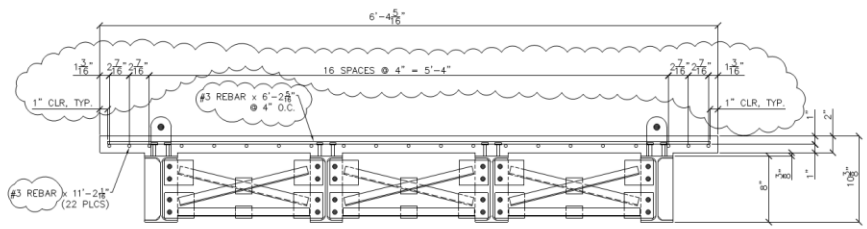
- Takeda, S., Kosa, K., Miyajima, M., & Shimizu, H. (2011). Summary of the field survey on the damage of bridges in the 2011 off the Pacific Coast of Tohoku. In *International Symposium on Engineering Lessons Learned from the 2011 Great East Japan Earthquake*. Tokyo, Japan.
- Unjoh S., (2007). Bridge damage caused by tsunami, *Bulletin Japan Association Earthquake Engineering*, 6, 26–28 (in Japanese).
- Wei, Z., & Dalrymple, R. A. (2016). Numerical study on mitigating tsunami force on bridges by an SPH model. *Journal of Ocean Engineering and Marine Energy*, 2(3), 365–380. <https://doi.org/10.1007/s40722-016-0054-6>
- Xiang, T., Istrati, D., Yim, S. C., Buckle, I. G., & Lomonaco, P. (2020). Tsunami loads on a representative coastal bridge deck: Experimental study and validation of design equations. *Journal of Waterway, Port, Coastal, and Ocean Engineering*, 146(5), 04020022. [https://doi.org/10.1061/\(asce\)ww.1943-5460.0000560](https://doi.org/10.1061/(asce)ww.1943-5460.0000560)
- Xu, G., Cai, C. S., & Chen, Q. (2016). Countermeasure of air venting holes in the bridge Deck–Wave interaction under solitary waves. *Journal of Performance of Constructed Facilities*, 31(1), 04016071. [https://doi.org/10.1061/\(asce\)cf.1943-5509.0000937](https://doi.org/10.1061/(asce)cf.1943-5509.0000937)
- Yashinski, M. (2012). *Miyagi Japan's bridges: Tsuya railway bridge (1)* [Photograph]. Retrieved from <http://www.bridgeofweek.com/2012/10/>
- Yim, S., & Azadbakht, M. (2013). *Tsunami forces on selected California coastal bridges (CA13-1983)*. Sacramento CA: California Department of Transportation. Retrieved from <https://dot.ca.gov/-/media/dot-media/programs/research-innovation-system-information/documents/f0016556-final-report-65a0384-task-1983.pdf>
- Yim, S., Boon-intra, S., Nimmala, S., Winston, H., Azadbakht, M., & Cheung, K. (2011). *Development of a guideline for estimating tsunami forces on bridge superstructures (OR-RD-12-03)*. Salem, OR: Oregon Department of Transportation. Retrieved from https://www.oregon.gov/odot/Programs/ResearchDocuments/TsunamiForces_SR500_342.pdf
- Zhu, M., Elkhatali, I., & Scott, M. H. (2018). Validation of OpenSees for tsunami loading on bridge superstructures. *Journal of Bridge Engineering*, 23(4), 04018015. [https://doi.org/10.1061/\(asce\)be.1943-5592.0001221](https://doi.org/10.1061/(asce)be.1943-5592.0001221)

APPENDIX A DESIGN DRAWINGS OF THE STRAIGHT BRIDGE

THINK SAFETY



REBAR LAYOUT PLAN FOR STRAIGHT BRIDGE



SECTION-A-A

APPROVER TO VERIFY/CONFIRM ALL CLOUDS

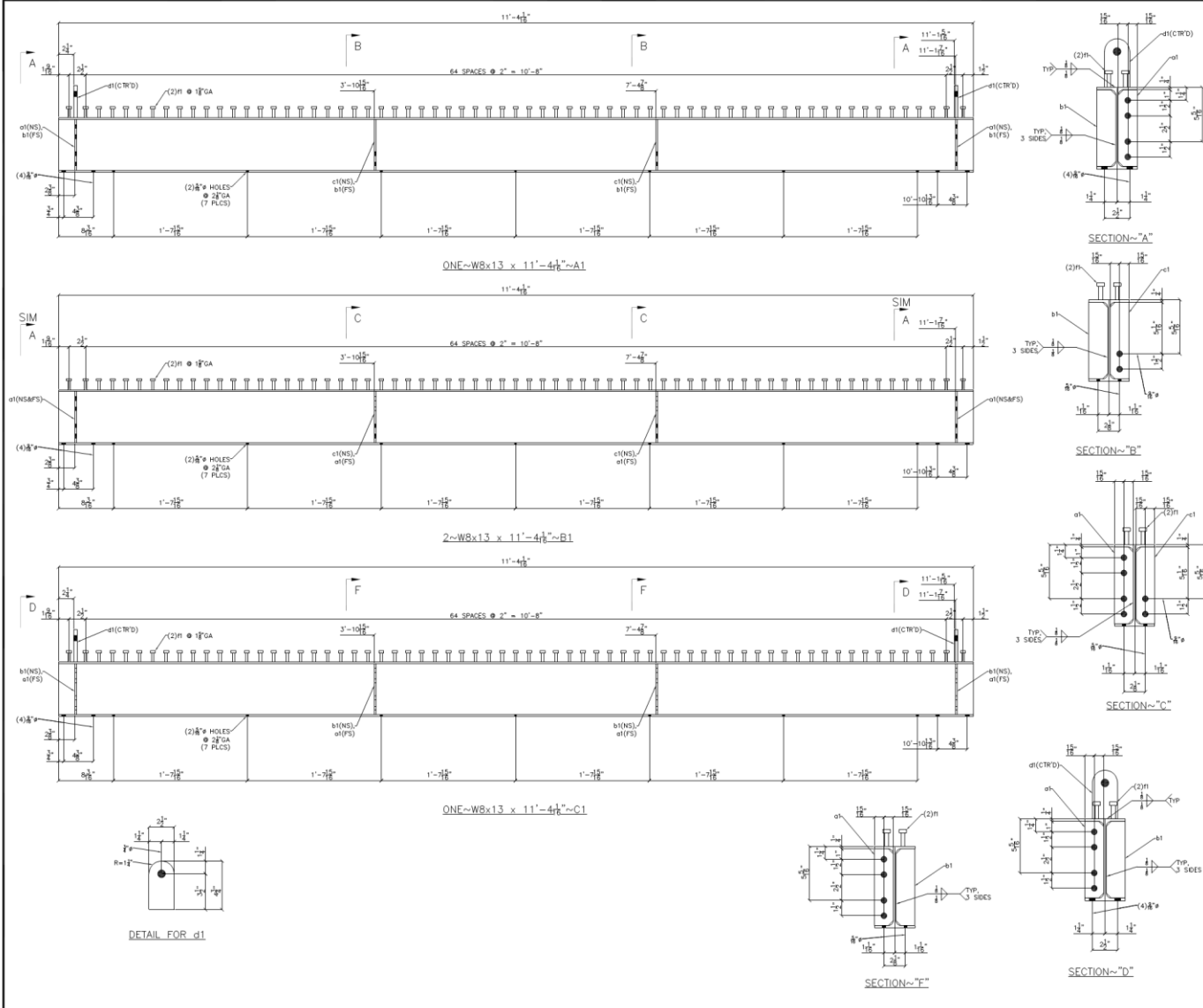
- NOTES:
- 1) ALL REBAR SHALL BE ASTM A615
 - 2) USE 16-GA TIE WIRE
 - 3) USE 1\" PLASTIC REBAR CHAIRS
 - 4) USE 2\"-0\" O.C. MAX., BOTH DIRECTIONS
 - 5) WEDGE/SHIM GIRDERS UNTIL BRIDGE FRAMING IS SQUARE AND LEVEL.

PLACE PIECE MARK ON LEFT END OF MEMBER AS DETAILED

ERECT WITH PIECE MARK TO END SHOWN ON PLACING PLAN

REV. NO.	REVISION DESCRIPTION	BY	DATE
Holes: N/A			
SHOP PAINT: NONE			
MATERIAL SPECIFICATIONS:		ISSUE STAMP	
REBAR: ASTM A615 GR. B TIES: ASTM A900 GR. B WEDGE FLOES & GIRDERS: ASTM A992 GR. 50 OTHER SHAPES: ASTM A36 PLATE: ASTM A36		RENO IRON WORKS 333 East Parr Blvd. RENO, NV 89512 Ph: 775 329-1111 Fax: 775 329-3555	
DRAWING TITLE: STRAIGHT BRIDGE REBAR LAYOUT			
PROJECT: UNR SIMPLE BRIDGE			
LOCATION: RENO, NV			
DRAWN BY: ME	DATE: 11/6/14	JOB NO. 4390	
CHECKED BY: MPE	DATE: 11/6/14	SHT NO. R1	
DESIGN REF: SHEET 2			

THINK SAFETY



BILL OF MATERIAL					
MARK	QTY.	DESCRIPTION	LENGTH FT. IN.	WT	REMARKS
A1	ONE	WBx13	11	4 1/2	
a1	2	PL 1/2 x 18	0	7 1/2	
b1	4	PL 1/2 x 18	0	7 1/2	
c1	2	PL 1/2 x 18	0	7 1/2	
d1	2	PL 1/2 x 22	0	4 1/2	
f1	134	3/8\"/>			
B1	2	WBx13	11	4 1/2	
a1	12	PL 1/2 x 18	0	7 1/2	
c1	4	PL 1/2 x 18	0	7 1/2	
f1	268	3/8\"/>			
C1	ONE	WBx13	11	4 1/2	
a1	4	PL 1/2 x 18	0	7 1/2	
b1	4	PL 1/2 x 18	0	7 1/2	
d1	2	PL 1/2 x 22	0	4 1/2	
f1	134	3/8\"/>			
REV. NO. REVISION DESCRIPTION BY DATE HOLES: AS NOTED SHOP PAINT: NONE MATL. SPEC: PFER: ASTM A53 GR. B (WALD) TUBES: ASTM A500 GR. B WELD: FLG. BUTT & ORDERS: ASTM A992 GR. 50 OTHER SHAPES: ASTM A36 PLATE: ASTM A36 ISSUE STAMP RENO IRON WORKS 333 East Parr Blvd. RENO, NV 89512 Ph: 775 329-1111 Fax: 775 329-3555 DRAWING TITLE: STRAIGHT BRIDGE GIRDERS PROJECT: UNR SIMPLE BRIDGE LOCATION: RENO, NV DRAWN BY: ME DATE: 11/6/14 JOB NO. 4390 CHECKED BY: MPE DATE: 11/6/14 SHEET NO. 1 DESIGN REF. SHEET 1-5					